

**Study of the Hydro-transport of Agricultural Biomass Residue in Vertical and
Inclined Pipelines**

by

Kashif Javed

A thesis submitted in partial fulfillment of the requirements for the degree of

Doctor of Philosophy

in

Engineering Management

Department of Mechanical Engineering

University of Alberta

© Kashif Javed, 2023

Abstract

The increasing energy demand, dependency on fossil fuels, reduction in their reserves, and rise in greenhouse gas (GHG) emissions have drawn global attention toward a more viable alternative, such as biofuels produced from agricultural residue biomass which is an abundantly available type of lignocellulosic biomass globally. Currently, commercial-scale bio-based energy facilities have capacities significantly below those of fossil fuel-based plants, mainly due to high transportation cost of biomass feedstocks. Earlier research has demonstrated that transporting biomass as water-based slurries through horizontal pipes from farms to bio-refineries significantly reduces the transportation costs. However, for a long-distance large-scale biomass pipeline network, inclined and vertical pipe sections will be needed in addition to the horizontal pipe sections to meet the on-site processing at the biomass-based facility or to adapt to the route's topography throughout the pipeline layout. There is very limited understanding of the behavior of biomass slurry when flowing through inclined and vertical pipes. This study designed and built a 29 m closed-circuit lab-scale pipeline facility with vertical and inclined test sections to examine the hydro-transport of knife-milled and pre-classified agricultural residue biomass (ARB) particles through pipes at different angles. The aqueous suspensions (or slurries/mixtures) of two different ARB feedstocks (i.e., wheat straw and corn stover) were prepared over a wide range of particle size and slurry saturated mass concentrations. The slurry was pumped over a range of slurry bulk velocities through a closed pipeline loop with vertical and inclined pipe sections at different angles. The research's primary goals are to (1) experimentally investigate the frictional behaviour and delivered concentration of a specific particle size group of wheat straw water suspensions in vertical upward flows at varied flow conditions, (2) experimentally study how particle size, slurry solid mass concentration, and bulk velocity affect frictional pressure drops and delivered concentrations of

wheat straw-water slurries in vertical upward flows, (3) compare the frictional behaviour of corn stover and wheat straw-water slurries in vertical upward flows under varying flow conditions, (4) develop empirical correlation to predict the frictional pressure drop of ARB slurry flows across vertical pipes, (5) experimentally examine how different pipe inclinations impact the frictional behaviour of wheat-straw water suspensions under varying flow conditions. The study findings indicate that several factors, including feedstock, particle size, particle type, slurry concentration, slurry velocity, and pipe inclination, significantly influence the frictional behaviour of the ARB slurries. ARB slurries exhibit drag reduction, which increases with particle size and concentrations. The maximum drag reduction for a particular particle size depends on slurry velocity, feedstock, and pipe tilt; however, the associated critical concentration ($(C_m)_{cr}$) is a vital function of particle size and suspension velocity regardless of the pipe slope. Most corn stover suspensions in vertical upward flows reduce drag better than wheat straw for velocities $\geq 2.5 \text{ m s}^{-1}$, while wheat straw suspensions dominate for low rates (i.e., $\leq 2.0 \text{ m s}^{-1}$). The proposed empirical correlation precisely predicts the frictional pressure drop of ARB slurry flows in vertical pipes, providing a base case for other fibrous biomass materials. Furthermore, the onset velocity of drag reduction (v_{OD}) reduces for most ARB suspensions in vertical or inclined flows initially up to a specific threshold concentration, after which the slurry behaviour reverses and v_{OD} increases. Finally, the inclined flows of wheat straw slurries demonstrate maximum drag reduction and minimum v_{OD} compared to uphill flows for all the flow conditions. However, uphill flows show nonmonotonic variations in v_{OD} and drag reduction, requiring further investigation involving various particle sizes and higher slopes. The research outcomes may assist in designing and operating a long-distance integrated pipeline network for biomass transportation to produce biofuels on a large scale.

Preface

This thesis is an original intellectual work by the author, Kashif Javed. The following are some published sections from this work:

Chapter 2 of this thesis was published as Javed, K., Vaezi, M., Kurian, V., & Kumar, A. Frictional behaviour of wheat straw-water suspensions in vertical upward flows, *Biosystems Engineering Journal*, 2021, 212: 30-45. Kashif Javed was the principal author of this publication. Dr. Mahdi Vaezi and Dr. Vinoj Kurian provided intellectual guidance and support with manuscript writing. The conceptual design, installation, and commissioning of the vertical test section attached to the slurry loop were developed mainly by Kashif Javed, with a partial contribution from Dr. Mahdi Vaezi. Kashif Javed conducted the biomass-water suspension experiments through the vertical test section and TGA analysis in collaboration with Dr. Mahdi Vaezi and Dr. Vinoj Kurian, respectively. Dr. Amit Kumar supervised this work, from the conceptual design of the slurry loop to the experimentation, assisted with data interpretation, and proofread the manuscript before submission.

Chapter 3 of this thesis was published as Javed, K., Kurian, V., & Kumar, A. Effect of particle size and concentration on the frictional behaviour of vertical upward flows of wheat straw aqueous slurries, *Chemical Engineering Research and Design Journal*, 2022, 186: 614-627. Kashif Javed was the principal author of this publication. Dr. Vinoj Kurian provided intellectual guidance and manuscript writing assistance. The experiments on vertical test section and TGA analysis were mainly carried out by Kashif Javed in collaboration with Dr. Vinoj Kurian. Dr. Amit Kumar supervised this work, assisted with data interpretation, and provided intellectual guidance and support with manuscript composition and proofreading before submission.

Chapter 4 of this thesis was published as Javed, K., Kurian, V., & Kumar, A. Comparison of maize stover and wheat straw slurries flow in vertical pipes, *Biosystems Engineering Journal*, 2022, 224: 259-282. Kashif Javed was the principal author of this publication. Dr. Vinoj Kurian provided intellectual guidance and support with manuscript writing. The experiments on vertical test section were mainly carried out by Kashif Javed in collaboration with Dr. Vinoj Kurian. Dr. Amit Kumar supervised this project, helped with data analysis, and provided intellectual guidance and support with manuscript composition and proofreading before submission.

Chapter 5 of this thesis was published as Javed, K., Kurian, V., & Kumar, A. The development of empirical correlation to understand the frictional behaviour of aqueous biomass slurry flows in vertical pipes, *Journal of the American Society of Agricultural and Biological Engineers*, 2023 (in Press). Kashif Javed was this publication's principal author, including model development, analysis, and manuscript composition. Dr. Vinoj Kurian provided intellectual guidance and support with manuscript writing. Dr. Amit Kumar supervised this work, assisted with data interpretation, and provided intellectual guidance and support with manuscript composition and proofreading before submission.

Chapter 6 of this thesis has been accepted for publication and is under review as Javed, K., & Kumar, A. Experimental study on two-phase (solid-liquid) flows of ground wheat straw in inclined pipes, *Journal of the American Society of Agricultural and Biological Engineers*. Kashif Javed was the principal author of this publication. The conceptual design, installation, and commissioning of the inclined test section attached to the slurry loop were developed mainly by Kashif Javed in collaboration with Dr. Vinoj Kurian. Dr. Amit Kumar supervised this work, assisted with data interpretation, and provided intellectual guidance and support with manuscript composition and proofreading before submission.

Dr. Amit Kumar was the supervisory author of the entire work and was actively involved in concept development and manuscript edits throughout the research.

*Dedicated to my wonderful and loving mother,
Surriya Begum (late), and my great father Naimat-ullah (late),
for their unconditional love and support*

Acknowledgements

I want to thank my supervisor, Dr. Amit Kumar, for allowing me to conduct this research. This thesis would not have been possible without his vast expertise, insightful feedback, and enthusiastic engagement in the research. The research and writing for this thesis were only possible with his direction. I am grateful for everything I learned throughout my graduate studies at the University of Alberta and for the opportunity to work with Dr. Kumar. I cannot express enough gratitude for his support and kindness. The authors thank Canada's Natural Sciences and Engineering Research Council (NSERC) for financial support. As a part of the University of Alberta's Future Energy Systems research initiative, this research was made possible thanks to funding from the Canada First Research Excellence Fund.

I want to thank Dr. Rajender Gupta, Dr. Bipro Dhar, Dr. Cagri Ayranci, Dr. Igathinathane Cannayen, Dr. Rafiq Ahmad, and Dr. Prashant Waghmare for their helpful feedback and inquiries as part of my supervisory and examination committees.

I am thankful to one of my postdoctoral fellows, Dr. Mahdi Vaezi, for his advice and guidance in the initial phase of my Ph.D. I want to especially thank my postdoctoral fellow, Dr. Vinoj Kurian, for his guidance, time, advice, and ideas that helped me with most of my Ph.D. Dr. Vinoj Kurian was amiable, helpful, and encouraging.

I want to thank my beloved brother, Tahir Javed, for his unwavering support and advice throughout my life. As an engineer and beautiful human being, he has been the first inspiration and academic mentor for me to grow in the professional field. I also want to thank my sisters and mother-in-law for their invaluable spiritual encouragement and devout prayers.

Above all, I especially want to thank my loving wife, Sameera, and my children for their affection, encouragement, supplication, and strong faith in my ability to succeed despite the numerous challenges I encountered throughout my doctoral studies.

Ms. Astrid Blodgett deserves many thanks for proofreading and editing numerous pages of my papers and thesis. Throughout the editing process, her comments helped me become a better writer. I appreciate the help with administrative tasks from Dr. Kumar's group's project administrators, Rachel Schofield, Ashley Chomiak, and Caitlin Aspland.

I also want to express my gratitude to the Mechanical Engineering Department's administrative support, Machine Shop supervisor Roger Marchand, design engineer Liam Abrams and technicians, particularly Andrew and Daniel Moony, for their assistance in modifying and fabricating the pipeline loop. I want to thank Mr. Farooq Mir from Cameron (Calgary) for his technical support in installing and calibrating different pressure transmitters and Mr. Artin Afacan from the University of Alberta.

I want to acknowledge the members of the Sustainable Energy Research Group for their assistance during my time in this group. I also want to thank my friends Dr. Neelanjana Bhattacharjee, Umar Shafique, Madhumita Patel, Ali Raza, Muhammad Islam, Md Mustafizur Rahman, Krishna Sapkota, Prashant Patel, and Wasel-Ur-Rehman for their unwavering support, encouragement, and friendship.

Table of Contents

Abstract.....	ii
Preface.....	iv
Acknowledgements	viii
List of Tables	xvi
List of Figures.....	xviii
List of Symbols	xxvi
Chapter 1: Introduction	1
1.1 Background	1
1.2 Objectives.....	12
1.3 Scope and limitations	14
1.4 Organization of the thesis.....	14
Chapter 2: Frictional Behaviour of Wheat Straw-Water Suspensions in Vertical Upward Flows.....	16
2.1 Introduction	16
2.2 Method	21
2.2.1 Experimental setup.....	21
2.2.2 Calibration of the differential pressure transmitter (DPT).....	22
2.2.3 Standard method for assessing in situ concentrations.....	24
2.2.4 Wheat straw feedstock and slurry preparation.....	30
2.2.5 Procedure for measuring delivered concentrations of wheat straw-water mixtures	32

2.2.6	Uncertainty analysis.....	33
2.3	Experimental results and discussion	35
2.3.1	Delivered concentrations of wheat straw-water mixtures.....	35
2.3.2	Frictional loss measurements of vertical upward flows of wheat straw-water suspension	37
2.3.3	Flow regions in vertical upward flows of wheat straw-water suspensions.....	39
2.3.4	Drag reduction in upward flows of wheat straw-water suspension	42
2.4	Conclusions	45
Chapter 3: The Effect of Particle Size and Concentration on the Frictional Behaviour of Vertical Upward Flows of Wheat Straw Aqueous Slurries		48
3.1	Introduction	48
3.2	Method	52
3.2.1	Experimental setup.....	52
3.2.2	Calibration.....	54
3.2.3	Wheat straw feedstock preparation.....	55
3.2.4	Wheat straw slurry preparation procedure	57
3.2.5	In situ concentration measurement	58
3.2.6	Friction factor and viscosity measurements.....	59
3.2.7	Uncertainty analysis.....	61
3.3	Experimental results and discussion	62

3.3.1	Delivered concentration measurements of wheat straw aqueous slurry	62
3.3.2	Frictional loss measurements of wheat straw-aqueous slurries	65
3.4	Conclusion.....	77
Chapter 4: Comparison of Corn Stover and Wheat Straw Slurry Flow in Vertical Pipes..		80
4.1	Introduction	80
4.2	Method	85
4.2.1	Experimental setup.....	85
4.2.2	Calibration.....	87
4.2.3	Feedstock preparation	88
4.2.4	Particle size analysis	88
4.2.5	Types of ground corn stover particles.....	94
4.2.6	Corn stover slurry preparation	98
4.2.7	Uncertainty analysis.....	100
4.3	Experimental results and discussion	101
4.3.1	Frictional loss measurements of corn stover-water suspension.....	101
4.3.2	Comparison of frictional loss behaviour of different feedstocks in hydro transport through a vertical pipe section	119
4.4	Conclusion.....	127
Chapter 5: The Development of Empirical Correlations to Understand the Frictional Behaviour of Aqueous Biomass Slurry Flows in Vertical Pipes		129
5.1	Introduction	129

5.2	Materials and method	136
5.2.1	Feedstock preparation	136
5.2.2	Particle size and shape analysis	137
5.2.3	Experimental setup.....	140
5.2.4	Slurry preparation and pressure drop measurements	142
5.2.5	In situ concentration measurements.....	144
5.3	Experimental results and discussion	145
5.3.1	Vertical upward flows of biomass and classical solids-water slurries.....	145
5.3.2	Development of empirical correlation	151
5.3.3	Onset velocity of drag reduction (v_{OD})	167
5.4	Conclusion.....	169
 Chapter 6: Experimental Study on Two-Phase (Solid-Liquid) Flows of Ground Wheat		
Straw in Inclined Pipes		171
6.1	Introduction	171
6.2	Materials and method	176
6.2.1	Experimental setup.....	176
6.2.2	Physical arrangement for various pipe inclinations	179
6.2.3	Locations of pressure ports	181
6.2.4	Feedstock preparation and particle size analysis	182
6.2.5	Slurry preparation	185

6.2.6	Slurry pressure drop measurements	186
6.2.7	Moisture content and density measurements	187
6.2.8	Calibration of the inclined pipe section	189
6.3	Experimental results and discussion	194
6.3.1	Frictional behaviour of various solids-water mixtures in inclined flows	194
6.3.2	Effect of inclination on frictional behaviour of wheat straw-water slurries	200
6.3.3	Uncertainty analysis.....	216
6.4	Conclusion.....	217
Chapter 7: Conclusions and Recommendations for Future Work		220
7.1	Conclusions	220
7.1.1	Estimation of ARB suspension's in situ concentration	220
7.1.2	Effect of particle size and flow conditions on frictional behaviour of wheat straw-water suspension in vertical upward flows	221
7.1.3	Effect of particle size and flow conditions on frictional behaviour of corn stover-water suspension in vertical upward flows	222
7.1.4	Comparison of frictional behaviour of ARB feedstock in vertical upward flows	223
7.1.5	Modeling the frictional behaviour of ARB slurries in vertical upward flows	224
7.1.6	Effect of pipe inclination on frictional behaviour of wheat straw suspensions	224
7.2	Recommendations for Future Work.....	226
7.2.1	Investigate the effect of large slopes in inclined pipes on the frictional behaviour of agricultural residue biomass-water suspensions	227

7.2.2	Develop empirical correlation to model aqueous-based agricultural residue biomass slurry flow behaviour in inclined pipe sections	227
7.2.3	Examine the impact of pipe diameter on the frictional behaviour of agricultural residue biomass-water slurry	228
7.2.4	Techno-economic analysis of pipeline hydro-transport of agricultural residue biomass slurries for an integrated long-distance pipeline network.....	228
7.2.5	Investigate the effect of wide particle size range and slurry temperature on the frictional behavior of agricultural residue biomass-water slurry flows through pipes.	229
7.2.6	Investigate local velocity and concentration profiles of agricultural residue biomass-water slurry flows through horizontal, vertical and inclined pipes.....	230
Bibliography		231
Appendix A		256
Appendix B		284
Appendix C		296
Appendix D		301

List of Tables

Table 2.1: Physical properties of the conventional solid materials used in concentration-measurement experiments.....	25
Table 3.1: Particle morphology of wheat straw (Vaezi et al., 2014)	56
Table 3.2: Volume and mass percentages of saturated and dry solids of wheat straw-water mixtures	58
Table 4.1: Particle morphology of agricultural residue biomass using Camsizer	93
Table 4.2: Volume and mass percentages of saturated and dry solids of corn stover-water mixtures	99
Table 4.3: Average fiber distance and crowding number for corn stover- and wheat straw-aqueous slurries of 19.2 mm, 6.4 mm, 3.2 mm, and <3.2 mm particle sizes.....	106
Table 4.4: The suspensions of agricultural residue biomass in vertical upward flows exhibiting abrupt drag increase just after their $(C_m)_{cr}$'s	127
Table 5.1: Physical properties of wheat straw, corn stover, and classical solids particles used in experiments (reprinted from Javed et al. [2022a] with permission from Elsevier)	139
Table 5.2: Physical properties of aqueous slurries of wheat straw, corn stover, and classical solids particles used in experiments	144
Table 5.3: Estimated regression coefficients for the proposed empirical correlation given in Equation 5.5	156
Table 5.4: The p-values of the empirical models with higher degrees of independent variables	159

Table 5.5: Estimated regression coefficients for the modified empirical correlations presented in Equation 5.6	161
Table 5.6: Correlations of v_{OD} for vertical upward flows of aqueous suspensions of different agricultural residue biomass feedstocks.....	168
Table 6.1: The locations of the high- and low-pressure ports of the DPT and PTs on the inclined pipe section in the closed pipeline loop	182
Table 6.2: Particle morphology for knife-milled wheat straw particles of the 6.4 mm nominal size using the Camsizer (Javed et al., 2022a).....	183
Table 6.3: Volume and mass percentages of saturated and dry solids of wheat straw-water mixtures	188
Table 6.4: Physical properties of the fine sand solids used in the calibration of the inclined pipe section	190
Table 6.5: Mechanistic properties to comprehend the flow behaviour of the 6.4 mm nominal particle size wheat straw-water suspension	209

List of Figures

Figure 2.1: Schematic diagram of experimental setup.....	21
Figure 2.2: Friction factor vs. Reynolds number of water flowing through a vertical test section.	24
Figure 2.3: (a) The effect of particle size on the delivered concentration of conventional solids- water slurries at a bulk velocity of 3.0 m s^{-1} and (b) The effect of bulk velocity on the delivered concentration (C_{vd}) for medium sand.	27
Figure 2.4: Frictional pressure drops for vertical upward flows of medium sand-water mixtures considering (a) a prepared concentration (C_{vp}) and (b) a delivered concentration (C_{vd}).....	29
Figure 2.5: Delivered concentration measurement. (a) Location of in situ concentration in the vertical test section, (b) Inside view of mixing tank, (c) Wheat straw sample after water was filtered from the mixture with fine strainer, and (d) Wheat straw sample after surface water was removed.	32
Figure 2.6: Repeatability of two sets of experiments on medium sand, glass beads, and wheat straw slurries in a 50 mm diameter vertical test section.	34
Figure 2.7: (a) Effect of bulk velocities on delivered concentrations (C_{md}) and (b) average ratios of C_{md} and C_{mp} at 3.0 m s^{-1} for 19.2 mm wheat straw.	35
Figure 2.8: Frictional pressure drops for water-based mixtures of 19.2 mm wheat straw particles using saturated solid concentrations (% mass) through (a) a vertical test section and (b) a horizontal test section (results reproduced from Vaezi et al. [2014]; used with permission from Elsevier).	37

Figure 2.9: The friction factor versus generalised Reynolds number for velocities $\geq 1.0 \text{ m s}^{-1}$ for vertical upward flows of water-based mixtures of 19.2 mm wheat straw particles measured in the experimental setup (flow regions 1, 2, and 3 were adopted from Radin et al. [1975] for vertical upward flows).	40
Figure 2.10: (a) Drag ratio versus mixture bulk velocity for several solid concentrations of 19.2 mm wheat straw particles flowing through a vertical test section and (b) Drag reduction as a function of a slurry solid concentration of 19.2 mm wheat straw particles at maximum slurry velocities flowing through a horizontal test section (results reproduced from Vaezi et al. [2014]; used with permission from Elsevier) and vertical upward flows (current investigation).	43
Figure 3.1: Schematic of integrated pipeline facility.	53
Figure 3.2: (a) Delivered flow rate test for water and (b) Frictional pressure drop vs. bulk velocity of water through a vertical test section.	54
Figure 3.3: The repeatability of two sets of experiments on wheat straw aqueous slurries of 6.4 mm, 3.2 mm, and <3.2 mm particle sizes in a 50 mm diameter vertical test section.	61
Figure 3.4: The effect of bulk velocities on delivered concentrations (C_{md} 's) of wheat straw aqueous slurries of different particle sizes.	62
Figure 3.5: The effect of particle size on the average ratio of C_{md} to C_{mp} of wheat straw aqueous slurries at 3.0 m s^{-1} (the results for the 19.2 mm particles were taken from Javed et al. [2021]).	64
Figure 3.6: Frictional pressure drops for aqueous slurries of 6.4 mm wheat straw particles through (a) a vertical test section and (b) a horizontal test section (results reproduced from Vaezi et. al. [2014] (Vaezi et al., 2014); used with permission from Elsevier).	66

Figure 3.7: The effect of particle size in vertical upward flows of wheat straw-aqueous slurries on (a) frictional pressure drop for the entire range of bulk velocities at the saturated mass concentration of 25% and (b) drag reduction for a range of saturated mass concentrations at the highest achievable bulk velocity.....	68
Figure 3.8: The effect of bulk velocity in vertical upward flows of several wheat straw-aqueous slurry sizes for $C_{mp} = 5\text{-}30\%$ (the results for the 19.2 mm particles were adopted from our earlier study (Javed et al., 2021)).	71
Figure 3.9: Friction factor versus generalised Reynolds number for velocities $\geq 1.0 \text{ m s}^{-1}$ for vertical upward flows of wheat straw-aqueous slurries of (a) 6.4 mm, (b) 3.2 mm, and (c) <3.2 mm particle sizes.....	75
Figure 4.1: Schematic of a closed-circuit pipeline facility.	86
Figure 4.2: (a) Calibration of differential pressure transmitter and (b) frictional pressure drop vs. bulk velocity of water and fine sand through a vertical test section.	87
Figure. 4.3: Microscopic Camsizer camera images (not to scale) of corn stover of nominal sizes: (a) 19.2 mm, (b) 6.4 mm, (c) 3.2 mm, and (d) <3.2 mm	90
Figure 4.4: Particle size distribution of several sizes of corn stover (C.S) and wheat straw (W.S): (a) Cumulative distribution by volume and (b) frequency distribution by volume.	91
Figure 4.5: Microscopic images of sub-categories of particles obtained from samples of a 19.2 mm nominal size of corn stover (ground leaves and stalks) samples. Type A: Rib-like particles with plain surfaces, Type B: Rib-like particles with rough surfaces, Type C: Hair-like particles, Type D: Flake-like particles, Type E: Wide flake-like particles, Type F: Irregular-shaped thick particles, and Type G: Mixed form particles.....	95

Figure 4.6: (a) Average mass percentages and (b) Percentage number distribution obtained from ImageJ of the sub-categories of corn stover particles as a function of their shape for a 19.2 mm nominal particle size. Type A: Rib-like particles with plain surfaces, Type B: Rib-like particles with rough surfaces, Type C: Hair-like particles, Type D: Flake-like particles, Type E: Wide flake-like particles, Type F: Irregular-shaped thick particles, and Type G: Mixed form particles.....	96
Figure 4.7: The repeatability of two sets of experiments on corn stover-aqueous slurries of 19.2 mm, 6.4 mm, 3.2 mm, and <3.2 mm particle sizes in a 50 mm diameter vertical test section. ..	100
Figure 4.8: Friction factor versus generalised Reynolds number for velocities $\geq 1.0 \text{ m s}^{-1}$ in vertical upward flows of corn stover-water suspensions of (a) 19.2 mm, (b) 6.4 mm, (c) 3.2 mm, and (d) <3.2 mm particle sizes.	102
Figure 4.9: Logarithmic plot of the frictional pressure drop and bulk velocity of aqueous corn stover slurries of 19.2 mm, 6.4 mm, 3.2 mm, and <3.2 mm in vertical upward flows for several mass concentrations and the complete range of bulk velocities (point D in Figure 4.8).....	108
Figure 4.10: Contact numbers for corn stover- and wheat straw-aqueous slurries of 19.2 mm, 6.4 mm, 3.2 mm, and <3.2 mm at various mass concentrations.	109
Figure 4.11: The effect of particle size in vertical upward flows of corn stover-aqueous slurries for a range of slurry bulk velocities ($1.0\text{-}4.0 \text{ m s}^{-1}$) on the frictional pressure drop at saturated mass concentrations of (a) 20% (mass), (b) 15% (mass), and (c) drag reduction for a range of mass concentrations (5-25%).	111
Figure 4.12: Onset velocity of drag reduction obtained at several mass concentrations of corn stover-aqueous slurries of 19.2 mm, 6.4 mm, 3.2 mm, and <3.2 mm while flowing upward in the vertical pipe.....	116

Figure 4.13: Slurry solid concentration versus frictional pressure drop at constant nominal velocities for 19.2 mm, 6.4 mm, 3.2 mm, and <3.2 mm corn stover (C.S) and wheat straw (W.S) particle slurries measured using the current experimental setup (the wheat straw slurry results were adopted from our earlier studies (Javed et al., 2022b; Javed et al., 2021)).....	120
Figure 4.14: Drag reduction of different feedstocks of similar particle sizes of corn stover (C.S.)- and wheat straw (W.S.)-water slurries in vertical upward flows for a range of saturated mass concentrations (5-35%) and nominal velocities at (a) 4.0 m s ⁻¹ , (b) 3.5 m s ⁻¹ , (c) 3.0 m s ⁻¹ , (d) 2.5 m s ⁻¹ , (e) 2.0 m s ⁻¹ , and (f) 1.5 m s ⁻¹ . The wheat straw slurry results were adapted from our earlier work (Javed et al., 2022b; Javed et al., 2021).....	123
Figure 4.15: Critical mass concentration versus slurry bulk velocity for vertical upward flows of corn stover (C.S.)- and wheat straw (W.S.)-water suspensions of 19.2 mm, 6.4 mm, 3.2 mm, and <3.2 mm.	125
Figure 5.1: Microscopic images (not to scale) captured by high-speed digital Camsizer cameras for wheat straw particles of nominal sizes (a) 19.2 mm, (b) <3.2 mm and corn stover particles of nominal sizes (c) 19.2 mm, (d) <3.2 mm.	138
Figure 5.2: Schematic of the experimental setup: (1) centrifugal slurry pump, (2) drain valve-1, (3) glycol chiller, (4) counter-flow heat exchanger, (5) thermocouple, (6) flow visualisation section, (7) magnetic flow meter, (8) temperature sensor, (9) drain valve-2, (10) 90° bend, (11) differential pressure transmitter, (12) return pipe, (13) mixer with double impeller, (14) mixing tank, (15) water supply tank, (16) data logger, (17) watt transducer, (18) variable frequency drive.....	140
Figure 5.3: (a) Variation and (b) Percentage change per hour in the measured pressure drops and velocities of typical corn stover and wheat straw-water slurries pumped through a 50 mm diameter closed pipeline circuit.	143

Figure 5.4: Friction factor versus generalised Reynolds number for velocities $>0.5 \text{ m s}^{-1}$ in a 50 mm diameter pipeline for vertical upward flows of various volumetric and saturated mass concentrations of slurries of (a) fine sand particles and (b) wheat straw and corn stover particles.	146
Figure 5.5: Logarithmic plot of frictional pressure drop and slurry bulk velocity ($0.5\text{-}4.3 \text{ m s}^{-1}$) in vertical upward flows of corn stover- and wheat straw-water slurries of various particle sizes and high mass concentrations (25%-40%).	150
Figure 5.6: The plot of the complete set of data points (2511) of experimentally obtained frictional pressure drops of agricultural residue biomass-water slurries at their corresponding velocities in vertical upward flows.....	152
Figure 5.7: Predicted versus experimental results for the entire 2511 data points.	157
Figure 5.8: Residuals of the modified numerical model for 754 data points.....	164
Figure 5.9: (a) Accuracy of the numerical model to predict frictional pressure drops for 754 experimental measurements (i.e., the test set) and (b) A comparison of numerically predicted and experimentally measured frictional pressure drops for different particle sizes and concentrations of agricultural residue biomass-water slurries in vertical upward flows.	165
Figure 6.1: Schematic of the experimental setup: (1) centrifugal slurry pump, (2) drain valve-1, (3) drain tub, (4) counter-flow heat exchanger, (5) glycol chiller, (6) thermocouple, (7) flow visualisation section, (8) magnetic flow meter, (9) temperature sensor, (10) semicircular pipe bend, (11) inclined pipe section, (12) pressure transducer, (13) inclinometer, (14) differential pressure transmitter, (15) lifting mechanism for inclined pipe, (16) drain valve-2, (17) return pipe, (18)	

mixer with double impeller, (19) mixing tank, (20) water supply tank, (21) data logger, (22) watt transducer, (23) variable frequency drive. 177

Figure 6.2: (a) Supporting structure and lifting mechanism for the inclined pipe section, (b) The inclined pipe section in ascending position for an inclination angle (θ) = 21° , and (c) The inclined pipe section in horizontal position at a height of 0.43 m above the ground. 180

Figure 6.3: Microscopic images for the 6.4 mm nominal size of wheat straw particles taken by (a) high-speed Camsizer digital cameras (not to scale) and (b) light microscope (Zeiss Stemi 508). 184

Figure 6.4: Calibration of the inclined pipe section at (a) $\theta = -7^\circ$ to $+21^\circ$ using clear water and (b) $\theta = +14^\circ$ and 0° using fine sand-water slurries of $d_{50} = 0.103$ mm for solid particles at volumetric concentrations of 5% and 1%, respectively 193

Figure 6.5: Frictional pressure drops for fine sand-water mixtures for velocities ≥ 1.0 m s⁻¹ and volumetric concentrations of $C_V = 1$ -5% flowing through a 50 mm diameter inclined pipe section of (a) $\theta = +14^\circ$ and (b) $\theta = +21^\circ$ 194

Figure 6.6: Frictional pressure drops for aqueous slurries of a 6.4 mm particle size of wheat straw for velocities ≥ 0.5 m s⁻¹ and $C_m = 5$ -30% flowing through a 50 mm diameter inclined pipe section at (a) $\theta = +14^\circ$ and (b) $\theta = +21^\circ$ 197

Figure 6.7: Friction factor versus generalised Reynolds number for velocities ≥ 0.5 m s⁻¹ of the 6.4 mm particle size of wheat straw-water slurry flows through a 50 mm inside diameter pipe section with inclination angles of (a) $\theta = 0^\circ$, (b) $\theta = -7^\circ$, (c) $\theta = +7^\circ$, (d) $\theta = +14^\circ$, (e) $\theta = +21^\circ$ relative to the x-axis 203

Figure 6.8: Onset velocity of drag reduction (v_{OD}) for the 6.4 mm particle size wheat straw-water slurries of several mass concentrations flowing through an inclined pipe section of varying inclinations (i.e., $\theta = -7^\circ$ to $+21^\circ$) relative to the x-axis.	208
Figure 6.9: Drag reduction of the 6.4 mm particle size of wheat straw-water slurries for $C_m = 5$ -30% flowing through an in inclined pipe section of various inclinations (i.e., -7° to $+21^\circ$) and slurry bulk velocities of (a) 4.5 m s^{-1} and (b) 2.0 m s^{-1}	213
Figure 6.10: The repeatability of the experimental measurements for various mass concentrations of the 6.4 mm nominal particle size of wheat straw-water slurry flow through a 50 mm inside diameter pipe section at different angles of inclination.	217

List of Symbols

D	Inner diameter of the pipe (m)
L	Span of vertical, inclined, or horizontal test section (mm)
ρ_m	Density of the mixture (kg m^{-3})
ρ_w	Density of water (kg m^{-3})
ρ_f	Density of the carrier fluid (kg m^{-3})
ρ_s	Density of the solid particles (kg m^{-3})
f_D	Darcy-Weisbach friction factor
h_f	Loss of head due to friction (m)
S	Specific gravity or relative density $\left(\frac{\rho_s}{\rho_w}\right)$
R_{pipe}	Inner radius of the pipe (m)
R_C	Radius of the curvature of the bend (m)
$\frac{R_C}{D}$	Ratio of the radius of the curvature of 90° bend to the pipe's inner diameter
v_D	Critical deposition velocity (m s^{-1})
v_4	Pseudo-homogenous velocity (m s^{-1})
v_m	Bulk velocity of the mixture (slurry) (m s^{-1})
v_w	Bulk velocity of water (m s^{-1})
v_f	Bulk velocity of the carrier fluid (m s^{-1})
v_t	Terminal settling velocity (m s^{-1})
v_{OD}	Onset velocity of drag reduction (m s^{-1})

v_{max}	Maximum velocity in the plug flow region (m s^{-1})
v_{wt}	Suspension velocity at onset of turbulence in the water annulus (m s^{-1})
C_{Vd}	Delivered concentration (% volume)
C_{Vp}	Prepared concentration (% volume)
C_{md}	Delivered concentration (% mass)
C_{mp}	Prepared concentration (% mass)
C_V	Volumetric concentration (% volume)
$C_{in-situ}$	In situ concentration (% volume)
C_m	Saturated mass concentration (% mass)
$(C_m)_{cr}$	Critical mass concentration for maximum drag reduction (%)
Re_g	Generalised Reynolds number, $\left(\frac{\rho_m v_m D}{\mu_f}\right)$
μ_f	Dynamic viscosity of carrier fluid (Pa s)
μ_w	Dynamic viscosity of water (Pa s)
ρ_f	Density of carrier fluid or water (kg m^{-3})
ϑ_f	Kinematic viscosity of carrier fluid or water ($\text{m}^2 \text{s}^{-1}$)
g	Acceleration due to gravity (m s^{-2})
e	Absolute roughness of the pipe (mm)
ε	Relative roughness of the pipe (mm mm^{-1})
d_p	Mean particle diameter or d_{50} , (mm)
$\frac{\Delta P_T}{L}$	Total pressure drop (kPa m^{-1})

$\frac{\Delta P_{MD}}{L}$	Measured pressure drop (kPa m ⁻¹)
$\left(\frac{\Delta P_f}{L}\right)_m$	Frictional pressure drop of the mixture (kPa m ⁻¹)
$\left(\frac{\Delta P_f}{L}\right)_w$	Frictional pressure drop of water (kPa m ⁻¹)
$\left(\frac{\Delta P_f}{L}\right)_{m,\theta}^{Exp}$	Experimental frictional pressure drops of the mixture flowing through an inclined test section
$\left(\frac{\Delta P}{L}\right)_{m,\theta}^{Md}$	Measured/manometric pressure drops of the mixture flowing through an inclined test section
$\left(\frac{\Delta P}{L}\right)_{m,\theta}^{Total}$	Total pressure drop of the mixture flowing through an inclined test section
θ	Angle of inclination of the pipe with respect to the x-axis
P_x	Precision uncertainty (corresponding unit)
B_x	Bias uncertainty (corresponding unit)
U_x	Total uncertainty, $\left(U_x = \sqrt{\sum(B_x^2 + P_x^2)}\right)$, (corresponding unit)
d_{c_min}	Shortest cord diameter (mm)
d_{FE_max}	Feret diameter (mm)
φ_p	Particle/fiber aspect ratio
D_{XX}	Feret or shortest cord diameter in mm at respective XX^{th} percentiles of the cumulative distributions of particles
Q_3	Cumulative distribution based on volume (%)
q_3	Frequency distribution based on volume ($q_3 = dQ_3/d_x$) (% mm ⁻¹)

n	Fiber number fraction, $\left(\frac{4}{\pi} C_V \frac{1}{X_{gl} X_{gw}^2}\right)$
h_{av}	Average inter-fiber distance
X_{gw}	Geometric mean width (mm)
X_{gl}	Geometric mean length (mm)
X_{ig}	Graphic mean length (mm)
$X_{ig,w}$	Graphic mean width (mm)
σ_{ig}	Graphic standard deviation (mm)
n_c	Fiber contact number
N	Fiber crowding number
DRs	Drag ratios
MC	Moisture content, (% mass)
%DR	Drag reduction (%)
$a_n, b_n, d_n, e_n, h_n, j_n,$ $k_n, l_n, p_n, q_n, r_n, t_n,$ $u_n, w_n, y_n, z_n, \alpha_n, \beta,$ δ	Constants for empirical model of frictional pressure drop
k, n	Subscripts for model coefficients
Q	Volume flow rate (L s ⁻¹)
V_w	Volume of water (m ³)
ID	Inner diameter of the pipe (mm)
ARB	Agricultural residue biomass
C.S	Corn stover

W.S	Wheat straw
GHG	Greenhous gas
EJ	Exajoule
PSD	Particle size distribution
SEM	Standard error mean
LOOCV	Leave-one-out cross validation
IQR	Interquartile range
LOESS	Locally estimated scatter plot smoothing
PVC	Polyvinylchloride
DPT	Differential pressure transmitter
AIC	Akaike information criterion
SD	Standard deviation
asc	Ascending position of the inclined pipe with respect to the x-axis
desc	Descending position of the inclined pipe with respect to the x-axis
horiz	Horizontal position of the inclined pipe section with respect to the x-axis
DFC	Distance fixed cost
DVC	Distance variable cost

Chapter 1: Introduction

1.1 Background

Substantial growth in global human population coupled with technological developments, industrialization, urbanization, and increased transportation have significantly raised the global energy requirement. Over the past 70 years (i.e., 1950-2022), the world population increased from 2.5 billion to approximately 7.97 billion (United Nations, 2022); global energy demand increased five fold during this time span (Valone, 2021). To meet global energy demand, energy producers rely heavily on the use of non-renewable fossil fuels (i.e., crude oil, natural gas, coal, etc.). At present, more than 85% of global energy consumption is from fossil fuels; this consumption not only increases the prospects of exhausting these reserves in the near future (Halder et al., 2019; Vohra et al., 2014) but has adversely impacted the earth's atmosphere by emitting greenhouse gases (GHGs) (Goldemberg, 2008). GHGs generally contain carbon dioxide (CO_2), methane (CH_4), nitrous oxide (N_2O), and fluorinated gases (synthetic). GHGs are approximately 76% CO_2 . Since 1950, global atmospheric CO_2 emissions have increased approximately seven times their value at the time (i.e., 5000 million metric tonnes CO_2 in 1950). Without modifications to global energy policies, these emissions are projected to increase more than tenfold by 2050, increasing the earth's average yearly temperature, i.e., increased global warming (Center for Climate and Energy Solutions, 2023).

In order to reduce CO_2 emissions, policymakers reviewed various energy policies and came up with a new global energy model by combining independent plans for advanced economies, emerging markets, and developing economies with a primary target to achieve net zero emissions

by 2050 (International Energy Agency, 2021). This model focusses mainly on using more renewable resources (i.e., hydropower, solar, wind, nuclear, solid biomass, biogas, liquid biofuels, etc.) with a considerable decrease in fossil fuel use to just over 20% of the total energy supply in all energy sectors by 2050. That said, regardless of the steps taken to reduce dependence on fossil fuels in this new global energy model, transportation sector consumption of non-renewable oil (e.g., diesel or gasoline with a high energy density and low cost) in 2050 is expected to remain almost the same as what it is now (International Energy Agency, 2021).

At present, global energy demand in the transportation sector is met primarily by non-renewable oil, and approximately 50% of global fossil fuel energy is consumed by the sector (Halder et al., 2019). In 2050, of a total energy supply of 200 EJ from oil to all the energy sectors, the final energy consumption of non-renewable liquid fuels (i.e., oil) by the transportation sector is estimated to be 100 EJ. This is attributed to differences in technology maturity among advanced economies, emerging markets, and developing economies. The difference in maturity level is expected to be in two major technology transitions: (1) the shift to electric and fuel cell vehicles and (2) the shift to higher fuel blending ratios of renewable fuels with conventional petro-fuels and the direct use of low-carbon fuels (i.e., hydrogen-based fuels and biofuels) (International Energy Agency, 2021). Specifically, the complete phase-out of light- and heavy-duty vehicles running on non-renewable liquid fuels will not be possible in emerging markets and developing economies by 2050.

To overcome the transportation sector's heavy dependence on conventional petro-fuels, the blending of non-renewable liquid fuels with biofuels at a specific ratio could be replaced with the use of biofuels alone (Canada's Net Zero Future, 2021). The ratios of blending conventional petro-fuels with biofuels vary according to the available technology and energy policies in advanced economies, emerging markets, and the developing economies in the new global energy model.

Bioethanol and biodiesel are used as a blending agent with gasoline or conventional diesel, respectively, to achieve higher octane levels and reduce carbon monoxide and other emissions. This technology transition in the transportation sector seems more promising than a shift to electric and fuel cell vehicles in emerging markets and developing economies, primarily because rather than making huge investments in large infrastructure for distribution and consumption systems to meet supply and demand for electric and fuel cell vehicles, emerging markets and developing economies could more easily import biofuels from advanced economies. However, this requires that biofuels be available on a larger scale and at a lower cost than petro-fuels.

Biomass (a product obtained from a living organism or its by-products) is available in abundance the world over in various forms including as agricultural crops and wastes, animal manure, human sewage, wood and wood wastes from wood processing, and biogenetic materials retrieved from municipal solid wastes and can be used to generate biofuels (i.e., biodiesel, bioethanol, biohydrogen, jet fuel, etc.) (Kim & Dale, 2004; Saleem, 2022; U.S. Energy Information Administration, 2023). Biomass-derived biofuels have a higher energy density than “as received” biomass. They are the most reliable, carbon neutral, and sustainable fuels that have the potential to replace petroleum-based fuels (Pootakham & Kumar, 2010). Bioethanol is the most appealing of the renewable biofuels because of the low toxicity of both the fuel itself and the by-products generated through the incomplete oxidation of this type of fuel (Vohra et al., 2014). The process of producing bioethanol depends on the feedstock. The feedstocks for bioethanol can be divided into four main categories: first- (edible food, e.g., kernel and starchy crop biomass), second- (non-edible crops, e.g., lignocellulosic biomass and municipal solid wastes), third- (algal biomass), and fourth-generation (industrial waste CO₂) feedstocks (Halder et al., 2019; Lee & Lavoie, 2013). Today, biomass facilities rely largely on edible food crops (first-generation feedstock) to produce

bioethanol; however, their capacities are limited because of food security issues (Canada's Net Zero Future, 2021; Mohanty & Swain, 2019), and these issues will be larger in 2050, when the world population will reach approximately 9.7 billion (United Nations, 2022) and global food demand will increase by approximately 70% (Van Dijk et al., 2021). Commercial-scale bioethanol produced from third- and fourth-generation feedstocks is still in the early stages of development (Fetyan et al., 2022; Halder et al., 2019; Maity & Mallick, 2022).

Second-generation feedstocks, specifically agricultural and forest residues, seem to have greater potential for large-scale biofuel production globally than the other types of feedstocks. Bioethanol production from agricultural residue biomass has been gaining attention in the biofuel industry because of (1) the consistent and large availability of this feedstock around the world (Balat & Balat, 2009; Banerjee et al., 2010), (2) its low initial cost at agricultural farms (Balat & Balat, 2009), (3) clean combustion with a high potential of reducing GHG emissions (Banerjee et al., 2010; Halder et al., 2019), and (4) the absence of food security issues with respect to the present and future needs of the world's growing population (Halder et al., 2019). However, there are technological constraints in bioethanol production from lignocellulosic biomass (e.g., straw from canola, wheat, and corn) at biorefineries, as well as the logistics of transporting biomass feedstock from farms to biofuel plants, that prevent bio-based energy facilities from increasing their capacities to compete with the capacities of plants producing fossil-based fuels.

The main logistical constraint is the high cost of conventional truck or rail transport of biomass bales from farms to biorefineries (Aden et al., 2002; Kumar et al., 2005a). There is a trade-off between plant capital cost per unit output and transportation cost in the attempt to reach an economic optimum size (i.e., 2 M dry tonnes/yr) to produce low-cost fuel at bio-based energy facilities (Kumar et al., 2005a; Ruth, 1999). Unfortunately, the highest achievable capacity of a

biorefinery (based on the economic optimum size) would still be 25 times lower than a typical fossil fuel refinery's. Moreover, because of the low bulk density of biomass bales, the higher frequency of truck deliveries (15 standard highway trucks at 20 tonnes capacity each) associated with the economic optimum size of the biorefineries would increase traffic congestion and damage to the environment and local communities, and even then biofuel would not be able to compete with current fossil fuel production capacities (Sokhansanj et al., 2002).

The transportation cost of field/forest-based lignocellulosic biomass rises considerably with biorefinery capacity because more feedstock needs to be transported to meet the required biofuel production at the plant (Kumar et al., 2003; Sokhansanj et al., 2002). Earlier research by Kumar et al. (2004) proposed a novel solution to this problem and found that pipeline hydro-transport of agricultural residue biomass from farms to biorefineries (after chopping off biomass bales at pre-processing facilities located close to the farms) could be more economical than trucking for large-scale biofuel production. The authors demonstrated that establishing a pipeline network for hydro-transporting biomass from farms to biorefineries involves an initial truck delivery of dry biomass bales from farms to the pipe inlet at pre-processing facilities, which would encounter fixed costs associated with both truck transport and hydro-transport. However, the overall transportation cost of the biomass slurry through a long-distance pipeline network would be significantly lower compared to conventional truck delivery. In their techno-economic study, the authors assessed one- and two-way pipelining of biomass-water mixtures and found that pipeline delivery benefits from economies of scale (the capital cost per unit output decreases with an increase in scale), there are no traffic congestion issues found in overland transportation, and there is no process penalty at biorefineries using aqueous-based processes, i.e., fermentation, hydrothermal liquefaction, and hydrothermal hydrolysis for bioethanol production (Kumar et al., 2004, 2005a, 2005b). However,

these studies used pre-established correlations for the frictional pressure drop of wood chip-water slurries (originally developed by Hunt [1976]).

Agricultural residue biomass (i.e., corn stover and wheat straw) is fibrous and the particles have a wide range of aspect ratios (ARs) compared to wood chips. Therefore, to investigate the flow characteristics of these types of biomass-water slurries, Mohamadabadi (2009) and later Luk (2010) designed and fabricated a laboratory-scale closed pipeline loop with an ID (inner diameter) = 50 mm and determined the mechanical feasibility of the hydro-transport of agricultural residue biomass (wheat straw) of three nominal particle sizes (3.2 mm, 6.4 mm, and 19.2 mm) to saturated concentrations of up to 30% (by mass). The nominal sizes were selected because of the opening size of the classifier sieves. The term “nominal size” was used to assign each group of particles obtained in the four bottom-most sieves of the classifier a specific number, and these sizes were not a true representative of the particle size distribution. Luk et al. (2014) observed that agricultural residue biomass slurries behave differently than wood chips during pipeline hydro-transport and show decreasing pressure gradients compared to water alone and, hence, reduced drag (reduced friction loss in a slurry with respect to that of water alone at the same bulk velocity) with increasing solid mass concentrations and particle sizes (Luk et al., 2014).

Vaezi et al. further enhanced this research for different feedstocks (wheat straw and corn stover), particle sizes (<3.2 mm, 3.2 mm, 6.4 mm, 19.2 mm), and slurry solid mass concentrations (5-40%) of agricultural residue biomass and claimed through experimental evidence and techno-economic analysis that pipelining chopped aqueous-based agricultural residue biomass slurries at specific mass concentrations will reduce the transportation cost of the feedstock required for large-scale biofuel production enough that biorefineries can compete with the production capacity of fossil fuel-based plants (Vaezi et al., 2014; Vaezi et al., 2015). Vaezi et al. also found that the general

correlations for frictional pressure drop for wood chips derived by others (Brebner, 1964; Elliott, 1960; Faddick, 1963; Faddick, 1970; Gow, 1971; Hunt, 1976) were not applicable to agricultural residue biomass slurry (water-based) flows in pipelines because they had different flow characteristics. Subsequently, Vaezi and Kumar (2014a) derived a universal correlation for predicting the frictional pressure drop of agricultural residue biomass slurry flow through any diameter of horizontal pipeline as a function of slurry specifications and operating conditions (Vaezi & Kumar, 2014a).

Vaezi et al. performed a techno-economic assessment of long-distance pipeline hydro-transport of agricultural residue biomass using the corresponding frictional pressure drop correlation for two feedstocks (wheat straw and corn stover) over a distance of 50-300 km and a dry matter solid mass content of 2-8.8% (i.e., 40% saturated mass concentration) (Vaezi et al., 2014; Vaezi et al., 2015). They proposed an integrated pipeline system consisting of short hauls of biomass bales from each farm to its nearest preprocessing facility (each with a mixing tank, a commercial mill, and a pump), booster station, main pipeline pumping station, and long-distance pipeline extending 200-300 km from the main pumping station to the biorefinery. The material chopped by a commercial mill will be combined with water in a mixing tank to make a known mass concentration slurry. The booster pump station(s) will deliver this slurry to the branch line connected to the main pipeline pumping station. Vaezi et al. (2015) suggested a certain number of booster stations to maintain slurry velocity that might be reduced by friction and the addition of slurry from other preprocessing facilities within a certain radius spanning a specific number of farms. The diameter of the pipe was determined based on the pipeline's transport capacity and the slurry's speed, and the number of booster stations was evaluated by dividing the pipeline's total pressure drop by the total head produced by the main pump and the booster pumps (Vaezi et al., 2015).

Based on an 8.8% slurry solid mass content of <3.2 mm particle size, 2.5 m s⁻¹ slurry velocity, a 150 km medium-range distance, and the lowest published truck delivery cost estimate (0.22 \$ dry t⁻¹ km⁻¹), Vaezi et al. found pipeline hydro-transport to be economically more viable than trucking at capacities of 0.45 M dry t yr⁻¹ or more for a one-way pipeline and 1.4 M dry t yr⁻¹ or more for a two-way pipeline (2015). Further, considering the same quality of slurry (i.e., 8.8% slurry solid mass content with a wheat straw particle size <3.2 mm) and the highest published truck delivery cost estimate (0.46 \$ dry t⁻¹ km⁻¹), Vaezi et al. declared that one-way pipeline hydro-transport would always cost less than truck delivery and a two-way pipeline would cost less than truck delivery at capacities above 0.35 M dry t yr⁻¹ (2015). In their techno-economic study, Vaezi et al. (2015) also conducted a comparative analysis of the distance fixed cost (DFC) and distance variable cost (DVC) associated with pipeline hydro-transport and truck delivery of biomass for both one-way and two-way pipelines. These costs were calculated for a slurry of <3.2 mm wheat straw particles at the optimum operating conditions of 8.8% solid mass content (dry basis) and slurry velocity of 2.5 m s⁻¹. All one-way pipelines with throughputs of 1 M dry t yr⁻¹ or more had lower DFCs and DVCs than truck transport and could compete with truck hauling based on the lowest estimated truck delivery cost up to 228 km with 0.5 M dry t yr⁻¹ throughputs. In the case of two-way pipelines with throughputs of 2 M dry t yr⁻¹ or above, pipeline hydro-transport was consistently found to be more cost-effective compared to truck transport (Vaezi et al., 2015).

Vaezi et al.'s pressure drop correlations used for agricultural residue biomass slurry flows through a pipeline were based on experiments conducted in a horizontal pipeline only (2015). However, long-distance, large-scale pipeline setups and on-site processing require integrated pipeline systems that include pipe sections of different inclinations (i.e., vertical and inclined) rather than simply horizontal. The slurry's frictional behaviour in vertical and inclined flows differs from the

horizontal flows because of various factors, including particle type, particle size, slurry density, slurry velocity, carrier fluid, pipe diameter, pipe roughness, and slope, which eventually affects the pump's performance. Further, the effect of gravity (negligible in horizontal flows) in vertical and inclined pipes plays a vital role in evaluating the slurry's total pressure drop (frictional pressure drop \pm hydrostatic head) in pipes and the pump's total head (Doron & Barnea, 1996; Vlasak et al., 2018; Wilson et al., 2006). The magnitude and sign of slurry's hydrostatic component in a pipe depends upon the in situ (local) density and hence the in situ concentration of the specific slurry, angle of pipe tilt, and the slurry flow direction (i.e., against or with the gravity) (Vlasak et al., 2017; Vlasak et al., 2019a; Wilson et al., 2006). Therefore, the frictional behaviour of agricultural residue biomass slurries at various flow conditions through vertical and inclined pipes needs to be studied to find the corresponding empirical correlations for frictional pressure drops that could assist in evaluating the optimum operating conditions and the exact pumping requirements to modify Vaezi et al.'s (2015) proposed techno-economic model for a long-distance pipeline network to produce biofuels on a large scale.

Many studies on the pipeline hydro-transport of conventional solid (sand, coal, glass beads, various minerals) slurries through vertical and inclined pipe sections provide a comprehensive understanding of slurry's frictional behaviour with considerable experimental data, and the corresponding frictional pressure drop correlations (Bartosik, 1996, 2010; Kesely et al., 2019; Krampa, 2009; Matousek, 2005; Matousek et al., 2019; Miedema, 2015; Newitt et al., 1961; Shook & Bartosik, 1994; Shook et al., 1974; Talmon, 2013; Vlasak et al., 2018; Worster & Denny, 1955). Vertical flows are uniform because there is no bed formation in the vertical pipe, and they can start at velocities above the solid phase's hindered settling velocity (Roitto, 2014; Wilson et al., 2006). Whereas the critical deposition velocity dominates the hindered settling velocity for horizontal

flows because of bed formation in these flows, ensuring slurry flow through pipes at the desired concentration (Agrawal, 2016; Krampa, 2009; Matousek, 1997; Vaezi et al., 2018). In contrast, the flow of mixtures of solids and water through inclined pipes exhibits a higher complexity level than horizontal and vertical pipes due to the concurrent occurrence of phase separation and slippage (Polanský, 2014). The pipe inclination affects the pressure drop, concentration distribution across the pipe cross-section, velocity profile, and deposition limit velocity of settling slurries. Thus, slurries might be homogeneous, pseudo-homogeneous, heterogeneous, stratified with sliding beds, or fully stratified (Kao & JL, 1980; Meng & Lucas, 2017; Vauhkonen et al., 2019; Vlasak et al., 2018; Vlasak et al., 2019a). These studies on conventional solids could help design and calibrate an integrated pipeline loop involving various pipe inclinations. Nevertheless, employing them as a base case to develop pressure drop correlations for agricultural residue biomass-water slurry flows in vertical or inclined pipes is not feasible due to their entirely different flow characteristics, as Vaezi et al. (2014) explored for horizontal pipe flows.

The frictional behaviour of agricultural residue biomass-water suspension flows through pipes resembles those of synthetic (nylon, polyester, rayon, acrylic, and microfibers, etc.) or natural (e.g., wood pulp fiber suspension processed by some mechanical or chemical means) fiber suspensions (Vaezi et al., 2014). The analysis of these slurries is challenging due to the coexistence of many particle types (fibers, floccettes, flocs, and networks) inside the flow. One unique feature of fiber suspensions is their ability to reduce drag (the percentage reduction in suspension friction loss compared to water alone at the same bulk velocity) in specific flow circumstances. These characteristics set them apart from conventional solid-water slurries (where the frictional pressure drop is always higher than clear water), making them a unique flow system (Duffy, 2006; Vaezi et al., 2014). A comprehensive literature review found several studies on fiber suspension flows

through vertical pipes with limited studies through inclined pipe sections. (Ahmed & Takach, 2009; Bobkowicz & Gauvin, 1965; Elgaddafi & Ahmed, 2020; Faia et al., 2020; Kerekes, 1971; Radin et al., 1975; Seely, 1968; Steen, 1989). As the frictional behaviour of these slurries is challenging to analyze and model due to their intricate nature and distinctive rheological features (Cui & Grace, 2007; Derakhshandeh et al., 2011; Duffy, 2006), most studies have aimed to investigate the flow regions of these suspensions and the underlying mechanisms suppressing their turbulence intensities to comprehend their flow characteristics under different flow conditions (Bobkowicz & Gauvin, 1965; Kerekes, 1971; Radin et al., 1975; Seely, 1968; Steen, 1989).

However, these studies for natural or synthetic fiber suspensions could provide some fundamental but not in-depth understanding of the frictional behavior of ARB slurries because the former fiber types usually come with a narrow particle size range or are mono-sized with minimal particle diameters (in microns), whereas, the ground ARB exhibits significant heterogeneity in particle dimensions, encompassing a broad size range that includes particles of different shapes (such as rectangular and complex), physical characteristics of the surface, and particle widths (Vaezi et al., 2013). Therefore, the hydrodynamic interaction of the particles with each other and the surrounding fluid would be more complicated in the case of ARB compared to synthetic or natural fibers (Djalili-Moghaddam & Toll, 2006). Furthermore, modeling studies on frictional pressure drops of synthetic and natural fiber suspensions through vertical and inclined pipes are scarce.

Few studies model the flow behavior of wood pulp and nylon fiber suspensions in vertical upward flows. However, with limited scope, they looked into different aspects of suspension's behavior, including the empirical correlations in specific flow regimes in terms of friction factor (Seely, 1968), drag reduction (Kerekes, 1971), and radial distribution of the suspension's viscosity (Ogawa et al., 1990). Nevertheless, the current study's baselines cannot be adequately established

based on these data alone. Therefore, it is crucial to comprehend and simulate the frictional characteristics of ARB suspensions in pipes with varying inclinations by including biomass feedstock's relevant parameters and corresponding slurry properties. The present research proposes a comprehensive investigation into the frictional behavior of agricultural residue biomass slurry flows in vertical and inclined pipe sections to determine the accurate pumping power for an integrated pipeline network that can transport slurries from bio farms to biorefineries for large-scale biofuel production.

1.2 Objectives

The overall objective of the study is to experimentally examine the hydro-transport of agricultural residue biomass through vertical and inclined pipes (at various ascending and descending inclinations) in terms of frictional behaviour. The experimental facility was designed and built in an earlier research work with horizontal pipe sections (Mohamadabadi, 2009) and later modified by Jason Luk (2010) and Mahdi Vaezi (2014). The pipeline loop was redesigned for this research and upgraded to include vertical and inclined pipe sections along with associated instruments for pressure measurements and a chiller (heat exchanger) to maintain slurry temperature (in order to minimise water consumption).

The specific objectives of the current research are:

1. To design, fabricate, calibrate, and commission a 50 mm diameter closed-circuit pipeline facility, including vertical and inclined pipe sections, for biomass slurry transport.
2. To develop a method to investigate the in situ concentration of water-based conventional solid (fine sand, medium sand, and glass beads) slurries in vertical pipes and subsequently

implement it to measure in situ concentrations of water-based agricultural residue biomass slurries in the absence of a concentration-measuring device.

3. To investigate the effect of particle size and slurry bulk velocity on delivered concentrations and hence the in situ concentrations of wheat straw-water suspensions in upward vertical flows.
4. To identify and evaluate the effect of particle size and slurry solid concentrations on the frictional pressure drop and drag reduction of wheat straw-water suspensions in upward vertical flows.
5. To investigate the effect of particle size and concentration on the frictional pressure drop and drag reduction of corn stover-water suspensions in upward vertical flows and compare them with the corresponding results of wheat straw-water suspension.
6. To establish an empirical correlation to model the frictional behaviour of agricultural residue biomass slurry flow in vertical pipe section that could eventually help predict the biomass slurry pressure drop across the corresponding pipelines on a commercial scale.
7. To study the effect of pipe inclinations (in both ascending and descending positions) on the frictional pressure drop of wheat straw-water mixtures at various flow rates and mixture concentrations.
8. To design and fabricate a 100 mm diameter pipeline to study the rheological characteristics of transporting biomass slurries.

The research objectives mentioned above are in combined form, in which objectives 2 to 4 constitute two chapters, and each of the objectives 5 to 7 represent independent chapters of the thesis.

1.3 Scope and limitations

1. The current investigation focuses on two types of agricultural residue biomass, wheat straw and corn stover, of four nominal particle sizes, <3.2 mm, 3.2 mm, 6.4 mm, and 19.2 mm.
2. The closed pipeline loop in the experimental setup is 50 mm in diameter and 29 m long.
3. The experimental setup is not equipped with a concentration measuring device.
4. The angles of inclination of the inclined pipe section used in this study are limited to 0° to 7° (descending) and 0° to 21° (ascending) because of space constraints in the lab.

1.4 Organization of the thesis

This thesis has seven chapters and is compiled in a paper-based format. Each chapter, except the introduction and the conclusion and recommendations, is an independent paper. Most of these chapters have been published in different peer-reviewed journals, while the last one has been accepted for publication to a scholarly journal. As this thesis is a consolidation of research papers and each chapter is meant to be read separately, the background information and data are sometimes repeated.

1. Chapter one introduces the research background, the research problem and motivation, the overall objectives, and the scope and limitations of the research.
2. Chapter two has two sections. The first describes and validates the hypothesis to measure the in situ concentration of conventional solids-water slurries in vertical upward flows. The second section establishes an experimental framework to measure the in situ concentration of wheat-straw water slurries and discusses the frictional behaviour of these slurries in upward flows through a vertical pipe.

3. Chapter three investigates the in situ concentration measurement of various particle sizes of wheat straw aqueous slurries. It also examines the effect of particle size, slurry concentration, and bulk velocity on the flow friction and drag reduction of wheat straw-water slurries in vertical upward flows.
4. Chapter four explores the effect of particle size, slurry concentration and slurry bulk velocity on the frictional pressure drop and drag reduction of corn stover-water slurries during their flows through vertical pipe. It also describes the detailed comparative assessment of the effect of feedstock on the mechanisms governing the frictional behaviour of agricultural residue biomass-water suspensions in vertical upward flows.
5. Chapter five describes the procedure to model the frictional behaviour of wheat straw and corn stover aqueous slurry flows through vertical pipe sections (using the large amount of data obtained during the entire course of experiments) and proposes empirical correlations for frictional pressure drop and onset velocity of drag reduction.
6. Chapter six highlights the challenges encountered during the calibration and commissioning of the inclined pipe section of the closed pipeline loop. It also investigates the effect of pipe inclination on the frictional behaviour of wheat straw-water slurries during their flows in inclined pipe section at various flow conditions.
7. Chapter seven summarizes the study and makes recommendations for future work.

Chapter 2: Frictional Behaviour of Wheat Straw-Water

Suspensions in Vertical Upward Flows¹

2.1 Introduction

There is significant interest in the use of biomass to produce fuels and chemicals as a means of reducing greenhouse gas emissions. Biomass transportation cost is a significant component of the total delivered cost of biomass from farms to biomass conversion facilities. For large-scale biofuel production with long transportation distances, pipeline hydro-transport of agricultural residue biomass, for example chopped wheat straw or corn (or maize) stover mixed in water to form a slurry, has been shown to be technically feasible and more economical than truck delivery. Pipeline delivery not only benefits from economies of scale but also reduces traffic congestion issues for overland transport and favours aqueous-based bioethanol production processes such as fermentation and other conversion processes at biorefineries like hydrothermal liquefaction and hydrothermal hydrolysis (Vaezi et al., 2015). However, techno-economic and experimental investigations into transporting biomass-water mixtures (slurry) have been limited to horizontal pipelines (Kumar et al., 2004, 2005b; Vaezi, 2014; Vaezi et al., 2014; Vaezi et al., 2015). In practice, long-distance, large-scale pipeline setups and on-site processing will require integrated pipeline systems that include horizontal, vertical, and inclined pipe sections. Therefore, a comprehensive study on the frictional behaviour of water-based biomass slurries of agricultural

¹ A version of this chapter has been published as Javed, K., Vaezi, M., Kurian, V., & Kumar, A. “Frictional behavior of wheat straw-water suspensions in vertical upward flows”, *Biosystems Engineering*, 2021, 212, 30-45.

residues in pipe sections of various inclinations is required to determine exact pump power, optimum flow properties (i.e., slurry velocity, concentration, particle size. etc.), and costs.

Several studies on the hydraulic transport of slurries of conventional solids (such as sand, glass beads, and other minerals) through vertical pipelines have been carried out (Agrawal, 2016; Chung et al., 1998; Durand & Condolios, 1952a; Faraj, 2013; Krampa, 2009; Link et al., 1977; Matousek, 2005; McKibben, 1993; Newitt et al., 1955; Newitt et al., 1961; Shook & Bartosik, 1991; Sumner et al., 1990; Toda et al., 1969; Wilson et al., 2006). The studies on vertical hydro-transport of conventional solids either report experimental data on frictional pressure drops or develop frictional pressure drop correlations to predict the frictional behaviour of these slurries in vertical upward flows, but none has included a biomass-water slurry (Bartosik, 1996, 2010; Krampa, 2009; Matousek, 2005; Miedema, 2015; Newitt et al., 1961; Shook & Bartosik, 1994; Talmon, 2013). Because, unlike in horizontal pipes, bed formation of slurry does not occur in vertical pipelines, vertical flows are uniform and can be initiated at mixture velocities above the hindered settling velocity of the solid phase (Roitto, 2014; Wilson et al., 2006). The minimum mixture velocity required to transport a conventional solid-water slurry through a vertical pipe section has been reported to be, as a rule of thumb, 4 to 5 times the settling velocity of the largest particle in the quiescent medium (Wilson et al., 2006). However, for horizontal flows, the critical deposition velocity dominates the hindered settling velocity, and this ensures slurry transport through pipelines at the desired concentration (Agrawal, 2016; Krampa, 2009; Matousek, 1997; Vaezi et al., 2018).

A few studies on vertical upward flows for fibrous material suspensions focus on understanding flow regions and frictional behaviour (Bobkiewicz & Gauvin, 1965; Kerekes, 1971; Radin et al., 1975; Seely, 1968; Steen, 1989). These slurries are challenging to analyse because of the

simultaneous existence of up to four particle types (fibers, floccettes, flocs, and networks) in the flow, which makes them a unique flow system compared to conventional solid-water slurries (Duffy, 2006). Another interesting feature of fiber suspensions is their drag-reducing capabilities under certain flow conditions, which are opposite to conventional slurry flows. The percent reduction in friction loss of suspensions with respect to that of water alone at the same bulk velocity is a measure of drag reduction. In conventional slurries, frictional pressure drops are always greater than those of clear water. Fiber suspension behaviour was first explored in the early nineteenth century, when significant drag reduction was observed in the dilute suspensions of mainly wood fibers during pressure drop measurements in horizontal pipes (Daily et al., 1961; Forrest & Grierson, 1931; Mih, 1967; Robertson, 1957). Three distinct regions – plug flow, mixed flow, and fully turbulent flow – were delineated directly or indirectly through visual, photographic, frictional pressure drop, and velocity profile observations (Daily et al., 1961; Forrest & Grierson, 1931; Mih, 1967; Robertson, 1957; Seely, 1968).

The fully turbulent region in a vertical upward flow of dilute wood fiber suspensions of 0.05-0.5% (mass) through steel pipes was further categorised into two sub-regions, “damped turbulence” and “Newtonian turbulence” (Seely, 1968). Seely found the drag-reduction effect to be a strong function of the aspect ratio of the fiber and the mass concentration of the suspension, and this effect was only linked with the damped turbulence sub-region. At higher flow rates, the damped turbulence sub-region disappeared and a sub-region, known as the Newtonian turbulence sub-region, appeared. In this region, the friction loss of the suspension became identical to that of the suspended liquid. The Newtonian turbulence sub-region in the fully turbulent flow region was also observed by Radin et al. (1975) during pressure drop measurements of a large range of fibrous suspensions (nylon, rayon, asbestos) flowing through a vertical pipe at high flow rates in which

the friction factor became equal to the suspending Newtonian fluid. Radin et al. (1975) investigated the effects of particle shape, size, mass concentration, fluid viscosity, and tube diameter on friction factor over a wide range of Reynolds numbers and found that the drag-reducing capabilities of all the fibrous additives increased with increases in mass concentration and aspect ratio. In addition, Kerekes (1971) proposed quantitative criteria for the upper and lower limits of suspension conditions verified by frictional loss measurements. The study showed the strong dependence of turbulent drag reduction on the aspect ratio and mass concentration of nylon fibers (Kerekes, 1971).

In vertical flows of solid-water mixtures, the in situ concentration is needed to predict the in situ density of the mixture in the vertical column and thus calculate the frictional pressure drop of the slurry (Bartosik, 2010; Ferre & Shook, 1998; Kerekes, 1971; Shook & Bartosik, 1994). Several techniques have been developed for measuring in situ concentrations of fiber suspensions; however, they are limited to mass concentrations up to 10% (Belyachits et al., 2014; Nakayama, 1994; Törmänen et al., 2006). Commercially available concentration-measuring devices that measure higher concentrations are scarce, and they are confined to maximum mass concentrations of 16% (BTG, 2023). For conventional slurries, when there is no slip (i.e., velocity difference) between the solid and liquid phases, the in situ concentration becomes equal to the delivered concentration (Wilson et al., 2006). In the absence of a dedicated concentration-measuring device, a flow diversion sampling method to obtain a delivered concentration of slurry (Addie et al., 2005; Faraj, 2013; Kaushal et al., 2017; Kelly, 2013; Seitshiro, 2013) could be used to measure in situ concentrations in vertical test sections as long as the solids are fully suspended in the mixture. The same approach can be used for fiber suspension flows in vertical pipes to find the in situ mass concentration.

Although the mechanisms of transporting wheat straw and corn stover (lignocellulosic biomass) suspensions have been comprehensively determined by measuring their longitudinal frictional losses flowing through a horizontal pipeline for saturated concentrations of 5-40% (mass) (Vaezi et al., 2014), frictional pressure drop measurements of lignocellulosic biomass slurry flows in vertical pipes have not been made. This study aims to address this key gap in the research.

The current study attempts to investigate experimentally the pipeline hydro-transport of wheat straw-water suspensions in vertical upward flows and to quantitatively explore the delivered concentrations of wheat straw and different conventional solid-water mixtures to predict their corresponding in situ concentrations. The main objectives of the research are to:

- Predict, for a given experimental setup, the in situ concentrations of various conventional solid slurry flows in a vertical test section by developing correlations for delivered concentrations of corresponding slurries flowing in a pseudo-homogenous regime.
- Validate the applicability of the derived correlations of delivered concentrations of conventional solid slurries for the entire range of flow conditions while flowing in the vertical test section by comparing experimental frictional pressure drops with pre-existing empirical models.
- Apply the standard method of measuring delivered concentrations to predict in situ concentrations of wheat straw slurry suspensions.
- Investigate the frictional behaviour and analyse the flow regions of a wheat straw-water slurry when transported through a vertical pipeline test section at various concentrations and flow rates.

2.2 Method

2.2.1 Experimental setup

An experimental setup for the current investigation is shown in Figure 2.1. The setup consisted of a 29 m long, 50 mm internal diameter closed pipe circuit with a slurry pump, Schedule 40 steel and PVC pipe sections, a heat exchanger, a magnetic flow meter, a flow visualisation section, semi-circular and 90° bends, pressure transducers, flexible PVC pipe sections, a differential pressure transmitter (DPT), and a mixing tank. All the instruments were connected with a data acquisition system (LabView V.9.0.1f2; National Instrument Corp., Austin, TX, USA) for recording and processing the data.

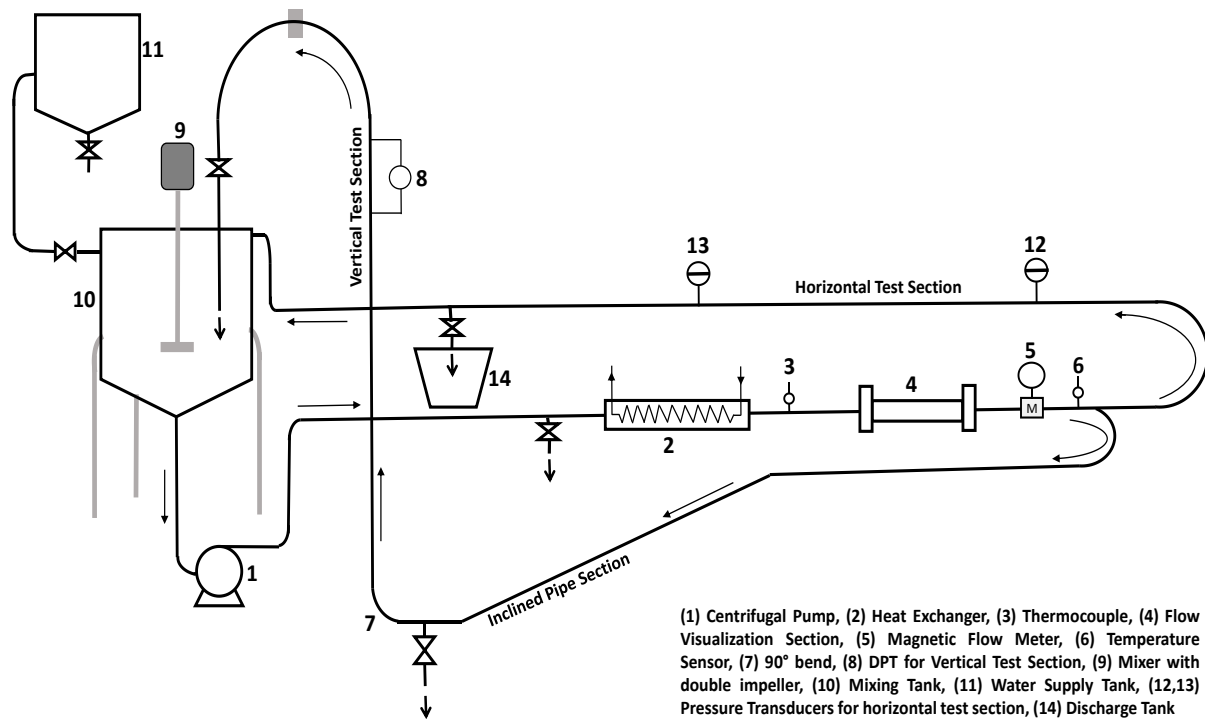


Figure 2.1: Schematic diagram of experimental setup.

The specifications of the instruments have been reported in earlier studies (Vaezi, 2014; Vaezi & Kumar, 2014b; Vaezi et al., 2018). The magnetic flow meter (FMG-424; Omega Eng., Stamford,

CT, USA) was located at a distance of $200D$ (D is the inside diameter of the pipeline) downstream of the slurry pump (Vaezi et al., 2014). The heat exchanger maintains the slurry temperature at 12-15 °C. The vertical pressure drop measuring section (test section) with a span (L) of $10D$ is located on a 2.8 m long vertical PVC pipe.

A highly accurate differential pressure transmitter (Fuji Electric Ltd–Model: FKCT22V5) with a span range and accuracy of 0-6 kPa and $\pm 0.04\%$ (of the adjusted span), respectively, was selected for the current setup (Fuji Electric, 2010, 2014). The DPT attached to the vertical test section was installed at the farthest possible point (i.e., downstream tangent) of $41.85D$ from 90° bend. The generally agreed upon range for the optimum length of the downstream tangent of the 90° bend is $40\text{--}50D$ (Chowdhury et al., 2016; Ito, 1960; Verma et al., 2006) with respect to the downstream end of the 90° bend at the bottom of the vertical pipe (see Figure 2.1). This eliminates the effects of secondary flows (Enayet et al., 1982; Kalyanraman et al., 1973; Kim et al., 2014) and the decay of swirl intensity (Chowdhury et al., 2016), develops smooth velocity profiles (Hellström et al., 2013), and reduces bend losses (Ito, 1960) downstream of the 90° bend. The DPT was connected to the vertical test section at low and high pressure locations with copper tube impulse/sensing lines, following ISO standards (ISO, 2007) and the manufacturer’s manual (Fuji Electric, 2014; Reader-Harris & McNaught, 2005) (Figure 2.1).

2.2.2 Calibration of the differential pressure transmitter (DPT)

The DPT was calibrated by measuring the frictional pressure drop of clear water flowing in a vertical test section using the DPT and comparing the results with those obtained from Churchill’s model (Churchill, 1977), which is applicable to all the flow regimes (laminar, transitional, and turbulent) of fluid flow over smooth or rough pipe surfaces. Water was used as a pressure-sensing fluid in the impulse lines to sense the pressure of the fluid flowing inside the vertical test section.

The theoretical frictional pressure drop of water flowing with a bulk velocity (v_w) through a test section of the span (L) with an inside diameter of D can be specified by the following general relationship (Equation 2.1):

$$\Delta P_f = \rho_w g h_f = \frac{\rho_w f_D L v_w^2}{2D} \quad (2.1)$$

where ρ_w and f_D are the density of water and the Darcy-Weisbach friction factor, respectively. The absolute roughness value for the vertical pipe was taken as 0.0015 mm from standards available (Chaurette, 2003; White, 2009). A general expression to obtain the experimental frictional pressure drop of the mixture $(\Delta P_f/L)_m$ in the vertical test section, including measured (or manometric) pressure gradient ($\Delta P_{MD}/L$) and the static head (Equation 2.2) was derived by Ferre and Shook (Ferre & Shook, 1998) and is given as:

$$\left(\frac{\Delta P_f}{L}\right)_m = \frac{\Delta P_{MD}}{L} - [\rho_m - \rho_w]g \quad (2.2)$$

where ρ_m is the mixture density at any specific concentration flowing in a vertical test section of the span (L) with a mixture's bulk velocity (v_m). When water is present in the impulse lines and flowing through the vertical test section, the static head in Equation 2.2 is nullified, and the differential pressure measured by the DPT will be equivalent to the frictional pressure drop of water flow across the test section. The plot of the Darcy-Weisbach friction factor (f_D) versus the water Reynolds number (Re) is shown in Figure 2.2, where friction factor values were obtained by using pressure drop measurements of clear water at 18 °C and Equations 2.1 and 2.2 and were compared with the corresponding theoretical values obtained from Churchill's model. For water, the subscript m in Equation 2.2 will be replaced by w .

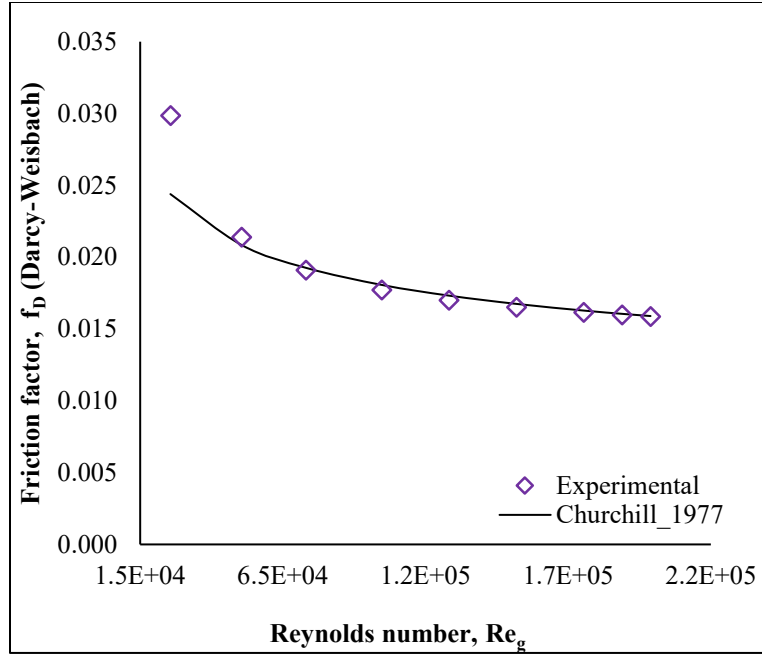


Figure 2.2: Friction factor vs. Reynolds number of water flowing through a vertical test section.

The experimental values of the friction factor agree well with Churchill's model results except at low bulk velocities $\leq 0.5 \text{ m s}^{-1}$ because of instrument and control limitations (Kazi et al., 1999; Vaezi et al., 2014).

2.2.3 Standard method for assessing in situ concentrations

To find the frictional pressure drop of a solid-water mixture in vertical upward flows, an in situ mixture density (from Equation 2.3) and hence the $C_{in-situ}$ is needed. A standard approach was used in the current study to measure the in situ concentration of conventional solids-water mixtures in the vertical test section without using any dedicated concentration-measuring device. This approach was later used to calculate frictional pressure drops of upward flows of wheat straw-water mixtures. Three different closely/uniformly graded conventional solids (Eliason, 2002; Masch & Denny, 1966; Uesugi & Kishida, 1986; Viswanadham, 2018) (medium sand, glass beads,

and fine sand with angular, sub-angular, and spherical particle shapes, respectively) were selected; their physical properties are given in Table 2.1.

Table 2.1: Physical properties of the conventional solid materials used in concentration-measurement experiments

Material Type	Particle density (kg m^{-3}) (ρ_s)	Mean particle diameter (mm) (d_{50})	Terminal settling velocity (mm s^{-1}) (v_t)	Critical deposition velocity (Wasp & Aude, 1970; Wasp et al., 1977) (m s^{-1}) (v_D)	Critical velocity for pseudo-homogeneous regime (Newitt et al., 1961) (m s^{-1}) (v_4)
Fine sand ^a	2500	0.103	10.06 (Newitt et al., 1961)	0.52–0.76	0.895
Medium sand ^b	2650	0.447	59 (Sumner et al., 1990)	0.893–1.210	1.84
Glass beads ^c	2500	0.5	74.1 (Mordant & Pinton, 2000)	0.86–1.3	1.90

^aTarget Products, AB, Canada; Material grade: LM–125

^bSil Industrial Minerals, AB, Canada; Material grade: Sil–3

^cPotter Industries, SK, Canada; Material grade: P–0230

2.2.3.1 Hypothesis

In an integrated pipeline setup, where vertical pipes connect with horizontal ones, the critical deposition velocity becomes more important than the hindered settling velocity and should be lower than the mixture velocity to convey the desired solid concentration (Bartosik, 1996). Normally the value of the hindered settling velocity for sand particles with a mean diameter $d_{50} \leq 0.6$ mm is lower than their terminal settling velocity. Consequently, the ratio of the hindered settling velocity of these particles to the corresponding mixture velocity (greater than the critical deposition velocity) becomes a smaller fraction. This small ratio leads to a reasonable

approximation (hypothesis) of an in situ concentration of slurry similar to the delivered concentration (C_{Vd}) (Wilson et al., 2006). Although several techniques (both intrusive and non-intrusive) have been used for online measurements of local (in situ) concentrations of conventional slurry during vertical upward flows (Faraj, 2013; Faraj & Wang, 2012; Krampa, 2009; Matousek, 2005; Sumner, 1993), the flow diversion sampling method (to obtain the C_{Vd} of slurry for comparison with the local concentration (Addie et al., 2005; Faraj, 2013; Kaushal et al., 2017; Kelly, 2013; Seitshiro, 2013) could be an alternate approach to predict in situ concentrations ($C_{in-situ}$) in vertical test sections as long as the solids are fully suspended in the mixture.

2.2.3.2 Estimation of delivered concentration

Since the current experimental setup was not equipped with a flow diversion sampling apparatus as used by many researchers (Addie et al., 2005; Faraj, 2013; Kelly, 2013; Matousek, 1997) because of process limitations, the C_{Vd} was measured manually by collecting the samples through the return pipe at the end of the loop, which goes into the mixing tank (Figure 2.5 [b]). The end was selected because most researchers suggest it for measuring the C_{Vd} in the slurry loop with the flow diversion sampling method (Faraj, 2013; Faraj & Wang, 2012; Frizzel, 1985; Kaushal et al., 2013; Kelly, 2013; Kumar et al., 2019; Moujaes, 1984); moreover, it was the location closest to the vertical test section in the current investigation and thus helped accurately predict an in situ slurry density in the test section based upon C_{Vd} measurements with minimum errors. The required mass of solids for a desired prepared concentration (C_{Vp}) was added to the mixing tank. A slurry bulk velocity (v_m) of 3.0 m s^{-1} was maintained for the C_{Vd} measurements. This specific bulk velocity was greater than the critical deposition velocity (v_D) and the critical velocity for a pseudo-homogeneous regime (v_4) (Table 2.1) for all the selected materials to ensure the homogeneous flow. The manually collected slurry samples (18 to 25 L) were then dewatered to calculate the C_{Vd} .

The complete procedure of measuring the delivered concentration is explained in Appendix C. The delivered concentrations (C'_{vd} s) obtained for medium sand, glass beads, and fine sand are shown in Figure 2.3 (a). The single C_{vd} value for material (Figure 2.3 and Table C1 in Appendix C) represents an average of three samples collected for corresponding C_{vp} 's.

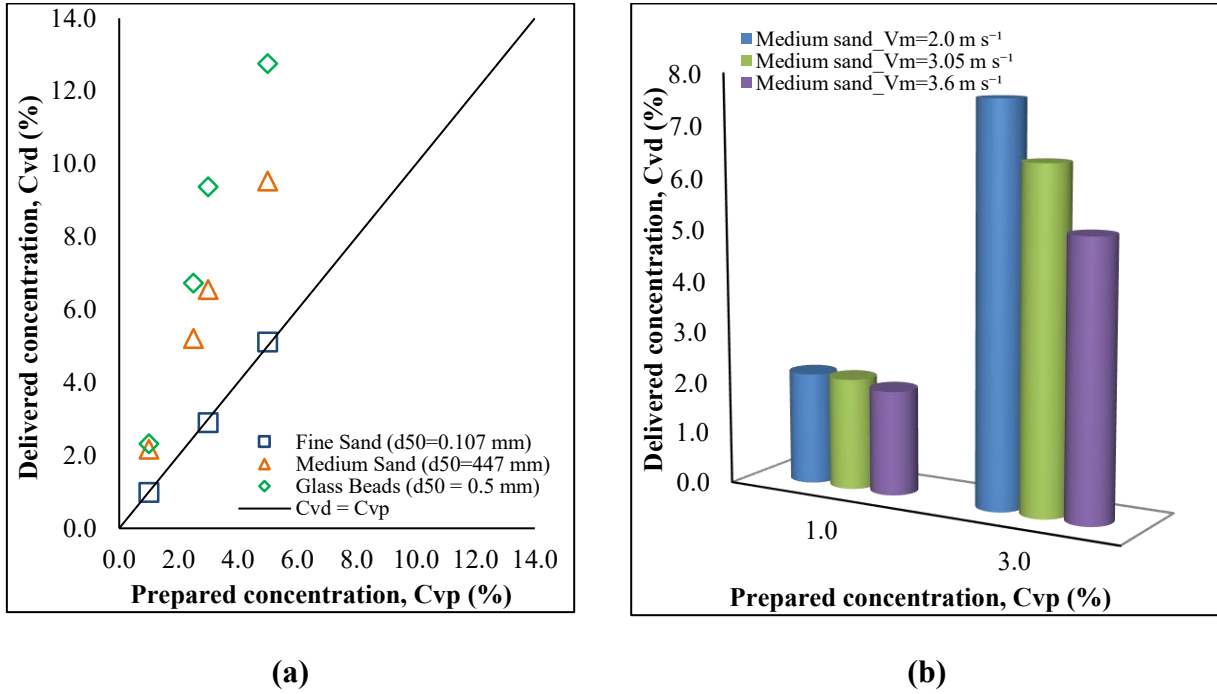


Figure 2.3: (a) The effect of particle size on the delivered concentration of conventional solids-water slurries at a bulk velocity of 3.0 m s⁻¹ and (b) The effect of bulk velocity on the delivered concentration (C_{vd}) for medium sand.

A perfect correlation between C_{vd} and C_{vp} was sought for each material tested, and the ratio of $(C_{vd}/C_{vp})_{avg}$ was found to be a proper representative factor (Figure 2.3 [(a)]). For medium sand, glass beads, and fine sand, these factors were found to be 2.08, 2.52, and 0.99, respectively. A visual observation through the sight glass of the mixing tank (in this case a conical vessel with a double impeller) found stratified concentrations near the bottom of the tank for both medium sand and glass beads, resulting in different $C_{in-situ}$'s in the pipeline compared to C_{vp} 's prepared in the

mixing tank. For fine sand, the mixture was almost homogeneous in the mixing tank with negligible stratified concentrations because the particles were buoyant. Other studies have pointed out similar issues (i.e., different C_{Vp} 's in the mixing tank than $C_{in-situ}$'s in the pipeline), suggesting the reasons for this difference are (i) improper mixing in the tank, (ii) a conical bottom shape of the tank, (iii) physical characteristics of the solid particles (e.g., mean diameter, density), (iv) mixer impeller design (single or double impeller, impeller's blade design, length of the impeller shaft, etc.), (v) mixing speed of the impeller, and (vi) low viscosity of the carrier fluid (Hosseini, 2008; Mahdavi et al., 2016; Selima et al., 2008). However, it is worth mentioning here that the non-homogeneous mixing in the current investigation was only part of the experimental setup, i.e., it was a localised finding and not a generalised or universal phenomenon.

An analysis of the mixing tank is beyond the scope of the current investigation; we instead analysed the effect of slurry bulk velocity on the C_{Vd} for medium sand slurry flows through the vertical test section at $C_{Vp} = 1.0\%$ and 3.0% (volume) and slurry bulk velocities above v_4 , i.e., $v_m = 2.0$ and 3.6 m s^{-1} . The results showed a change of C_{Vd} with changes in bulk velocity (v_m) and C_{Vp} ; however, ratios $(C_{Vd}/C_{Vp})_{avg.}$ of 2.37, 2.08, and 1.91 at $v_m = 2.0, 3.0, 3.6 \text{ m s}^{-1}$, respectively, were found, as shown in Figure 2.3 (b).

2.2.3.3 Verification of the hypothesis

The hypothesis proposed in section 2.2.3.1 was validated by pressure drop measurements of all the conventional solid-water slurries (given in Table 2.1) through the vertical test section at prepared/feed concentrations (C_{Vp} 's) ranging from 1.0-5.0% (volume) and a wide range of bulk velocities ($v_m = 0.5\text{-}4.5 \text{ m s}^{-1}$). Some studies have developed empirical correlations for frictional pressure drops of conventional solid-water slurries flowing in vertical pipelines (Bartosik, 1996,

2010; Matousek, 2005; Miedema, 2015; Newitt et al., 1961; Shook & Bartosik, 1994; Talmon, 2013). However, for the current research, Newitt et al.'s correlation (1961) was used because its parameters (e.g., inside diameter of the vertical pipe, mean diameter of particles, volumetric concentration, etc.) are somewhat similar to ours. The mixture density was calculated using the following relation:

$$\rho_m = \rho_w[1 + C_V(S - 1)] = \rho_w + C_V(\rho_s - \rho_w) \quad (2.3)$$

Figure 2.4 shows the frictional pressure drops found for medium sand using C_{Vp} and C_{Vd} .

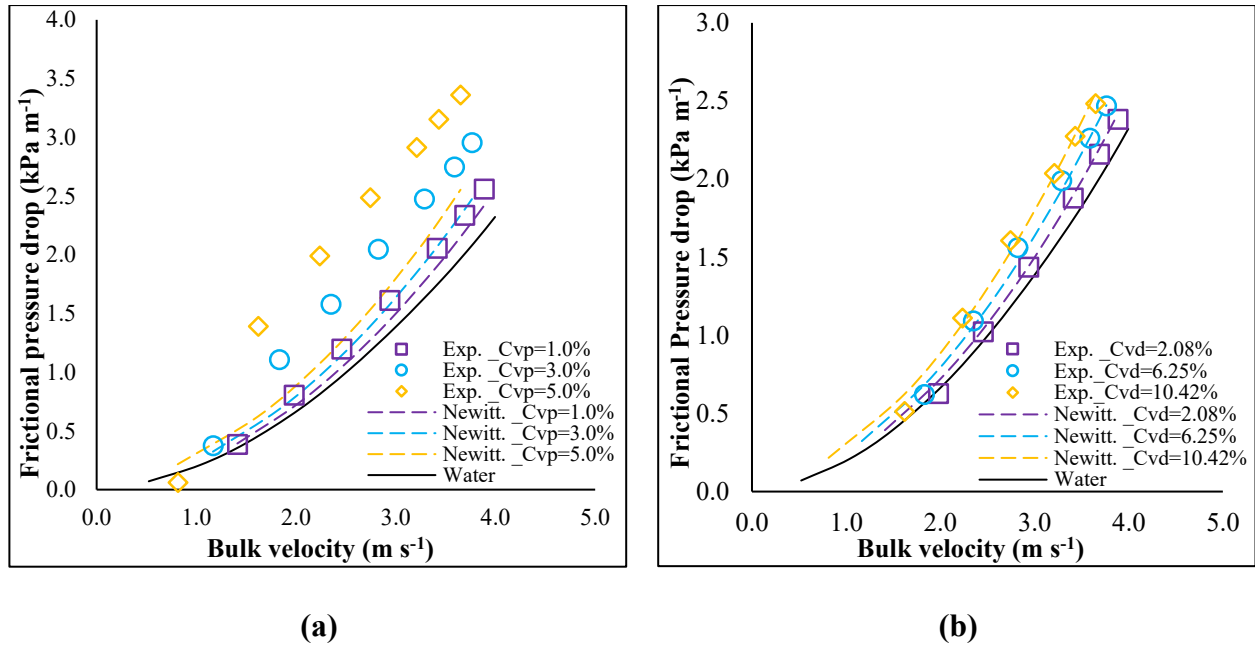


Figure 2.4: Frictional pressure drops for vertical upward flows of medium sand-water mixtures considering (a) a prepared concentration (C_{Vp}) and (b) a delivered concentration (C_{Vd}).

The frictional pressure drops for the medium sand and glass beads using $C_{Vp} = 1.0\text{--}5.0\%$ showed significant deviation from Newitt et al.'s correlation (1961) for the entire range of bulk velocities

and concentrations (1.0-5.0%). Figure 2.4 (a) gives the results for medium sand, including the largest deviation from the correlation at $C_{vp} = 5\%$, as 162%.

With respect to the C_{vd} , the pressure drop results obtained for medium sand were found to be in good agreement with Newitt et al.'s corresponding correlation (1961) for the entire range of concentrations ($C_{vp} = 1.0\text{-}5.0\%$) and bulk velocities ($2.0\text{-}5.0 \text{ m s}^{-1}$) with a maximum deviation of 3.10% (Figure 2.4 [b]). These outcomes reflect the presence of entirely different in situ concentrations in the vertical test section of the closed loop compared to what was prepared in the mixing tank. At bulk velocities of $<2.0 \text{ m s}^{-1}$, the frictional pressure drops deviated from Newitt et al.'s model (1961) for the entire range of C_{vp} , reflecting the limitation of the hypothesis. The main reason for this difference is the non-homogeneous nature of the flow, which changes the $C_{in-situ}$ with respect to C_{vd} because of the slip between the solid and liquid phases. The bed formation of the medium sand-water mixture in horizontal pipe sections at lower bulk velocities ($<2.0 \text{ m s}^{-1}$) means the derived relation for $(C_{vd}/C_{vp})_{avg}$ could not be used to calculate accurate $C_{in-situ}$ in the vertical test section.

2.2.4 Wheat straw feedstock and slurry preparation

Dry wheat straw bales obtained from farms in Alberta, Canada were milled using a commercially available cutting mill (SM 100; Retsch Inc., Newtown, PA, USA) and classified using a commercially available classifier (BM&M Inc., Surrey, BC, Canada) into four major groups with nominal sizes (classifier sieve opening sizes) of 19.2 mm, 6.4 mm, 3.2 mm, and <3.2 mm. The complete details of the sizes of classified wheat straw particles as well as morphology can be seen in previous work by Vaezi et al. (2014, 2013).

The current investigation focuses on the vertical transport of the largest particle size (i.e., 19.2 mm) in the wheat straw-water mixture in order to have a higher aspect ratio in the particles and obtain higher frictional pressure drops than the other three particle sizes at the same concentrations (Vaezi et al., 2014). The first step in making a wheat straw slurry was measuring the wet-basis moisture content (MC) of the classified material. The MC was measured using ASABE S358.3 standard (ASABE, 2012). In the current research, four samples weighing at least 25 g were randomly picked and oven-dried at 103 °C for 24 h to find the initial MC of the material. Wheat straw (and other agricultural residue biomass) absorbs moisture when mixed with water. Hence the properties of a wheat straw-water mixture constantly change as it is pumped through the pipeline; after several hours it became stable at a fully saturated state with a MC of 82%, as reported earlier (Vaezi et al., 2014).

To prepare wheat straw slurry in the current research, the required mass of 19.2 mm-particle size wheat straw was calculated for a specific saturated concentration of $C_{mp} = 25\%$ (mass) using the initial MC (wet basis) and the saturated MC value (82%). This was the maximum concentration achieved in our experimental setup for the largest particle size (i.e., 19.2 mm) of wheat straw aqueous slurries (because of the smaller diameter of the pipe, i.e., 50 mm; the loop clogged at low flow rates and slurry mass concentrations $>25\%$). After the required volume of water from the closed-loop pipeline system was deaerated, a premeasured mass of wheat straw was gradually added to the mixing tank with the mixer on. The prepared slurry was continuously circulated through the loop for about 12 h until it became fully saturated and stable at a maximum concentration of $C_{mp} = 25\%$ (mass). In stable slurry conditions, the pressure and velocity fluctuations of wheat straw slurries were damped down to approximately $1.0\% \text{ h}^{-1}$. The operating velocity was changed from 0.5 to 4.0 m s^{-1} and the solid concentrations from 25-5.0% (mass),

equivalent to 24.1-4.8% (volume) by diluting the slurry by increments of 5% (by mass) during this process. The corresponding total pressure drop values were recorded and ultimately used in Equation 2.2 to obtain the frictional pressure drops. The saturated and dry matter (oven-dried) solid volume and mass contents of wheat straw slurries, considering a saturated particle density of wheat straw as 1050 kg m^{-3} , can be found in our earlier work (Vaezi, 2014).

2.2.5 Procedure for measuring delivered concentrations of wheat straw-water mixtures

To measure delivered concentrations (C_{md}) of wheat straw slurry, a series of tests was conducted using a return pipe with a 50 mm inside diameter (Figure 2.5[a]) directed towards the mixing tank.

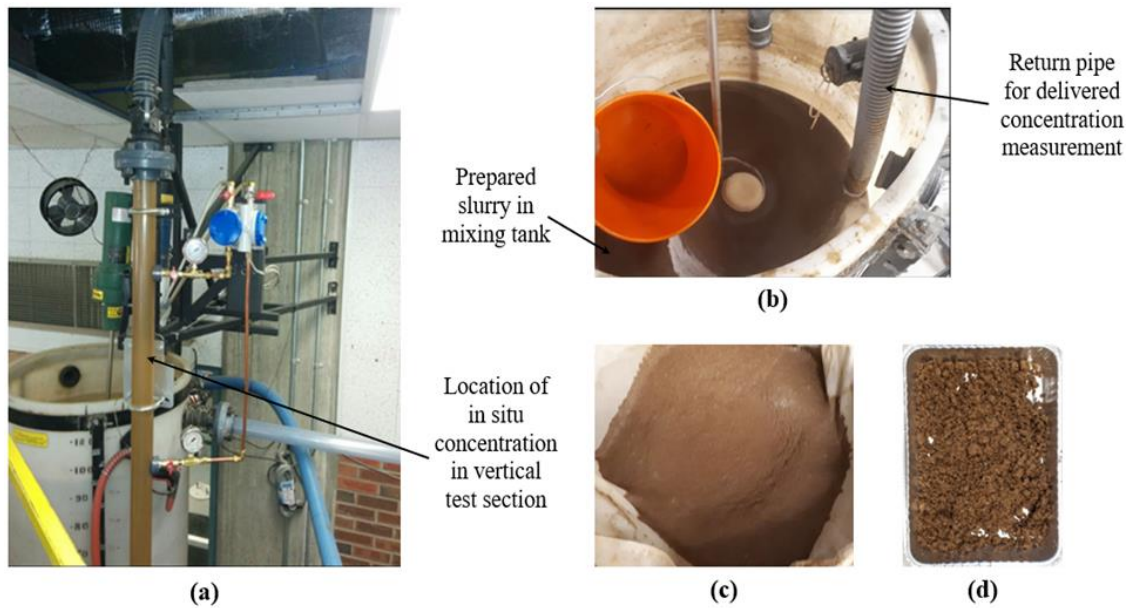


Figure 2.5: Delivered concentration measurement. (a) Location of in situ concentration in the vertical test section, (b) Inside view of mixing tank, (c) Wheat straw sample after water was filtered from the mixture with fine strainer, and (d) Wheat straw sample after surface water was removed.

After the desired saturated slurry mass concentration was obtained ($C_{mp} = 25\%$ [mass]) for the 19.2 mm particle size wheat straw, pressure drops were measured over the entire range of bulk velocities. The slurry was then diluted to $C_{mp} = 20\%$ and, after 15 min of pumping to assure homogeneous mixing and deaeration, three mixture samples were collected at a bulk velocity of 3.0 m s^{-1} at 5.0 min time intervals between collections. The same procedure was repeated for $v_m = 2.0 \text{ m s}^{-1}$ at $C_{mp} = 20\%$. Slurry samples were obtained for $C_{mp} = 15\%$ and 10% at both bulk velocities of 3.0 m s^{-1} and 2.0 m s^{-1} to obtain 18 samples for the entire course of delivered concentration tests. The delivered masses of the mixture samples containing both solids and water were measured first, then water was removed by gravity with great care using a very fine fabric strainer. The wheat straw sample, after the water had been removed, still contained some surface water (shown in Figure 2.5[c]). The final samples thus obtained did not contain any surface water (i.e., they were approximately saturated) (see Figure 2.5[d]). The masses of these final samples were recorded after their physical appearance was analysed and found to be free of surface water. They were then further divided into three smaller groups (to increase statistical accuracy) to obtain 36 subsamples for the entire test. The MC of each subsample was estimated using a thermogravimetric analyser (TGA701; LECO Corporation, St Joseph, MI, USA) (Patel et al., 2019) to find the mass of the dry wheat straw for all 18 samples collected. From these dry mass values, the corresponding dry matter solid mass concentrations were evaluated and the delivered saturated solid mass concentrations obtained.

2.2.6 Uncertainty analysis

The uncertainty and repeatability of the pressure drop measurements was obtained by conducting two sets of experiments on each conventional solid (see Table 2.1) as well as the 19.2 mm wheat straw biomass slurries. Uncertainty was calculated through the standard approach of uncertainty

analysis by finding the precision uncertainty (P_X) of the differential pressure measurements and the biased uncertainty (B_X) of the DPT to get total uncertainty (U_X) (MECE 301, 2018; Moffat, 1988; Vaezi et al., 2014). The repeatability of the experiments is reported here in terms of frictional pressure drops for glass beads, medium sand, and wheat straw slurries at different prepared concentrations and shown in Figure 2.6.

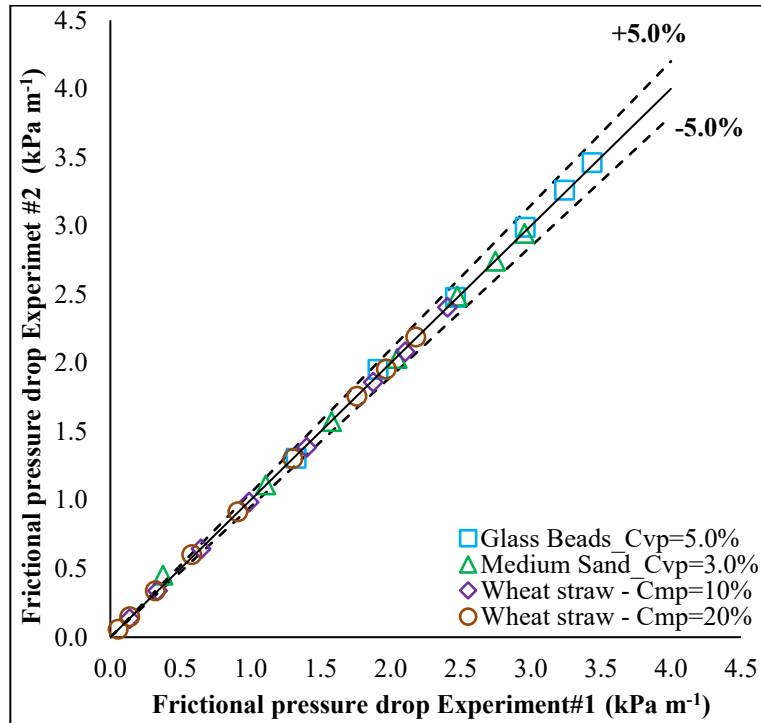


Figure 2.6: Repeatability of two sets of experiments on medium sand, glass beads, and wheat straw slurries in a 50 mm diameter vertical test section.

The results show good agreement between the corresponding pressure tests with minimum and maximum uncertainties of $\pm 0.0062 \text{ kPa m}^{-1}$ and $\pm 0.22 \text{ kPa m}^{-1}$, respectively, for all the slurries.

2.3 Experimental results and discussion

2.3.1 Delivered concentrations of wheat straw-water mixtures

The C_{md} results for the wheat straw-water mixtures at corresponding C_{mp} values, keeping the bulk velocity constant at $v_m = 3.0 \text{ m s}^{-1}$ and 2.0 m s^{-1} , are shown in Figure 2.7.

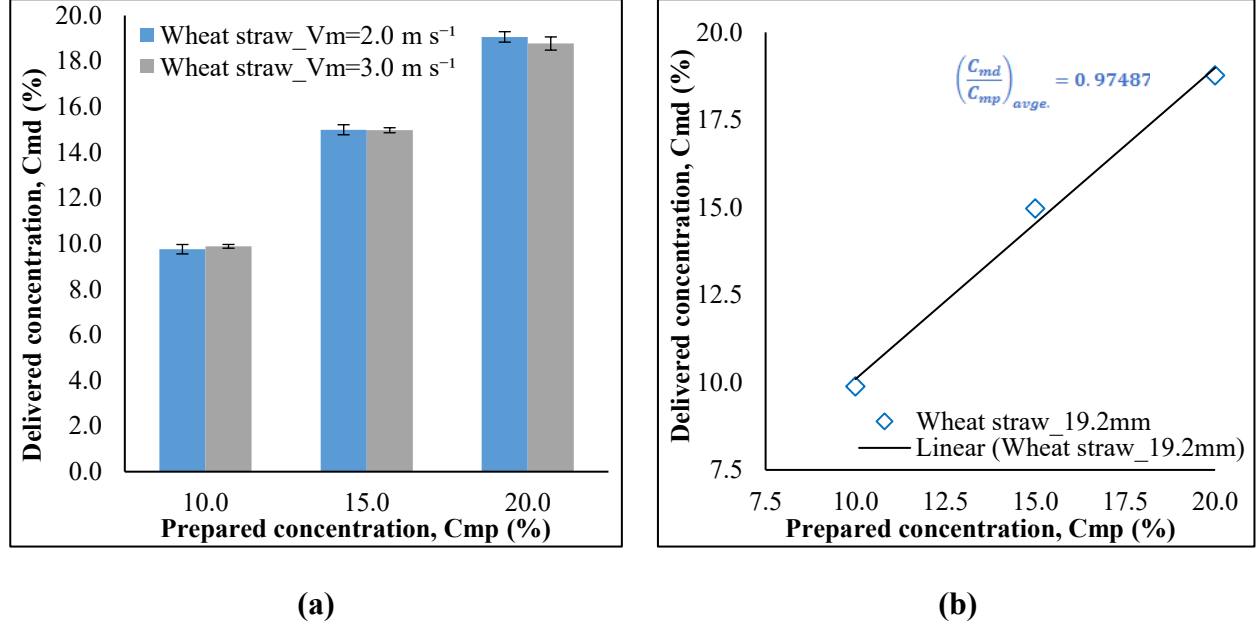


Figure 2.7: (a) Effect of bulk velocities on delivered concentrations (C_{md}) and (b) average ratios of C_{md} and C_{mp} at 3.0 m s^{-1} for 19.2 mm wheat straw.

The single C_{md} value in Figure 2.7 (a) represents an average (mean) of three samples collected at a corresponding specific C_{mp} value. The bulk velocities of the slurries chosen for the analysis were considerably greater than the critical deposition velocity ($v_D = 0.8 \text{ m s}^{-1}$) of the 19.2 mm particle size wheat straw evaluated by Vaezi et al. (Vaezi et al., 2018) and eventually confirmed the pseudo-homogeneous flow regime of slurries flowing through the pipe loop (Abulnaga, 2002). For the entire range of C_{mp} 's, the corresponding measured values of C_{md} were found to be less than those of C_{mp} at both bulk velocities (i.e., $2.0 ; 3.0 \text{ m s}^{-1}$) as seen in Figure 2.7 (a). However, the

difference was not large, with a decrease of up to 4% and 6% for 2.0 and 3.0 m s⁻¹, respectively, compared to that obtained for medium sand and glass beads and shown in Figure 2.3 (a). Generally, the concentration ratio $(C_{md}/C_{mp})_{avg.}$ was found to be 0.9749 and 0.9759 for bulk velocities of 3.0 and 2.0 m s⁻¹, respectively, for the range of concentrations tested. These figures indicate that a homogeneous wheat straw slurry was attained following saturation after 12 h of pumping. Figure 2.3 (b) shows the concentration ratio $(C_{md}/C_{mp})_{avg.}$ of the wheat straw-water mixture flow at a bulk velocity of 3.0 m s⁻¹. Therefore, it was concluded that improper mixing, as shown for medium sand and glass beads, did not have a significant effect on the wheat straw-water slurries. One of the main reasons could be the neutrally buoyant nature ($\frac{v_t}{v_m} \leq 0.021$) of the wheat straw particles, similar to fine sand (Kada & Hanratty, 1960), as described in section 2.2.3.2, demonstrating the absence of slip and giving rise to a reasonable approximation of $C_{in-situ}$ to be equivalent to C_{md} . Figure 2.7 (a) shows that the error bars, obtained using plus or minus one standard error means, at the similar concentrations (C_{mp}) and different bulk velocities of wheat straw slurries, overlapped. Thus, the difference of the mean values of C_{md} was statistically insignificant at two bulk velocities. These results indicate the very small effect of bulk velocity on the C_{md} of wheat straw slurries. The effect of velocity was found to be very small and was not as prominent as observed for medium sand, as seen in Figure 2.3 (a). Therefore, it was concluded that using $(C_{md}/C_{mp})_{avg.}$ obtained at a single bulk velocity of 3.0 m s⁻¹ was suitable for determining an in situ density for the entire range of bulk velocities for the analysis.

2.3.2 Frictional loss measurements of vertical upward flows of wheat straw-water suspension

The frictional pressure drops obtained for the 19.2 mm wheat straw slurry flowing upward through a vertical test section at prepared mass concentrations (saturated) of $C_{mp} = 5\text{-}25\%$ and a wide range of slurry bulk velocities ($v_m = 0.5\text{-}4.0 \text{ m s}^{-1}$) are given in Figure 2.8 (a).

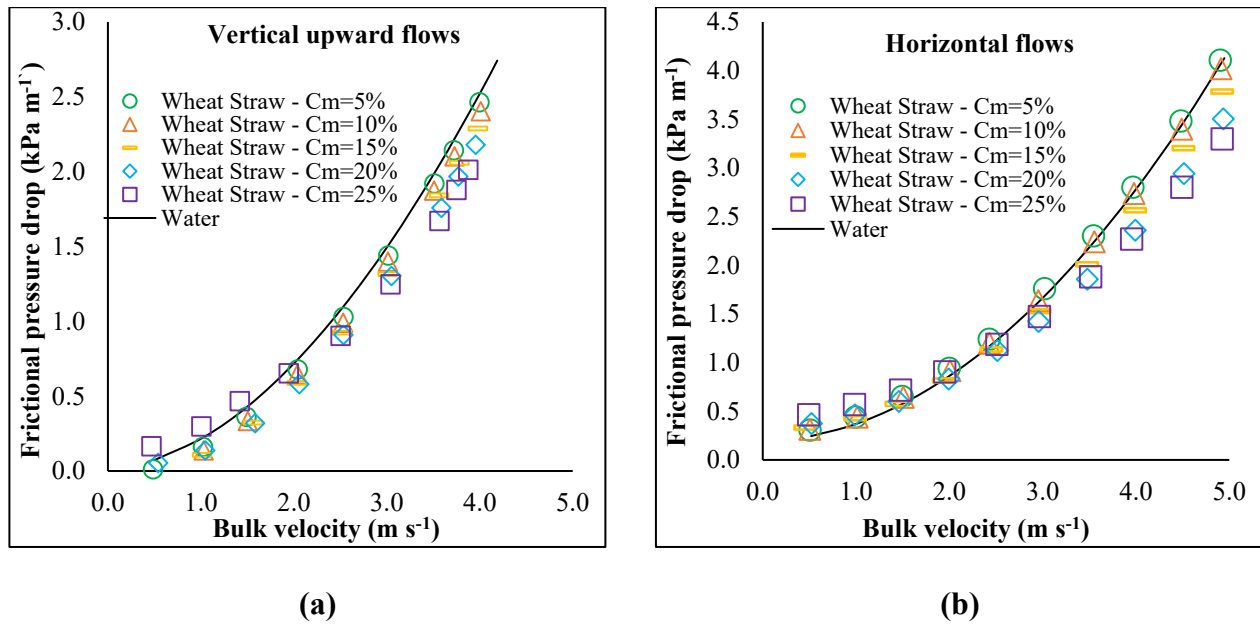


Figure 2.8: Frictional pressure drops for water-based mixtures of 19.2 mm wheat straw particles using saturated solid concentrations (% mass) through (a) a vertical test section and (b) a horizontal test section (results reproduced from Vaezi et al. [2014]; used with permission from Elsevier).

To find the in situ density of a mixture at different C_{mp} values, the delivered concentration (C_{md}) obtained (see section 2.3.1) was used, although it was not significantly different to the C_{mp} . For all velocities $\geq 1.0 \text{ m s}^{-1}$ and $C_{mp} = 5\text{-}20\%$ (mass), the friction pressure drops were observed to be below the curve for water in a similar fashion as reported by Bobkiewicz and Gauvin (1965) for vertical upward flows of short nylon fiber suspensions. At the highest concentration (i.e., $C_{mp} =$

25%), similar results were found for bulk velocities $\geq 1.9 \text{ m s}^{-1}$, as previously explained. However, for velocities $< 1.9 \text{ m s}^{-1}$, frictional pressure drops were found to be above the water curve, as noted by Kerekes and Douglas (1972) and Radin et al. (1975) for rayon, asbestos, and nylon fiber suspension flows in vertical pipes. For higher concentrations, and therefore higher apparent suspension viscosities and lower velocities, the flow of suspension appeared to be in plug flow, as explained in detail in section 2.3.3, causing an increase in the pressure drop, as explained by Radin et al. (1975).

For all of the experiments in this study, the effect of an increase in C_{mp} on the frictional pressure drop of wheat straw was considerable. For specific velocity ranges, at any given bulk velocity, an increase in slurry concentration increased the particle-particle interaction and eventually caused a corresponding fall in the frictional pressure drop curves, which increased with increased concentration below the water curve and generally conformed to similar findings that there is a decrease in friction factor with an increase in concentration with fiber suspension flows in pipelines (Kerekes, 1971; Radin et al., 1975; Vaezi et al., 2014). However, some flow characteristics found in our results, for vertical upward flows (Figure 2.8 [a]), were different from those reported by Vaezi et al. (2014). In Figure 2.8 (b), the data for wheat straw slurries of the same particle size and range of concentrations flowing in a horizontal pipeline (Vaezi et al., 2014) are plotted to allow comparison with our results in a similar diameter vertical section. For instance, for all bulk velocities $\leq 2.0 \text{ m s}^{-1}$ in the horizontal flows, the frictional pressure drop curves for $C_{mp} = 10\text{-}25\%$ were found to be above the water curve and for $C_{mp} = 5\%$, the frictional pressure drop was always above the water curve for the whole range of bulk velocities ($0.5\text{-}5.0 \text{ m s}^{-1}$, as shown in Figure 2.8 [b]). This was mainly due to the nature of the flow of wheat straw suspensions in the horizontal pipe section. At low velocities, the suspension scraped along the wall of the horizontal

pipe, with some rolling of fibers at the wall that increased the frictional pressure drop. As the velocity increases, the suspension moved with no physical contact with the inside walls of the horizontal pipe, decreasing the wall shear and consequently reducing friction loss (Vaezi et al., 2014). By contrast, in vertical flows of wheat straw suspensions, there was no bed formation (either sliding or stationary) at low velocities, and this eventually decreased the frictional pressure drops even at low velocities (Figure 2.8 [a]).

Another interesting feature in vertical upward flows of wheat straw-water mixtures was a significant decrease in frictional pressure drops in particles with lower aspect ratios than the pressure drop values obtained in vertical upward flows of fibrous suspensions using fibers with large aspect ratios. Despite the low aspect ratio of 6.3 of the wheat straw used in the current investigation, the frictional pressure drop was found to be much lower than reported by Bobkowicz and Gauvin (1965) and Radin et al. (1975), who used nylon and rayon fibers with aspect ratios of 51.0 and 86.0, respectively. The main reason the pressure drop was lower is the fibrous nature of the wheat straw particles, wide particle size distribution, and the potential for forming networks, as found by Vaezi et al. (Vaezi et al., 2014).

2.3.3 Flow regions in vertical upward flows of wheat straw-water suspensions

To determine the flow behaviour of wood fiber suspensions in pipelines, researchers have reported three more or less distinct regions – plug flow, transition flow, turbulent flow – through visual observation, photography, and velocity profile measurements (Daily et al., 1961; Forrest & Grierson, 1931; Mih, 1967; Robertson, 1957). These regions were further investigated by Radin et al. (1975) and Seely (1968) for fiber suspensions flowing in vertical pipe sections of different diameters. We attempted to interpret these regions for the current investigation using friction factor measurements for the entire range of mass concentrations (5-25%) of wheat straw-water

suspension flowing upward in a vertical test section. Figure 2.9 shows these regions by describing a relationship between the friction factor (obtained from Equation 2.1) and the generalised Reynolds number (Re_g).

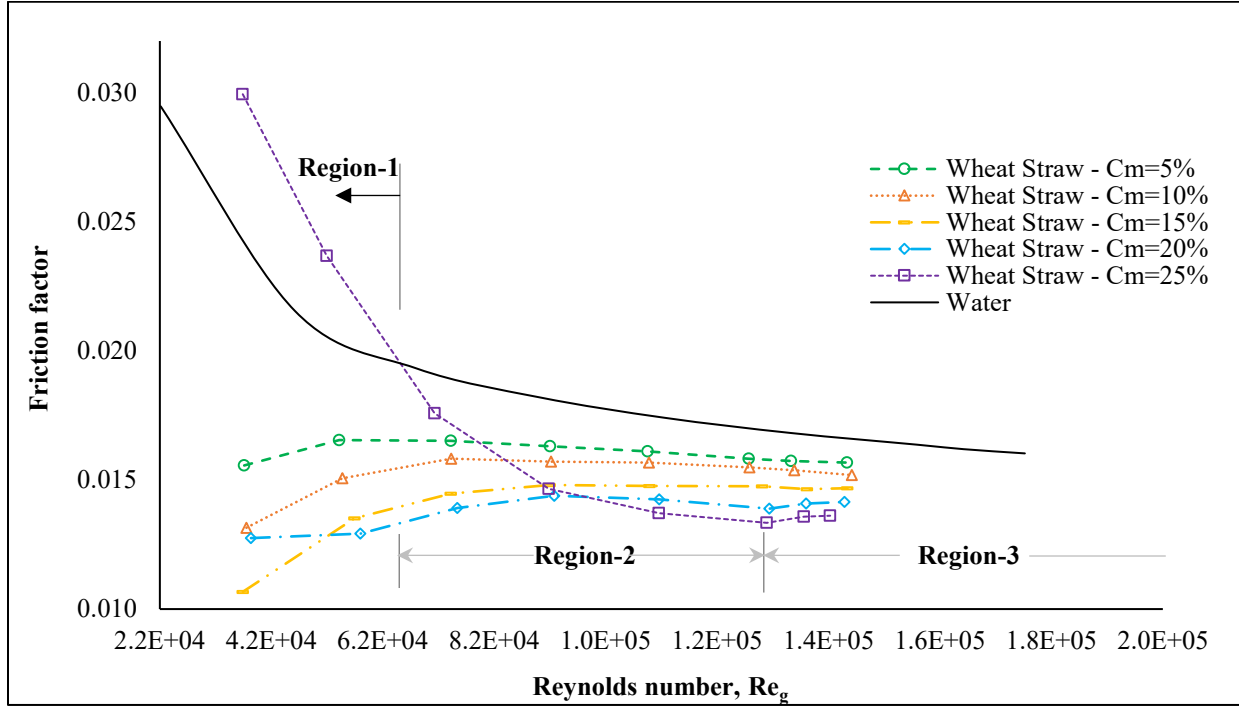


Figure 2.9: The friction factor versus generalised Reynolds number for velocities $\geq 1.0 \text{ m s}^{-1}$ for vertical upward flows of water-based mixtures of 19.2 mm wheat straw particles measured in the experimental setup (flow regions 1, 2, and 3 were adopted from Radin et al. [1975] for vertical upward flows).

The generalised Reynolds number was calculated using the standard relation including mixture density (ρ_m) as a function of C_{mp} , ρ_s , carrier fluid density (ρ_f), carrier fluid viscosity (μ_f), v_m , and D , as explained by Vaezi et al. (2014). The carrier fluid viscosity was taken from rotational viscometer measurements performed by Vaezi et al. (2014) and was found to exhibit Newtonian behaviour. Region 1, the plug flow region, has a low Reynolds number; the flow appears without any plug-wall interaction and with a gradual increase in the annulus size and a sharp decrease in

the friction factor. In this region, the plug is always surrounded by a fiber-free annulus of fluid (Radin et al., 1975). In Region 2, also known as the mixed flow region, the fluid in the annulus is always turbulent and the plug disintegrates at the annulus-plug interface (i.e., high shear region); the plug diameter and friction factor decrease with an increase in the Reynolds number, and the friction factor decreases at a rate slower than observed in the plug flow but faster than Newtonian fluid in turbulent flow in smooth pipes. In Region 3, the fully turbulent region, the friction factor does not decrease rapidly with increases in the Reynolds number (unlike Newtonian fluid); instead, in most cases, it increases with the Reynolds number (Bobkowicz & Gauvin, 1965; Kerekes, 1971; Radin et al., 1975; Seely, 1968).

For wheat straw-water suspension flows with the highest mass concentration, i.e., 25% (4.5% dry solid mass) in the vertical pipe section, Region 2 was clearly identified for the velocity range of 1.9-3.5 m s⁻¹ up to the maximum achievable drop in friction factor at 3.5 m s⁻¹ (see Figure 2.9); for velocities <1.9 m s⁻¹ the suspension appeared to be in the plug flow region (Region 1). For low velocities (<1.9 m s⁻¹) and high concentrations 25% (mass), the viscous nature of the suspension changed (Radin et al., 1975; Vaezi et al., 2014), which caused a sharp increase in the friction factor. The apparent viscosity (which considers the rheology of the entire suspension) changes linearly at lower solid concentrations and is proportional to the cube of higher solid concentrations (Djalili-Moghaddam & Toll, 2006). Hence, lower concentrations (5-20% [mass]) had negligible effect on the apparent viscosity of the wheat straw suspension under consideration for the entire range of velocities. Similar unusual concentration effects were found by Kerekes and Douglas (1972) for vertical upward flows of nylon fiber suspensions in a 50 mm diameter pipe and dry mass concentrations ranging from 1.95-5.73% (mass), where, for concentrations greater than 4.63% (mass), suspensions were found to be in plug and transition flow regions over the entire range of

Reynolds numbers. For concentrations $\leq 4.63\%$ (mass), the nylon fiber suspensions showed a transition flow region for the entire flow rate range (Kerekes & Douglas, 1972). Radin et al. (1975) found similar concentration effects for asbestos fiber suspensions in vertical upward flows through a 6.3 mm diameter pipe.

Furthermore, a slight increase in friction factor was observed at a concentration of 25% (by mass) above a suspension velocity of 3.5 m s^{-1} for wheat straw at the end of Region 2, agreeing with the second possibility mentioned for Region 3 that the friction factor increases mostly with increasing Reynolds number. However, the suspension still showed drag reduction and was found to be in the damped turbulence sub-region, as explained by Seely (1968). Because of the limitations of the slurry pump, higher velocities could not be achieved, which restricted our further analysis on the Newtonian turbulence sub-region (where the friction loss of the suspension and the suspended liquid are similar (Seely, 1968)). For concentrations of wheat straw suspensions of 5-20% (mass), all the friction factors obtained were found to be below the water curve for the entire range of Reynolds numbers and exhibited the characteristics of Regions 2 and 3. The primary reason for this outcome was the absence of bed formation, even at low velocities in vertical upward flows where the wheat straw suspension was moving with reduced friction.

2.3.4 Drag reduction in upward flows of wheat straw-water suspension

To calculate changes in the drag-reducing capabilities of wheat straw slurry, drag ratios (DRs) (the pressure drop of fiber suspension divided by the pressure drop of the carrier fluid at the same pumping velocity) were used for all the concentrations (C_{mp}) and ranges of bulk velocities. They are shown in Figure 2.10 (a).

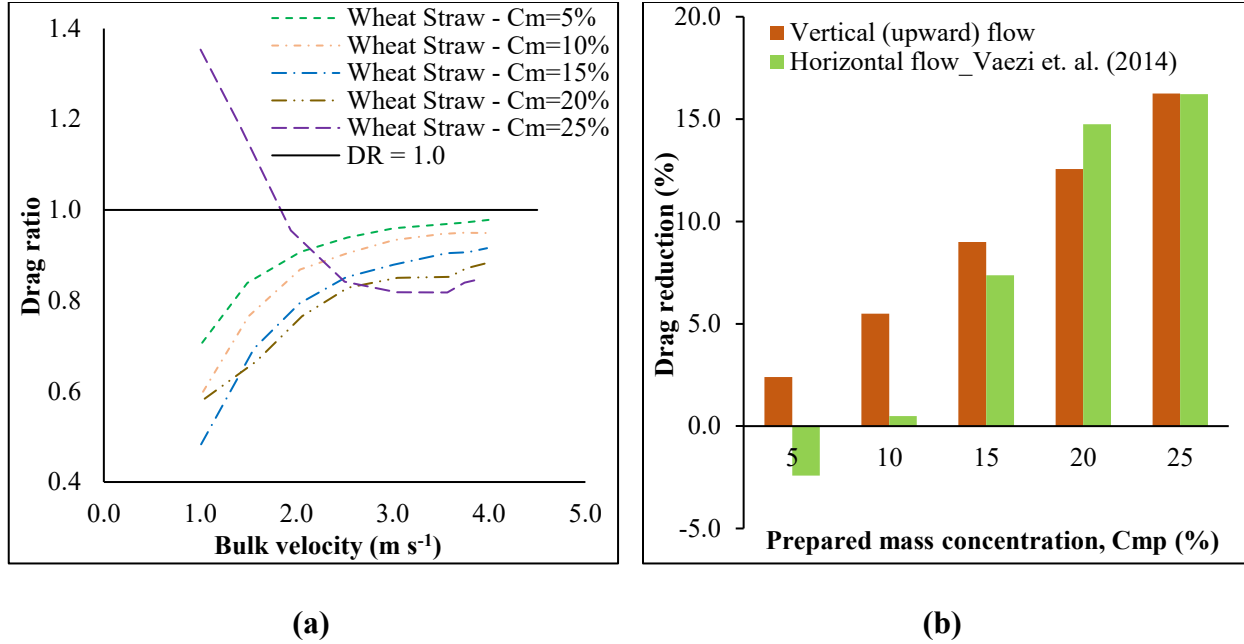


Figure 2.10: (a) Drag ratio versus mixture bulk velocity for several solid concentrations of 19.2 mm wheat straw particles flowing through a vertical test section and (b) Drag reduction as a function of a slurry solid concentration of 19.2 mm wheat straw particles at maximum slurry velocities flowing through a horizontal test section (results reproduced from Vaezi et al. [2014]; used with permission from Elsevier) and vertical upward flows (current investigation).

For the entire velocity range and a $C_{mp} = 5\text{-}20\%$ (mass), an increase in DR was noticed in the corresponding increase in slurry bulk velocity at any specific C_{mp} value. It is worth mentioning that the DR was less than unity at all velocities and concentrations in the range 5-20% (by mass); this is a unique feature of upward flows of the wheat straw-water suspension compared to the horizontal flows reported by Vaezi et al. (2014) where the DR was less than unity for specific velocity ranges. On the other hand, at the highest concentration ($C_{mp} = 25\%$), the DR decreased with increased slurry bulk velocity and was less than unity for all bulk velocities $\geq 1.9 \text{ m s}^{-1}$. However, for bulk velocities $\leq 1.9 \text{ m s}^{-1}$ and $C_{mp} = 25\%$, the DR was greater than unity, indicating

that no drag-reducing capabilities for wheat straw particles were evident because of the plug flow of the suspension, as mentioned by Radin et al. (1975). The lowest attainable DR of 0.818 was observed at the highest concentration, i.e., 25% (by mass), at a mixture velocity of 3.5 m s^{-1} . Furthermore, a sharp increase or decrease in DR became almost consistent within a percentage change of 4.0% between 3.5 m s^{-1} and the highest achievable bulk velocities for the entire range of concentrations tested (5-25% [mass]). Moreover, the DR decreased from 0.98 to 0.85 at the highest slurry bulk velocities for all the concentrations (C_{mp}) from 5-25% (mass). These observations show DR to be a strong function of slurry bulk velocity and concentration for the upward slurry flow of wheat straw particles, as Vaezi et al. (2014) also found for horizontal flows.

Figure 2.10 (b) shows the highest achievable drag reductions (%DR) for wheat straw-water slurries flowing through the vertical test section at maximum bulk velocities and various solid concentrations (C_{mp}). An increase in C_{mp} from 5-25% increased the drag reduction from 2.4-16.3% at maximum bulk velocities; this was due to an increase in particle-particle interactions (Bobkiewicz & Gauvin, 1965; Radin et al., 1975). As concentration, and hence particle-particle interaction, increases, drag reduction at a certain flow rate increases to a maximum value. Vaezi et al. (2014) reported similar behaviour for horizontal flows of slurry of the same wheat straw size and the same range of concentrations, as shown in Figure 2.10 (b). The highest attainable drag reduction (19%) was observed at the highest concentration, i.e., 25% (mass), at a mixture velocity of 3.6 m s^{-1} . Furthermore, in this investigation, the percentage drag reduction achieved at the highest attainable bulk velocities for $C_{mp} = 5\text{-}15\%$ was greater than that obtained in horizontal flows. For the highest concentration at $C_{mp} = 25\%$, drag reduction was similar for both vertical and horizontal flows, whereas at $C_{mp} = 20\%$, the percentage drag reduction in vertical flows was less than that observed in the horizontal pipe (Figure 2.10 [b]). The overall wheat straw slurry

friction loss behaviour for larger particle sizes in vertical upward flows was influenced differently by solid mass concentration and velocity than in horizontal flows, thus offering new insights (and suggestions for further investigations) in optimising the design and operation of pipeline hydro-transport of biomass slurry for commercial applications.

2.4 Conclusions

Pipeline hydro-transport of the 19.2 mm particle size agricultural residue biomass wheat straw was examined in a vertical test section to explore the particle's frictional behaviour at various flow conditions. In the calibration phase, a standard method was used to measure the delivered concentrations of three conventional slurries of medium sand, glass beads, and fine sand in water to predict their corresponding in situ concentrations while flowing in the vertical test section. Despite differences in the measurements of the delivered concentrations of water-based slurries of conventional solids with respect to bulk velocities and prepared concentrations, a reasonable correlation was developed in the form of an average ratio, i.e., $(C_{vd}/C_{vp})_{avg}$, for a single bulk velocity of 3.0 m s^{-1} , which was in a pseudo-homogeneous regime, to represent a common factor for each individual material. The correlations, which apply only to the current investigation's experimental setup and for delivered concentrations of medium sand and glass beads, were found to be two and two and a half times greater than the corresponding prepared concentrations, respectively. However, for fine sand slurry, both the prepared and delivered concentrations were found to be almost similar. The significant difference in delivered and prepared concentrations for larger conventional solids with high terminal settling velocity was due to the stratified concentration near the bottom of the mixing tank, which did not appear for fine sand with comparatively very low terminal settling velocity. The standard method used to measure in situ concentrations in vertical upward flows was validated for the entire range of slurry flow rates

above the critical deposition velocity when the pressure drop measurements of conventional solid-water slurries were compared with the results from Newitt et al.'s model (1961). These findings using conventional solids during the calibration phase helped predict the delivered concentration of wheat straw slurries to be similar to their corresponding prepared concentrations because biomass particles also seemed to exhibit very low terminal settling velocities like fine sand. The delivered concentrations of wheat straw-water suspensions were measured, found almost similar to the prepared concentrations, and subsequently used as in situ concentrations to evaluate the frictional pressure drops in vertical upward flows. The drag-reducing capabilities of the wheat straw-water suspensions were investigated using frictional loss measurements. The different flow regions were identified to elaborate frictional behaviour of the wheat straw-water suspension as functions of velocity and mass concentrations. The increase in concentration considerably reduced the frictional pressure drops of wheat straw slurry suspensions in vertical upward flows, and the highest drag reduction was found at the highest concentrations.

For the parameters studied in the present work, the following conclusions can be made: The use of delivered concentration as in situ concentration for homogenous flow regimes of medium sand, fine sand, and glass beads slurries proved to be a rational approach for vertical upward flows. The delivered concentration of the wheat straw-water mixture showed the $(C_{md}/C_{mp})_{avg}$ to be 0.9749, indicating the slurry is homogenous. A maximum drag reduction of 19% was achieved with a 25% (mass) slurry of wheat straw at a slurry bulk velocity of 3.5 m s^{-1} , although at low velocities ($<1.9 \text{ m s}^{-1}$) the suspension showed plug flow. At the maximum achievable bulk velocity and highest concentration of 25% (mass), the suspension was found to be in the damped turbulence sub-region with a drag reduction of 16.3%. For concentrations of 5-20% (mass), all the wheat straw suspensions demonstrated drag reduction for the entire range of bulk velocities, showing the

characteristics of mixed (transition) and fully turbulent regions (whereas horizontal flows showed plug and mixed flow regions). The overall behaviour of wheat straw slurry friction loss in a vertical upward flow was therefore found to be greatly influenced by solid mass concentrations and velocity quite differently than in horizontal flows, thus suggesting a new approach is required to optimise the design and operation of the pipeline hydro-transport of biomass slurry for commercial applications. The developed information in this paper is important for the design of large-scale biomass slurry pipelines for the development of biomass conversion facilities.

Chapter 3: The Effect of Particle Size and Concentration on the Frictional Behaviour of Vertical Upward Flows of Wheat Straw Aqueous Slurries²

3.1 Introduction

The increase in energy demand from population growth and industrialization severely impacts the environment through increased greenhouse gas (GHG) emissions, especially from the use of fossil fuels, the largest source of GHGs around the world (Natural Resources Canada, 2022; The Conference Board of Canada, 2023). One of the promising and sustainable means of mitigating GHG emissions is to produce biofuel from lignocellulosic biomass (such as agricultural or forest residue) to replace fossil fuels. Biomass (a product obtained from a living organism or its by-products) can be directly converted into liquid fuels and thus can replace fossil fuels. The bio-energy sector currently produces liquid fuels at low capacities, largely because of the high cost of transporting biomass by truck and in part because of the low technology readiness level of biomass conversion pathways (Aden et al., 2002; Kumar et al., 2005a, 2005b). The pipeline hydro-transport of agricultural residue biomass (wheat straw, corn stover) from farms to biorefineries has been verified to be techno-economically viable for large-scale biofuel production; however, all the corresponding studies are limited to horizontal pipeline arrangements (Kumar et al., 2004, 2005a, 2005b; Vaezi et al., 2014). A topography of a long-distance pipeline network would likely include different inclinations of pipe segments.

² A version of this chapter has been published as. Javed, K., Kurian, V., & Kumar, A. “Effect of particle size and concentration on the frictional behavior of vertical upward flows of wheat straw aqueous slurries”, *Chemical Engineering Research and Design Journal*, 2022, 186, 614-627.

There is some research on the effect of particle size or aspect ratio (fiber length to diameter ratio), slurry solid concentrations, and slurry bulk velocity on the frictional behaviour of fiber suspensions in vertical upward flows (Bobkiewicz & Gauvin, 1965; Kerekes, 1971; Radin et al., 1975; Seely, 1968; Steen, 1989). Modeling the frictional behaviour of fiber suspension flows is challenging because these flows are complex and have unique rheological properties (Cui & Grace, 2007; Derakhshandeh et al., 2011; Duffy, 2006). Therefore, the intention of most investigations has been to explore the flow regions of the suspensions and mechanisms affecting the frictional pressure drop in vertical upward flows to understand their flow behaviour at various flow conditions (Bobkiewicz & Gauvin, 1965; Kerekes, 1971; Radin et al., 1975; Seely, 1968; Steen, 1989). Radin et al. studied the flow regions (plug flow, mixed flow, and fully turbulent flow) in vertical upward flows of rayon fiber suspensions and examined the effect of aspect ratio, mass concentration, and pipe diameter on friction factor over a wide range of Reynolds numbers. They learned that these types of suspensions cause drag reduction (the percent reduction in friction loss of a suspension with respect to that of water alone at the same bulk velocity) at certain flow conditions and that drag reduction increased with the addition of the fibers (i.e., concentration) and their aspect ratio (Radin et al., 1975). Kerekes examined the frictional behaviour of various sizes and concentrations of nylon fiber suspensions in vertical upward flows and found the strong effect of aspect ratio and mass concentration on turbulent drag reduction (which increases with increases in the aspect ratio and concentration for certain velocity ranges) (Kerekes, 1971).

Bobkiewicz and Gauvin investigated the mechanisms behind drag reduction by pressure drop measurements in a turbulent range of aqueous nylon fiber suspensions in a vertical copper tube as a function of bulk velocity, fiber aspect ratio, and mass concentration (up to 6.0%) (Bobkiewicz & Gauvin, 1965). The damping of turbulent structures by the solid particles was found to be

responsible for drag reduction, which increases with increases in the aspect ratio of fibers at a fixed mass concentration. For fibers with a low aspect ratio, drag reduction was almost negligible (Bobkowicz & Gauvin, 1965). Kerekes and Douglas postulated the particulate-inertial mechanism of fiber suspension flow based on interference by suspended solids with turbulent motion near the wall of vertical pipe (Kerekes & Douglas, 1972). They further verified this postulate from the velocity profile results while investigating drag reduction in the turbulent flow of aqueous suspensions of inelastic fiber (short, smooth, rigid nylon) with dilute concentrations (0.07% mass) through a vertical circular cross-section pipe (Kerekes & Douglas, 1972). A quantitative criterion was proposed for the upper and lower limits of the suspension conditions verified by the frictional loss measurements. The study showed strong dependence of turbulent drag reduction on aspect ratio and mass concentration of nylon fibers (Kerekes & Douglas, 1972). Although the mechanisms behind drag reduction were illustrated by Bobkowicz and Gauvin and later Kerekes and Douglas (Bobkowicz & Gauvin, 1965; Kerekes & Douglas, 1972), Steen carried out a comprehensive study on these mechanisms by evaluating turbulent structures in vertical flows of fiber suspensions (Steen, 1989). Steen measured the radial profiles of axial velocity and turbulence spectra for the suspensions of glass fibers in alcohol at various concentrations during upward flow in a vertical pipe. The author observed that the suspensions with long fibers and high concentrations showed plug flow specifically in various parts of the core, which reduced turbulence, especially at shorter scales. In contrast, at low concentrations, short fibers showed an increase in turbulent energy in the spectrum at smaller length scales (Steen, 1989).

A few studies on vertical hydro-transport of lignocellulosic biomass have been performed at laboratory scale. Our own work includes a recent study on the effect of concentrations on the frictional behaviour of wheat straw aqueous slurry with particle sizes of 19.2 μm (aspect ratio of

6.3) through a vertical pipe section ($D = 50$ mm) in a 29 m long closed-circuit pipeline facility (Javed et al., 2021). In vertical upward flows of wheat straw aqueous slurries of that particle size, 19% drag reduction was found at the highest velocity (4.0 m s^{-1}) and a concentration of 25% (mass) despite the low aspect ratio of the wheat straw particle size compared to the other fiber suspensions (i.e., nylon, rayon, and asbestos fibers). Slurries of low concentrations and the entire range of velocities were found to remain in the mixed flow region (i.e., still exhibiting drag-reducing capabilities). This recent study includes the indirect investigation of the in situ concentrations of wheat straw aqueous slurries through delivered concentration measurements, and we observed the homogenous nature of the suspension (Javed et al., 2021).

Although the frictional behaviour of wheat straw aqueous slurries has been experimentally studied for a specific group of particles with a large nominal size (i.e., 19.2 mm) by measuring the frictional pressure drops in a vertical pipe section (Javed et al., 2021), no work has been done to understand the effect of particle size on frictional behaviour and in situ concentrations of these kinds of suspensions.

The purpose of the present study is to experimentally examine the frictional behaviour of the upward flow of wheat straw aqueous slurries of different particle sizes in a vertical pipe and to explore their in situ concentrations by quantitatively analyzing their delivered concentrations. The specific objectives include:

- Investigating the effect of particle size on the frictional behaviour of wheat straw aqueous slurries at various concentrations and velocities in vertical upward flows.
- Investigating the conditions of drag reduction for wheat straw aqueous slurries.

- Examining in situ concentrations of wheat straw aqueous slurries by experimentally measuring delivered concentrations of corresponding slurries flowing in a pseudo-homogenous regime.
- Exploring the effect of particle size and bulk velocity on delivered concentrations of wheat straw aqueous slurries.

3.2 Method

3.2.1 Experimental setup

The apparatus used in this study (Figure 3.1) comprises a 29 m long, 50 mm diameter closed pipeline loop, a centrifugal slurry pump (CD80M; Godwin Pumps Ltd., Bridgeport, NJ, USA), Schedule 40 steel and PVC transparent pipe sections, heat exchanger, magnetic flow meter (FMG-424; Omega Eng., Stamford, CT, USA), flow visualisation section, semi-circular and 90° bends, flexible PVC pipe sections, differential pressure transmitter (Fuji Electric Ltd-Model: FKCT22V5), mixing tank with mixer (EV6P50M; Lightning Inc., Rochester, NY, USA) and temperature sensor (RTD-E; Omega Eng., Stamford, CT, USA). For online recording and data processing, all the instruments (except the mixer) are hooked up to LabView (a data acquisition program). The complete details of the instruments, data acquisition system, and data acquisition program (LabView) are given in our earlier studies (Javed et al., 2021; Vaezi, 2014; Vaezi & Kumar, 2014b; Vaezi et al., 2018). The magnetic flow meter is located at $200D$ downstream of the slurry pump (D is the inside diameter of the pipeline) (Vaezi et al., 2014). The heat exchanger (CIMCO Industries limited, 2021) consists of a chiller that encompasses two independently operating closed circuits, i.e., a refrigeration cycle (KEZA030H8; KeepRite Refrigeration Corp., ON, Canada) and a glycol/water (solution) circulating pumping system (FKC75K; Franklin Electric, Fort Wayne, IN, USA).

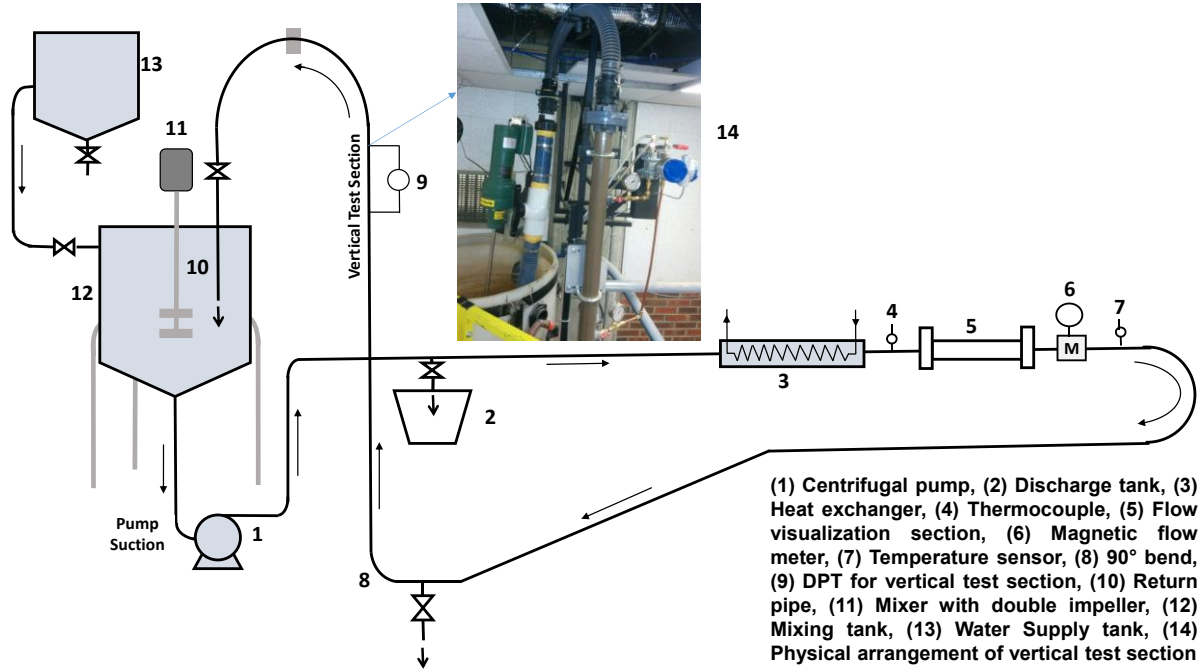


Figure 3.1: Schematic of integrated pipeline facility.

The cold glycol/water solution flows from the evaporator (of the refrigeration cycle) toward the main pipe loop (containing slurry) to maintain the slurry temperature at 12-15 °C. The vertical test section of span L equal to $10D$ contains a highly accurate differential pressure transmitter (DPT) (Fuji Electric, 2010, 2014). The DPT is installed at $42D$ downstream of the 90° bend to eliminate the effect of secondary flows (Enayet et al., 1982; Kalyanraman et al., 1973; Kim et al., 2014), reduce bend loss (Ito, 1960), and develop smooth velocity profiles (Hellström et al., 2013). The DPT senses pressure differences through high- and low-pressure impulse lines (water is the pressure sensing fluid) and converts it to an electrical output signal of 4-20 mA (DC). The electrical output signal is transformed into the pressure output signal (psi) using LabView to give the fluid flow pressure drop at a specific bulk velocity.

3.2.2 Calibration

Calibration is essential to ensure accurate performance of the vertical loop and the reliability of the experimental measuring techniques and the data acquisition system used in the current research. The performance of the electromagnetic flow meter was checked through the delivered volume flow rate analysis (Spelay, 2007) done at the end of the vertical loop, where the return pipe enters the mixing tank (shown in Figure 3.1). Three samples of delivered volumes of water were collected at each bulk velocity for the entire velocity range ($0.5\text{--}4.5\text{ m s}^{-1}$) achievable in the current setup. The time to collect each sample of delivered volume was measured with an electronic stopwatch. The delivered volume flow rates (L s^{-1}) of water obtained by averaging the three samples (collected at each velocity) were compared with the corresponding “measured flow rates” by the flow meter and recorded in LabView. The results showed a very good agreement, confirming the proper functioning of the flow meter (Figure 3.2 [a]).

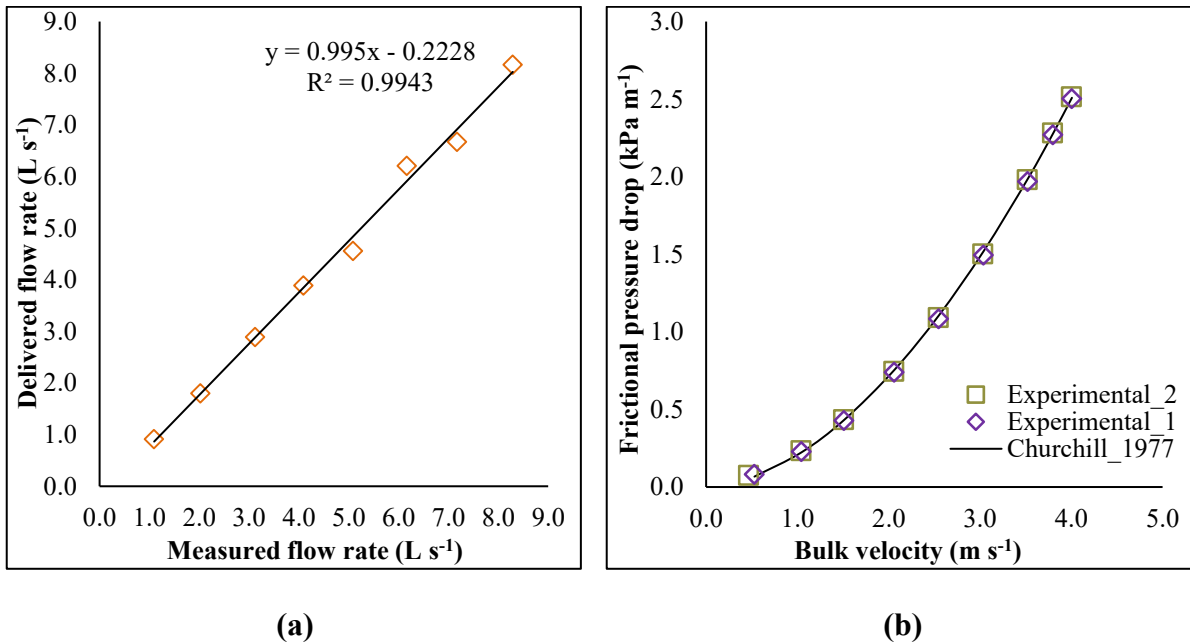


Figure 3.2: (a) Delivered flow rate test for water and (b) Frictional pressure drop vs. bulk velocity of water through a vertical test section.

The DPT was calibrated by running clear water through a closed pipeline loop and comparing the experimental frictional pressure drops obtained in a vertical test section with Churchill's pressure drop correlation (applicable in all flow regimes of fluid flows through smooth or rough pipes) (Churchill, 1977). The absolute roughness value for a vertical PVC pipe section was taken as 0.0015 mm from standards available (Chaurette, 2003; Pipeflow, 2023; Talmon, 2013; White, 2009). The following general expression was used to find the experimental frictional pressure drops of fluids in the vertical test section (Ferre & Shook, 1998; Krampa, 2009):

$$\left(\frac{\Delta P_f}{L}\right)_m = \frac{\Delta P_{MD}}{L} - [\rho_m - \rho_w]g \quad (3.1)$$

where $(\Delta P_f/L)_m$, $(\Delta P_{MD}/L)$, ρ_m , and ρ_w are the frictional pressure drop of the mixture, measured pressure drop, the densities of the mixture, and water, respectively. In the case of water present in the impulse lines and flowing through the vertical PVC pipe section, the static head term (i.e., $[\rho_m - \rho_w]g$) in Equation 3.1 will become zero. The plot of the frictional pressure drop versus the bulk velocity of water at 18 °C is shown in Figure 3.2 (b). Excellent agreement was found between the corresponding values.

3.2.3 Wheat straw feedstock preparation

Dry wheat straw bales obtained from farms in Northern and Southern Alberta (a western province in Canada) were chopped with a cutting mill (SM-100; Retsch Inc., Surrey, BC, Canada) and classified with a commercial classifier (BM&M Inc., Surrey, BC, Canada) into four major groups with nominal sizes (classifier sieve opening sizes) of 19.2 mm, 6.4 mm, 3.2 mm, and <3.2 mm in the laboratory. This classification of particle sizes of chopped wheat straw based on the classifier sieve sizes has been discussed in earlier study by Vaezi et al. (Vaezi et al., 2013). The basic morphological features of each of the four groups of the classified wheat straw particles, derived

from Vaezi et al. (2014, 2013), are given in Table 3.1. D_{50} represents the median length obtained at a 50th percentile of the cumulative size distribution. The other dimensions, i.e., X_{gl} ^a, X_{gw} , σ_{gl} ^b, and σ_{gw} , represent the geometric mean length, geometric mean width, geometric standard deviation of mean length, and width of the particles, respectively. The complete procedure to determine these dimensions along with the other morphological characteristics of the biomass particles has been elaborated in earlier study (Vaezi et al., 2013) and is beyond the scope of this paper. The frictional behaviour of the largest particle size (i.e., 19.2 mm) has already been explored in our earlier work (Javed et al., 2021). In the current study, the frictional behaviour of the remaining three particle sizes (Table 3.1) was analyzed in detail.

Table 3.1: Particle morphology of wheat straw (Vaezi et al., 2014)

Nominal size (mm)	Median length (mm)	Geometric length (mm)	Geometric width (mm)	Length (mm)			Width (mm)		Aspect ratio	
	D_{50}	${}^aX_{gl} \pm \sigma_{gl}{}^b$	$X_{gw} \pm \sigma_{gw}$	Min.	Max.	Mean \pm S.D.	Min.	Max.	Mean \pm S.D.	(φ_p)
~19.2	8.29	8.42 ± 1.49	1.34 ± 1.54	1.69	27.49	8.92 ± 3.61	0.18	4.31	1.43 ± 0.58	6.28
~6.4	5.00	4.79 ± 1.57	1.07 ± 1.56	0.95	12.79	5.15 ± 2.09	0.19	3.62	1.16 ± 0.51	4.47
~3.2	3.92	3.96 ± 1.41	1.12 ± 1.51	0.98	7.87	4.13 ± 1.34	0.22	3.02	1.19 ± 0.46	3.53
<~3.2	2.42	2.57 ± 1.43	0.74 ± 1.46	0.97	6.94	2.70 ± 0.99	0.18	3.22	0.78 ± 0.30	3.47

^a $X_{gl} = Ln^{-1}[\sum(N_i \times \ln X_i)/\sum N_i]$; N_i , and X_i are the number of particles of a particular distinct dimension and the distinct length of the particle, respectively.

^b $\sigma_{gl} = Ln^{-1}[\sum N_i (\ln X_i - \ln X_{gl})^2 / \sum N_i]^{1/2}$

^cEvaluated from samples of 400-2000 particles. The number of particles was different for each of the four nominal sizes. Mean length indicates the average length of the particles.

^dEvaluated from samples of 400-2000 particles. The number of particles was different for each of the four nominal sizes. Mean width indicates the average width of the particles.

3.2.4 Wheat straw slurry preparation procedure

The wet-basis moisture content (MC) of the classified material was measured using ASABE S358.3 standard (ASABE, 2012). We randomly picked four samples of a specific particle size of wheat straw weighing at least 25 g, adopted from our earlier work (Vaezi et al., 2014), and oven-dried the samples at 103 °C for 24 h to find the initial MC of the material. Wheat straw (and other agricultural residue) absorbs moisture when mixed with water (Luk, 2010; Mohamadabadi, 2009). Hence the rheology of a wheat straw-water mixture constantly changes over several hours of pumping until the mixture becomes stable at a fully saturated state with a MC of 82%, as reported by Vaezi et al. (2014).

Keeping in view of these characteristics of wheat straw, the required mass of a specific particle size for a maximum possible saturated mass concentration (i.e., C'_{mp} s of 30%, 35%, and 40% for 6.4 mm, 3.2 mm, and <3.2 mm sizes, respectively) was evaluated using the initial MC (wet basis) and the saturated MC value (82%). Once the required volume of water was deaerated from the closed-circuit pipeline system, the premeasured mass of wheat straw was added to the mixing tank with the mixer on and continuously circulated the prepared slurry through the loop for about 12-15 hours (depending on particle size and concentration) until it became fully saturated (stable) at the highest possible mass concentration (e.g., $C_{mp} = 40\%$ for a <3.2 mm particle size). The stability of the wheat straw-water slurry was determined by continuously monitoring its pressure and velocity fluctuations (on an hourly basis) while it flowed through the closed pipeline loop. We observed these fluctuations in both velocity and pressure to be too high initially. However, in stable slurry condition (i.e., fully saturated), the pressure and velocity fluctuations of wheat straw slurries were damped down to approximately 1.0% per hour. The operating velocity was varied from 0.5-4.0 m s⁻¹ and the solid concentrations from 40-5% (mass), equivalent to 38.8-4.8% (volume)

(through slurry dilutions at 5% increments). During this process, the corresponding total pressure drop values were recorded and used in Equation 3.1 to obtain the frictional pressure drops of the corresponding slurries. The same procedure was used for the 6.4 mm and 3.2 mm particle sizes to the $C_{mp} = 30\%$ and 35% (mass), respectively. The visual observations showed that all the wheat straw particles followed the flow of the carrier fluid even at the minimum slurry velocity of 0.5 m s^{-1} for the entire range of mass concentrations of all three particle sizes. The volume and mass percentages of saturated and dry solids (oven-dried) of wheat straw slurries are shown in Table 3.2, considering a saturated particle density of wheat straw of 1050 kg m^{-3} (from (Vaezi, 2014)).

Table 3.2: Volume and mass percentages of saturated and dry solids of wheat straw-water mixtures

Mass percentage of saturated solids	Volume percentage of saturated solids ^e	Mass percentage of dry solids	Volume percentage of dry solids	Saturated slurry density
(%)	(%)	(%)	(%)	(kg m^{-3})
40	38.83	7.2	7.15	1019.42
35	33.90	6.3	6.24	1016.95
30	28.99	5.4	5.34	1014.49
25	24.10	4.5	4.44	1012.05
20	19.23	3.6	3.54	1009.62
15	14.39	2.7	2.65	1007.19
10	9.57	1.8	1.76	1004.79
5	4.77	0.9	0.88	1002.39

^eThe volume percentages of dry and saturated solids were evaluated by dividing the volume of the dry or saturated solids with the total volume of slurry loop

3.2.5 In situ concentration measurement

In slurry transport through an integrated pipeline setup (with horizontal, vertical, and inclined sections), an accurate assessment of in situ concentration ($C_{in-situ}$) is essential to predict the frictional behaviour of the slurry, particularly in vertical and inclined pipe orientations because of

the effects of gravity (Bartosik, 2010; Ferre & Shook, 1998; Kerekes, 1971; Shook & Bartosik, 1994). To find the in situ concentrations and hence an in situ density (required for Equation 3.1) for the current investigation, we followed a standard approach known as flow diversion sampling without using any online concentration measuring device (because, as others note, there is no higher concentration measuring device for fiber suspensions (Belyachits et al., 2014; Nakayama, 1994; Törmänen et al., 2006)). In this approach, we manually collected the delivered concentration (C_{md}) samples (18-25 L) through the return pipe (going inside the mixing tank) at the end of the loop (Figure 3.1) at mixture bulk velocities (v_m) of 3.0 m s⁻¹ and 2.0 m s⁻¹. These velocities were selected such that they remain greater than the critical deposition velocity ($v_D = 0.8$ m s⁻¹) of wheat straw aqueous slurries (Vaezi et al., 2018), which allowed us to reasonably approximate the delivered concentrations to be equal to the corresponding in situ concentrations (Wilson et al., 2006). Three samples were collected for each prepared concentration (C_{mp}) and both velocities (3.0 and 2.0 m s⁻¹), and their MCs were measured using the Thermogravimetric Analyzer (TGA701; LECO Corporation, St Joseph, MI, USA) (Patel et al., 2019) after removing surface water (Javed et al., 2021). These MCs were used to find the dry matter solid mass concentrations and hence the delivered saturated solid mass concentrations using the values provided in Table 3.2.

3.2.6 Friction factor and viscosity measurements

Once the experimental frictional pressure drops of wheat straw-water slurries at various flow conditions were obtained as explained in section 3.2.4, the experimental friction factors of the corresponding slurries were evaluated using Equation 3.2:

$$(\Delta P_f)_m = \frac{\rho_m f_D L v_m^2}{2D} \quad (3.2)$$

where ρ_m , f_D , L , v_m , and D are the slurry density (saturated), the Darcy-Weisbach friction factor, a span of the vertical test section, the slurry bulk velocity, and the inside diameter of the vertical pipe, respectively. The saturated slurry densities (ρ_m) of wheat straw at different concentrations were obtained using Equation 3.3 below and are given in Table 3.2.

$$\rho_m = \rho_w[1 + C_V(S - 1)] = \rho_w + C_V(\rho_s - \rho_w) \quad (3.3)$$

Where C_V , S , and ρ_s are the volumetric concentration of slurry, specific gravity of the solid particle, and particle density in the saturated state, respectively. The generalised Reynolds (Re_g) number was evaluated using the standard relation including slurry density (ρ_m), carrier fluid viscosity (μ_f), v_m and D , as shown in Equation 3.4.

$$Re_g = \frac{\rho_m v_m D}{\mu_f} \quad (3.4)$$

In the case of water flow through the vertical pipe section, the experimental friction factor and generalised Reynolds number were evaluated using Equation 3.2 and Equation 3.3 by replacing ρ_m and v_m with ρ_w and v_w , respectively. Since the biomass-water slurries contain fine particles ($\leq 50 \mu\text{m}$) in addition to the larger particles used during their flow through the pipeline, the carrier fluid for biomass slurries is considered “fine particles + water” instead of water only. The presence of these fine particles makes the carrier fluid a non-settling homogeneous mixture. In one of our previous studies (Vaezi et al., 2014), the samples of biomass-water slurries were filtered using a $50 \mu\text{m}$ woven wire filter to obtain the mixture of only fine particles + water. The viscosity of this fine solid-liquid mixture was experimentally measured using a rotational viscometer (AR 2000: TA Instrument, New Castle, DE, USA) at various shear rates and temperatures. The carrier fluid viscosities for agricultural residue biomass aqueous slurries were found to display Newtonian characteristics. (Vaezi et al., 2014). In our current investigation, the viscosities and densities of

carrier fluid (fine particles + water) were used while evaluating Re_g for wheat straw aqueous slurry. We did not experimentally measure the apparent viscosity (the viscosity of the entire suspension at a specific solid mass concentration) of the wheat straw suspensions in the present work due to the non-availability of the required apparatus. However, we developed a method to theoretically calculate the apparent suspension viscosity by using the morphological characteristics of the wheat straw particles (given in Table 3.1), as explained in section 3.3.2.2.

3.2.7 Uncertainty analysis

The uncertainty in the pressure drop measurements (Figure 3.3) was checked by conducting two sets of experiments on each aqueous slurry of each particle size (6.4 mm, 3.2 mm, and <3.2 mm) of wheat straw (Table 3.1) in vertical upward flows.

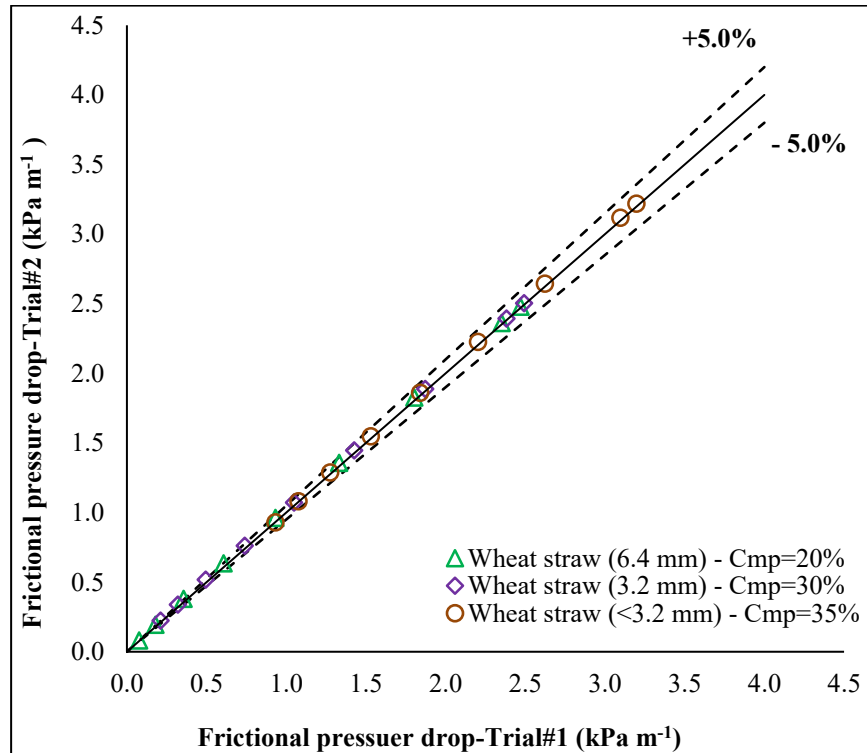


Figure 3.3: The repeatability of two sets of experiments on wheat straw aqueous slurries of 6.4 mm, 3.2 mm, and <3.2 mm particle sizes in a 50 mm diameter vertical test section.

A standard uncertainty analysis was used by finding the precision uncertainty (P_X) of differential pressure measurements and the biased uncertainty (B_X) of the DPT to obtain the total uncertainty (U_X) (MECE 301, 2018; Moffat, 1988; Vaezi et al., 2014). The repeatability of the experiments for $C_{mp} = 20\%$, 30% , and 35% of solid concentrations of the three particle sizes is shown in Figure 3.3. The uncertainty measurements demonstrated a very good agreement between the corresponding pressure tests with an uncertainty ranging from $\pm 0.005 \text{ kPa m}^{-1}$ to $\pm 0.15 \text{ kPa m}^{-1}$ for wheat straw experiments.

3.3 Experimental results and discussion

3.3.1 Delivered concentration measurements of wheat straw aqueous slurry

3.3.1.1 The effect of bulk velocity

The C_{md} results for the three particle sizes (6.4 mm, 3.2 mm, and $<3.2 \text{ mm}$) of wheat straw aqueous slurries at corresponding values of the C_{mp} , keeping the bulk velocity constant at $v_m = 3.0$ and 2.0 m s^{-1} , are shown in Figure 3.4.

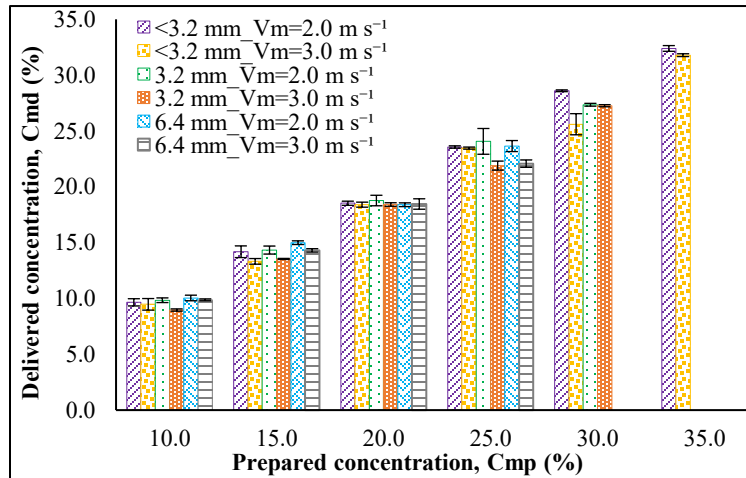


Figure 3.4: The effect of bulk velocities on delivered concentrations (C_{md} 's) of wheat straw aqueous slurries of different particle sizes.

The bulk velocities of slurries chosen for the analysis were considerably larger than the critical deposition velocity ($v_D = 0.8 \text{ m s}^{-1}$) of the largest particle size (19.2 mm) (Vaezi et al., 2018) and hence confirmed (as explained by Abulnaga) the pseudo-homogeneous flow regime of these slurries flowing through the pipe loop (Abulnaga, 2002). The single value of the C_{md} for each particle size in Figure 3.4 represents an average (mean) of the three samples collected at a corresponding specific value of the C_{mp} and bulk velocity. For the entire range of C'_{mp} s, the corresponding measured (mean) values of the C_{md} were found to be less than those of the C_{mp} at both bulk velocities (i.e., 2.0 and 3.0 m s^{-1}) and for all three particle sizes; however, the difference was not large (e.g., a maximum decrease of up to 8.0% and 11.7% was observed for 2.0 and 3.0 m s^{-1} , respectively, for 6.4 mm particles). These figures indicate that a homogeneous wheat straw aqueous slurry was attained following saturation (i.e., after 12 hours of pumping). Figure 3.4 also shows that the C_{md} decreases with an increase in slurry bulk velocity from 2.0-3.0 m s^{-1} for most C_{mp} values and every particle size.

However, the precision of each mean value of the C_{md} in Figure 3.4 was quantified by constructing the error bars to represent plus or minus one standard error of the mean (i.e., standard error means), taking into account both the standard deviation and the sample size (which is 3, in this case). Because one standard error of the mean is always smaller than the 95% confidence interval, the results of error bars (in the current study) using standard error means were considered more precise. For most of the C_{mp} values at both bulk velocities (2.0 and 3.0 m s^{-1}) (Figure 3.4), the error bars overlapped, showing that the differences in the mean values of C_{md} are not statistically significant, which corresponds to a negligible effect of slurry bulk velocity on delivered concentrations of wheat straw aqueous slurries. Further, for the C_{mp} values in which error bars did not overlap for the same velocities of any specific particle size, the maximum percentage change in the mean

values of the C_{md} was found to be approximately 12%, which is not enough to cause obvious variation in the in situ density of the mixture.

3.3.1.2 The effect of particle size

Figure 3.5 shows the relationship between the concentration ratio (i.e., $(C_{md}/C_{mp})_{avg.}$) and particle size at a constant bulk velocity of 3.0 m s^{-1} . The evaluation of $(C_{md}/C_{mp})_{avg.}$ for aqueous slurries of the largest particle size (i.e., 19.2 mm) was discussed in our earlier study (Javed et al., 2021).

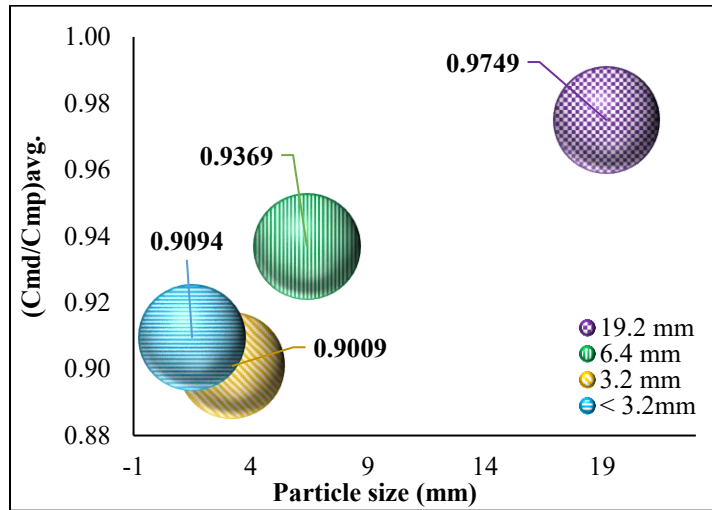


Figure 3.5: The effect of particle size on the average ratio of C_{md} to C_{mp} of wheat straw aqueous slurries at 3.0 m s^{-1} (the results for the 19.2 mm particles were taken from Javed et al. [2021]).

It can be seen in Figure 3.5 that the concentration ratio increases with increases in particle size. Decreases of 7.0-10% in concentration ratios were observed for the three particle sizes of 6.4 mm to <3.2 mm (where the lowest value corresponds to 6.4 mm and the highest to <3.2 mm). Our previous work found the decrease in concentration ratio for 19.2 mm particles to be very small (i.e., 2.5% [Figure 3.5]). This observed difference in delivered concentration is not large; therefore,

wheat straw-aqueous slurries of all particle sizes and concentrations were assumed to be homogeneous. Hence, improper mixing (observed for medium sand and glass bead slurries in our earlier experimental setup (Javed et al., 2021)) was not observed in the current study of wheat straw slurries. One of the main reasons could be the neutrally buoyant nature (i.e., $\frac{v_t}{v_m} \leq 0.021$, where v_t and v_m are terminal settling velocity and mixture velocity, respectively) of the wheat straw particles, like some fibrous suspensions (Kada & Hanratty, 1960), demonstrating the absence of slip and giving rise to a reasonable approximation of the $C_{in-situ}$ to be equivalent to the C_{md} . To the best of our knowledge, there are no experimental evaluations of the terminal settling velocity of agricultural residue biomass particles. The highest increase (5.4%) was observed in the value of $(C_{md}/C_{mp})_{avg.}$ obtained at two bulk velocities of 3.0 and 2.0 m s⁻¹ for 3.2 mm wheat straw particle sizes, indicating no major change in the delivered concentration. Therefore, we concluded that using $(C_{md}/C_{mp})_{avg.}$ (obtained at a single bulk velocity, i.e., 3.0 m s⁻¹) was a reasonable way to find an in situ density of wheat straw-aqueous slurries for the entire range of bulk velocities.

3.3.2 Frictional loss measurements of wheat straw-aqueous slurries

To investigate the frictional behaviour of wheat straw-aqueous slurries of three particle sizes at several concentrations during upward flows in a vertical test section, we conducted a complete course of experiments for the 6.4 mm, 3.2 mm, and <3.2 mm particle sizes up to their corresponding maximum achievable $C_{mp} = 30\%$, 35%, and 40%, respectively, by following the procedure explained in sections 3.2.3 and 3.2.4. The in situ densities of mixtures of the particle sizes at corresponding C_{mp} values were evaluated using the delivered concentration (C_{md}) results described in Figure 3.5.

3.3.2.1 The effect of concentration

The frictional pressure drops results for a 6.4 mm wheat straw-aqueous slurry at prepared concentrations (saturated) of $C_{mp} = 5.0\text{-}30\%$ and a wide range of slurry bulk velocities ($v_m = 0.5\text{-}4.0 \text{ m s}^{-1}$) are given in Figure 3.6 (a).

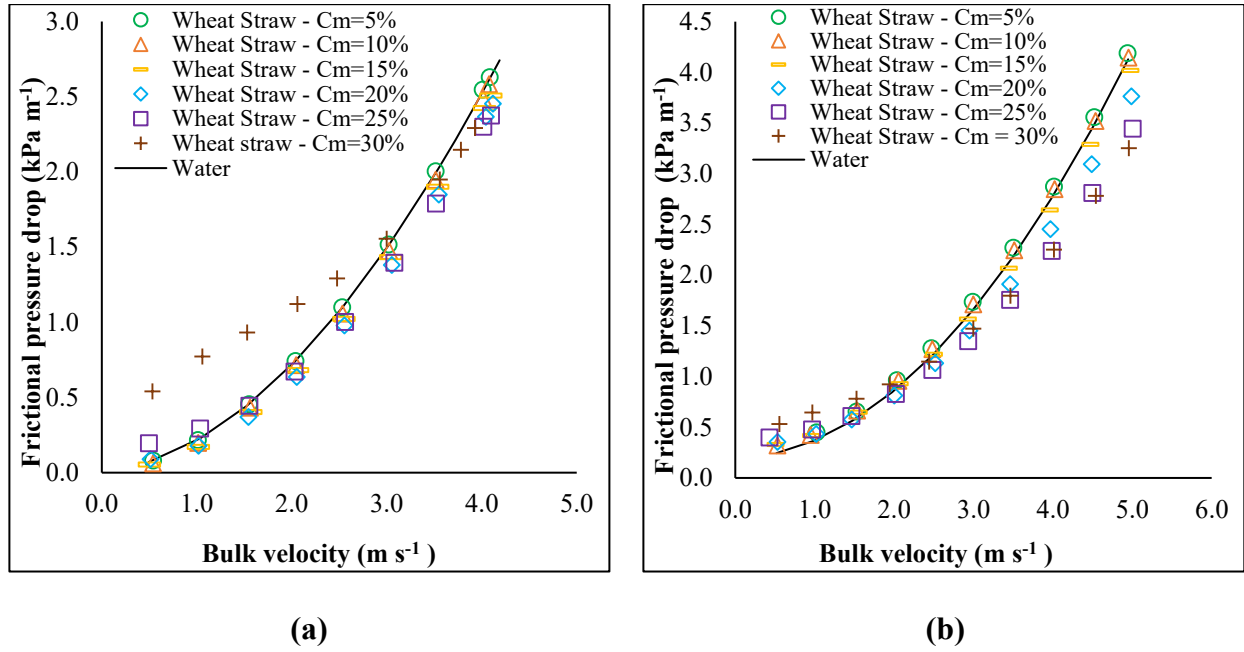


Figure 3.6: Frictional pressure drops for aqueous slurries of 6.4 mm wheat straw particles through (a) a vertical test section and (b) a horizontal test section (results reproduced from Vaezi et. al. [2014] (Vaezi et al., 2014); used with permission from Elsevier).

The frictional pressure drops were found to be below the water curve for velocities $>0.5 \text{ m s}^{-1}$ and concentrations of $C_{mp} = 5.0\text{-}20\%$. For these ranges, the depression of the slurries below the water curve increased when the slurry concentration increased (at any specific value of velocity $>0.5 \text{ m s}^{-1}$). Similar observations were found for vertical upward flows of wheat straw-aqueous slurries with a 19.2 mm particle size (where the depression below the water curve was greater than that for 6.4 mm particles for the entire range of concentrations) (Javed et al., 2021). Actually, the increase in slurry concentration increases the particle-particle interaction, which in turn increases the

corresponding depressions of frictional pressure drops below the water curve (Kerekes, 1971; Radin et al., 1975; Vaezi et al., 2014). Bobkowicz and Gauvin reported similar concentration effects for vertical upward flows of nylon fiber suspensions (1965). The frictional drop results for wheat straw-aqueous slurries with particle sizes of 3.2 mm and <3.2 mm up to the prepared C_{mp} = 35% and 40%, respectively, in vertical upward flows are shown in Figure 3.9 and will be discussed in their relevant sections.

Figure 3.6 (b) shows the pressure drop results from our earlier study of similar particle size (6.4 mm) wheat straw-aqueous slurries of similar mass concentration ranges flowing in horizontal pipelines of the same diameter (Vaezi et al., 2014) as for the current investigation (i.e., vertical upward flow). For all bulk velocities <2.0 m s⁻¹ in the horizontal flows and concentrations of C_{mp} = 5.0-25%, the frictional pressure drops were observed to be above the water curve, whereas at the highest concentration (i.e., C_{mp} = 30%), the pressure drops were above the water curve for bulk velocities <2.5 m s⁻¹. These results showed entirely different flow characteristics of horizontal flows than of vertical flows, particularly at lower velocities (i.e., <2.0 m s⁻¹) because of the different nature of the flows. In horizontal flows of wheat straw-aqueous slurries, some of the fibers roll along the pipe wall at low velocities, increasing the friction, which eventually increases the frictional pressure drops of the suspension (Derakhshandeh et al., 2011; Vaezi et al., 2014). However, in vertical flows, there is no bed formation at low velocities, so the frictional pressure drops of the slurries ultimately decreases. For higher concentrations of C_{mp} = 25% and 30% (hence higher apparent suspension viscosities), the frictional pressure drops were below the water curve only for bulk velocities ≥1.5 m s⁻¹ and 3.4 m s⁻¹, respectively. However, for velocities below these values (i.e., 1.5 m s⁻¹ and 3.4 m s⁻¹), the pressure drops were above the water curve for both

aforementioned concentrations (i.e., 25% and 30%), showing the flow of suspension to be like plug flow (further details are given in section 3.3.2.4).

3.3.2.2 The effect of particle size

To explore the effect of particle size (or aspect ratio, in this case) on frictional pressure drop measurements, some of the results for the four wheat straw-aqueous slurry particle sizes are illustrated in Figure 3.7.

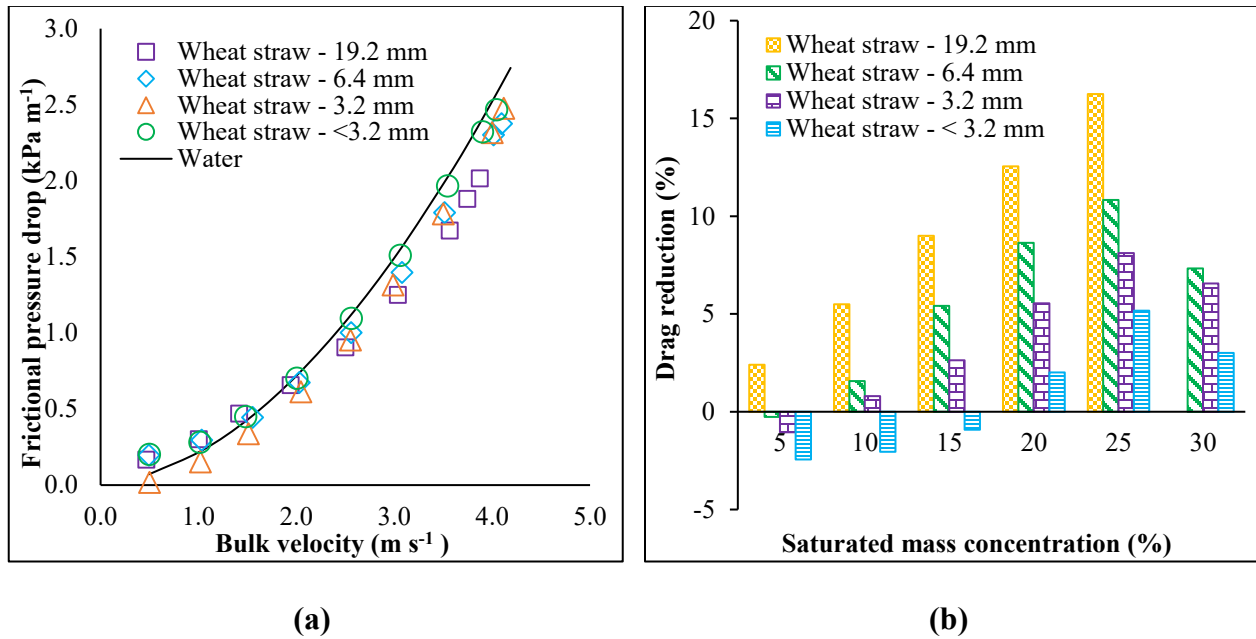


Figure 3.7: The effect of particle size in vertical upward flows of wheat straw-aqueous slurries on (a) frictional pressure drop for the entire range of bulk velocities at the saturated mass concentration of 25% and (b) drag reduction for a range of saturated mass concentrations at the highest achievable bulk velocity.

The pressure drop results for wheat straw-aqueous slurries with 19.2 mm particles were reproduced from our previous work (Javed et al., 2021). Figure 3.7 (a) shows the change in the pressure drop of slurries for all four particle sizes at a $C_{mp} = 25\%$. The frictional pressure drop was clearly observed to be a strong function of particle size, concentration, and mixture velocity. The frictional

pressure drop for the slurry of the largest particle size (19.2 mm) with a $C_{mp} = 25\%$ was lower than the slurries of the other three particle sizes at velocities $\geq 2.5 \text{ m s}^{-1}$. The greatest difference was noticed at the highest bulk velocity of $\approx 4.0 \text{ m s}^{-1}$, where the pressure drop for the largest particle size was approximately 18% lower than that of the smallest particles ($< 3.2 \text{ mm}$). For all other mass concentrations (i.e., 5.0-20%) and the highest achievable velocities (Figure A1 in Appendix A), the pressure drops for the slurries of the largest particle size were always found to be below those of the smaller particles (i.e., the pressure drop decreased when particle size increased), in a similar fashion as was observed for $C_{mp} = 25\%$. These results highlight the strong effect of particle size on frictional pressure drop measurements. This effect could be due to the broader particle size distribution (PSD) of solids in any type of slurry flowing at high velocities (Duffy & Lee, 1978; Schaan et al., 2000), a decrease in the apparent (or relative) suspension viscosity (Djalili-Moghaddam & Toll, 2006), and the larger floc size (by virtue of longer fiber length) suppressing the turbulence intensities at specific flow rates (Kerekes & Schell, 1995).

The larger wheat straw particles (19.2 mm) exhibit a wide size range up to 18.4 mm compared to the smaller size particles ($< 3.2 \text{ mm}$) that have a narrow size range up to 5.2 mm (Vaezi et al., 2013) and eventually reduced the pressure drop further. Vaezi et al. made this same observation in their study of wheat straw-aqueous slurry flows in horizontal pipes (Vaezi et al., 2014). Moreover, an increase in adhesive forces and flocculation of fiber suspension caused by low average inter-fiber distance (defined as $h_{av} = (nX_{gl})^{-\frac{1}{2}}$, where n and X_{gl} are the fiber number fraction and geometric mean length, respectively; see Table 3.1 for the values of X_{gl}) increases the apparent suspension viscosity of the slurry of fibrous materials. At $C_{mp} = 25\%$, the fiber number fraction (n) of the 19.2 mm wheat straw particle size is ten times smaller than the smallest particle ($< 3.2 \text{ mm}$); this

means the inter-fiber distance of the largest particles is two times greater than the smallest particle size. Consequently, the apparent viscosity of the suspension of 19.2 mm straw decreases, which reduces the pressure drop, unlike with fine particles (Djalili-Moghaddam & Toll, 2006; Vaezi et al., 2014). Furthermore, the longer fiber length (aspect ratio) promotes floc size, which eventually affects the frictional pressure drop behaviour (by influencing turbulence intensities) of fiber suspensions at specific flow rates (Kerekes & Schell, 1995; Vaezi et al., 2014). The tendency of the larger fiber lengths to interlock with each other to make strong networks, particularly at higher concentrations of the suspensions, damped down the longitudinal turbulence intensities, causing the highest drop in frictional pressure, especially at higher concentrations (Bobkiewicz & Gauvin, 1965; Radin et al., 1975). In the current investigation, the larger particle sizes (i.e., 19.2 mm, 6.4 mm) exhibited smaller drops in frictional pressure than water compared to the other two sizes of the wheat straw-aqueous slurries (Figure 3.7 [a]) because the turbulence intensities are suppressed at higher concentrations (i.e., $C_{mp} = 25\%$).

Figure 3.7 (b) shows the percentage drag reduction (% reduction in friction loss with respect to water at the same bulk velocity) for the range of prepared concentrations ($C_{mp} = 5\text{--}30\%$) for all four wheat straw-aqueous slurry sizes at the highest achievable bulk velocity ($\approx 4.0 \text{ m s}^{-1}$). It is obvious that the drag reduction is directly proportional to the particle size and also increases with increases in the prepared concentration up to $C_{mp} = 25\%$, where it was found to be the highest for each particle size. For instance, drag reductions of 11%, 8.2%, and 5.2% were obtained for particle sizes of 6.4 mm, 3.2 mm, <3.2 mm, respectively, in the current investigation at $C_{mp} = 25\%$, whereas our previous study found this value to be 16.2% for a 19.2 mm particle size at the same concentration (Javed et al., 2021) (see Figure 3.7 [b]). At higher concentrations ($C_{mp} > 25\%$) and the highest achievable velocity, the drag reduction for all particle sizes decreased more than the

corresponding values found at $C_{mp} = 25\%$; however, the drop in drag reduction followed the same trend with respect to particle size (i.e., an increase with the increase in particle size and vice versa). We further observed that the wheat straw slurries at concentrations higher than the upper limits used in the current investigation for each particle size were not pumpable because of the limitations of the slurry pump.

3.3.2.3 The effect of bulk velocity on drag reduction

Figure 3.8 shows an effect of bulk velocity on percentage drag reduction in vertical upward flows of all four wheat straw-aqueous slurry sizes for the range of prepared concentrations ($C_{mp} = 5.0$ -30%).

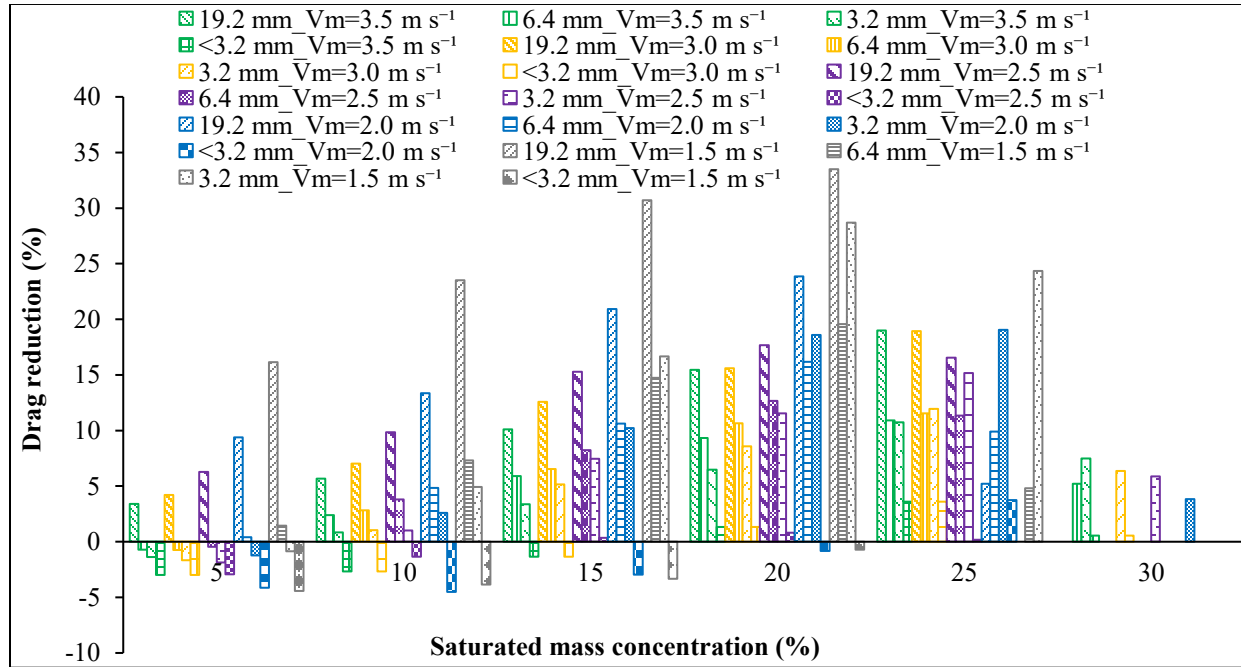


Figure 3.8: The effect of bulk velocity in vertical upward flows of several wheat straw-aqueous slurry sizes for $C_{mp} = 5$ -30% (the results for the 19.2 mm particles were adopted from our earlier study (Javed et al., 2021)).

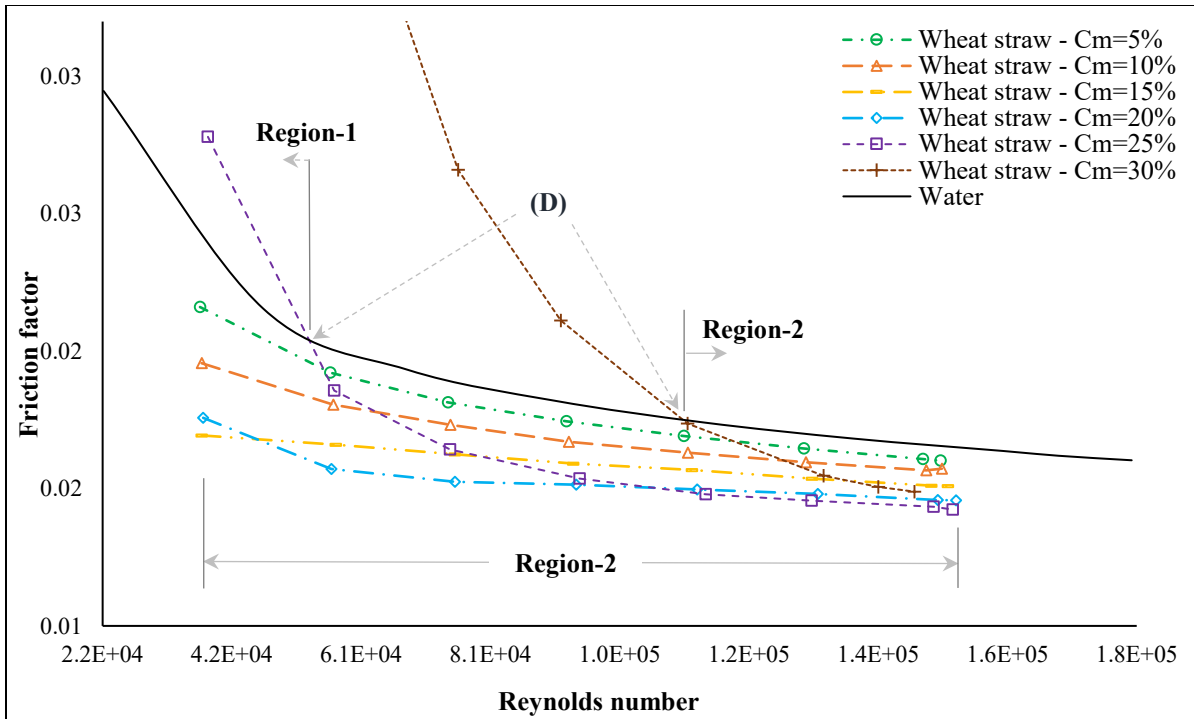
The drag-reducing capabilities of all the wheat straw-aqueous slurry particle sizes were identified even at comparatively low bulk velocities (e.g., 1.5 m s^{-1} and 2.0 m s^{-1}) and every concentration with some exceptions at certain flow conditions for 6.4 mm and 3.2 mm and most of the fine particle size slurries (Figure 3.8). This is a unique feature of these kinds of slurries in vertical upward flows compared to horizontal flows, where, for low velocities, no drag reduction was observed (Vaezi et al., 2014). At these low bulk velocities of 1.5 m s^{-1} and 2.0 m s^{-1} in the current investigation (as for the highest achievable velocity of 4.0 m s^{-1} , Figure 3.7 [b]), drag reduction was observed to be highest at $C_{mp} = 20\%$ and increased with increases in particle size. Wheat straw-aqueous slurries of fine particles (i.e., $<3.2 \text{ mm}$) did not display drag-reducing characteristics at low bulk velocities because of the low aspect ratio. Bobkiewicz and Gauvin reported similar effects for vertical upward flows of particles with low aspect ratios of nylon fiber slurries, where all the frictional pressure drop data seemed to cluster close to the water curve, exposing negligible drag reduction (1965). However, for wheat straw-aqueous slurries with 6.4 mm and 3.2 mm particles, drag reductions up to 19.7% and 28.7%, respectively, were found at a bulk velocity of 1.5 m s^{-1} and concentration $C_{mp} = 20\%$.

In our previous work for vertical upward flows of the largest particle size (i.e., 19.2 mm) of wheat straw-aqueous slurries, drag reduction up to 33.5% was obtained at 1.5 m s^{-1} velocity and increased with further reductions in velocity (Javed et al., 2021). The drag reduction at low bulk velocities for all three particle sizes (except fine particles) appeared to be due to the nature of the vertical flow of wheat straw-aqueous slurries. As there is no bed formation of wheat straw slurries in vertical upward flows (Javed et al., 2021), unlike in horizontal flows (Vaezi et al., 2014), this eventually caused the slurry to remain in drag-reducing mode even at low velocities. Generally, at fixed concentrations (C_{mp}) and bulk velocities, drag reduction increased with increased aspect

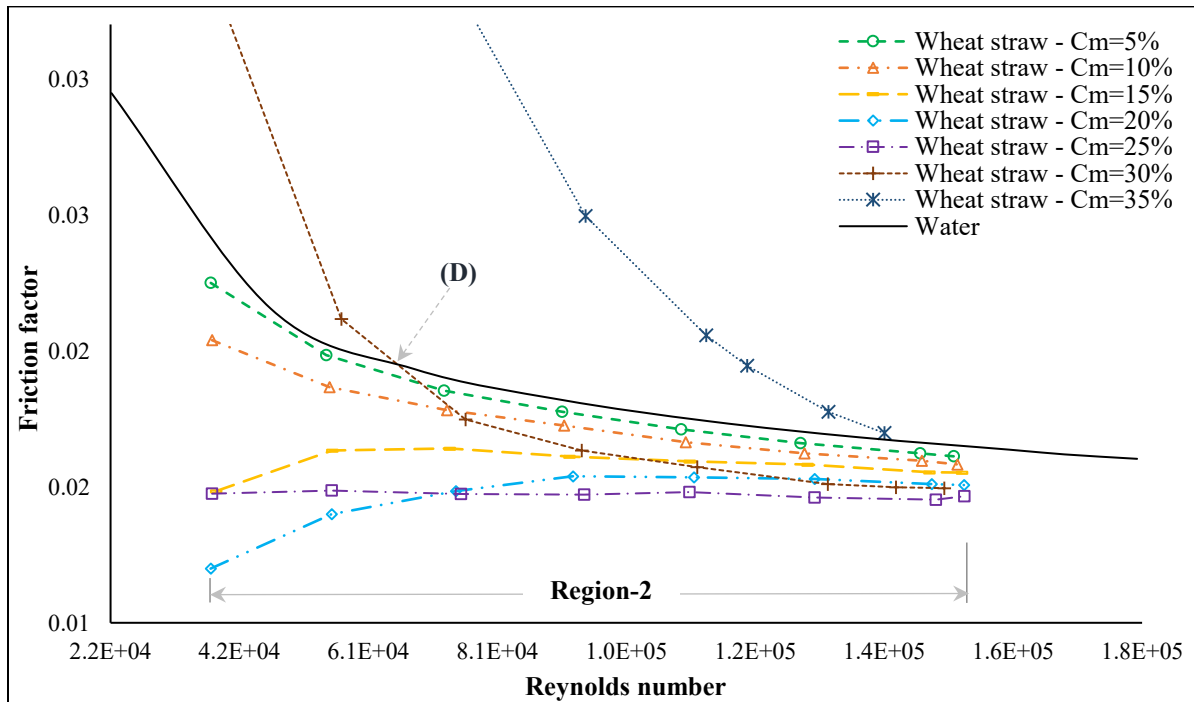
ratios (ϕ_p) (or size, i.e., length) of the wheat straw particles. Bobkowicz and Gauvin (1965) and Radin et al. (1975) made a similar observation in vertical upward flows of nylon and rayon fiber slurries, as did Vaezi et al. in horizontal flows of wheat straw and corn stover slurries (2014). These results show that the size (or aspect ratio) of the wheat straw particles is one of the key variables for lowering the frictional pressure drops of vertical upward slurry flows, which is also observed in horizontal flows (Vaezi et al., 2014). The range of the aspect ratios used in the current study was 3.47 to 4.47 (see Table 3.1), whereas in our previous work we used wheat straw particles with an aspect ratio of 6.3 (i.e., a nominal particle size of 19.2 mm). In spite of the low range of aspect ratios for wheat straw particles compared to those used by other researchers for vertical upward flows of rayon and nylon fibers (Bobkowicz & Gauvin, 1965; Radin et al., 1975), these types of suspensions present drag-reducing capabilities quite effectively in vertical upward flows even at low velocities and concentrations.

3.3.2.4 Plug flow at higher concentrations

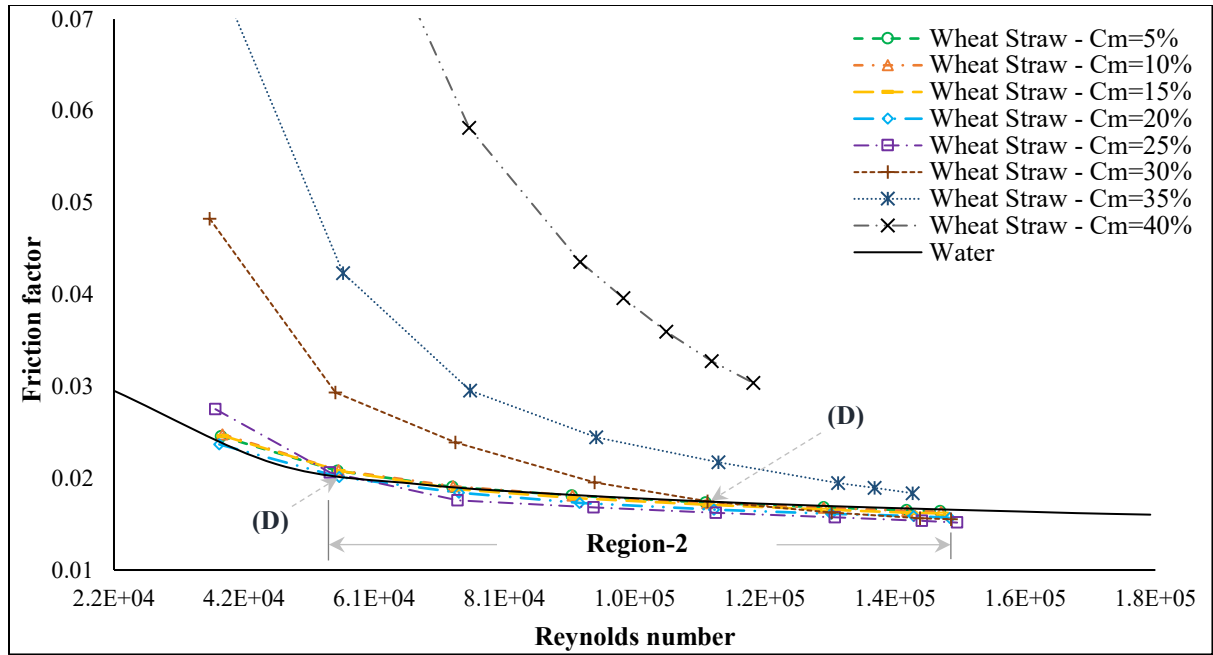
Figure 3.9 shows the behaviour of wheat straw-aqueous slurries flowing upward in a vertical test section for concentrations of $C_{mp} = 5.0\text{-}40\%$ and velocities of $1.0\text{-}4.2 \text{ m s}^{-1}$ for the three particle sizes (6.4 mm, 3.2 mm, and $<3.2 \text{ mm}$) in plots showing the friction factor versus the Reynolds number. Representing the experimental friction factor as a function of the generalised Reynolds number is a common way to understand the frictional behaviour of fiber suspension flows in pipes. For the most part, three flow regions (i.e., plug flow, transition flow, and turbulent flow) evolve in vertical upward flows of fiber suspension (Radin et al., 1975; Seely, 1968). The plug flow region (or Region 1 shown in Figure 3.9 [a]) appears at a low Reynolds number, where the plug of fibers moves without any interaction with the inner wall of the pipe. In this region, a carrier fluid annulus with almost negligible fibers exists between the pipe wall and the fiber plug (Radin et al., 1975).



(a)



(b)



(c)

Figure 3.9: Friction factor versus generalised Reynolds number for velocities $\geq 1.0 \text{ m s}^{-1}$ for vertical upward flows of wheat straw-aqueous slurries of (a) 6.4 mm, (b) 3.2 mm, and (c) <3.2 mm particle sizes.

As the Reynolds number of the fiber suspension increases, the size of the annulus increases gradually with a sharp decrease in the friction factor of the suspension until it reaches a transition point (D in Figure 3.9 [a]) where the friction factors of both the fiber suspension and water become equal (Duffy et al., 1976). The transition (mixed) flow region (Region 2 shown in Figure 3.9 [a]) appears after the transition point (D), where the fiber plug starts to disintegrate at its interface with the surrounding annulus. A further increase in the suspension velocity causes a decrease in both the plug diameter and the friction factor. However, the rate of decrease in the friction factor in the transition flow region is always slower than that in the plug flow region. The turbulent flow region develops when the fiber plug entirely vanishes by further increases in the suspension velocity. In this region, an increase in the suspension velocity causes the friction factor to increase instead of

decrease. However, the value of the friction factor still remains lower than the Newtonian fluid (water) (Kerekes, 1971; Radin et al., 1975). These three flow regions are important to highlight the existence or non-existence of drag-reducing capabilities of fiber suspension with respect to the Reynolds number. The drag reduction of fiber suspension appears in transition flow or turbulent flow regions. In an earlier study, we identified three regions for vertical upward flows of a wheat straw-aqueous slurry particle size of 19.2 mm at various concentrations. The significance of these regions is detailed in that study (Javed et al., 2021). In the present research, we explored these flow regions for the three wheat straw-aqueous slurry particle sizes. Broadly speaking, the friction factors obtained for wheat straw-aqueous slurry flows of all three sizes (except <3.2 mm) and mass concentrations of 5.0-20% (Figure 3.9) were found to be below the water curve for the entire range of Reynolds numbers and to exhibit the characteristics of Region 2 (i.e., transition flow).

For wheat straw-aqueous slurries of all the particle sizes flowing at higher mass concentrations of $C_{mp} = 25\text{-}40\%$, both plug (Region 1) and transition (Region 2) flows were observed in combination (i.e., between a specific range of Reynolds numbers at a specific concentration), or plug flow (i.e., Region 1) was observed alone for the entire range of Reynolds numbers (Figure 3.9). Similar kinds of unusual effects of slurry concentrations were described by Kerekes and Douglas for vertical upward flows of rayon fiber suspensions (1972) and recently in our work on vertical upward flows of wheat straw-aqueous slurries of 19.2 mm particle size at a saturated concentration of 25% (mass) (Javed et al., 2021). This rapid change of friction loss for all particle sizes at higher concentrations ($\geq 25\%$) over a certain range of Reynolds numbers occurs because of a change in the viscous nature of the suspension (Vaezi et al., 2014). The apparent viscosity of the slurry is a strong function of both the slurry concentration and dimensions of solids (fibers). With a decrease in the fiber dimension, the apparent suspension viscosity increases (Djalili-Moghaddam & Toll, 2006). On the

other hand, the apparent suspension viscosity changes in a linear fashion at lower solid concentrations of slurries, and, at higher solid concentrations, there is a cubic relationship between the apparent viscosity and solid concentration (Powell et al., 2001). Hence, lower concentrations (5-20%) had negligible effects on the apparent viscosity of the suspension for the entire range of velocities for all the particle sizes except for those <3.2 mm, which exhibited plug flow at concentrations of 5-15%.

Further, for higher concentrations, i.e., $\geq 25\%$ and low bulk velocities, the friction factor decreased sharply (conversely, pressure drop increased rapidly) because of the drastic increase in the apparent suspension viscosity that indicates plug flow (see Figure 3.9). However, these highly concentrated suspensions appeared as transition flow (Region 2) at higher velocities (indicating drag-reducing capabilities), known as onset velocities of drag reduction (which increase with increases in particle size and concentration). The onset of drag reduction (the start of Region 2, which varies by concentration and particle size) for highly concentrated slurries at a corresponding Reynolds number is indicated by the letter D in Figure 3.9. Some slurries of small wheat straw particle sizes (3.2 mm, <3.2 mm) at higher concentrations (35-40%) demonstrated plug flow region only (Figure 3.9 [b] and [c]) because of low achievable bulk velocities (i.e., between 3.19 m s^{-1} and 3.85 m s^{-1}) linked with pump limitations. These highly concentrated slurries could still achieve drag reduction (Region 2) if the pump is upgraded.

3.4 Conclusion

The effect of particle size and flow conditions on the frictional behaviour of wheat straw-aqueous slurries in upward flows through a vertical pipe section was experimentally studied. Except for the fine particles (<3.2 mm), in all the particle sizes for the entire range of slurry bulk velocities studied here, it was clearly established that increasing the slurry concentration considerably reduced the

frictional pressure drop except at higher concentrations (i.e., $C_{mp} \geq 25\%$). For mass concentrations of 5-20%, all the wheat straw suspensions (except for particle sizes < 3.2 mm up to $C_{mp} = 15\%$) demonstrated drag-reducing capabilities in line with mixed (transition) and fully turbulent regions over the entire range of slurry velocities. A maximum drag reduction of 19.7% was obtained for a wheat straw-aqueous slurry of a 6.4 mm nominal particle size at $C_{mp} = 20\%$ and bulk velocity of 1.5 m s^{-1} . At the maximum achievable slurry bulk velocity for all the suspensions, the largest drag reduction for all the particle sizes (except fine particles) was found at a slurry solid concentration of $C_{mp} = 25\%$ and increased with an increase in particle size. For wheat straw-aqueous slurries of all the particle sizes flowing at high concentrations of $C_{mp} = 25\text{-}40\%$, both plug (Region 1) and transition (Region 2) flows were observed in combination (i.e., between a specific range of Reynolds numbers at a specific concentration) or plug flow (Region 1) alone for the entire range of Reynolds numbers. Some slurries of small-sized wheat straws (3.2 mm, < 3.2 mm) at high concentrations (35-40%) demonstrated plug flow region only because of the low achievable bulk velocities (between 3.19 m s^{-1} and 3.85 m s^{-1}) associated with pump limitations. It is expected that these highly concentrated slurries could still achieve drag reduction (Region 2) at higher velocities. The delivered concentration measurements for every wheat straw slurry showed a reduction of 7.0-10% in the concentration ratios (between delivered and prepared concentrations) for particle sizes of 6.4 mm to < 3.2 mm (the lowest drop for the largest particles and the highest for the smallest particles), indicating the homogeneity of the biomass slurries flowing in the pipeline. The in situ concentrations were reasonably approximated to be equivalent to the delivered concentration due to the neutrally buoyant nature of the wheat straw particles. The onset velocities of drag reduction were different in different flow conditions and increased with increases in particle size and concentration. Wheat straw-aqueous slurries of all three particle sizes in vertical upward flows

behaved quite differently than those in the horizontal flows, particularly at low velocities. These experimental observations exposed some useful findings on drag reduction and flow conditions in vertical upward flows of wheat straw-water suspensions that would help determine optimum flow conditions while designing an integrated pipeline network for biofuel production.

Chapter 4: Comparison of Corn Stover and Wheat Straw Slurry Flow in Vertical Pipes³

4.1 Introduction

The steady rise in energy needs along with developments in many sectors around the world are responsible for increasing carbon footprints and the great reliance on fossil fuels. The atmospheric concentration of CO₂ increased by approximately 11% between 2005 and 2021 and is expected to increase in the future despite several worldwide renewable energy initiatives in many energy sectors (Abas et al., 2015; Bragg-Sitton et al., 2020; Chapman et al., 2018; Nasa, 2021; Zidanšek et al., 2009). The transportation sector alone is responsible for 15% of the world's total greenhouse gas emissions (Lamb et al., 2021). Compared with other renewable energy resources, biomass is a viable means of reducing the carbon footprint because of two significant factors: first, it is carbon neutral and second, it can be directly used to produce various types of biofuels and chemicals at bio-based energy facilities (Pootakham & Kumar, 2010). There is great potential for biomass in countries like Canada with vast agricultural land and forests (Kumar et al., 2003); however, biorefineries presently produce biofuels at capacities considerably lower than fossil fuel-based plants do (Kumar et al., 2005a, 2005b). The major barrier is the high overland transportation cost of biomass due to its low bulk density (Vaezi et al., 2015). This is also directly relevant to other jurisdictions around the world.

³ A version of this chapter has been published as Javed, K., Kurian, V., & Kumar, "A. Comparison of maize stover and wheat straw slurries flow in vertical pipes", *Biosystems Engineering*, 2022, 224, 259-282.

The hydro-transport of chopped agricultural and forest residue biomass by pipeline over a long distance could be the most sustainable and economical mode of delivering biomass for the production of biofuels on commercial scale (on par with fossil fuels) (Vaezi et al., 2014; Vaezi & Kumar, 2014a, 2014b; Vaezi et al., 2015). Furthermore, experiments have verified that the hydro-transport of agricultural residue biomass through pipelines does not affect the chemical composition of these slurries (Ghatora et al., 2016). Laboratory-scale investigations on pipelining biomass feedstocks mostly focus on horizontal pipe arrangements (Vaezi et al., 2014; Vaezi & Kumar, 2014b; Vaezi et al., 2018), but pipeline transport of solid-based slurries over a long distance must, depending on the topography, include pipe sections at different inclinations. Vertical pipe sections are mostly found at on-site processing facilities. More pumping power is needed to transport solid slurries through vertical pipes because of the effect of gravity, and the amount depends on various factors such as particle type and size, slurry density, slurry concentration and velocity, and direction of the slurry flow (i.e., upwards or downwards) (Wilson et al., 2006). To accurately evaluate the size and cost of a long-distance pipeline network, it is imperative to understand and quantify the frictional behaviour and rheological properties of different types and sizes of materials through pipe sections at various inclinations (Abulnaga, 2002; Wilson et al., 2006). Thus, some aspects of the pipeline transport of biomass-water slurries over a long distance need to be explored further, such as the frictional behaviour of different agricultural residue biomass feedstocks through vertical sections.

Studies on the vertical upward flows of different fiber suspensions (i.e., natural or synthetic) have focussed on understanding their frictional behaviour (Bobkowicz & Gauvin, 1965; Kerekes, 1971; Radin et al., 1975). In practice, fiber suspensions are not uniform during flow and contain simultaneously four types of particles (fibers, floccettes, flocs, and networks), making the

suspension complex and difficult to analyse (Duffy, 2006). One way to depict the frictional behaviour of any kind of fiber suspension in a pipeline is to plot its experimentally obtained friction factors against corresponding generalised Reynolds numbers and examine the development of flow regions on these plots at various flow conditions (Luetzgen et al., 1991; Radin et al., 1975; Steen, 1989; Walmsley & Berry, 2001). Radin et al. (1975) discussed the three flow regions (plug, transition, and turbulent flow) in upward flows of rayon fiber-water suspensions of various particle sizes and concentrations through a vertical pipe section. The plug flow region shows greater fiber suspension friction than water, and the transition and turbulent flow regions show less suspension friction than water. These flow regions appear for a specific range of Reynolds numbers and provide basic knowledge of drag-reducing characteristics (which are mainly associated with the transition flow and turbulent flow regions) of the fiber suspensions. The evolution of these flow regions depends on several factors (the type of fiber suspension, the flexibility of the fibers and their surface features, the aspect ratio of fibers, the suspension concentration, the suspension velocity, the apparent viscosity of the suspension, the carrier fluid, the density ratio between the fiber and the carrier fluid, the pipe diameter, etc. (Cotas, 2016; Kazi et al., 1999; Radin et al., 1975)). Radin et al. (1975) also found that fibers with irregular surfaces and greater flexibilities exhibited higher drag reduction.

Another aspect of the frictional behaviour of fiber suspensions is understanding their rheology by identifying regimes of fiber suspension behaviour, types of forces at fiber contacts, the formation of flocs, the strength of the fiber network, and the flow properties of the fiber suspensions (Kerekes, 2006). Several approaches have been used to describe the regimes of fiber suspension behaviour, and they mostly focus on evaluating dimensionless crowding numbers (N) or contact numbers (n_c) (Dodson, 1996; Kerekes & Schell, 1992; Kerekes et al., 1985; Pan, 1993; Philipse,

1996; Soszyński, 1987). Kerekes et al. defined crowding number (N) as the number of fibers in a controlled volume made by sweeping the length of similar fibers around its centre (Kerekes et al., 1985). Later, Kerekes and Schell (1992) and Soszyński (1987) assigned ranges to the crowding numbers to recognise the dilute (chance collision), semi-concentrated (forced collision), and concentrated regimes (continuous contact) of the fiber suspensions of $N < 1$, $1 < N < 60$, and $60 < N$, respectively. Keeping in view of the findings of several investigators (Kerekes & Schell, 1992; Pan, 1993; Soszyński, 1987), Dodson (1996) tried to quantify the effect of fiber characteristics on flocculation to better predict fiber performance in the suspension. He considered random arrangements of the fibers in space and defined n_c as the expected number of fiber contacts per fiber piece in a unit volume. Dodson (1996) also found that the fiber suspension was in the concentrated regime for $n_c \geq 3.0$, where flocs or coherent networks would be developed. The criteria defined by Kerekes and Schell (1992) and Kerekes (2006) for regime identification were based on specific concentration ranges (0.017-15% by mass) of fibers of uniform length and diameter with aspect ratios of 20-100 used in papermaking, whereas the biomass particles used by Vaezi et al. (2014) in pipeline hydro-transport had high mass concentrations (5-40%) and specific particle size distributions with small aspect ratios (2.9-6.3). To determine the regimes of fiber suspension behaviour for biomass slurries, different N ranges than those used by Kerekes and Schell (1992) are required.

There is limited research on vertical upward flows of lignocellulosic biomass-aqueous slurries. In our recent studies we explored the effect of particle size, slurry concentration, and slurry velocity on the frictional behaviour of wheat straw-aqueous slurries flowing through a section of vertical pipe ($D = 50$ mm) in a 29 m long, closed-circuit pipeline facility. We found that wheat straw slurries of all particle sizes except the fines (i.e., < 3.2 mm) showed drag reduction for all the flow

rate ranges and saturated mass concentrations (5-20%). Thus most of the suspension exhibited the characteristics of either the transition or the transition and fully turbulent regions together (Javed et al., 2022b; Javed et al., 2021). Drag reduction increased with increasing particle size and concentration for specific slurry velocities. For higher mass concentrations (i.e., $\geq 25\%$), most of the slurries exhibited both plug flow and transition flow regions, except for some smaller particles (i.e., 3.2 and < 3.2 mm), which exhibited plug flow for the complete flow rate range. Furthermore, we measured the delivered concentrations of all the particle sizes of wheat straw slurries and found the largest deviation from the prepared concentrations to be 10%, which is negligible. We also found that the delivered concentrations of all the wheat straw suspensions were approximately equal to the in situ concentrations in the vertical test section (Javed et al., 2022b; Javed et al., 2021).

Corn stover, a form of agricultural leftover biomass, is a vital feedstock for the generation of biofuels on a large scale, owing to its widespread availability around the globe. Corn stover particles have irregular surfaces and shapes, have greater longitudinal flexibility, and are approximately 7 times rougher than wheat straw (Vaezi et al., 2013). Vaezi (2014) reported the saturated mass density of chopped corn stover to be similar to wheat straw. The rheology of chemically treated and untreated corn stover-water suspensions has been studied using different kinds of rheometers; however, these studies are limited to specific particle sizes, especially for untreated corn stover (Knutsen & Liberatore, 2009; Pimenova & Hanley, 2003; Samaniuk et al., 2011; Szeto et al., 2021; Viamajala et al., 2009). To the best of our knowledge, no work has been done to understand the effect of particle size and concentration on the frictional behaviour of corn stover-aqueous slurry flows through vertical pipes.

The current research experimentally investigates the hydro-transport of corn stover slurries in an upward direction through a vertical pipe section and explores the key factors affecting slurry rheology during the flow. The specific objectives are:

- To investigate the effect of particle size on the frictional behaviour of corn stover-aqueous slurries at various concentrations and velocities.
- To investigate the flow regions and conditions of drag reduction in corn stover-aqueous slurries.
- To compare the frictional behaviour of corn stover- and wheat straw-water suspensions of different particle sizes and concentrations at similar flow conditions.
- To investigate the effect of particle size, concentration, and feedstock type on the onset velocity of drag reduction.

4.2 Method

4.2.1 Experimental setup

The experimental setup used in this research is shown in Figure 4.1. The setup consists of a 29 m long, 50 mm inside diameter closed pipeline loop, a centrifugal slurry pump (CD80M; Godwin Pumps Ltd., Bridgeport, NJ, USA) connected to a 7.45 kW electric motor (CC 068A; Madison Industrial Equipment, Vancouver, BC, Canada) for pumping slurry, Schedule 40 carbon steel and PVC transparent pipe sections, a heat exchanger (KEZA030H8; KeepRite Refrigeration Corp., ON, Canada) for maintaining slurry temperature, a magnetic flow meter (FMG-424; Omega Eng., Stamford, CT, USA) for slurry velocity measurements, a flow visualisation section, semi-circular and 90° pipe bends, a temperature sensor (RTD-E; Omega Eng., Stamford, CT, USA) for

measuring slurry temperature, flexible PVC pipe sections, a differential pressure transmitter (Fuji Electric Ltd-Model: FKCT22V55) connected to a vertical pipe for pressure drop measurements of biomass slurry, and a mixing tank connected to a 0.37 kW double impeller mixer (EV6P50M; Lightning Inc., Rochester, NY, USA) for slurry mixing.

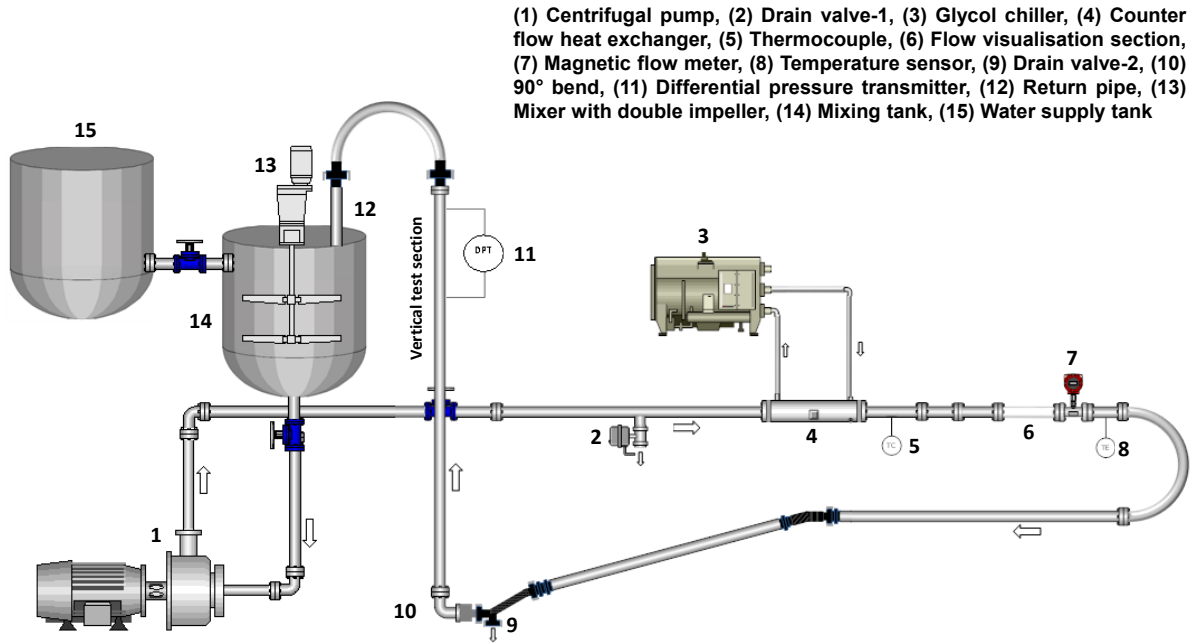


Figure 4.1: Schematic of a closed-circuit pipeline facility.

The 0.508 m long vertical test section is located 2.14 m downstream of a 90° bend to eliminate the bend effect (Enayet et al., 1982; Ito, 1960; Kalyanraman et al., 1973; Kim et al., 2014). All the instruments are connected to a data acquisition system (NI9219; National Instrument Corp., Austin, TX, USA) and program (LabView V.9.0.1f2; National Instrument Corp., Austin, TX, USA) for online recording and data processing. Further details on the equipment and experimental setup can be seen in our earlier work (Javed et al., 2022b; Javed et al., 2021; Vaezi et al., 2014; Vaezi et al., 2013).

4.2.2 Calibration

The differential pressure transmitter (DPT) was calibrated through a bench test. An excellent agreement was found between the pressures applied to the inlet ports of the DPT and the output pressures measured by the DPT, as shown in Figure 4.2 (a). The electromagnetic flow meter was calibrated through the delivered volume flow rate analysis (or bucket test) (Spelay, 2007). The complete procedure and results of the bucket test are explained in our previous work (Javed et al., 2022b).

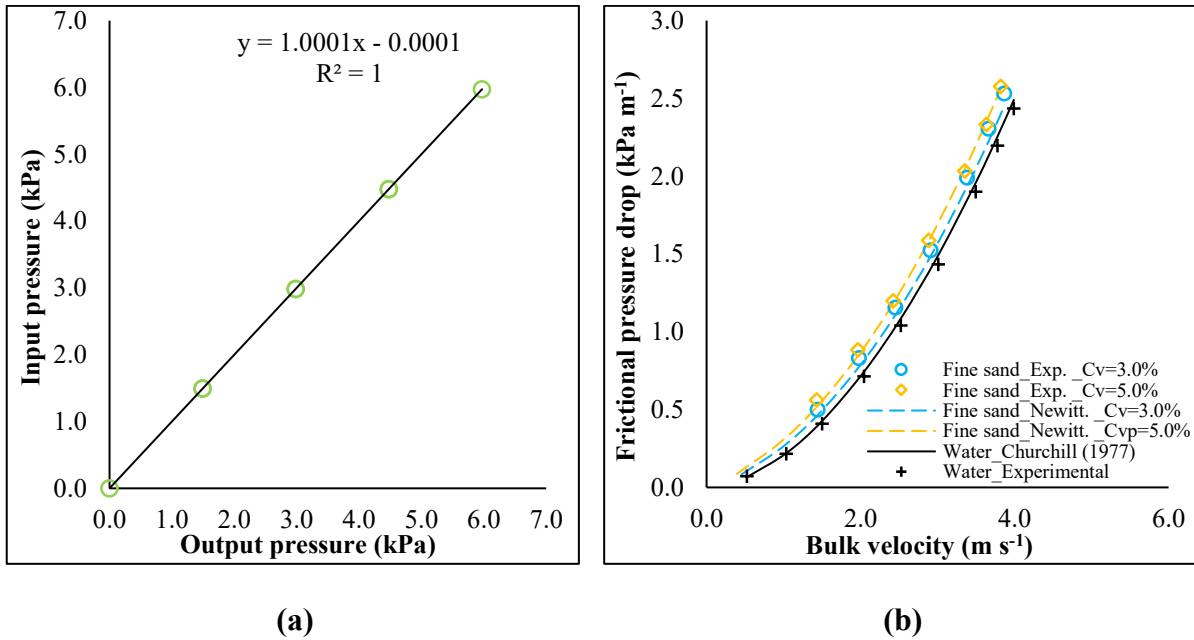


Figure 4.2: (a) Calibration of differential pressure transmitter and (b) frictional pressure drop vs. bulk velocity of water and fine sand through a vertical test section.

The vertical test section was calibrated by measuring the frictional pressure drops of both water and fine sand ($d_{50} = 0.103$ mm; $\rho_s = 2500$ kg m⁻³)-aqueous slurries (at known volumetric concentrations) at different velocities and comparing the results with those from their corresponding correlations available in the literature (Churchill, 1977; Newitt et al., 1961). Good

agreement was found between the experimental and theoretical measurements (as shown in Figure 4.2 [b]), indicating accurate performance of the vertical test section.

4.2.3 Feedstock preparation

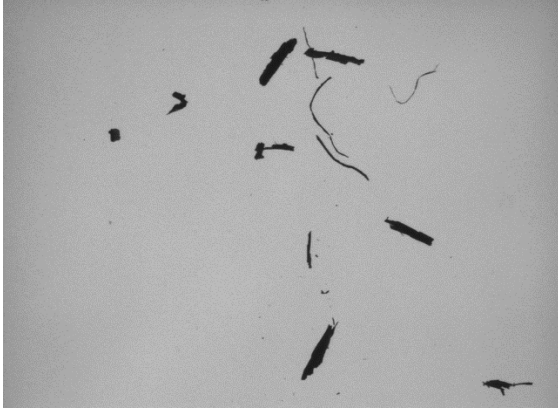
Dry corn stover (*Zea mays L.*) bales harvested in 2018 at the Sereda Farms near Rolling Hills in Southeastern Alberta were milled with a knife mill cutter (SM 100 mill; Retsch Inc., Surrey, BC, Canada). The ground material was classified with a classifier (BM & M Inc., Surrey, BC, Canada) into four nominal sizes of 19.2 mm, 6.4 mm, 3.2 mm, and <3.2 mm at a laboratory scale. These sizes were selected because of the opening size of the classifier sieves and were used in an earlier study by Vaezi et al. (2013). The term nominal size was used to designate each group of particles obtained in the four bottom-most sieves of the classifier to a specific number. It is worth mentioning here that these four nominal sizes were not the actual representative numbers of the real dimensions of the four groups of particles. The nominal sizes in the present research were used simply to compare the particle morphology obtained in our present research in each group of particles with the earlier investigation by Vaezi et al. (2013). The corn stover bales consisted of stems, leaves, and cobs. To avoid damaging the knife mill cutter blades, the corn cobs were not milled, given the very small clearance between the rotor blades and the stator (inner housing of the mill cutter).

4.2.4 Particle size analysis

Particle size distribution (PSD) and shape analysis of corn stover were performed through a Camsizer that uses dynamic digital image processing to yield PSD and material morphology (Horiba). A sample from each group (19.2 mm, 6.4 mm, 3.2 mm, and <3.2 mm) was subsampled using a riffle splitter. The main sample of a specific group was first passed through the top of the riffle splitter into the two collecting pans to divide it into two subsamples. Each subsample was

again passed through the top of the riffle splitter to divide the main sample into four subsamples. This procedure was repeated by alternating the pans on each side of the riffle splitter (to eliminate the side bias) until we obtained a sufficient number of subsamples (a representative proportion of the main sample) to use in the Camsizer. The selection of the final population size of the subsample was completely dependent on the size of the particles in order to keep the time frame reasonable (i.e., 3 to 6 minutes). For the samples of a larger particle size (19.2 mm) of corn stover, the riffle splitter was used on average 4 times (i.e., 1/16 portion of the main sample), whereas for the samples of a smaller particle size, the riffle splitter was used on average 5 to 6 times to obtain a final subsample.

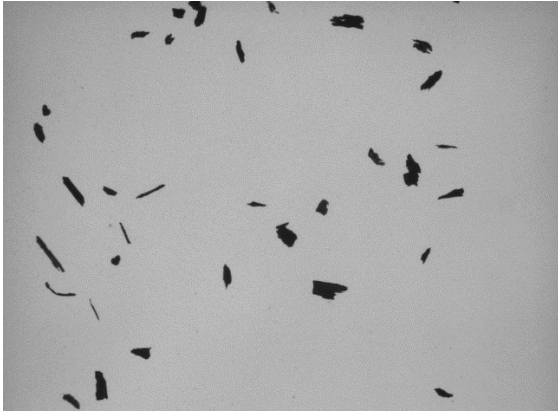
Three subsamples of each nominal size of corn stover were prepared for PSD analysis. Each subsample of each nominal size was guided by a vibratory chute that dropped individual biomass particles by gravity into a slot opening in the Camsizer, where they reached a measurement field (with two high-speed digital cameras and a light source) and were projected. The projected areas of the biomass particles were clearly identified in the measurement field and digitised. The recorded images were processed and evaluated in the Camsizer software (the Retsch Particle Library software version 4.1) in accordance with the selection of the specific parameters (Retsch Technology, 2007). The image acquisition rate of both high-speed digital cameras was 60 images s^{-1} . Typical microscopic images of the corn stover particles captured by the high-speed cameras are shown in Figure. 4.3.



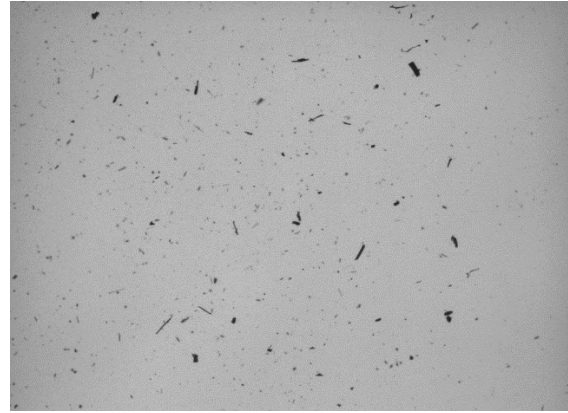
(a)



(b)



(c)



(d)

Figure. 4.3: Microscopic Camsizer camera images (not to scale) of corn stover of nominal sizes: (a) 19.2 mm, (b) 6.4 mm, (c) 3.2 mm, and (d) <3.2 mm

With the Camsizer, several characteristics of the particles were evaluated including the Feret diameter (d_{FE_max}), shortest cord diameter (d_{c_min}), cumulative distribution (Q_3) and frequency distributions ($q_3 = dQ_3/d_x$) based on volume, and aspect ratio (d_{c_min}/d_{FE_max}), among others (Retsch Technology, 2007). The Feret diameter is defined as the longest distance between two parallel tangents of a particle at any arbitrary angle, and d_{c_min} is the shortest of the measured set of longest chords of a particle projection (Retsch Technology, 2007). The particle size distributions of several sizes of corn stover and wheat straw are shown in Figure 4.4.

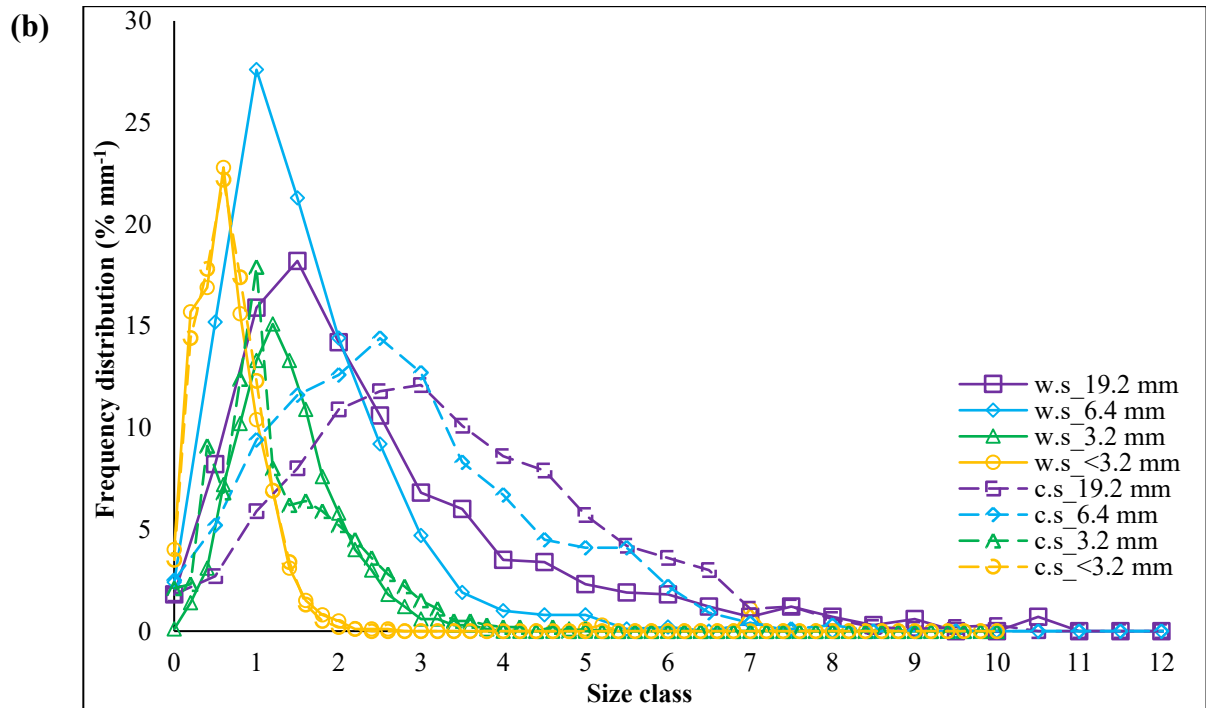
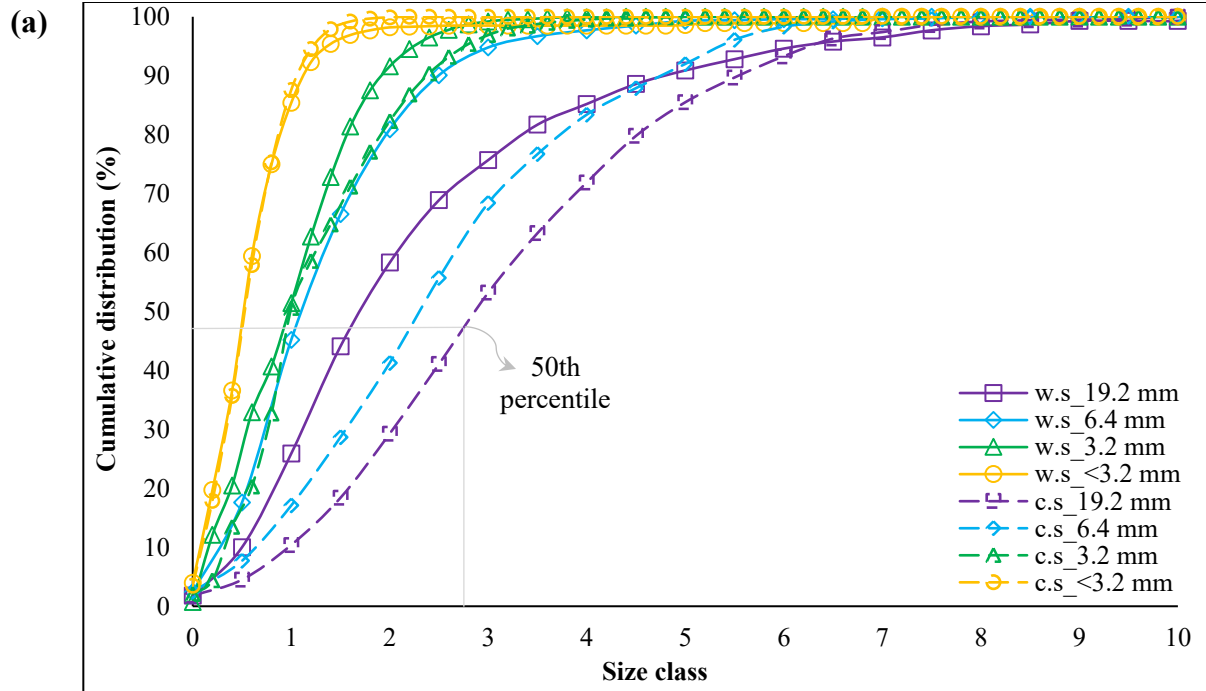


Figure 4.4: Particle size distribution of several sizes of corn stover (C.S) and wheat straw (W.S): (a) Cumulative distribution by volume and (b) frequency distribution by volume.

The size classes are the sizes we chose in the Camsizer software to display our data. The complete data for one subsample of each nominal particle size of both feedstocks obtained from the Camsizer analysis is given in Table A1 in Appendix A. The full data table (Table A1 in Appendix A) for a specific nominal size of any feedstock shows the q_3 (in percentage) obtained for each size class chosen during the analysis of the images captured by the Camsizer. There can be as many sizes as needed in a size class that can be represented in many different size types such as sieve sizes or millimetres. For a particular size class of each nominal size of a specific feedstock (Figure 4.4 a), there are different sets of Feret diameters, shortest chord diameters, and other associated particle shape factors (i.e., aspect ratio, circularity, roundness, symmetry, etc.) for different percentiles of the cumulative distributions (Table A1 in Appendix A).

For instance, the size class of 3 for a nominal particle size of 19.2 mm of corn stover (Figure 4.4 a) has the cumulative percentage of 53.2% and d_{FE_max} and d_{c_min} of 9.104 mm and 3.237 mm, respectively (Table A1 in Appendix A). Some of the morphological features of corn stover and wheat straw obtained from the Camsizer analysis using the cumulative distributions of Feret or shortest cord diameters are listed in Table 4.1. The dimensions D_{10} , D_{50} , and D_{90} in the table represent the 10th, 50th, and 90th percentiles of the cumulative distributions of the corresponding parameters (i.e., Feret or shortest cord diameters). Each value in Table 4.1 was evaluated by taking the average of the results of the corresponding parameters of all three subsamples for a specific nominal size of a typical feedstock.

Table 4.1: Particle morphology of agricultural residue biomass using Camsizer

Feedstock		Corn stover				Wheat straw			
Nominal particle size ^a (mm)		~19.2	~6.4	~3.2	<~3.2	~19.2	~6.4	~3.2	<~3.2
d_{FE_max} (mm)	D_{90}	15.07	10.00	4.55	2.37	14.65	6.04	4.13	2.72
	D_{50}	9.37	6.00	4.39	1.66	8.53	4.85	3.63	2.19
	D_{10}	7.01	4.74	3.91	0.58	6.68	3.58	3.39	0.88
	X_{ig}^b	9.90±	6.64±	4.13±	1.55±	9.37±	4.84±	3.68±	1.97±
	$\pm \sigma_{ig}^c$	3.14	1.93	0.35	0.69	3.24	0.93	0.34	0.73
	Max.	25.52	16.73	10.55	4.96	28.09	11.44	9.00	9.63
	Min.	2.21	3.90	1.92	0.38	5.26	3.35	0.80	0.66
d_{c_min} (mm)	D_{90}	6.49	4.77	2.54	1.24	5.23	2.87	2.22	1.32
	D_{50}	3.49	2.40	1.20	0.70	2.19	1.52	1.29	0.71
	D_{10}	1.50	0.82	0.59	0.29	1.06	0.59	0.57	0.27
	$X_{ig} \pm \sigma_{ig}$	3.47±	2.26±	1.30±	0.63±	2.34±	1.37±	1.22±	0.64±
		1.97	1.57	0.75	0.36	1.62	0.87	0.64	0.4
	Max.	10.70	8.55	5.57	2.55	10.57	6.14	4.86	4.61
	Min.	0.24	0.24	0.08	0.15	0.38	0.28	0.12	0.14
Aspect ratio (φ_p)		6.10	7.81	7.30	2.17	9.09	8.70	7.52	3.29

^aNominal size based on the size of the openings of the classifier (BM&M Inc., Surrey, BC, Canada) sieves

^b $X_{ig} = [(D_{16} + D_{50} + D_{84})/3]$, Graphic mean (Vaezi et al., 2013)

^c $\sigma_{ig} = \{[(D_{84} - D_{16})/4] + \{(D_{95} - D_5)/6.6\}\}$, Graphic standard deviation (Vaezi et al., 2013)

The Camsizer software regards the particle aspect ratio as the ratio between the shortest cord and the Feret diameter; however, based on work by Vaezi et al. (2013) and the standard practice of presenting the aspect ratios of biomass particles as length over width (Lam et al., 2008; Schroeder et al., 2020), we represented the aspect ratio (φ_p) of the biomass particles using Equation 4.1:

$$\varphi_p = \frac{d_{FE_max}}{d_{c_min}} \quad (4.1)$$

The number of particles used in the Camsizer for the current research was approximately 0.05-3.6 million based on the fineness of the subsamples of each group of nominal sizes (19.2 mm, 6.4 mm, 3.2 mm, and <3.2 mm) of both feedstocks. The selection of a large number of particles for the

analysis indicates the reliability and precision of the results obtained from this equipment. The graphic mean length (X_{ig}) and graphic standard deviation (σ_{ig}) for each particle size of both feedstocks given in Table 4.1 were evaluated using the arithmetic approach described by Folk and Ward (1957) that helps assess complex sediment parameters (Bunte & Abt, 2001; Folk & Ward, 1957; Vaezi et al., 2013). Table 4.1 shows that the graphic mean lengths and widths (X_{ig}) of all four corn stover particle sizes were larger than those of wheat straw; however, their aspect ratios were lower than the corresponding wheat straw particles.

4.2.5 Types of ground corn stover particles

The ground corn stover obtained through knife milling consists of several particle types of non-uniform shapes with different aspect ratios. Gil et al. performed a shape analysis of milled corn stover and identified six different particle shapes: circle ($\phi_p < 1.15$; curl < 1.15), square ($\phi_p < 1.15$; curl > 1.15), rectangle ($1.15 < \phi_p < 3.3$; solidity > 0.7), rectangle fibrous ($\phi_p > 3.3$; solidity > 0.7), hook ($1.15 < \phi_p < 3.3$; solidity < 0.7), and hook fibrous ($\phi_p > 3.3$; solidity < 0.7). For a given particle, curl is the ratio of the Feret diameter to the particle length, and solidity is the ratio of the particle's actual area to the area enclosed by the smallest convex hull containing the particle. Solidity is equivalent to 1 for convex, void-free particles. The rectangle shapes had the highest mass percent and the hook fibrous particles the second highest (Gil et al., 2013; Gil et al., 2014). Vaezi et al. (2013) analysed particle size distribution, surface roughness features, and shape factors of knife-milled wheat straw and corn stover particles larger (< 3.2 mm- 19.2 mm) than those studied by Gil et al. (2013, 2014). Vaezi et al. (2013) found that corn stover particles have higher roughness parameter values (i.e., average roughness, highest peak, lowest valley, and maximum peak/valley height) than those of wheat straw. The authors also found that corn stover particles have less circularity but more roundness than wheat straw particles. However, they did not analyse biomass

particle shapes with the specific criteria used by Gil et al. (2014). In our current investigation, we tried to categorise the pre-classified corn stover particles both quantitatively and qualitatively based on physical appearance (i.e., shape, size, and surface roughness) as shown in Figure 4.5.

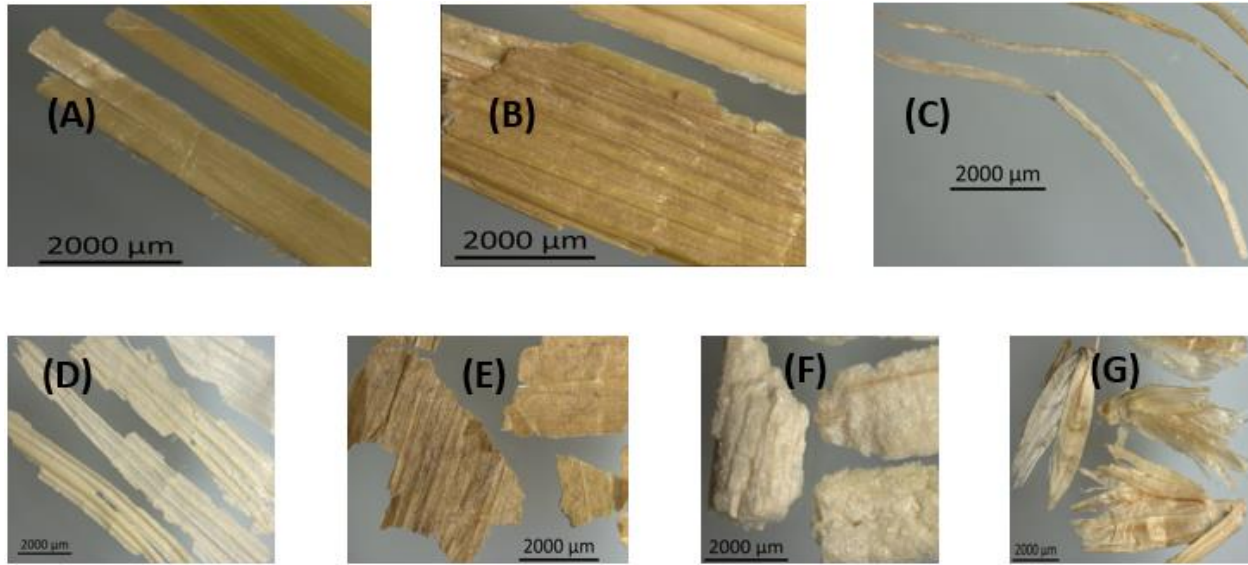


Figure 4.5: Microscopic images of sub-categories of particles obtained from samples of a 19.2 mm nominal size of corn stover (ground leaves and stalks) samples. Type A: Rib-like particles with plain surfaces, Type B: Rib-like particles with rough surfaces, Type C: Hair-like particles, Type D: Flake-like particles, Type E: Wide flake-like particles, Type F: Irregular-shaped thick particles, and Type G: Mixed form particles.

We randomly picked two 10 g (mass) nominal 19.2 mm samples from the pre-classified corn stover and then manually separated different particle types from each sample with extreme care to avoid any loss of material during segregation to obtain their exact mass percentages. We then identified seven sub-categories of particles in each sample. Because the process is time consuming and involves considerable manual effort, we did not analyse the other three corn stover particle sizes (<3.2 mm-6.4 mm). Figure 4.5 shows the microscopic images of the particle sub-categories captured by light microscope (Zeiss Stemi 508). Each sample from each sub-category was

individually collected and weighed with an electronic balance (± 0.01 g). Figure 4.6 (a) shows the average mass percentages of the seven particle types from both samples.

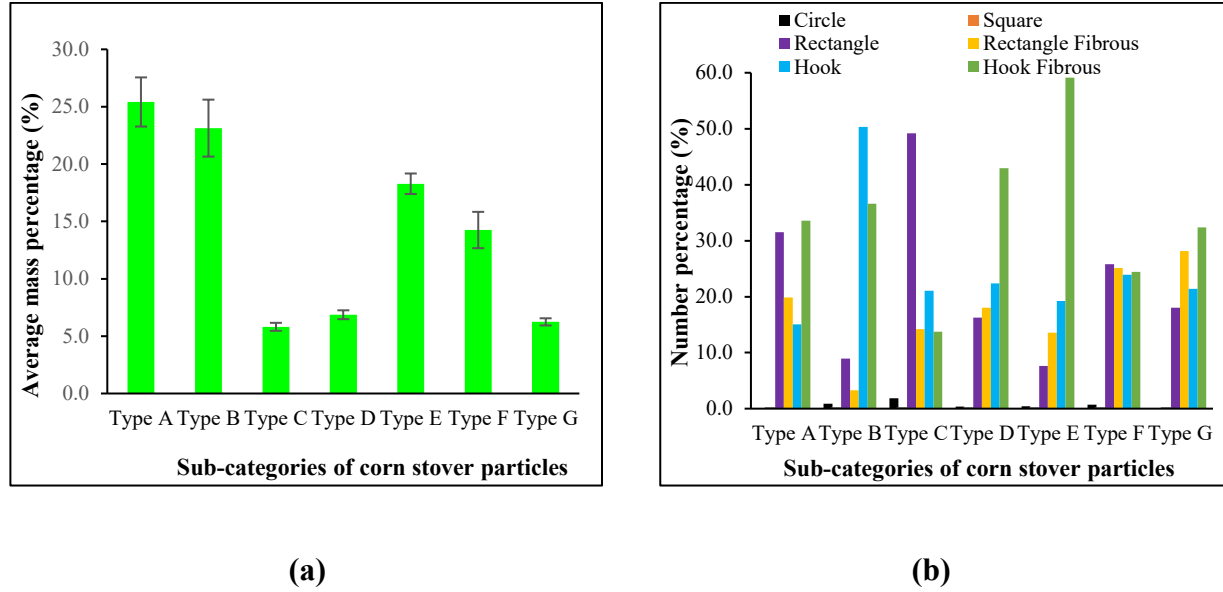


Figure 4.6: (a) Average mass percentages and (b) Percentage number distribution obtained from ImageJ of the sub-categories of corn stover particles as a function of their shape for a 19.2 mm nominal particle size. Type A: Rib-like particles with plain surfaces, Type B: Rib-like particles with rough surfaces, Type C: Hair-like particles, Type D: Flake-like particles, Type E: Wide flake-like particles, Type F: Irregular-shaped thick particles, and Type G: Mixed form particles.

As Figure 4.6 (a) shows, corn stover particle types A and B make up approximately 50% of the average mass of both samples. The next largest mass fractions are for types E and F. Types C, D, and G have the lowest mass fractions. Since the mass obtained in each sub-category was small, we performed a static image analysis to analyse the particle morphology instead of using dynamic digital image processing (described in section 4.2.4). Two-dimensional colour images (1200 dpi) of all the particles in all seven categories (types A-F) were captured using a flatbed scanner (HP

LaserJet 1536 dnf, Hewlett Packard, Boise, USA). The images were analysed using an open-source Java-based image analysis software, ImageJ, to obtain parameters like area, perimeter, Feret diameter, aspect ratio, solidity, and other dimensions of the best-fitted ellipse of each particle. Vaezi et al. (2013) explained the procedure of image processing of biomass particles using ImageJ in an earlier study. The criteria defined by Gil et al. (2013, 2014) were used to perform shape analysis of all seven particle categories.

Figure 4.6 (b) shows the percentage of the six particle shapes (circular, square, rectangle, rectangle fibrous, hook, hook fibrous) determined through ImageJ software for each type (A-F). The percentage was evaluated from the number of particles in any specific shape divided by the total number of particles of a specific type (A-F). For instance, the total number of particles in one of the two 19.2 mm corn stover samples is 4,114. Although the mass percent of type C particles is low (see Figure 4.6 [a]), C has more particles (around 1,260) than any other type. Type C has 744 particles with hook fibrous shapes; this number was divided by the total number of type C particles (i.e., 1,260) to determine the percentage of hook fibrous shaped particles. We found that most of the particles ($\approx 98\%$) in all types (A-F) are rectangle, rectangle fibrous, hook, or hook fibrous. However, some interesting features were discovered. The combined number percentages of rectangle fibrous and hook fibrous shapes in each of types A and D, and types B and G, were 60% and 50%, respectively. Yet type C particles had the highest number percentage, i.e., 75%, of the two shapes. Further, in types A, C, D, and G, hook fibrous shapes were dominant with longer lengths, whereas in types E and F, rectangle and hook shapes, respectively, were dominant. These observations are restricted to the 19.2 mm nominal particle size of corn stover.

4.2.6 Corn stover slurry preparation

Agricultural residue biomass absorbs moisture when water is added (Luk, 2010; Mohamadabadi, 2009), and the slurry rheology changes over time until the biomass is fully saturated with a moisture content (MC) of approximately 82% (Vaezi et al., 2014). As an initial step in making corn stover-aqueous slurry, we measured the wet basis MC of the classified corn stover material following ASABE S358.3 standards (ASABE, 2012). Four samples of random sizes of corn stover were picked, each weighing at least 25 g (net weight), and oven-dried for 24 h at 105 °C to find the initial MC. The desired mass of a particular particle size for a maximum accessible saturated mass concentration was calculated (i.e., C_m of 25%, 30%, 35%, and 40% [mass] for nominal 19.2 mm, 6.4 mm, 3.2 mm, and <3.2 mm sizes, respectively) using the initial MC (wet basis) and the saturated MC values. The saturated solid mass concentration was evaluated from the ratio of the saturated mass of solid materials (in a numerator) and the total mass of the slurry present in the loop (in a denominator). The total mass of the slurry was evaluated by adding together the saturated mass of the solid material and the total mass of unabsorbed water in the loop. After removing the air from the water in the closed pipeline loop, the required amount of corn stover was slowly loaded into the mixing tank with the slurry pump and the mixer turned on. The corn stover-aqueous slurry was circulated in the loop continuously for 15-18 h until the slurry was stable (i.e., fully saturated); at this point, the fluctuations in the pressure and velocity of corn stover slurry dropped to around 1.0-2.0% per hour. Once the slurry was stable, the bulk velocity was reduced from 4.3 m s⁻¹ to 0.5 m s⁻¹ at a maximum accessible saturated mass concentration and we obtained the corresponding frictional pressure drop values. The slurry solid mass concentration was changed by diluting the slurry in increments of 5% (mass), and the pressure and velocity values were recorded. The volume and mass percentages of saturated and dry solid (oven-dried) corn stover slurries are shown in

Table 4.2. The saturated densities of corn stover slurries were evaluated using their corresponding saturated particle densities measured according to ASTM C127 standards (ASTM, 2015). On average, the saturated particle density of corn stover was 1,048.73 kg m⁻³ (this value is similar to that found by Vaezi et al., who reported a corn stover saturated particle density of 1,050 kg m⁻³ [2014]).

Table 4.2: Volume and mass percentages of saturated and dry solids of corn stover-water mixtures

Saturated solid mass percentage	Saturated solid volume percentage^d	Dry matter solid mass percentage	Dry matter solid volume percentage	Saturated slurry density
(%)	(%)	(%)	(%)	(kg m⁻³)
40	38.83	6.28	7.2	1,019.42
35	33.90	5.48	6.3	1,016.95
30	28.99	4.69	5.4	1,014.49
25	24.10	3.90	4.5	1,012.05
20	19.23	3.11	3.6	1,009.62
15	14.39	2.33	2.7	1,007.19
10	9.57	1.55	1.8	1,004.79
5	4.77	0.77	0.9	1,002.39

^dThe saturated solid volume percentage was evaluated from the ratio of the saturated volume of solid materials (in a numerator) and the total volume of the loop (in a denominator). The saturated solid volume was determined by dividing the mass of saturated solids by the density of the saturated particles.

In our previous experiments, the delivered concentrations of wheat straw-water slurries at different velocities were examined and found to be similar to their corresponding prepared concentrations with minor differences (Javed et al., 2022b; Javed et al., 2021). In one of our ongoing laboratory studies, the terminal settling velocities (v_t) of different particle lengths (5-30 mm) of both wheat straw and corn stover (in saturated conditions) were evaluated in still water and the particles were found to be neutrally buoyant (i.e., $\frac{v_t}{v_m} \leq 0.021$, where v_m is the slurry/mixture velocity) at certain slurry velocities (as explained in detail in Appendix B). The saturated mass density of corn stover

is similar to that of wheat straw, and the particles of both feedstocks are neutrally buoyant. Therefore, we assumed in the current investigation that the delivered concentrations of corn stover slurries would be like their corresponding prepared concentrations.

4.2.7 Uncertainty analysis

To check the uncertainty in the pressure drop measurements, two sets of experiments were conducted for the slurries of all four particle sizes (19.2 mm, 6.4 mm, 3.2 mm, and <3.2 mm) of corn stover. A standard approach was used to find the total uncertainty (U_X) of the pressure drop measurements by evaluating the precision (P_X) and the biased uncertainties (B_X) (MECE 301, 2018; Moffat, 1988).

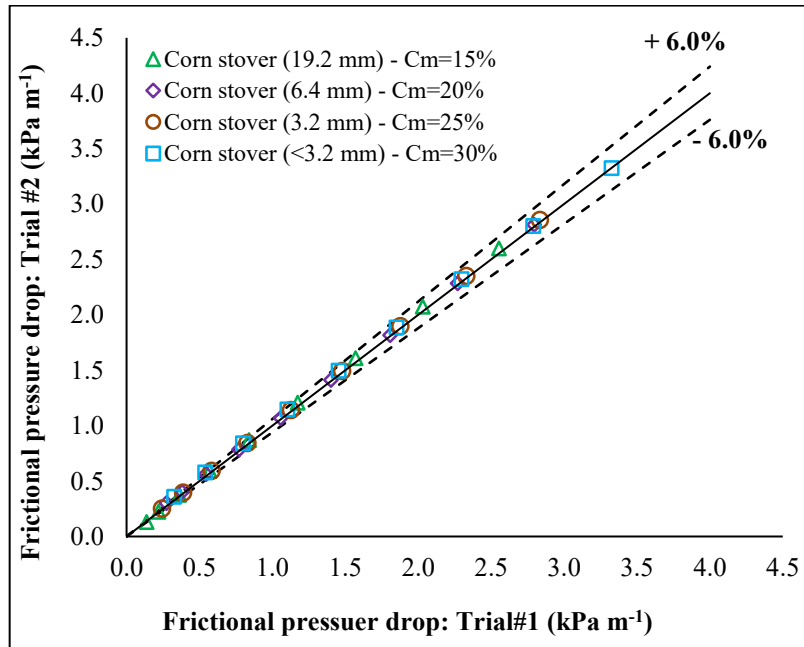


Figure 4.7: The repeatability of two sets of experiments on corn stover-aqueous slurries of 19.2 mm, 6.4 mm, 3.2 mm, and <3.2 mm particle sizes in a 50 mm diameter vertical test section.

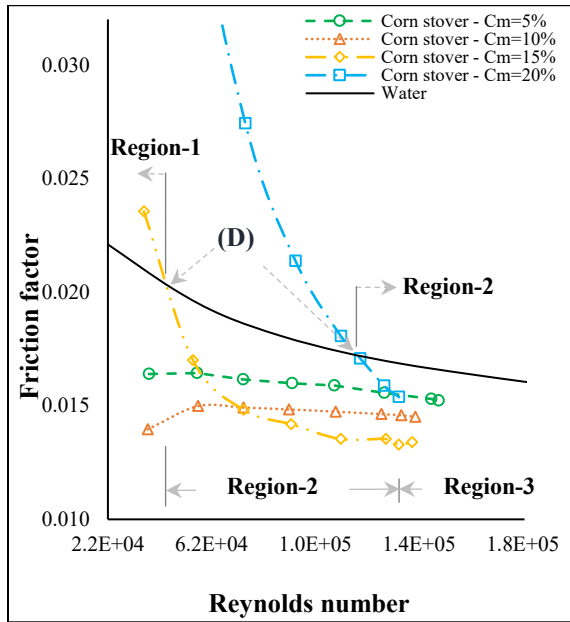
Generally, the uncertainty in the pressure drop measurements of corn stover is from $\pm 0.0145 \text{ kPa m}^{-1}$ to $\pm 0.0925 \text{ kPa m}^{-1}$. Figure 4.7 shows the repeatability of the experimental measurements of several particle sizes and mass concentrations of corn stover slurries in vertical upward flows. For the entire course of experiments on corn stover slurries, the range in the repeated measurements was found to be $\pm 6.0\%$.

4.3 Experimental results and discussion

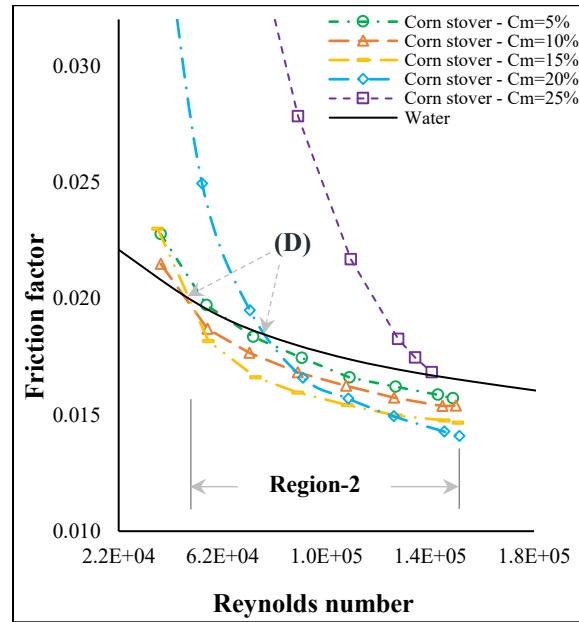
4.3.1 Frictional loss measurements of corn stover-water suspension

4.3.1.1 Flow regions and concentration effects

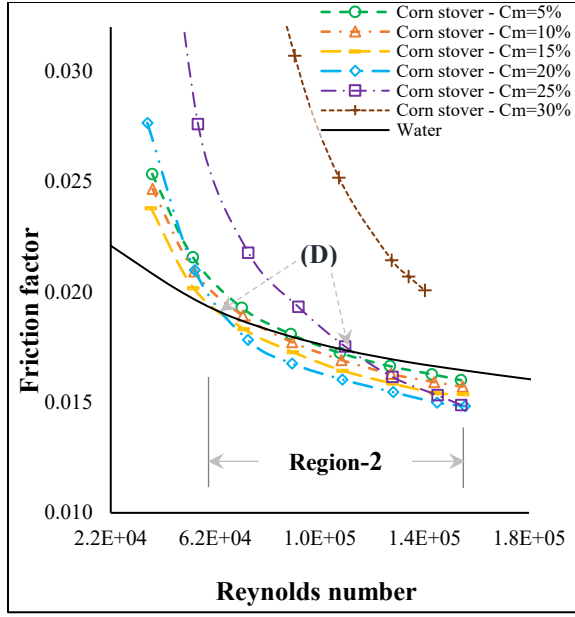
The friction factor measurements of the particle sizes (19.2 mm, 6.4 mm, 3.2 mm, and $<3.2 \text{ mm}$) in the corn stover-water suspension flowing upward in a vertical test section for a range of velocities ($1.0\text{--}4.3 \text{ m s}^{-1}$) and mass concentrations of $C_m = 5\text{--}35\%$ are shown in Figure 4.8.



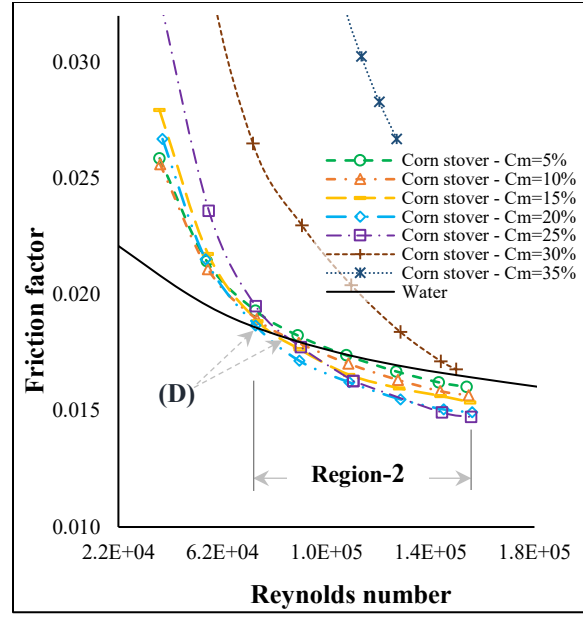
(a)



(b)



(c)



(d)

Figure 4.8: Friction factor versus generalised Reynolds number for velocities $\geq 1.0 \text{ m s}^{-1}$ in vertical upward flows of corn stover-water suspensions of (a) 19.2 mm, (b) 6.4 mm, (c) 3.2 mm, and (d) $<3.2 \text{ mm}$ particle sizes.

We considered a generalised Reynolds number ($Re_g = \frac{\rho_m v_m D}{\mu_f}$) here to represent the velocity of each suspension. Generally, most of the corn stover-aqueous suspensions in every particle size (see Figure 4.8) exhibited the characteristics of both the plug flow (Region 1) and the transition flow (Region 2) regions for a $C_m = 5\text{-}25\%$ over the entire flow range with few exceptions (i.e., most of the suspensions of the largest particles and high concentrations of the remaining three particle sizes). At low flow rates, a plug of fibers moves along the central core of the pipe surrounded by a clear water annulus (either free of fibers or with few fibers) between the inner wall of the pipe and the plug (Radin et al., 1975; Wiklund et al., 2008; Wiklund et al., 2006). The water annulus around the fiber plug is mainly due to a radial compression of the fiber network resulting from the forces of hydrodynamic shear stresses (Meyer, 1964) and the deflection of the

ends of the fibers (the blown-grass effect) (Moller & O'Sullivan, 1974). Fock et al. (2011) observed a homogeneity in the flow structures and fiber distribution within the plug at certain velocities in their investigation of the near-wall effects of pulp suspension flows in a circular pipe. They further found through particle image velocimetry (PIV) measurements that the plug contains flocs of fibers (with the fibers aligned with the flow direction) whose size depends largely on suspension velocity and concentration (Fock et al., 2011). There is a thin turbulent sheared layer with a sharp velocity gradient in the zone between the fiber plug and the pipe wall (Cotas, 2016; Kazi et al., 1999).

The friction factor decreases sharply in the plug flow region (Region 1), whereas the size of the water annulus increases (gradually) with increases in suspension velocity until a transition point (D in Figure 4.8; adapted from an earlier study (Vaezi et al., 2014)) was reached where the friction factor of the suspension becomes equal to that of water (i.e., a Newtonian fluid) (Cotas, 2016; Duffy et al., 1976). This transition point demonstrates a shift of flow region of a specific suspension from plug to transition flow at a certain suspension velocity and is known as the onset velocity of drag reduction. The flow region that develops after the transition point is known as the transition (or mixed) flow region (Region 2) (shown in Figure 4.8); in this region, a further increase in suspension velocity decreases the friction factor and eventually the plug diameter, albeit at a comparatively lower rate than in the plug flow region (Radin et al., 1975). At this point, the water annulus surrounding the plug of fibers does not increase in size with an increase in suspension velocity because of the compressed fibers in the plug. The higher shear flow in the water annulus disrupts the plug at the plug-annulus interface (Sumida, 2013). This disentanglement of the fibers from the plug continues with an increase in suspension velocity until the fiber plug disappears and the suspension reaches the turbulent flow region (i.e., Region 3, Figure 4.8 [a]), at which point the friction factor increases with velocity (instead of decreasing, as observed earlier) and eventually

makes the suspension's friction curve parallel to and below that of the turbulent water curve with a certain offset (Cotas, 2016).

In our current investigation, the largest particle size of corn stover-water suspension at a low C_m of 5-10% (Figure 4.8 [a]) demonstrated the transition flow region only; there, the friction factor was always below the water curve over the complete range of Reynolds numbers. One of the reasons for this typical behaviour could be the long hair-like particles (i.e., type C, Figure 4.5) in the corn stover slurries; these particles might cause drag reduction even at low Reynolds numbers. These hair-like particles are longer than the other particles (shown in Figure 4.5). Although the mass percentage of these hair-like particles is low (Figure 4.6 [a]), ImageJ showed that these particles have the highest number percentage (i.e., 30%) of the six types. Fibers interact with each other through rotation as well as in translation during shear flow, and longer fiber lengths contribute more to drag reduction (Kerekes, 2006). Therefore, there is a high chance that these hair-like particles will bend more than the other particle types (i.e., E and F) to develop hooking forces even in the corn stover's dilute suspension phase (5-10%). The hooking forces are a mechanical force that emerges from the curls or kinks of the hair-like particles during their flow and eventually cause them to cohere (instead of sliding over one another) in the dilute regime of the suspension (Kerekes, 2006). Ellis found drag reduction by large asbestos fibers in a dilute suspension flow through circular pipes (Ellis, 1970). Hoyt et al. reported an increase in the effectiveness of drag reduction in proportion to the long hair-like asbestos fibers (with the smallest diameter and large aspect ratios) for all the concentrations used in their studies (Hoyt, 1972). The authors found that types A, B, and D were longer and had more rectangular fibrous and hook fibrous characteristics, like type C. Therefore, hair-like particles, as well as types A, B, and D, might develop floccettes or sometimes flocs at low concentrations of the slurries of the largest

particle size of corn stover at even low turbulent flow rates. However, these floccettes/flocs would not be large enough (with respect to the inner diameter of the vertical pipe section in the current research) to cause plug flow at low Reynolds numbers. Hence, these low concentration suspensions of the largest particle size of corn stover eventually show drag reduction at low turbulent flows (Figure 4.8 [a]).

As the solid mass concentration of corn stover suspension increases to 15% (Figure 4.8 [a]), the hydrodynamic interactions of particles with the fluid surrounding them and the interactions among the particles themselves increase, which increases the apparent suspension viscosity (Djalili-Moghaddam & Toll, 2006) compared to the low concentration suspensions (i.e., 5-10%). This phenomenon eventually causes larger flocs (and hence higher friction) to develop at low flow rates. We surmise that this corn stover suspension can still reduce drag at low flow rates if the pipeline diameter is increased. However, this needs to be studied further by scaling up the current setup. The corn stover suspensions of other sizes (i.e., 6.4 mm, 3.2 mm, and <3.2 mm) did not fall entirely into the transition flow region for the complete flow rate range, nor any of the mass concentrations (Figure 4.8 [b,c,d]). The average inter-fiber distance (i.e., $h_{av} = [nX_{ig}]^{-1/2}$, where n ($n = \left[\frac{4}{\pi} C_V \frac{1}{X_{ig}X_{ig,w}^2} \right]$), X_{ig} , and $X_{ig,w}$ are the fiber number fraction, graphic mean length, and graphic mean width, respectively; see Table 4.1 for the values of X_{ig} and $X_{ig,w}$) in these suspensions was 1.5 to 6.0 times lower than that of the largest particle size (shown in Table 4.3), which could result in increasing the adhesive forces and ultimately allowing flocs to grow even at low mass concentrations and Reynolds numbers.

Table 4.3: Average fiber distance and crowding number for corn stover- and wheat straw-aqueous slurries of 19.2 mm, 6.4 mm, 3.2 mm, and <3.2 mm particle sizes

Feedstock	Nominal particle size (mm)	Saturated mass concentration (%)	Average inter-fiber distance (h_{av})	Crowding number (N)
Corn stover	~19.2	5-25	14.1-6.3	1.2-6.0
	~6.4	5-30	9.2-3.7	1.9-11.8
	~3.2	5-35	5.3-2.0	1.7-12.0
	<3.2	5-40	2.6-0.9	0.15-1.22
Wheat straw	~19.2	5-25	9.5-4.2	2.6-13.3
	~6.4	5-30	5.6-2.3	2.4-14.6
	~3.2	5-35	4.9-1.9	1.8-12.8
	<3.2	5-40	2.6-0.9	0.34-2.8

The maximum achievable drop in the friction factor below the water curve was found for the suspension flow of the largest particle size at a 15% mass concentration and a velocity of 3.65 m s⁻¹ (see Figure 4.8 [a]). At higher velocities (i.e., >3.65 m s⁻¹), this suspension reached the turbulent flow region (Region 3) (where the friction factor started increasing but was still below the water curve). A similar phenomenon was observed for vertical upward flows of 19.2 mm particle size wheat straw-aqueous slurries, reflecting the start of the turbulent flow region (i.e., damped turbulence sub-region) at a comparatively higher mass concentration (i.e., 25%) (Javed et al., 2021). The primary reason for the occurrence of this phenomenon in two different feedstocks (i.e., wheat straw and corn stover) at different concentrations (i.e., lower in the corn stover and higher in the wheat straw) is the complex nature of the ground corn stover (containing several particle shapes and sizes, as shown in Figure 4.5), which influences slurry viscosity. Barnes et al. (1989) found both particle shape and aspect ratio to be strong factors; both affect slurry viscosity. Larson et al. (1999) and Tadros et al. (2010) also found that the viscosity of slurries with complexly shaped particles largely depends on particle concentration (Larson, 1999; Tadros, 2010). Schmid et al. (2000) reported that fibers with shapes of irregular equilibrium have a large effect on the

flocculation (i.e., flocs increase) even at low crowding numbers ($N = \frac{2}{3}C_V(\phi_p)^2$, where C_V is the suspension volumetric concentration in fractions) compared to the straight stiff fibers with comparatively higher crowding numbers. In our current investigation, all four particle sizes of corn stover had low crowding numbers (N) for all the mass concentrations compared to the corresponding wheat straw particles (shown in Table 4.3), which are mostly composed of straight rib-like particles. Therefore, with the findings of previous studies (Barnes et al., 1989; Larson, 1999; Schmid et al., 2000; Tadros, 2010) in mind, we can state that flocculation increases when $C_m = 15\%$ of corn stover suspensions of the largest particle size at low flow rates. This increase eventually causes the development of a larger plug and hence a higher friction factor (Figure 4.8 [a]). However, this suspension shows characteristics of damped turbulence at higher flow rates.

No other corn stover suspensions (except 19.2 mm when $C_m = 15\%$) showed a turbulent flow region at any flow range and mass concentration tested (Figure 4.8). In the present work, we could not attain higher velocities (i.e., $>3.8 \text{ m s}^{-1}$) for the largest particle size of corn stover-water suspension when $C_m = 15\%$ because of limitations in the slurry pump capacity. This constraint meant we did not see any further increase in the friction factor until the Newtonian turbulence sub-region was achieved (at which point no further increase or decrease in the friction factor occurs with an increase in suspension velocity (Javed et al., 2021; Seely, 1968)). For the suspension of the three other particle sizes (i.e., 6.4 mm, 3.2 mm, and <3.2 mm, shown in Figure 4.8 [b,c,d]), the highest achievable drops in friction factor below the water curve were observed at the highest attainable slurry velocities and mass concentrations of 20%, 25%, and 25%, respectively.

4.3.1.2 Flow regions at the highest concentrations

Figure 4.9 shows a typical log plot of the frictional pressure drops and bulk velocities (0.5-2.96 m s⁻¹) for the highest mass concentrations of all the particle sizes of corn stover-aqueous slurries.

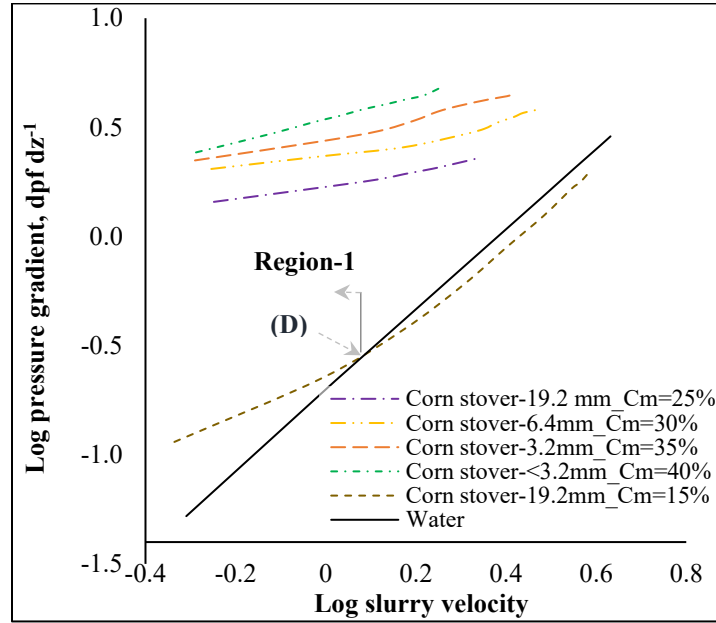


Figure 4.9: Logarithmic plot of the frictional pressure drop and bulk velocity of aqueous corn stover slurries of 19.2 mm, 6.4 mm, 3.2 mm, and <3.2 mm in vertical upward flows for several mass concentrations and the complete range of bulk velocities (point D in Figure 4.8).

The supplemental results for the largest particle size at a 15% mass concentration (in Figure 4.9) have been added to visualise the transition point D (from plug flow to transition flow region) on this type of plot. Fiber suspension is said to be in the dilute regime when the number of contacts per fiber (n_c), which can be evaluated as $n_c = 2C_V(\phi_p)^2$, is <1.0 and in the concentrated regime when $n_c \geq 3.0$ (Dodson, 1996; Kerekes, 2006). These regimes describe the constraints imposed on the translational and rotational motions of the fibers in the suspension. The larger the contact number, the more the chance of fiber-fiber interaction. Because the contact number has a quadratic

dependence on φ_p , the collisions induced by fiber asymmetry would be higher for larger particle sizes than for smaller ones at the same mass concentrations (Kerekes, 2006). For concentrated regimes (i.e., $n_c \geq 3.0$), the crowding number (N) will always be greater than the particle aspect ratio (φ_p). These regimes are most difficult to analyse and model as n_c exceeds the value of 3.0 (Samaniuk et al., 2011). Although some studies focus on the PSD instead of choosing a single particle size to find N and n_c (Huber et al., 2003; Kropholler & Sampson, 2001), we opted to select the aspect ratios given in Table 4.1 for each particle size of the biomass particles. The regimes of the aqueous biomass suspension behaviour identified using the fiber contact number approach are shown in Figure 4.10.

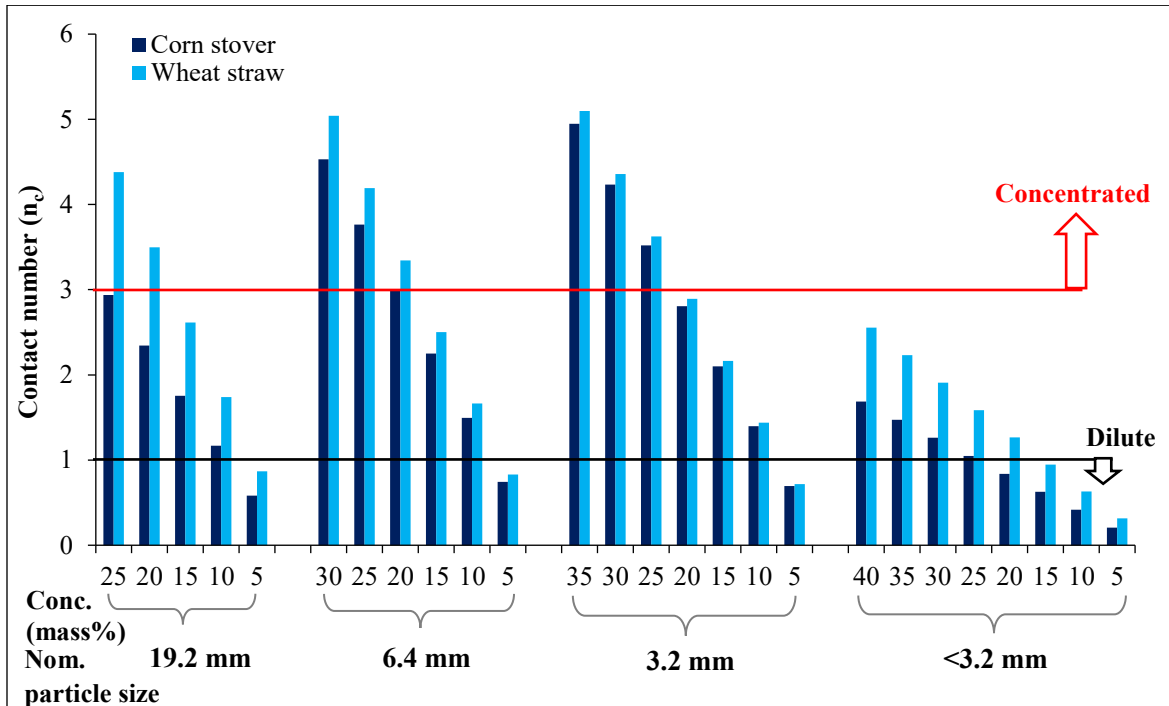


Figure 4.10: Contact numbers for corn stover- and wheat straw-aqueous slurries of 19.2 mm, 6.4 mm, 3.2 mm, and <3.2 mm at various mass concentrations.

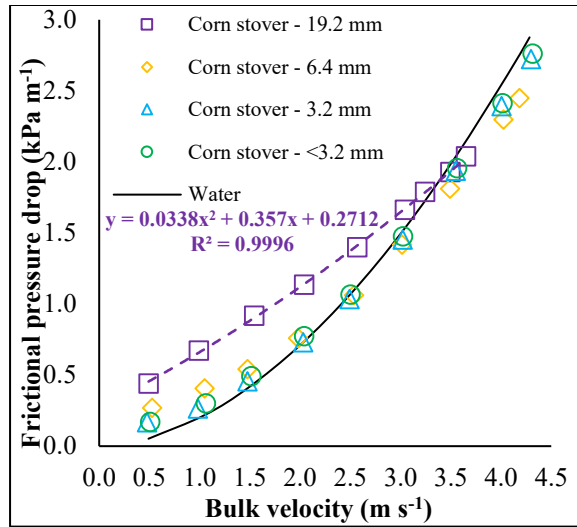
Figure 4.10 provides a reasonable approximation of the collision of biomass particles at the concentrations and particle sizes used in our current and past studies (Javed et al., 2022b; Javed et

al., 2021). At higher mass concentrations (25-40%) (Figure 4.9), most of the corn stover suspensions were found to be in the concentrated regime (i.e., $n_c \geq 3.0$) with high biomass loadings and continuous contact of the fibers with each other, thus developing coherent networks among the particles that increased flocculation and ultimately the size of the plug. It is expected that at this state of suspension, the size of the annulus would be small, which ultimately results in the high shear zone being between the annulus and the pipe walls by further increasing the flow rate. All the suspensions (except when $C_m = 25\%$ for both lower particle sizes) showed friction factors (or pressure drops) above those of water for the entire flow range (Figure 4.8 and Figure 4.9), thus displaying the characteristics of the plug flow region only with no drag reduction.

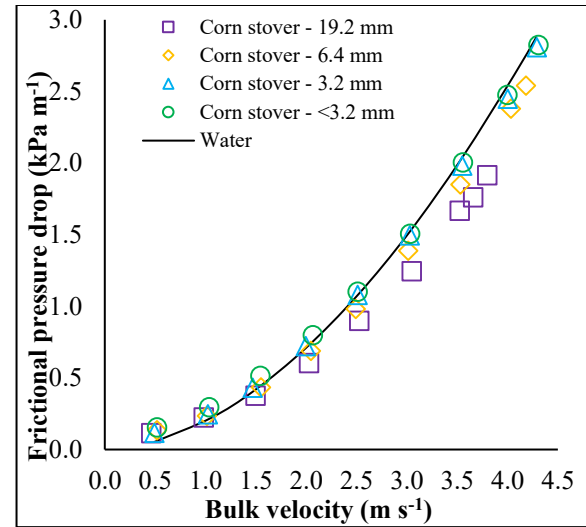
Higher velocities could not be achieved for any of the suspensions at their highest concentrations (e.g., for the smallest particle size, the highest achievable velocity was just 1.81 m s^{-1} at 40% mass concentration). However, based on the trend of the friction factor and pressure drop curves obtained for highly concentrated corn stover suspensions (shown in Figure 4.8 and Figure 4.9), it was observed that the transition flow region could be achieved for most of the suspensions at comparatively higher Reynolds numbers. For some of the suspensions of smaller particle sizes (i.e., 3.2 and $<3.2 \text{ mm}$) at the highest mass concentration, the corresponding pressure drop curves (if extrapolated) seemed to diverge away from the water curve at even very high flow rates, keeping themselves within the plug flow region only (Figure 4.9). This observation needs to be explored further at higher Reynolds numbers by measuring the slurry viscosities and upgrading our slurry loop pump.

4.3.1.3 The effect of particle size

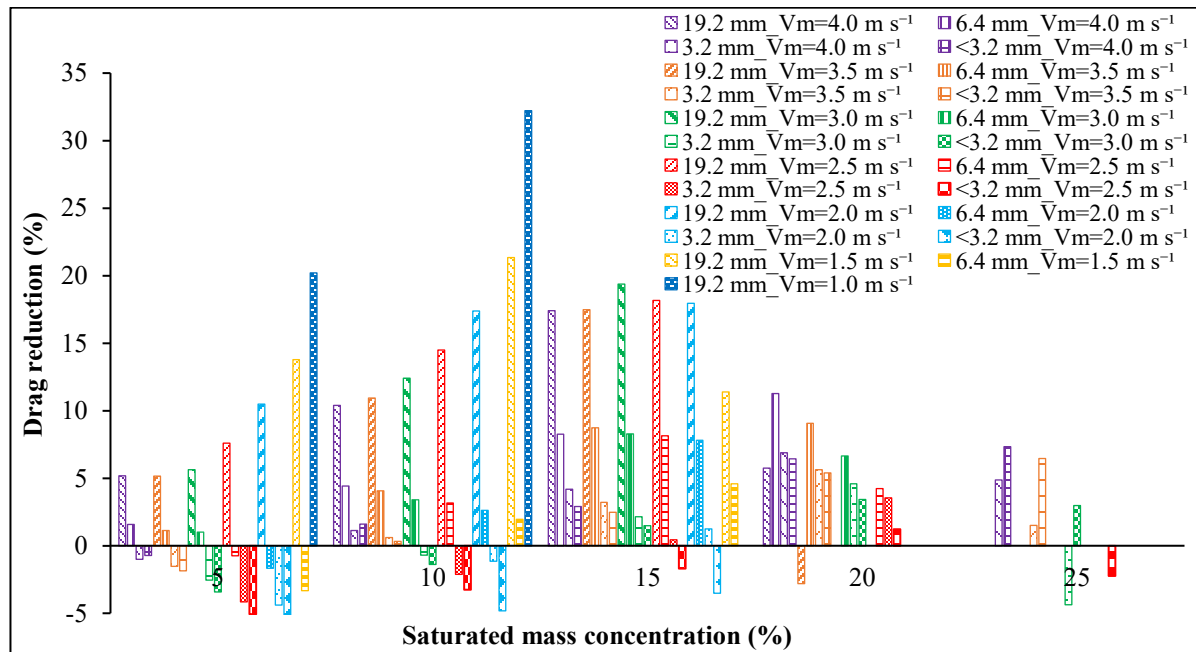
The effect of particle size on the frictional pressure drop and drag reduction of corn stover-water slurries in vertical upward flows for a range of mixture velocities is shown in Figure 4.11.



(a)



(b)



(c)

Figure 4.11: The effect of particle size in vertical upward flows of corn stover-aqueous slurries for a range of slurry bulk velocities (1.0-4.0 m s⁻¹) on the frictional pressure drop at saturated mass concentrations of (a) 20% (mass), (b) 15% (mass), and (c) drag reduction for a range of mass concentrations (5-25%).

Figure 4.11 (a) and (b) show the range of frictional pressure drop measurements for all four particle sizes of corn stover-aqueous slurries flowing at mass concentrations of 15% and 20% through a vertical test section. For both concentrations and a specific range of flow rates (i.e., above certain velocities) of all the suspensions, the frictional pressure drop decreases (with respect to that of clear water) with an increase in particle size. The highest decrease in the frictional pressure drop was observed for corn stover suspensions of the largest particle size at the maximum achievable bulk velocity of $\approx 3.8 \text{ m s}^{-1}$ and a mass concentration of 15%. At a higher mass concentration (i.e., 20%), the maximum achievable bulk velocity for the suspension of the largest particle size was lower (i.e., 3.65 m s^{-1}) than the corresponding value when the $C_m = 15\%$. However, it is expected that an increase in the bulk velocity will cause a further decrease in the frictional pressure drop at a higher C_m (i.e., 20%) of the suspensions of the largest particle size.

For lower mass concentrations (i.e., 5-10%) and maximum achievable velocities (Figure A2 in Appendix A), the frictional pressure drops for the suspensions of the largest particle size were always lower than those of the smaller particles. These results indicate the strong effect of particle size on the frictional pressure drop of corn stover-water suspensions for all the concentrations at specific flow ranges. Other studies have found similar effects of particle size on frictional pressure drops of various fiber suspension flows in vertical pipe sections (Bobkiewicz & Gauvin, 1965; Javed et al., 2022b; Radin et al., 1975). A decrease in the average inter-fiber distance (h_{av}) increases the adhesive forces and flocculation of fiber suspension, which ultimately increases the apparent suspension viscosity of the slurry. The fiber number fraction (n) of the largest particle size (19.2 mm) of corn stover is 200 times smaller than the fine particles (i.e., $<3.2 \text{ mm}$), hence its inter-fiber distance is approximately 6.0 times greater than that of the fine particles, and the apparent suspension viscosity of the larger corn stover-water suspensions is comparatively lower

than the suspensions of the fine particles. This decrease in the apparent suspension viscosity eventually reduces the pressure drops more for corn stover slurries of the largest particle size than those of the fine particles. Furthermore, longer fibers lead to more contact points, greater mechanical entanglement, a stronger fiber network, and hence larger and stronger flocs (Dodson, 1996; Huber et al., 2003). As a result of strong networking and larger flocs specifically at higher mass concentrations, the suspensions dampen the longitudinal turbulence intensities (Bobkiewicz & Gauvin, 1965; Radin et al., 1975), which ultimately increases the drop in the frictional pressure below the water curve after certain velocities, as shown in Figure 4.11 (a) and (b).

Figure 4.11 (c) shows the combined effect of particle size, velocity, and saturated mass concentration on percentage drag reduction in vertical upward flows of corn stover-aqueous slurries. The highest achievable bulk velocities of all the particle sizes of corn stover slurries particularly at higher mass concentrations were not the same. We observed maximum slurry velocities of 3.65, 2.95, 2.62, and 1.81 m s⁻¹ for particle sizes of 19.2 mm, 6.4 mm, 3.2 mm, and <3.2 mm at their corresponding mass concentrations of 20%, 30%, 35%, and 40%, respectively. Further, in our existing experimental setup, the highest pumping velocities for saturated slurries of the largest particles were found to be 3.8 and 3.84 m s⁻¹, respectively, at even comparatively lower mass concentrations of 10% and 15%, respectively, with respect to the other three particle sizes. Therefore, in Figure 4.11 (c), only those data points where we found the slurry bulk velocities to be consistent are presented, not the three suspensions of the larger particles, as explained. The bulk velocities of 4.0 m s⁻¹ shown in Figure 4.11 (c) for the slurries of the largest particle size at mass concentrations of 20%, 15%, and 10%, are 3.65, 3.8, and 3.84 m s⁻¹, respectively. In general, with increasing particle size, the percentage drag reduction (%DR) increases at any specific concentration and velocity of corn stover-aqueous slurries during vertical upward flow (Figure

4.11 [c]). However, some interesting features were observed in the drag reduction phenomena with respect to some flow conditions. The %DR of any specific particle size of corn stover slurry increases with increasing the slurry concentration up to a certain limiting value (critical concentration), which seems to be completely dependent on both the slurry velocity and particle size (Figure 4.11 [c]). After the critical concentration was reached, a decrease in %DR was observed for any specific particle size and slurry velocity. For instance, the critical concentration for the highest drag reduction ($(C_m)_{cr}$) was 15% for the largest particle size, 20% for the 6.4 mm and 3.2 mm particle sizes, and 25% for the smallest particle size of corn stover slurries at higher velocities (i.e., 3.5-4.0 m s⁻¹), whereas the $(C_m)_{cr}$ for the slurries of the larger particles (i.e., 19.2 mm and 6.4 mm) was 15% and for the smaller particles (i.e., 3.2 mm and <3.2 mm), 20% at velocities of 2.5-3.0 m s⁻¹. Similarly, the $(C_m)_{cr}$ was different for lower bulk velocities (i.e., ≤2.0 m s⁻¹) for both larger particles. The characteristics of the fiber suspension flow depend largely on their velocities (Bobkowicz & Gauvin, 1965; Sunny et al., 2021), as well as the corresponding regimes of the fiber suspension behaviour (Kerekes, 2006). Therefore, different $(C_m)_{cr}$ s were observed for the corn stover suspensions at different flow rates.

The onset of drag reduction in corn stover suspensions of the largest particle size when the $C_m = 15\%$ occurred at low velocity (i.e., 1.3 m s⁻¹; see Figure 4.11 [b]); therefore, it was observed that the drag reduction in this suspension was even up to a mixture velocity of 1.5 m s⁻¹ (Figure 4.11 [c]). At the lowest C_m (i.e., 5%) over the entire velocity range, none of the corn stover-water slurries except those of the larger particle size (i.e., 19.2 mm) showed any drag reduction (Figure 4.11 [c]). This was due to long hair-like fibers present in the largest particle size of the corn stover suspension (see section 4.3.1.1). However, the suspension of the 6.4 mm particle size of corn stover exhibited drag reduction to some extent at lower concentrations (i.e., $C_m = 5\%$) and high velocities

(i.e., $\geq 3.0 \text{ m s}^{-1}$) since the onset of drag reduction occurred in this suspension at 2.75 m s^{-1} . The corn stover slurries, which did not exhibit drag reduction over the entire course of experiments, are not shown in Figure 4.11 (c) (to avoid complexity in the graph), except for a few for the sake of clarification. At the lowest velocity (i.e., 1.0 m s^{-1}), the highest drag reduction of 32% was found in a corn stover slurry flow of the largest particle size at $C_m = 10\%$. None of the other slurries of the remaining three particle sizes showed any drag reduction at the lowest velocity even at higher concentrations because of the plug flow. We further noticed that the lowest velocity (i.e., 1.0 m s^{-1}) was still greater than the critical deposition velocity (i.e., 0.8 m s^{-1} (Vaezi et al., 2018)) of the largest particle size of the corn stover slurry flow. Therefore, no stationary bed formation was observed in the horizontal pipe section of the closed pipeline loop during the flow at the lowest flow rate (this observation was reconfirmed through the flow visualisation section [Figure 4.1]), and hence the in situ concentration in the vertical pipe section at the lower velocity value was expected to be equal to the prepared concentration. At a lower C_m of 5-10%, the %DR for corn stover-aqueous slurries of the largest particle size increased with decreasing velocity. The slurries of the remaining three particle sizes, however, showed the reverse behaviour for the entire range of concentrations (i.e., %DR decreased as the velocity decreased).

4.3.1.4 Onset velocity of drag reduction

Figure 4.12 shows onset velocities of drag reduction obtained in vertical upward flows of all four particle sizes of corn stover-water suspensions at several mass concentrations.

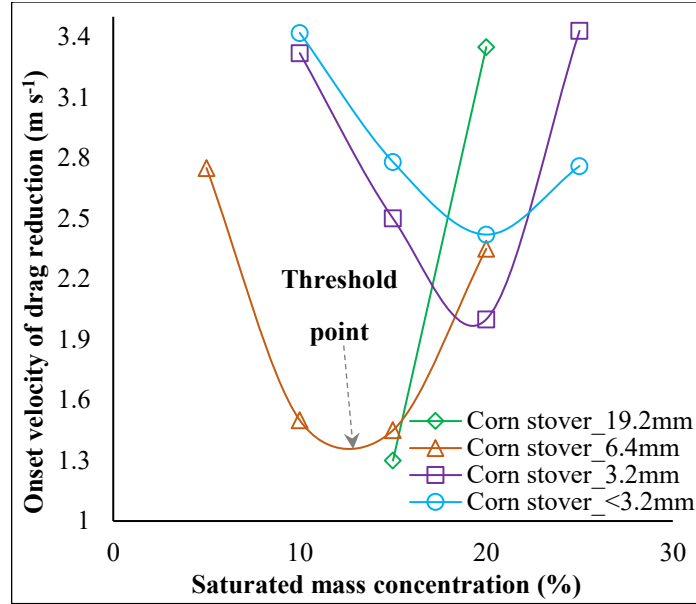


Figure 4.12: Onset velocity of drag reduction obtained at several mass concentrations of corn stover-aqueous slurries of 19.2 mm, 6.4 mm, 3.2 mm, and <3.2 mm while flowing upward in the vertical pipe.

It can be inferred for all particle sizes (except 19.2 mm) that the onset velocity of drag reduction decreases with increasing the slurry mass concentration up to a certain threshold, shown as the minimum on each curve in the figure. This typical behaviour of the corn stover suspension can be hypothesised in such a way that, at low fiber concentration (i.e., $C_m = 5\%$), the average inter-fiber distance (h_{av}) within suspensions of any particle size is greater (Table 4.3) than that in higher concentrations of a similar particle. As the flow rate increases, the h_{av} decreases. The suspension at this low fiber concentration will remain in the plug flow until it reaches a high flow rate, when the fibers come close enough to each other to make a plug with void spaces among the fibers small enough to get strong inter-fiber connections, where fiber-fiber interactions are dominant (Sunny et al., 2021). At this point, a further increase in the flow rate will cause the plug to disintegrate from the plug annulus interface, which will eventually bring about the onset of drag reduction at a high flow rate of suspensions of low mass concentration. Therefore, the onset velocity of drag

reduction is higher when the $C_m = 5\%$ for most of the suspensions shown in Figure 4.12. However, as the concentration of the slurry of any specific particle size increases, the corresponding fiber number fraction (n) also increases, and the average inter-fiber distance decreases; thus, comparatively low flow rates of specific slurries are needed to form a plug with minimum void spaces and strong inter-fiber connections. The onset point of drag reduction of a typical suspension occurs at comparatively lower slurry velocities compared to the low concentrations of the corresponding suspension. This statement is valid up to the threshold limit of each suspension, after which the slurry behaviour is reversed (Figure 4.12).

For the subsequent concentrations above the threshold limit of the suspensions of a specific particle size, the onset velocity of drag reduction increases with increases in the saturated mass concentration (Figure 4.12). This increase in onset velocity can be associated with the increase in the strength of the fiber network, as reported by Kazi et al. (1999) and Duffy and Lee (1978). With increasing mass concentration, the crowding number and hence the number of fiber contacts increase (Figure 4.10). Most of the suspensions at their threshold limit seem to exist above the dilute and below the concentrated regimes (i.e., $1.0 < n_c < 3.0$). Therefore, it can be inferred that the suspensions have sufficiently high inter-fiber connections at their corresponding threshold limits (due to increases in the adhesive forces and flocculation) that any further increase in the concentration beyond this limit increases the strength of the fiber network. Thus, higher flow rates are needed for these suspensions to disrupt the borders of the fiber plug. This eventually causes the onset velocity to increase with an increase in the concentration for any suspension of a specific particle size (as shown in Figure 4.12). The corn stover-water suspensions of smaller particle sizes (i.e., 3.2 mm and <3.2 mm) did not exhibit any drag reduction when the $C_m = 5\%$ (Figure 4.11 [c]). Moreover, the 19.2 mm particle size suspensions were observed to be in the transition flow

region when the $C_m = 5\text{-}10\%$ (Figure 4.8 [a]); therefore, the corresponding onset points of drag reduction of these suspensions are not shown in Figure 4.12.

With respect to the effect of fiber length on onset velocity of drag reduction, for suspension solid concentrations equal to or below the threshold limit of each particle size (i.e., 6.4 mm, 3.2 mm, and <3.2 mm, Figure 4.12), it was observed that the onset velocity of drag reduction decreases with increases in particle size. As the crowding number depends on the φ_p and C_v , it is possible in fiber suspensions of two different particle sizes to have the same crowding number at different concentrations. Fiber suspensions with the same crowding number were expected to have the same tendency to form flocs (Jing, 2009). This means that fiber suspensions of small particle sizes with larger crowding (contact) numbers than the suspensions of large particle sizes can exhibit stronger networks. At the threshold limit (i.e., $C_m = 20\%$), corn stover suspensions of a 3.2 mm particle size have a larger contact number than suspensions of 6.4 mm when the $C_m = 15\%$ and 19.2 mm when the $C_m = 10\%$. Therefore, the 3.2 mm particle size suspensions have stronger flocs and require a higher flow rate to disrupt the fiber plug to start drag reduction. However, for comparatively larger C_m (i.e., typically beyond the threshold limit of the suspensions of each particle size), the onset velocity increases with increases in particle size because of a corresponding increase in floc size and the creation of more solid links, as described by Huber et al. (2003) and Vaezi et al. (2014).

Corn stover-aqueous slurries of the largest particle size show less friction than water alone during their flow through a vertical pipe for the entire range of velocities (i.e., $0.5\text{-}4.0\text{ m s}^{-1}$) and lower C_m 's (i.e., $5\text{-}10\%$). This is the distinct feature of these kinds of suspensions compared to the other fibrous materials. However, if higher C_m 's (i.e., $>10\%$) for larger corn stover particles need to be delivered, higher slurry flow rates are needed to keep the minimum friction compared to water

alone. It is worth noting here that the pipeline used in the current investigation had a small inside diameter (i.e., 50 mm) and pipe diameter-to-particle length ratio of $D/D_{50} = 5.5$ (considering the largest nominal particle size of the corn stover). Some studies focus on the effect of pipe diameter on the frictional pressure drop of various fibrous slurries (e.g., asbestos, nylon, rayon, and wood pulp) and report an increase in both drag reduction and onset velocity with increases in pipe diameter (Duffy & Lee, 1978; Radin et al., 1975; Rao, 1985). Therefore, the onset velocity of drag reduction was further expected to increase at higher concentrations of corn stover-aqueous suspensions (beyond the threshold limit) with pipelines of larger inside diameters. Analysing the onset velocities of several particle sizes of corn stover-water slurries at low concentrations as well as their threshold limits in vertical upward flows in larger diameter pipelines with inside diameters of at least 100-200 mm would be interesting to explore. This analysis of the onset velocity of drag reduction for different particle sizes of corn stover-aqueous slurries in vertical upward flows could be useful during the design and selection of slurry pumps as well as in choosing the flow rate for onsite processing at biorefineries and pulp mills.

4.3.2 Comparison of frictional loss behaviour of different feedstocks in hydro transport through a vertical pipe section

4.3.2.1 Pressure drops at similar flow rates

The comparison of the frictional pressure drops of two different agricultural residue biomass feedstocks with respect to the slurry solid concentration at similar nominal velocities in vertical upward flows is illustrated in Figure 4.13.

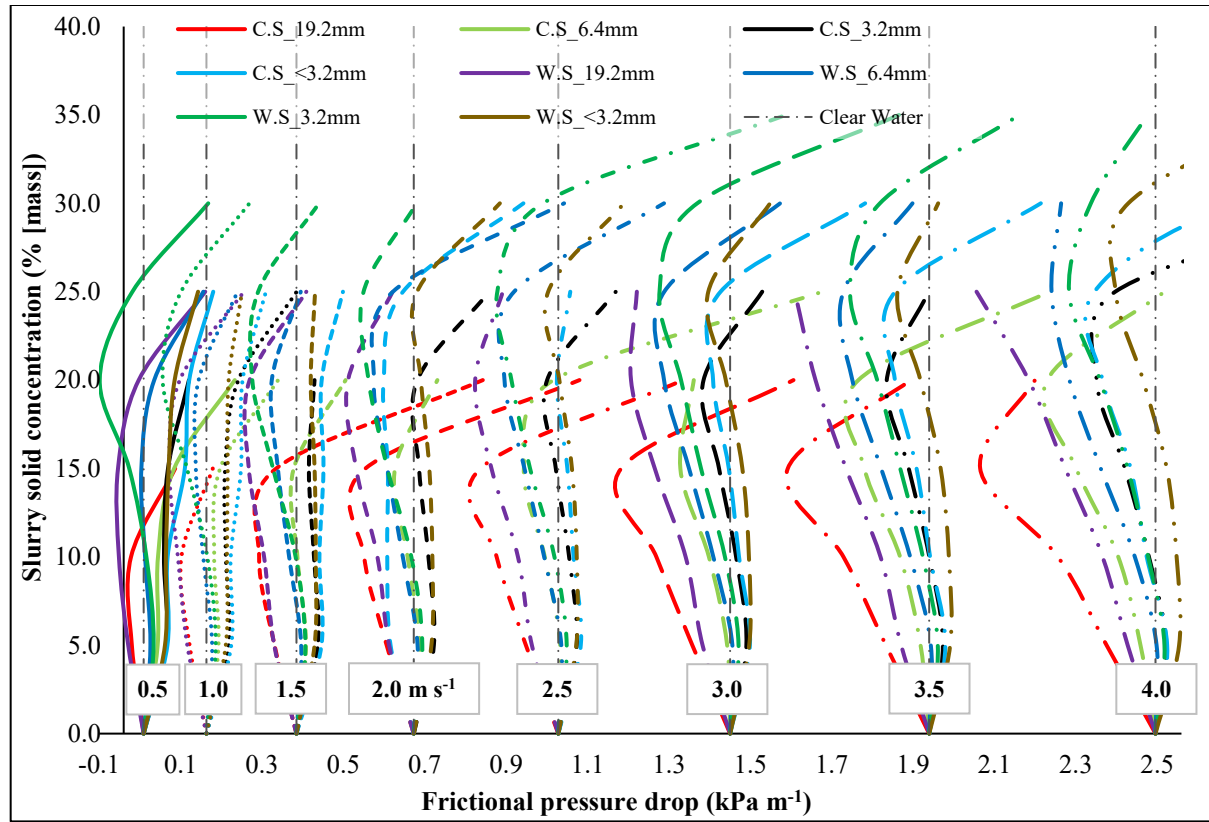


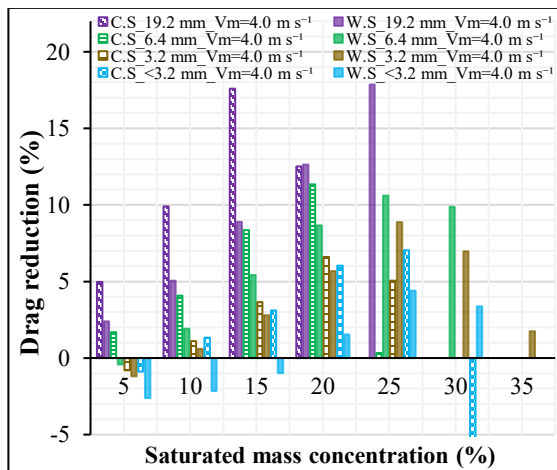
Figure 4.13: Slurry solid concentration versus frictional pressure drop at constant nominal velocities for 19.2 mm, 6.4 mm, 3.2 mm, and <3.2 mm corn stover (C.S) and wheat straw (W.S) particle slurries measured using the current experimental setup (the wheat straw slurry results were adopted from our earlier studies (Javed et al., 2022b; Javed et al., 2021)).

Given the inconsistency in the highest achievable bulk velocities specifically at higher C_m 's (i.e., 20-40%) for the slurries of all particle sizes from both feedstocks, we represented the frictional pressure drops at slurry nominal velocities with mutual intervals of 0.5 m s^{-1} (instead of actual slurry bulk velocities) in Figure 4.13. We found more inconsistencies in the highest achievable bulk velocities for corn stover than for wheat straw slurries. The highest achievable velocities for corn stover slurries, for instance, were found to be 3.65 , 4.18 , 4.29 , and 4.31 m s^{-1} for 19.2 mm, 6.4 mm, 3.2 mm, and <3.2 mm, respectively, when the $C_m = 20\%$, whereas for wheat straw slurries the highest achievable velocities were found to be 3.96 , 4.20 , 4.13 , and 4.01 m s^{-1} for 19.2 mm,

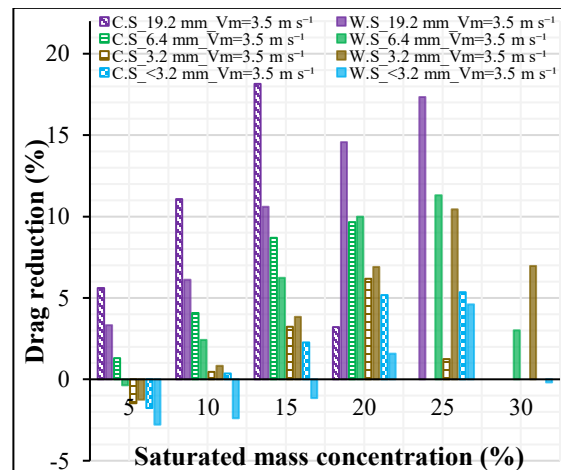
6.4 mm, 3.2 mm, and <3.2 mm, at 25%, 30%, 35%, and 40% mass concentrations, respectively. Corn stover slurries were found to be difficult to pump and consequently showed low maximum achievable velocities (section 4.3.1.1) compared to wheat straw slurries at higher mass concentrations despite having a similar particle size. This is because the highly concentrated corn stover slurries can act as a Bingham-like material exhibiting a large yield stress (Samaniuk et al., 2011). The frictional pressure drops at each nominal velocity were evaluated using second order polynomial expressions of each pressure drop curve of all the concentrations and particle sizes of corn stover and wheat straw slurries. One of the polynomial expressions representing the frictional pressure drop curve of the largest particle size of corn stover-water suspension when the $C_m = 20\%$ is shown in Figure 4.11 (a). For slurries at higher C_m 's, where it was not possible to obtain higher bulk velocities due to pump limitations, the corresponding pressure drop curves were extrapolated (using the corresponding polynomial expressions) up to a nominal velocity of 4.0 m s^{-1} to estimate their frictional pressure drops and are represented in Figure 4.13. Since the maximum achievable bulk velocity for corn stover slurries of the smallest particle size (used in the current investigation) is 1.81 m s^{-1} at $C_m = 40\%$, we represented the results up to $C_m = 35\%$, with minimal extrapolation. In Figure 4.13, only 8 data points out of 332 (i.e., approx. 2.5% of the complete data set) were obtained through extrapolation, wherein the actual bulk velocities were less than the corresponding nominal velocities by a maximum of 15% for corn stover and 7% for wheat straw slurries.

In Figure 4.13, the pressure drops for clear water are represented by the centred vertical lines at each nominal velocity ranging from $0.5\text{-}4.0 \text{ m s}^{-1}$. The regions to the left of each of the centred vertical lines represent the lower frictional pressure drops of slurries compared to water alone (i.e., they have drag-reducing characteristics) at any specific nominal velocity. At higher velocities ($\geq 1.5 \text{ m s}^{-1}$) up to certain mass concentrations, the pressure drops of corn stover-water slurries

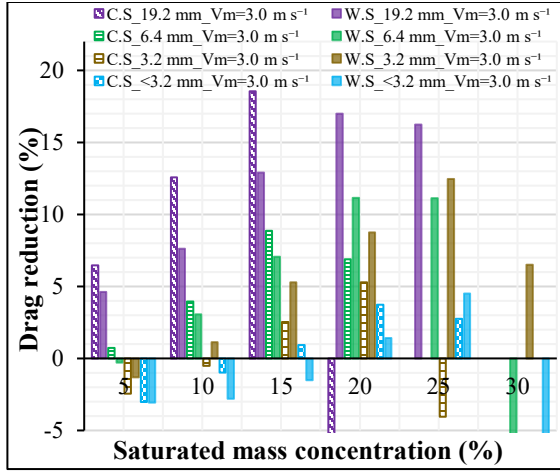
seem to fall into the low pressure region (unlike wheat straw) for both large particles. Further, this drop in the frictional pressure with respect to the clear water line increases with increases in C_m because of the increase in the particle-particle interaction (Bobkiewicz & Gauvin, 1965; Radin et al., 1975). More specifically, the deflection of the curves of corn stover suspensions of the largest particle size towards the low pressure region was the greatest among all the suspensions of both feedstocks for a specific range of concentrations and slurry velocities $\geq 1.5 \text{ m s}^{-1}$. Moreover, for the entire velocity range except 4.0 m s^{-1} , the corn stover suspensions of the largest particle size at a $C_m = 15\%$ exhibited more drag reduction than the corresponding wheat straw suspensions when the $C_m = 25\%$. All of these characteristics are associated with the complex nature of the ground material of corn stover with different particle shapes (shown in Figure 4.5 and Figure 4.6) and longer particles compared to wheat straw (see section 4.3.1.1). Further, an earlier study found that corn stover particles exhibit irregular surfaces and more longitudinal flexibility compared to wheat straw, which make them more effective in reducing the frictional pressure drop compared to water alone (Vaezi et al., 2013). Figure 4.14 shows the percentage drag reduction by all four particle sizes of corn stover and wheat straw slurries in vertical upward flows at several nominal velocities.



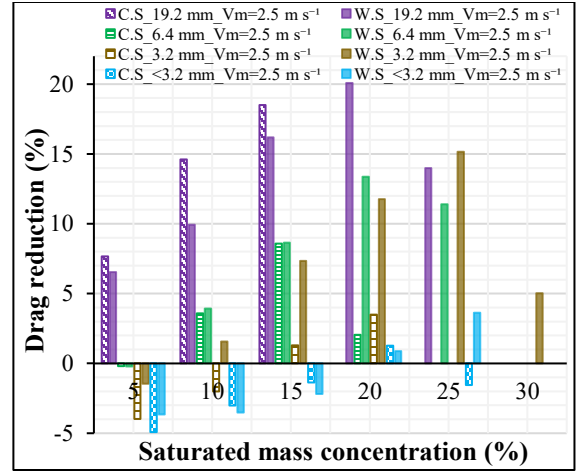
(a)



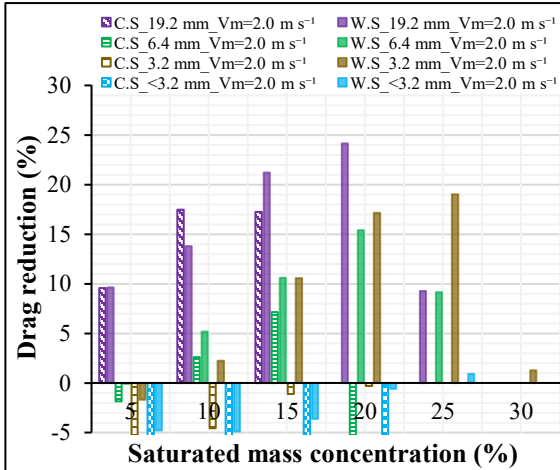
(b)



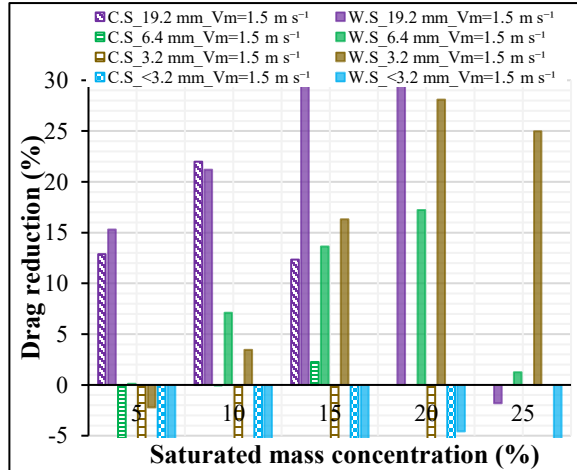
(c)



(d)



(e)



(f)

Figure 4.14: Drag reduction of different feedstocks of similar particle sizes of corn stover (C.S.)- and wheat straw (W.S.)-water slurries in vertical upward flows for a range of saturated mass concentrations (5-35%) and nominal velocities at (a) 4.0 m s^{-1} , (b) 3.5 m s^{-1} , (c) 3.0 m s^{-1} , (d) 2.5 m s^{-1} , (e) 2.0 m s^{-1} , and (f) 1.5 m s^{-1} . The wheat straw slurry results were adapted from our earlier work (Javed et al., 2022b; Javed et al., 2021).

The drag reduction of both feedstocks in two slurry velocity phases, higher (i.e., $\geq 2.5 \text{ m s}^{-1}$) and lower (i.e., $\leq 2.0 \text{ m s}^{-1}$), can be compared. In the first phase (i.e., slurry flows at nominal velocities

$\geq 2.5 \text{ m s}^{-1}$), corn stover-water suspensions of all particle sizes except 3.2 mm exhibited more drag reduction than the corresponding wheat straw slurries up to specific C_m values (Figure 4.14 [a-d]). The largest difference in the drag reduction was found in the corn stover slurries with the largest particle size when the $C_m = 15\%$. However, an unusual effect was observed for the 3.2 mm particle size, which showed slightly higher drag reduction for corn stover than for wheat straw of the same size at the highest velocity and a $C_m \leq 20\%$. For nominal velocities of $1.5\text{--}3.5 \text{ m s}^{-1}$, the drag reduction of wheat straw-water slurries of a 3.2 mm particle size was always above that of corn stover slurries. In the 2nd phase (i.e., slurry flows at nominal velocities $\leq 2.0 \text{ m s}^{-1}$), most of the wheat straw-water slurries (Figure 4.14 [e] and [f]) showed more drag reduction than the corresponding slurries of corn stover except in a few cases of the largest particle size. The reason for this is the development of different aqueous slurry flow regions for both feedstocks for the same particle size and concentration. It was found that most of the wheat straw-water slurries exhibited transition flow even at lower velocity ranges in vertical upward flows (Javed et al., 2022b; Javed et al., 2021), whereas corn stover-water slurries were found to be mostly in the plug flow at low velocity except for a few concentrations of the largest particle size (shown in Figure 4.8). These results show that corn stover slurries behave differently in a certain range of concentrations and velocities than the corresponding wheat straw slurries in vertical upward flows. One of the reasons could be the higher apparent viscosity of corn stover suspensions compared to wheat straw, particularly for small particles (i.e., 3.2 and $<3.2 \text{ mm}$) (Vaezi et al., 2014). The apparent suspension viscosity of a fiber suspension depends on its particle size and solid concentrations. The suspension viscosity increases with decreasing particle size and has a linear relationship with lower solid concentrations (Djalili-Moghaddam & Toll, 2006). However, the apparent suspension viscosity has also been shown to have a cubic relationship to higher solid

concentrations (Powell et al., 2001). Therefore, it is presumed that for a specific range of concentrations, the apparent suspension viscosity of corn stover suspensions (particularly for nominal particle sizes of 3.2 and <3.2mm) is high, which decreases their drag reduction capabilities. However, at higher velocities, some of these suspensions show more drag reduction than wheat straw. This variability in the consistency of corn stover-water slurry flow behaviour versus that of wheat straw, particularly at low velocities and higher mass concentrations and higher velocities, needs to be studied further through rheological measurements.

4.3.2.2 Critical mass concentration for maximum drag reduction $(C_m)_{cr}$

Figure 4.15 shows $(C_m)_{cr}$'s for slurries of four particle sizes from the two feedstocks (corn stover and wheat straw) for slurry nominal velocities of 1.0-4.0 m s⁻¹.

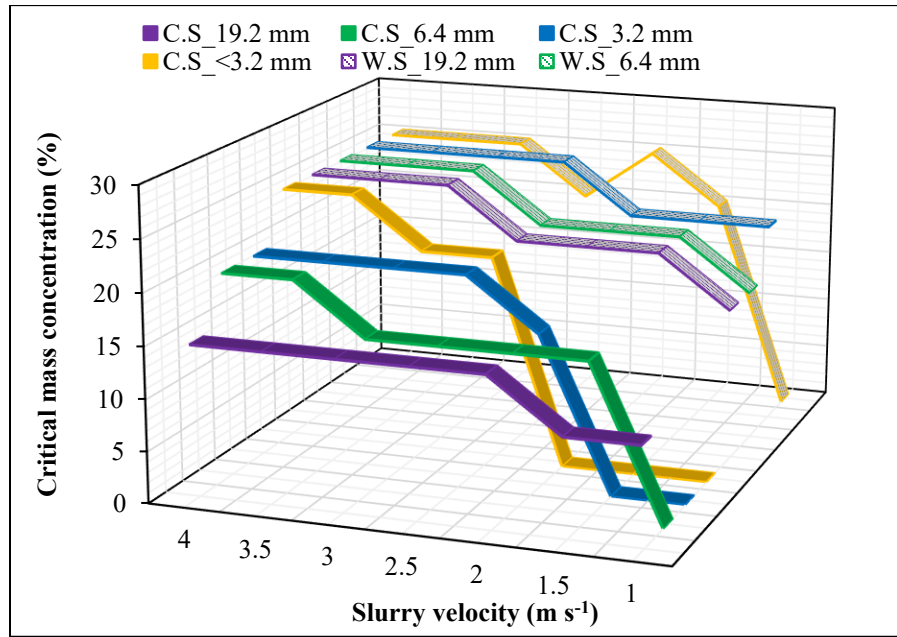


Figure 4.15: Critical mass concentration versus slurry bulk velocity for vertical upward flows of corn stover (C.S.)- and wheat straw (W.S.)-water suspensions of 19.2 mm, 6.4 mm, 3.2 mm, and <3.2 mm.

In general, the $(C_m)_{cr}$ for every particle size except the <3.2 mm corn stover-aqueous slurries was found to be less than that of wheat straw-water slurries for most nominal velocities (Figure 4.15). Further, we observed a variation in $(C_m)_{cr}$ with respect to the particle sizes of corn stover slurries specifically at the higher nominal velocities of 3.0-4.0 m s⁻¹, at which the $(C_m)_{cr}$ of these slurries increases with a decrease in particle size. A few studies explain the variation in the $(C_m)_{cr}$ of fiber suspensions with velocity and fiber length. Kerekes (1971) observed a $(C_m)_{cr}$ while investigating the behaviour of inelastic fiber suspensions in turbulent flows through a vertical pipe.

The study found that the $(C_m)_{cr}$ was directly linked with suspension velocity and fiber aspect ratio. An increase in suspension velocity for a particular fiber length increased the value of the $(C_m)_{cr}$, whereas at a specific suspension velocity, an increase in the fiber length caused the $(C_m)_{cr}$ to decrease. Yet Kerekes (1971) also found an abrupt decrease in the drag reduction of the fiber suspensions just after the critical concentration, at which point the behaviour of the suspensions turned into drag increase. However, the shorter fibers did not follow this trend and always exhibit drag reduction.

In the current study for agricultural residues, most of the suspensions exhibit drag reduction after their corresponding $(C_m)_{cr}$'s. Only few of the biomass suspensions demonstrated an abrupt drag increase just after their $(C_m)_{cr}$'s, as shown in Table 4.4. Further, for wheat straw-aqueous slurries, the values of $(C_m)_{cr}$ were similar for velocities of 3.0-4.0 m s⁻¹. These results demonstrate the dependence of $(C_m)_{cr}$ on feedstock type, particle size, and slurry velocity.

Table 4.4: The suspensions of agricultural residue biomass in vertical upward flows exhibiting abrupt drag increase just after their $(C_m)_{cr}$'s

Feedstock	Nominal particle size (mm)	~19.2	~6.4	~3.2	<~3.2
Corn stover	Suspension velocity (m s^{-1})	1.5-3.0	1.5-2.0	2.5-3.0	3.0
Wheat straw		—	3.0	—	3.0

The zero values of $(C_m)_{cr}$ at nominal slurry velocities in both feedstocks on the graph (Figure 4.15) means that there was no drag reduction for this range of conditions.

4.4 Conclusion

The effect of feedstock type, particle size, and flow conditions on the frictional pressure drop of water-based agricultural residue biomass slurry flows through a vertical pipe was experimentally investigated. Over the entire range of flow rates, corn stover-aqueous slurries of the largest particle size (19.2 mm) exhibited the transition flow region at low mass concentrations of 5-10%, whereas the other suspensions of all the particle sizes (except 19.2 mm at a $C_m = 15\%$) demonstrated either the plug and transition flow regions together or the plug flow region alone because of high biomass loadings (i.e., $C_m = 25\text{-}40\%$). Drag reduction in corn stover slurries increases with an increase in particle size and was highest (32%) for the largest particle size at a $C_m = 10\%$ and a slurry velocity of 1.0 m s^{-1} . Drag reduction for all corn stover suspension particle sizes reached a plateau at a specific concentration limit $((C_m)_{cr})$ and then started to decline. This limiting concentration of maximum drag reduction $(C_m)_{cr}$ was exclusively dependent on particle size and flow rate ranges. The onset velocity of drag reduction appeared to be a function of concentration and particle size

and reached its lowest value (threshold) with an increase in both concentration and particle size in the corn stover suspension. Beyond this threshold for a specific particle size, the onset velocity increases with an increase in the concentration of the corn stover suspension because of the strong fiber networks in the large fiber contact numbers.

Corn stover-water slurries behave differently than wheat straw slurries for a certain range of concentrations and velocities in vertical upward flows. For velocities $\geq 2.5 \text{ m s}^{-1}$, the corn stover suspensions of all the particle sizes (except 3.2 mm) exhibited higher drag reduction than the corresponding slurries of wheat straw for a certain range of C_m , and the greatest difference in drag reduction was observed in the larger particles (19.2 mm) of corn stover at a $C_m = 15\%$. However, for lower to mid-range slurry velocities $\leq 2.0 \text{ m s}^{-1}$, wheat straw suspensions were better able to reduce drag than the corn stover with a few exceptions in the largest particles. The $(C_m)_{cr}$ was lower for most of the corn stover suspensions than for the corresponding wheat straw suspensions except for fine particles. Beyond the $(C_m)_{cr}$, some suspensions in both feedstocks showed an abrupt drag increase at certain flow conditions with higher variability in the corn stover. Corn stover-aqueous suspensions were found to be more effective in reducing drag than wheat straw at specific flow conditions in vertical upward flows. The variations in the onset velocity of drag reduction, $(C_m)_{cr}$, and threshold concentration for minimum onset velocity with respect to the particle type, size, and slurry concentrations suggest it is worth looking at the corresponding results for larger diameter pipelines with higher D/D_{50} of 10-20 with respect to the largest nominal particle size (i.e., 19.2 mm) of corn stover used in the current investigation. The novel information obtained in this study can assist in finding the optimum flow conditions for the vertical hydro-transport of agricultural residue biomass, which is an important part of the design and operation of a large-scale integrated pipeline network for a commercial biorefinery.

Chapter 5: The Development of Empirical Correlations to Understand the Frictional Behaviour of Aqueous Biomass Slurry Flows in Vertical Pipes⁴

5.1 Introduction

Rapid developments in modern technology due to human needs, population growth, increased transportation, and industrialization have dynamically increased environmental problems as well as energy crises all over the world. The major role-players in this regard are the non-renewable fossil fuels (i.e., crude oil, natural gas, and coal) in the current global energy system model. On one hand, global energy consumption's inordinate dependence (i.e., more than 85%) on fossil fuels has increased the risk of the depletion of these fuels in the near future (Halder et al., 2019; Vohra et al., 2014). In addition, the excessive use of fossil fuels to meet global energy demand has severely damaged the environment around the world through the emissions of greenhouse gases (GHGs) (Goldemberg, 2008). Over the past 70 years, CO₂ emissions, which make up approximately 76% of the total GHGs, have increased sevenfold (Center for Climate and Energy Solutions, 2023). Replacing non-renewable liquid fuels with some renewable biofuels (i.e., bioethanol, biodiesel, biohydrogen, etc.) obtained from biomass (e.g., agricultural crops and wastes, wood and waste obtained from wood processing, municipal solid waste etc.) could be the most reliable, carbon-neutral (Pootakham & Kumar, 2010), and sustainable way to reduce the petroleum-based fuel consumption in the transportation sector. However, there are challenges in

⁴ A version of this chapter has been published as Javed K, Kurian V, Kumar A, "The development of empirical correlations to understand the frictional behavior of aqueous biomass slurry flows in vertical pipes", *Journal of American Society of Agricultural and Biological Engineers* (ASABE), 2023, 66(4), 969-986.

increasing bioethanol production to a commercial scale using ARB (wheat straw [W.S] or corn stover [C.S]) to compete with the capacity of plants producing fossil fuels (Aden et al., 2002; Kumar et al., 2005a), the major one being the high transportation cost of delivering biomass bales by ground transport (trucks, rail, etc.) from farms to biorefineries (Ruth, 1999).

The transportation cost of field/forest-based lignocellulosic biomass increases substantially with biorefinery capacity because more biomass feedstock needs to be transported as the size of the conversion plant increases (Kumar et al., 2003; Sokhansanj et al., 2002). Kumar et al. proposed a novel solution to hydro-transport agricultural and forest residue biomass through a long-distance pipeline network from farms to biorefineries instead of using ground transportation (Kumar et al., 2005a). That study used pre-established correlations for the frictional pressure drop of wood chip-water slurries in its techno-economic assessment (Kumar et al., 2004, 2005b). Later, Luk et al. designed and fabricated a laboratory-scale closed pipeline loop and experimentally found the mechanical feasibility of hydro-transport of ARB. The authors observed that ARB slurries behave in a different way than wood chips during pipeline hydro-transport (Luk et al., 2014). Vaezi et al. further enhanced this research for different feedstocks, particle sizes, and slurry solid mass concentrations of ARB and claimed through experimental evidence and techno-economic analysis that pipelining chopped aqueous-based ARB slurries at specific mass concentrations will significantly reduce the transportation cost of the feedstock required for large-scale biofuel production that can compete with the production capacity of fossil fuel-based plants (Vaezi et al., 2014; Vaezi et al., 2015).

In their techno-economic study, Vaezi et al. proposed a novel integrated pipeline system that would involve short hauls of biomass bales over a distance of 2-5 km from each bio farm to its nearest preprocessing facility (each containing a mixing tank, a commercial mill, and a pump), booster

station facility, a main pipeline pumping facility, and a main long-distance pipeline extending 200-300 km from the main pump station to the biorefinery (see Figure A3 in Appendix A) (Vaezi et al., 2015). At the preprocessing facility, a commercial mill will chop the biomass bales to the required particle sizes. The chopped material will then be mixed with water in a mixing tank to form a slurry of known mass concentration. The pump will deliver this slurry to the branch line connected to the main pipeline pumping station via the booster pump station(s). Vaezi et al. proposed a specific number of booster stations to maintain the slurry velocity that could be lowered due to friction and the addition of slurry coming from other preprocessing facilities scattered within a specific radius covering a definite number of bio farms. They used the pipeline's transport capacity and the slurry's speed to determine the pipeline's diameter. The number of booster stations was estimated by dividing the total pressure drop along the pipeline by the total head produced by the main pump and the booster pumps (Vaezi et al., 2015). The technical parameters and associated economics can be seen in Vaezi et al.'s paper and are outside the context of the present paper. The pressure drop correlation of ARB slurry flows through the pipeline used by Vaezi et al. was based on experiments conducted in the horizontal pipeline (Vaezi & Kumar, 2014a). The topography of a long-distance pipeline route for any specific region and on-site processing at biorefineries might involve horizontal, vertical, and inclined pipe sections. Therefore, the pressure drop correlations of biomass slurry flow for different pipe positions other than horizontal need to be investigated to predict the exact size and cost of various instruments, pipe sections, and the associated logistics involved in an integrated long-distance pipeline network.

Agricultural residue is a naturally occurring and unprocessed form of biomass feedstock. The aqueous slurries of chopped ARB flowing through a pipeline behave similar to different kinds of synthetic (nylon, polyester, rayon, acrylic, and microfibers, etc.) and natural fiber suspensions

(e.g., wood pulp fiber suspension processed by some mechanical or chemical means) (Vaezi et al., 2014). Duffy developed a frictional pressure drop correlation for wood pulp fiber suspension flows through a horizontal pipe section (Duffy, 1989). This research was a continuation of the previously proposed correlations by Duffy et al. and Moller (Duffy et al., 1974; Moller, 1976). Duffy proposed this correlation with minor differences in choosing the independent variables with respect to the three flow regions (1st region: up to the maximum velocity (v_{max}); 2nd region: up to the onset velocity of drag reduction (v_{OD}); and 3rd region: from v_{OD} onwards) that appear on a logarithmic plot between the head loss and slurry bulk velocity (v_m). For the two regions in the plug flow up to v_{OD} , the pressure drop correlation was found to be a function of v_m , concentration, and pipe diameter (D). A constant term (K) and the exponents of each independent variable introduced in these correlations were obtained based upon the type and flow conditions of the suspensions used in his study. For the third region beyond v_{OD} , Duffy modified the correlation based upon v_m and D only and left out the fiber concentration because in practice a very low fiber concentration is used while operating at the wet end of a typical paper machine in pulp and paper industry (Duffy, 1989). The correlation presented by Duffy for the plug flow region between v_{max} and v_{OD} did not consider the lower middle point, i.e., onset of turbulence in the water annulus. Further, for the plug flow region up to v_{max} , Duffy considered pipe roughness to be an important factor influencing the head loss curve in addition to the various pulp flow conditions.

Later, Ventura et al. introduced four new independent correlations for frictional pressure drops through horizontal pipes of different roughness for the flow region beyond the point of the “onset of turbulence in the water annulus” for four industrial pulp suspensions (eucalypt bleached Kraft pulp, eucalypt [90%] + pine [10%] bleached Kraft pulp, pine unbleached Kraft pulp, and recycled pulp) (Ventura et al., 2008). The ranges of fiber lengths (weighted mean), pulp consistencies (%)

mass), v_m , and ID's of pipes used in their study were 0.6-2.56 mm, 0.1%-4.3% (mass), 0.38-6.0 m s⁻¹, and 38-107 mm, respectively. The developed correlations for each wood pulp suspension were found to be a function of consistency, v_m , and pipe ID except for pine pulp suspensions, for which the corresponding correlation contained only the v_m and the consistency of the suspension. The reason for this is the limitation of the experimental setup in attaining the highest possible consistencies of pine pulp suspensions for all the pipe diameters tested. All of the correlations contained second-order polynomials with all the possible combinations including single effects, double interactions, and squares of each corresponding independent variable. Ventura et al. (2008) revisited and modified Duffy's correlation for the plug flow region before the v_{max} for all of the wood pulp suspensions used in their studies and found no significant effect from pipe roughness on the pressure drop models, but fiber characteristics and process conditions seemed to have a strong influence on the constant term (K). They also modeled the v_{max} and v_{wt} (suspension velocity corresponding to the onset of turbulence in the water annulus) except the v_{OD} for each type of fiber and found both the velocities to be strongly correlated with the suspension consistency (Ventura et al., 2008). Vaezi and Kumar established a single empirical correlation for the experimentally obtained frictional pressure drops (837 data points) in turbulent flows of two ARB feedstock (C.S and W.S)-water slurries through a horizontal pipe section with a 50 mm ID, 25 m long closed pipeline loop (2014a). They used range of nominal particle sizes, saturated slurry solid mass concentrations (C_m 's), and v_m 's (<3.2-19.2 mm, 5%-40%, and 0.5-5.0 m s⁻¹, respectively). In addition to v_m and C_m , Vaezi and Kumar introduced a particle shape factor corresponding to each of the nominal particle sizes of both ARB feedstocks to consider the particle shape characteristics and physical properties in the proposed empirical model. The developed correlation

was based on the polynomial of order four that included all the interactions of independent variables (Vaezi & Kumar, 2014a).

Our recent studies explored the frictional behaviour of ARB-water slurries in vertical upward flows, and it is well understood (Javed et al., 2022a, 2022b; Javed et al., 2021). A series of laboratory-scale experiments were conducted on the upward flow of aqueous suspensions of two different ARB feedstocks (W.S and C.S) in a transparent vertical PVC test section that was part of 29 m long, 50 mm inside diameter closed-circuit pipeline facility. The C_m , particle size (nominal size), and v_m of the slurries range from 5%-40%, <3.2-19.2 mm, and 0.5-4.3 m s⁻¹, respectively. It was demonstrated that aqueous-based slurries of ARB generally show three distinct regions, plug flow, transition flow, and turbulent flow (in transition and turbulent flow regions, the frictional pressure drops of biomass slurry are always below the water curve). The development of these regions was found to be a strong function of C_m , particle size, v_m , and the feedstock (Javed et al., 2022a, 2022b; Javed et al., 2021). The delivered concentrations (C_{md} 's) were also measured at various prepared concentrations (C_{mp} 's) and v_m of all the particle sizes of W.S slurries during vertical upward flows and the concentrations were found to be within a 10% difference (Javed et al., 2022b; Javed et al., 2021). One of the reasons behind this small difference in concentrations is the buoyant nature of these types of suspensions. Further, the v_{OD} for both C.S and W.S was found to be a strong function of particle size and C_m (Javed et al., 2022a).

A considerable number of studies is available on modeling the pressure drops of classical solids (e.g., sand, pebbles, perspex, polystyrene, coal etc.)-water mixtures during upward flows in vertical pipes (Bartosik, 1996, 2010; Matousek, 2005; Miedema, 2015; Newitt et al., 1961; Shook & Bartosik, 1994; Talmon, 2013). However, the frictional behaviour of these classical solids-water slurries is entirely different than the aqueous slurries of ARB flowing in pipes. The v_m , particle

size, and C_m enhance the frictional pressure drop of classical solids-water slurries more than pure water. At increasing v_m , φ_p , and C_m , the ARB aqueous slurries' frictional pressure drop decreases less than water's (the phenomenon of drag reduction) (Javed et al., 2021). Therefore, empirical correlations of classical solids-water mixes should not be used as a baseline when modeling biomass-water slurries. A few studies model the flow behaviour of wood pulp and synthetic fiber suspensions in vertical upward flows, but they looked into different aspects of suspension behaviour. Seely modeled the frictional behaviour of wood fiber suspensions of concentrations of 0.05%-0.5% (mass) in a damped turbulence flow region during their vertical upward flows through circular pipes 36 mm and 48 mm in diameter (1968). An empirical correlation was established for the Von Karman constant in terms of the friction factor of the suspension in the damped turbulence region. The drag reduction effect was found to be a strong function of fiber aspect ratio (φ_p) and mass concentration (Seely, 1968). Kerekes developed a simple correlation for the turbulent drag reduction of nylon fiber-water suspensions during upward flows in a vertical pipe section with a 50 mm ID for v_m , suspension consistencies, and φ_p of 1.2-3.0 m s⁻¹, 0.01%-0.07% (mass), and 12-74, respectively (1971). The correlation for turbulent drag reduction was found to be strongly dependent on the φ_p and the consistency (Kerekes, 1971). Ogawa et al. conducted an experimental study for the vertical upward flows of wood pulp fiber-water suspensions in the laminar plug flow region and proposed a correlation for the radial distribution of the suspension viscosity (Ogawa et al., 1990). Although we established basic understandings for the vertical upward flows of ARB-water slurries in earlier experimental studies, to the best of our knowledge, the frictional behaviour of ARB-water slurries in vertical upward flows has not been modeled.

The principal objective of the current research is to use experimental data on frictional pressure drops for ARB (W.S and C.S)-water slurry flows through a vertical pipe section (50.8 mm ID) of

a 29 m-long closed-circuit pipeline facility obtained during a large course of experiments and to propose (1) an empirical correlation for the pressure gradient of biomass slurry as a function of material type, φ_p , C_m , and v_m and (2) a correlation for v_{OD} as a function of C_m for various particle sizes of W.S and C.S.

5.2 Materials and method

5.2.1 Feedstock preparation

Two different ARB feedstocks, W.S (*Triticum sativum*; dry stalks of wheat) and C.S (*Zea mays*; leaves and stalks of corn), were obtained from Northern and Southern Alberta farms in the form of bales. The dry bales were chopped with a commercial knife mill (SM 100; Retsch Inc., Surrey, BC, Canada). The ground material was then classified using a commercially available classifier (BM&M Inc., Surrey, BC, Canada) into four groups with nominal sizes of 19.2, 6.4, 3.2, and <3.2 mm (sizes from (Vaezi et al., 2013)). Both the grinding and the classification of the biomass were done in the laboratory. The wet basis moisture contents (MCs) of the classified material of both feedstocks were measured using ASABE S358.3 standards (ASABE, 2012). Four samples of random particle sizes (each weighing at least 25 g net weight) were picked and dried in an oven for 24 h at 105 °C to evaluate the feedstock's initial MC. Then the saturated densities of the slurries of both feedstocks were measured using their corresponding saturated particle densities, which were estimated using ASTM C127 standards (ASTM, 2015). A perforated cylinder with the same height and diameter (i.e., 150 mm) was loosely filled by saturated biomass and then weighed in both air and water. The difference in these weights gave the buoyant force against the material and consequently the saturated density of the biomass.

5.2.2 Particle size and shape analysis

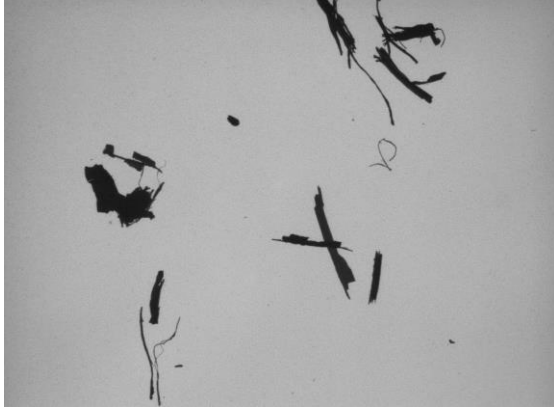
In our recent study (Javed et al., 2022a), particle size distribution (PSD) and shape analysis of all four size groups (nominally <3.2-19.2 mm) of both ARB feedstocks by dynamic image analysis (where the entire sample itself moves during measurements) using a Camsizer (Horiba) was conducted. Vaezi et al. evaluated the PSD of similar ARB through static image analysis on a flatbed scanner for a population size of only 500-2300 particles at nominal particle sizes of 19.2-<3.2 mm (2013). The results obtained from the Camsizer (which is faster and more flexible than a flatbed scanner) are quite promising (compared to Vaezi et al.'s static image analysis) because of the large population size (0.05-3.6 million particles depending on the fineness and type of feedstock) of the samples of the four particle groups. The work included sampling, subsampling, and dynamic digital image processing to obtain the PSD of the biomass particles using a Camsizer, as described in our recent study (Javed et al., 2022a). Figure 5.1 shows microscopic images of the largest and smallest nominal sizes of W.S and C.S particles captured by high-speed Camsizer cameras.



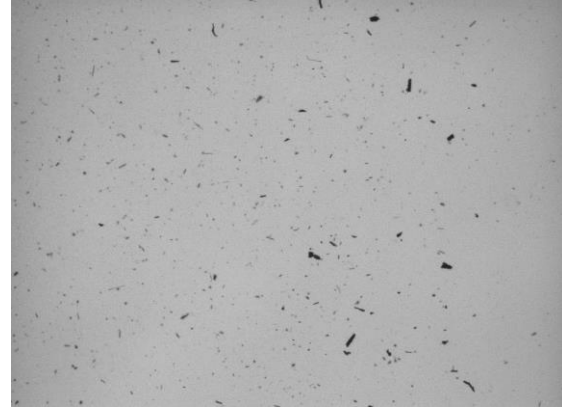
(a)



(b)



(c)



(d)

Figure 5.1: Microscopic images (not to scale) captured by high-speed digital Camsizer cameras for wheat straw particles of nominal sizes (a) 19.2 mm, (b) <3.2 mm and corn stover particles of nominal sizes (c) 19.2 mm, (d) <3.2 mm.

It can be observed from Figure 5.1 that knife-milled W.S is composed of rectangular rib-like particles, whereas C.S consists of several types of particles of non-uniform and complex shapes. In an earlier study, we categorised the ground C.S particles of a 19.2 mm nominal size into seven different sub-categories (rib-like particles with plain surfaces, rib-like particles with rough surfaces, hair-like particles, flake-like particles, wide flake-like particles, irregular-shaped thick particles, and mixed form particles) based on their physical appearance (Javed et al., 2022a). Table 5.1 shows the particle morphology of both ARB feedstocks used in the current study. The variables D_{90} , D_{50} , and D_{10} shown in the table indicate the 90th, 50th, and 10th percentiles obtained from the cumulative distributions for both the Feret and shortest cord diameters, and X_{ig} , and σ_{ig} are the graphic mean and standard deviation for the corresponding dimensions (i.e., Feret or shortest cord diameters) of the particles.

Table 5.1: Physical properties of wheat straw, corn stover, and classical solids particles used in experiments (reprinted from Javed et al. [2022a] with permission from Elsevier)

Feedstock		Wheat straw				Corn stover				Fine sand ^a
Nominal particle size (mm)		~19.2	~6.4	~3.2	<~3.2	~19.2	~6.4	~3.2	<~3.2	
d_{FE_max} (mm)	D_{90}	14.65	6.04	4.13	2.72	15.07	10.00	4.55	2.37	—
	D_{50}	8.53	4.85	3.63	2.19	9.37	6.00	4.39	1.66	0.103
	D_{10}	6.68	3.58	3.39	0.88	7.01	4.74	3.91	0.58	—
	X_{ig}^b	9.37±	4.84±	3.68±	1.97±	9.90±	6.64±	4.13±	1.55±	—
	$\pm \sigma_{ig}^c$	3.24	0.93	0.34	0.73	3.14	1.93	0.35	0.69	—
	Max.	28.09	11.44	9.00	9.63	25.52	16.73	10.55	4.96	—
	Min.	5.26	3.35	0.80	0.66	2.21	3.90	1.92	0.38	—
d_{c_min} (mm)	D_{90}	5.23	2.87	2.22	1.32	6.49	4.77	2.54	1.24	—
	D_{50}	2.19	1.52	1.29	0.71	3.49	2.40	1.20	0.70	—
	D_{10}	1.06	0.59	0.57	0.27	1.50	0.82	0.59	0.29	—
	X_{ig}	2.34±	1.37±	1.22±	0.64±	3.47±	2.26±	1.30±	0.63±	—
	$\pm \sigma_{ig}$	1.62	0.87	0.64	0.4	1.97	1.57	0.75	0.36	—
	Max.	10.57	6.14	4.86	4.61	10.70	8.55	5.57	2.55	—
	Min.	0.38	0.28	0.12	0.14	0.24	0.24	0.08	0.15	—
Aspect ratio (φ_p)		9.09	8.70	7.52	3.29	6.10	7.81	7.30	2.17	—
Initial density (kg m ⁻³)		1026±10				1169±10				2500
Saturated density (kg m ⁻³)		1050±10				1048.73±10				—
Wet basis mass content (initial) (%)		6.5±0.5				8.0±2.0				—
Wet basis mass content (saturated) (%)						82±0.5				—

^aTarget Products, AB, Canada; Material grade: LM-125

^b $X_{ig} = [(D_{16} + D_{50} + D_{84})/3]$, Graphic mean (Vaezi et al., 2013)

^c $\sigma_{ig} = [\{(D_{84} - D_{16})/4\} + \{(D_{95} - D_5)/6.6\}]$, Graphic standard deviation (Vaezi et al., 2013)

5.2.3 Experimental setup

The schematic of the experimental setup used in the current research is shown in Figure 5.2.

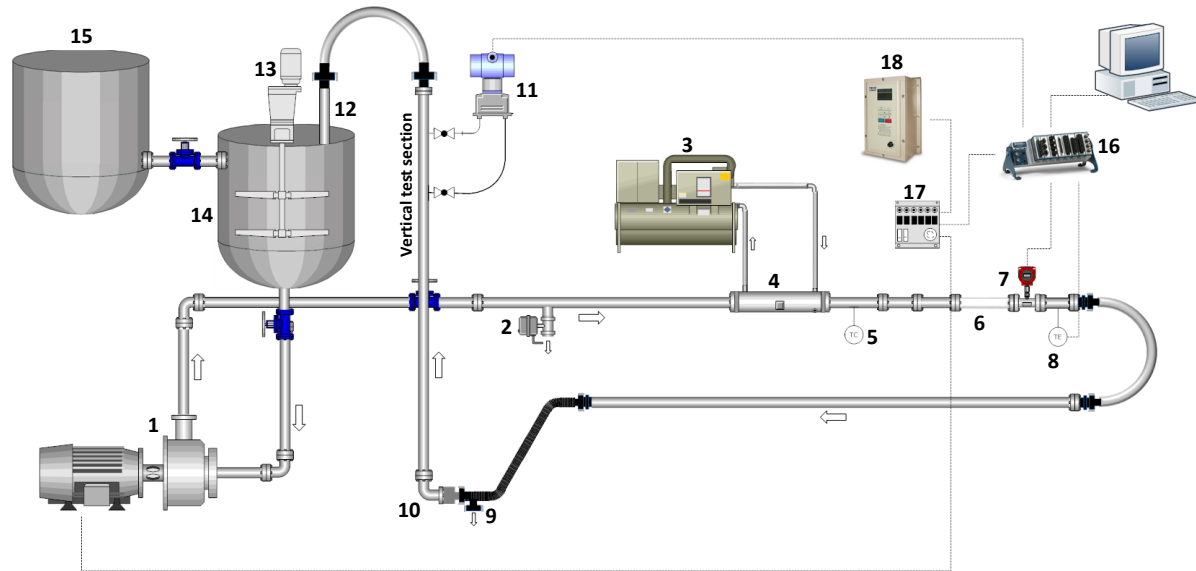


Figure 5.2: Schematic of the experimental setup: (1) centrifugal slurry pump, (2) drain valve-1, (3) glycol chiller, (4) counter-flow heat exchanger, (5) thermocouple, (6) flow visualisation section, (7) magnetic flow meter, (8) temperature sensor, (9) drain valve-2, (10) 90° bend, (11) differential pressure transmitter, (12) return pipe, (13) mixer with double impeller, (14) mixing tank, (15) water supply tank, (16) data logger, (17) watt transducer, (18) variable frequency drive.

The setup consists of a 29 m long, 50 mm inside diameter (ID) closed-circuit pipeline with Schedule 40 carbon steel and PVC transparent pipe sections, a centrifugal slurry pump (CD80M; Godwin Pumps Ltd., Bridgeport, NJ, USA) coupled with a 7.45 kW electric motor (CC 068A; Madison Industrial Equipment, Vancouver, BC, Canada) to pump the biomass slurry, a heat exchanger (KEZA030H8; KeepRite Refrigeration Corp., ON, Canada) to maintain the slurry

temperature around 12°C-15°C, a flow visualisation section, a magnetic flow meter (FMG-424; Omega Eng., Stamford, CT, USA) to measure the slurry velocity (v_m), a temperature sensor (RTD-E; Omega Eng., Stamford, CT, USA) to measure slurry temperature, semi-circular and 90° pipe bends, flexible PVC pipe sections, a highly accurate differential pressure transmitter (DTP) (FKCT22V55; Fuji Electric Ltd, France) with a range of 0-6 kPa and accuracy of $\pm 0.04\%$ (of the adjusted span) connected to a $10D$ (D is the ID of the pipeline) span (L) of a 2.8 m long vertical pipe section through copper tube impulse lines (ID = 9.5 mm) to measure the slurry pressure drop, a conical mixing tank of 0.8 m diameter and 455 L capacity connected to a 0.37 kW double impeller mixer (EV6P50M; Lightning Inc., Rochester, NY, USA) for mixing the slurry, a watt transducer (PC5; Flex-Core, Columbus, OH, USA) to measure the power consumption of the slurry pump motor, and a 14.91 kW variable frequency drive (VFD) controller (MA7200-2020-N1, TECO-Westinghouse Co., Round Rock, TX, US) to change the rotation of the slurry pump induction motor. The pressure difference sensed by the DPT through high- and low-pressure impulse lines that use water as a pressure sensing fluid was converted to an electrical output signal of 4-20 mA. All the output signals of 4-20 mA obtained from the DPT, magnetic flow meter, temperature sensor, and watt transducer were recorded at a rate of 100 data s⁻¹ on a data-acquisition system that has a current excitation module (NI9219; National Instrument Corp., Austin, TX, USA) with four channels and a data-acquisition program (LabView V.9.0.1f2; National Instrument Corp., Austin, TX, USA). All the instruments were located at sufficient lengths upstream or downstream of any flow disturbance to ensure flow field recovery. For instance, a magnetic flow meter was set $200D$ downstream of the slurry pump. Moreover, the DPT was installed with the vertical pipe section at approximately $42D$ downstream of the 90° bend. Based upon the literature review, this distance (i.e., $42D$) was quite satisfactory to suppress the effect of secondary flows

(Enayet et al., 1982; Kalyanraman et al., 1973; Kim et al., 2014) and develop smooth velocity profiles (Hellström et al., 2013) downstream of the 90° bend. Further information on the heat exchanger and the slurry pump with the electric motor used in the current experimental setup can be found in our other work (Javed et al., 2022b; Vaezi & Kumar, 2014b).

5.2.4 Slurry preparation and pressure drop measurements

The entire slurry loop was filled with water up to the desired level in the mixing tank and deaerated by continuous water circulation for several minutes with the slurry pump at full speed. The impulse lines of the DPT were flushed and filled with clear water to remove contamination and air bubbles from the lines for accurate pressure drop measurements. As the clear water (with negligible air) was circulated through the closed pipeline loop, the mixer operated at moderate speed to avoid cone formation on the water surface inside the tank. At this stage, the pre-measured amount of a specific particle type and size of ARB was gradually added to the mixing tank to prepare a biomass-water slurry of the desired C_{mp} , and the slurry was continuously circulated through the loop for 10-18 h (depending on particle type, size, and concentration) until it became stable (i.e., fully saturated) at the highest achievable C_{mp} . The highest achievable concentrations of biomass slurries for both feedstocks were 40%, 35%, 30%, and 25% for the <3.2, 3.2, 6.4, and 19.2 mm particle sizes, respectively, and were typically associated with the limitations of the slurry loop with the small inside diameter of the pipe, as we found in earlier studies (Javed et al., 2021; Vaezi et al., 2014). ARB has a tendency to absorb moisture when water is added (Luk, 2010; Mohamadabadi, 2009); as a consequence, its rheology consistently changes during pumping unless the slurry becomes stable with a saturated MC of approximately 82% for the suspended biomass particles (Vaezi et al., 2014). In stable condition, both the pressure and velocity curves of the slurry become smooth and almost parallel to the x-axis, shown in Figure 5.3 (a). The stability in the

biomass-water slurry was checked by continuously monitoring its pressure drop and velocity fluctuations after every hour of slurry circulation through the closed pipeline loop. The biomass slurry was considered stable once these fluctuations diminished to approximately $1.0\% \text{ h}^{-1}$ (Figure 5.3 [b]).

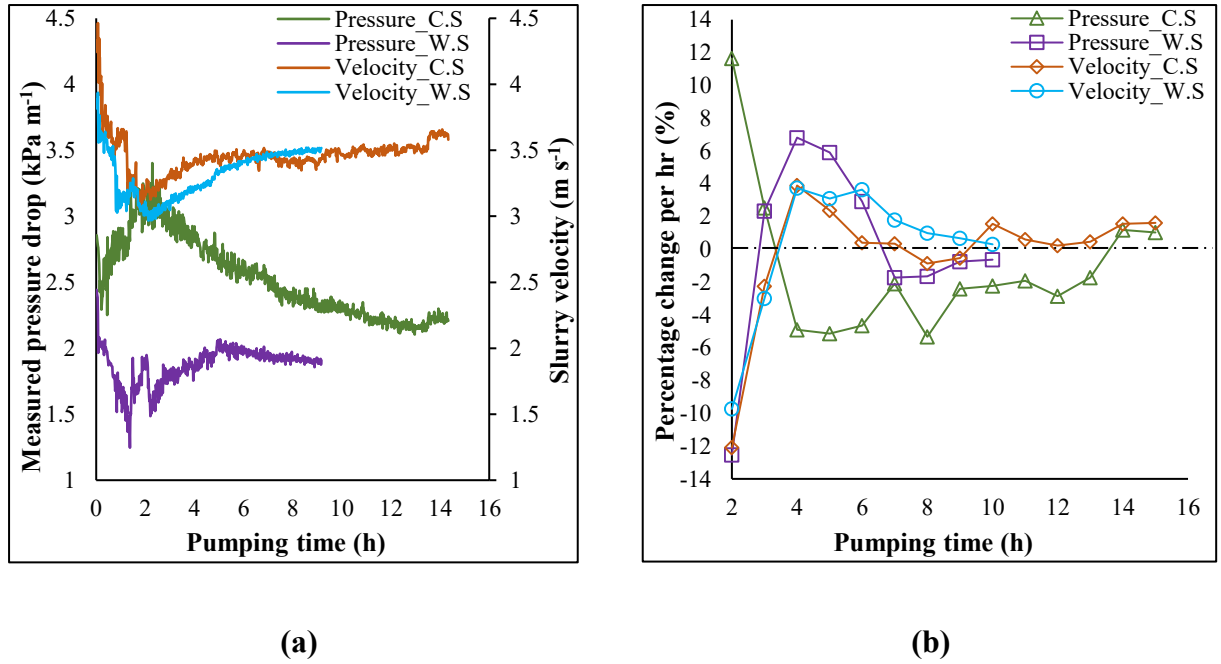


Figure 5.3: (a) Variation and (b) Percentage change per hour in the measured pressure drops and velocities of typical corn stover and wheat straw-water slurries pumped through a 50 mm diameter closed pipeline circuit.

After the stable slurry condition (i.e., fully saturated) was reached, the slurry velocities were varied from $0.5\text{--}4.3 \text{ m s}^{-1}$ and corresponding pressure drops in the vertical test section were recorded at the highest achievable C_{mp} of a specific particle size (e.g., $C_{mp} = 40\%$ for a $<3.2 \text{ mm}$ particle size). The C_{mp} of a specific particle size (e.g., $<3.2 \text{ mm}$) was reduced from 40% to 5% by diluting the slurry at 5% increments and recording the corresponding pressure drops at various velocities in each dilution phase. This was done for the other particle sizes of both feedstocks. The slurry

properties of all the particle sizes along with their corresponding saturated and dry matter (i.e., oven-dried) solid volume and mass contents are shown in Table 5.2.

Table 5.2: Physical properties of aqueous slurries of wheat straw, corn stover, and classical solids particles used in experiments

Material	Nominal particle size	Slurry solid mass content		Saturated slurry density	Slurry delivered concentration
	(mm)	Dry (%)	Saturated (%)	(kg m ⁻³)	(%)
Wheat straw	~19.2	0.9-4.5	5-25	1002.39 -1012.05	4.87-24.37
	~6.4	0.9-5.4	5-30	1002.39 -1014.49	4.68-28.11
	~3.2	0.9-6.3	5-35	1002.39 -1016.95	4.5-31.53
	<~3.2	0.9-7.2	5-40	1002.39 -1019.42	4.55-36.38
Corn stover	~19.2	0.9-4.5	5-25	1002.39 -1012.05	—
	~6.4	0.9-5.4	5-30	1002.39 -1014.49	—
	~3.2	0.9-6.3	5-35	1002.39 -1016.95	—
	<~3.2	0.9-7.2	5-40	1002.39 -1019.42	—
Fine sand	—	—	—	1012.84 -1072.19	0.99-4.94 ^d

^dThe delivered concentration for fine sand-aqueous slurries given in this table is on a volume (i.e., C_{vd}) and mass basis (i.e., C_{md}) for both wheat straw- and corn stover-water slurries.

5.2.5 In situ concentration measurements

As the slurry loop was not equipped with a concentration measuring device in earlier work, the in situ concentrations ($C_{in-situ}$) were evaluated by indirect measurements through C_{md} 's of both the classical and ARB solids-water slurries. The correlations obtained for $C_{in-situ}$'s were used to find the in situ densities of the corresponding mixtures. In the case of the classical solid-water mixtures (e.g., glass beads and play sand; not fine sand), large differences in C_{mp} 's and C_{md} 's were

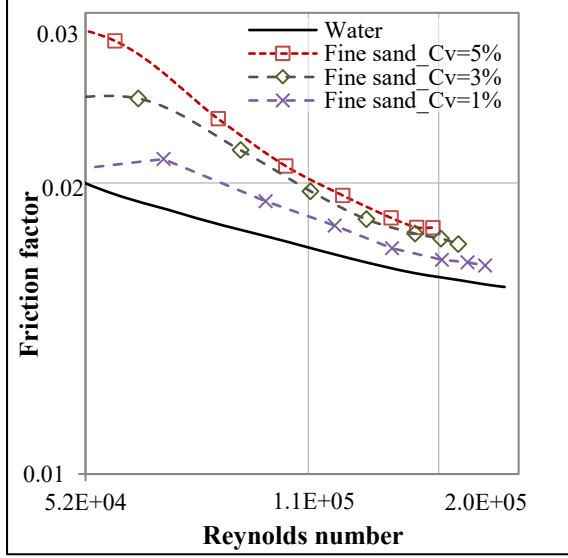
observed. However, in the case of aqueous W.S slurries, the differences were small (3%-10%) for the range of particle sizes (<3.2-19.2 mm) and C_{mp} 's (5%-40%) (Javed et al., 2022b; Javed et al., 2021). Similar observations were found for fine sand-water mixtures as well (Javed et al., 2021). The primary reason for small variations in the delivered and C_{mp} 's of both the W.S- and fine sand-water slurries (Table 5.2) was their neutrally buoyant nature (i.e., $\frac{v_t}{v_m} \leq 0.021$, where v_t is the terminal settling velocity).

In one of our earlier studies the v_t of various particle lengths (5-30 mm) and widths ≤ 2 mm of saturated particles of W.S and C.S in quiescent water present in a vertical column (50 mm ID and 0.305 m long) was evaluated and found to be in the range of 13-18 mm s⁻¹ and 14-33 mm s⁻¹, respectively (Appendix B). Because the W.S and C.S particles have similar saturated particle densities (see Table 5.2) and very small terminal settling velocities, it was assumed that the C_{md} 's of C.S slurries were approximately equal to their corresponding C_{mp} 's. Therefore, in the context of this study, the mass or volume concentrations refer to the prepared concentrations of the slurries unless otherwise specified. The reasons for not using a concentration measuring device in the experimental setup, as well as the procedure and results of measuring C_{md} 's at various C_{mp} 's, are discussed in detail in earlier studies (Javed et al., 2022b; Javed et al., 2021).

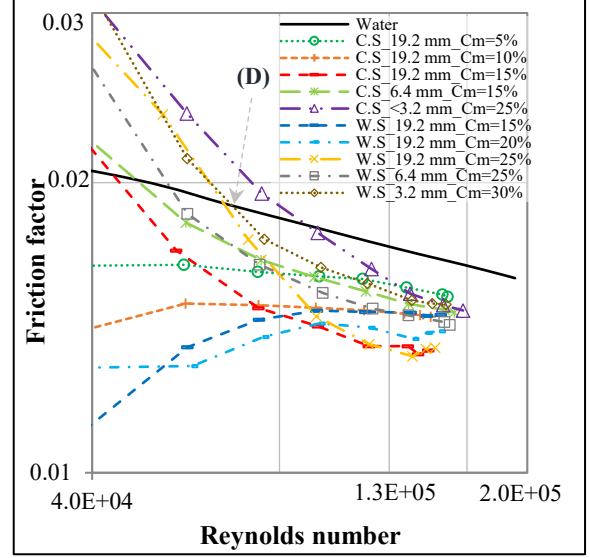
5.3 Experimental results and discussion

5.3.1 Vertical upward flows of biomass and classical solids-water slurries

Figure 5.4 shows the frictional behaviour of classical solids (fine sand)- and ARB-water slurries (see specifications of fine sand and agricultural residue in Table 5.1 and Table 5.2) in vertical upward flows for velocities > 0.5 m s⁻¹ and various concentrations and particle sizes through a 50 mm diameter pipe section of a closed-circuit pipeline facility.



(a)



(b)

Figure 5.4: Friction factor versus generalised Reynolds number for velocities $>0.5 \text{ m s}^{-1}$ in a 50 mm diameter pipeline for vertical upward flows of various volumetric and saturated mass concentrations of slurries of (a) fine sand particles and (b) wheat straw and corn stover particles.

The friction factor (f_D), generalised Reynolds number (Re_g), and mixture densities (ρ_m) were evaluated from the experimental measurements using Equations 5.1 to 5.4:

$$\Delta P_f = \rho_m g h_f = \frac{\rho_m f_D L v_m^2}{2D} \quad (5.1)$$

$$Re_g = \frac{\rho_m v_m D}{\mu_f} \quad (5.2)$$

$$\left(\frac{\Delta P_f}{L}\right)_m = \frac{\Delta P_{MD}}{L} - [\rho_m - \rho_w]g \quad (5.3)$$

$$\rho_m = \rho_w[1 + C_V(S - 1)] = \rho_w + C_V(\rho_s - \rho_w) \quad (5.4)$$

where ρ_w , g , h_f , v_m , μ_f , $(\Delta P_f L^{-1})_m$, $\Delta P_{MD} L^{-1}$, C_V , S , and ρ_s are the density of water, acceleration due to gravity, head loss due to friction, mixture velocity, carrier fluid viscosity, experimental frictional pressure drop of the mixture per unit length, measured (or manometric) pressure drop of the mixture per unit length, volumetric concentration of the mixture, specific gravity of the solid particle, and particle density (or saturated particle density, for biomass), respectively. In vertical upward flows, the static head component (i.e., $[\rho_m - \rho_w]g$) plays a vital role in determining the frictional pressure drop of the slurry. This static component depends on the in situ slurry density, which is directly linked to the $C_{in-situ}$ of the slurry. The procedure for measuring the $C_{in-situ}$ of the slurries was explained earlier.

The frictional behaviour of classical solids-water slurries appears to be completely opposite that of aqueous slurries of ARB in vertical upward flows. As can be seen from Figure 5.4 (a), the friction factor of fine sand-water slurries increases with increasing solid volume concentrations (C_V) and is always greater than the friction factor of clear water at the same Re_g values. In classical solid-water slurries, the pipe-wall friction consists of both the liquid friction and solids friction and depends on the solids-particle diameter, particle density, mean flow velocity, and the solids concentration. The component of solids friction is mostly higher than the liquid friction and is generated through the inter-particle collision and intermittent collisions of the solid particles with the pipe wall. Therefore, at the same flow velocity and particle diameter, an increase in the C_V increases the pipe wall friction (Matousek, 2009; Shook & Bartosik, 1994). Although the slurry friction factor decreases when the Re_g increases for any specific C_V , further decrement in the friction factor stops at a specific flow rate, at which the slurry curves become parallel to the water

curve but at a certain offset (which depends on the C_V and increases with increasing the C_V) above the water curve (Figure 5.4 [a]). This happens because of the development of a region with lower particle concentration adjacent to the pipe wall at high slurry velocities for a specific size of the solid particles. The reduction in the particle concentration at the pipe wall eventually reduces the components of the solids friction and hence the pipe wall friction. However, this phenomenon is completely dependent on the size of the solid particles (Shook & Bartosik, 1994). In our earlier study, similar results were observed for glass beads and medium sand-water slurries during their flow through a vertical pipe section, wherein the frictional pressure gradient of these slurries was always above that of clear water and increased with increasing C_V (Javed et al., 2021).

Unlike classical solids-water slurries at a similar Re_g range, the friction factor of aqueous suspensions of ARB of a specific particle size and C_m is either below that of clear water for the entire flow rate range and decreases with increasing Re_g , or the friction factor appears to be initially above that of clear water and then decreases with increasing Re_g and finally drops below that of water after a transition point, which is shown as intersection point D in Figure 5.4 (b). This phenomenon mainly occurs because of the change in the viscous nature of the suspension. The biomass particles are fibrous in nature (Javed et al., 2021). The apparent suspension viscosity of any fibrous material strongly depends on two factors, C_m and fiber dimension. Further, the apparent suspension viscosity has a linear relationship with the lower C_m 's and a cubic relationship with the higher C_m 's (Djalili-Moghaddam & Toll, 2006; Javed et al., 2022b). Therefore, for a low C_m , the apparent suspension viscosity of most of the biomass suspensions of similar particle size was low, causing the entire suspension to appear below the water curve for the entire range of Re_g (Figure 5.4 [b]).

Further, at a specific Re_g value, the friction factor of these biomass-water slurries decreases with an increase in particle size and C_m . At larger particle sizes and higher C_m 's of these slurries, the drop in friction factor is higher than the corresponding value of water (Figure 5.4 [b]). One of the reasons for this phenomenon is the increase in the particle-particle interaction of the biomass particles at higher C_m 's. The fibers with higher ϕ_p 's or longer lengths develop stronger fiber networks and cause an increase in the fiber floc size at higher fiber C_m 's, which ultimately suppresses longitudinal turbulence intensities to give the highest drop in the friction factor (Javed et al., 2022b). Further details on the effect of particle size, C_m , and feedstock of ARB-water slurries on corresponding friction factors are given in our earlier study (Javed et al., 2022a). Thus, most of the friction factor curves of ARB-water slurries in vertical upward flows are below that of the water curve at a higher Re_g , whereas some of them appear completely below the water curve for specific C_m 's and particle sizes over the entire Re_g range. These kinds of unusual concentration effects are common in some other types of natural or synthetic fiber suspensions (i.e., nylon or asbestos fibers) as well as in vertical upward flows (Kerekes & Douglas, 1972; Radin et al., 1975). The friction factor of biomass suspensions below that of water means the suspension has the capability to reduce drag and ultimately the energy consumed by the slurry pump (Figure 5.4 [b]).

In vertical upward flows of ARB-water slurries, it was further observed that some of the slurries at higher C_m 's could not reduce drag for the entire Re_g range, as shown in Figure 5.5.

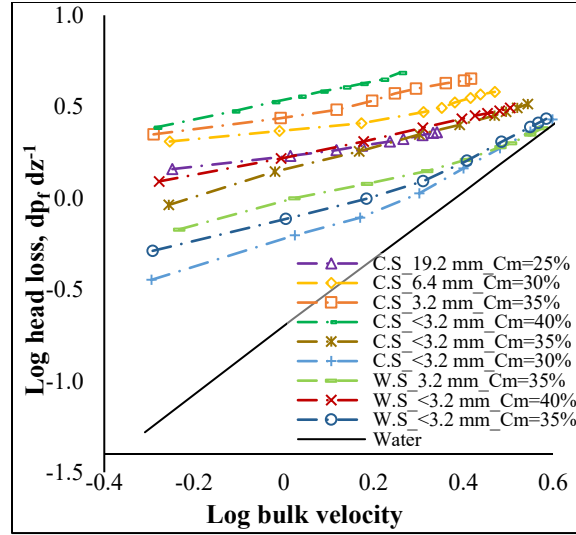


Figure 5.5: Logarithmic plot of frictional pressure drop and slurry bulk velocity (0.5–4.3 m s⁻¹) in vertical upward flows of corn stover- and wheat straw-water slurries of various particle sizes and high mass concentrations (25%–40%).

One of the reasons for this behaviour is low achievable slurry bulk velocities due to pump limitations (Javed et al., 2022a). However, it can be interpreted from the trend of the curves shown in Figure 5.5 that further increases in velocity through pump upgrading will cause these slurry curves to drop below that of water to exhibit drag reduction. The frictional behaviour of ARB-water slurries shown in Figure 5.4 (b) and Figure 5.5 is attributed to various factors including the type of fiber, fiber aspect ratio, the PSD of the fibers, fiber flexibility, fiber surface features, fiber specific gravity, suspension concentration, suspension velocity, apparent viscosity of the suspension, pipe diameter, and carrier fluid. The details on these factors and their effect on ARB slurries in vertical upward flows are discussed in our earlier studies (Javed et al., 2022a, 2022b; Javed et al., 2021). Figure 5.4 and Figure 5.5 show the experimental friction factors of water. The measured/experimental pressure drops and friction factors of water were compared to the

Churchill's correlation (Churchill, 1977) with a 2-5% error range during calibration. Figure A4 in Appendix A reflects these results.

5.3.2 Development of empirical correlation

5.3.2.1 Numerical model

Numerical modeling of the frictional behaviour of ARB-water slurries flowing against gravity through a vertical pipe section 50 mm diameter in a 29 m long closed-circuit pipeline facility was conducted using the open-source R programming software (4.0.5) (R, 2022; RStudio, 2023). The primary focus of this research was to develop an empirical model based on the 2511 measurements experimentally obtained earlier of the frictional pressure drop (Figure 5.6) for the entire range of particle sizes (<3.2-19.2 mm), C_m 's (5%-40% [mass]), and v_m 's (0.5-4.3 m s⁻¹) of the slurries of both feedstocks (W.S and C.S) that can predict the dependent/output variable (i.e., frictional pressure drop) as a function of the independent/input variables of particle aspect ratio (ϕ_p), v_m , and C_m .

The scatter shape of the entire set of experimental measurements shows a large number of C.S data points away from a specific general trend of most of the data set (Figure 5.6). This is associated with the different frictional behaviour of C.S compared to W.S water slurries, particularly at higher C_m 's in vertical upward flows (Javed et al., 2022a) and reflects the significance of considering the type of feedstock used in the numerical model. Ventura et al. proposed independent correlations for frictional pressure drops of each type of aqueous-based wood pulp suspension flows through horizontal pipes for flow regions beyond the v_{wt} .

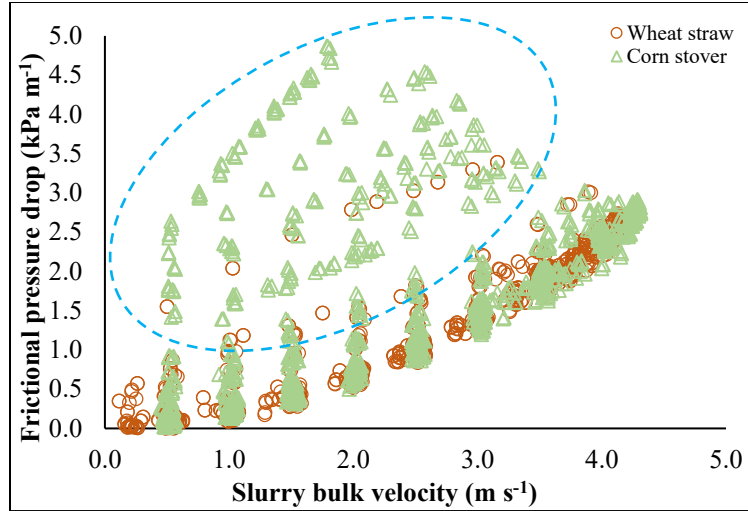


Figure 5.6: The plot of the complete set of data points (2511) of experimentally obtained frictional pressure drops of agricultural residue biomass-water slurries at their corresponding velocities in vertical upward flows.

In their study, each correlation for a typical wood pulp fiber suspension consisted of a second-order polynomial with all the possible interactions of the input variables (i.e., slurry concentration, v_m , and D) considered (Ventura et al., 2008). Most of the wood pulp fiber suspensions in horizontal pipe flows exhibit smooth profiles of their corresponding head loss curves beyond the v_{wt} (Duffy & Lee, 1978). The head loss curve Duffy obtained during horizontal flows of a typical wood pulp fiber suspension exhibited a smooth profile from the v_{wt} (suspension velocity related to the onset of turbulence in the annulus) in the plug flow region up to the point of maximum drag reduction obtained in the transition flow region of the wood pulp suspension (Duffy, 1989). Vaezi et al. also found smooth profiles of head loss curves during hydro-transport of ARB-water slurries for a wide range of C_m 's, particle sizes, and v_m 's through a horizontal pipe with a 50 mm ID (2014). With the experimental results from their previous investigation, Vaezi and Kumar developed an empirical correlation of frictional pressure gradients of these types of slurries that contained fourth-order polynomials with all the possible interactions of independent variables (i.e., slurry

concentration, slurry bulk velocity and particle shape factor) (Vaezi & Kumar, 2014a). These findings provided a base to progress further in the current research.

More than 30 regression models using different approaches in R programming were tried to find the best fit to our large number of data sets, and we finally came up with a fifth-order polynomial equation with all of the possible interactions of the independent variables (limiting ϕ_p up to the quadratic level) to be the most suitable model. A multiple linear regression analysis approach was used to estimate the regression coefficients of this model and included the qualitative factor, i.e., the type of feedstock (C.S or W.S), as well as to separately elaborate the coefficients of C.S and W.S. However, the number of coefficients in this model was quite large (i.e., 108 for each feedstock). This number was reduced by isolating the higher order (3-way) interaction terms of the independent variables using the criteria to attain minimum values of residual standard errors and LOOCV (leave-one-out cross validation), the highest values of multiple R^2 or coefficient of determination (a statistical measure of a percentage variation caused by the independent variable to predict the dependant variable) (Friedman et al., 2001), and the adjusted R^2 (a statistical approach to compare the explanatory power of regression models containing different independent variables).

In the LOOCV approach, from the total number of observations (say, N'), we consider each observation as the validation set, and the remaining observations ($N'-1$) are taken as a training set. Model fitting and predicting are accomplished by using one observation validation set. A similar method is repeated N' times for each observation as the validation set. Finally, a polynomial fifth-order equation (Equation 5.5) was proposed containing most of the two-way interactions of all the independent variables (i.e., a total of 47 variables and their mutual interactions for each feedstock)

using multiple linear regression analysis to estimate the regression coefficients ($a_k, b_k, d_k, e_k, h_k, p_k, q_k, w_k, \alpha_k, \beta_k, \gamma$).

$$\left(\frac{\Delta P_f}{L}\right)_m = \sum_{k=1}^5 \{a_k \varphi_p^k + d_k v_m^k + [b_k + e_k v_m + h_k v_m^2 + p_k v_m^3 + q_k v_m^4 + w_k v_m^5 + \alpha_k \varphi_p + \beta_k \varphi_p^2] C_m^k + \gamma\} \quad (5.5)$$

For the model shown in Equation 5.5, the values of residual standard errors, LOOCV, multiple R^2 , and adjusted R^2 were 0.1202, 0.0149, 0.9952, and 0.995, respectively. These values affirmed the good overall fit of the estimated regression model to the experimental data. The low LOOCV value indicates that the developed regression model was not overfitted and had low bias. The input variables for Equation 5.5 were selected based on our understanding developed while analysing the frictional behaviour of ARB-water slurries. In our past experimental studies on vertical upward flows of W.S- and C.S-water slurries through a pipe, we found the frictional pressure drops of these slurries to be strongly dependent on particle size or φ_p , C_m , and v_m . ARB is fibrous and contains various types of particles with a broad PSD. These particles interact with each other and form networks when mixed with water and flow through the pipeline under specific flow conditions (Javed et al., 2022a, 2022b; Javed et al., 2021). The interaction among the particles can be quantified by the fiber contact number ($n_c = 2C_V \varphi_p^2$, where C_V is the volumetric concentration of the suspension (Dodson, 1996)). With the increase in the φ_p , the fiber contact number increases sharply (because of its quadratic relationship with the φ_p), which increases the fiber-fiber interaction and eventually causes the development of coherent networks with increased flocculation at higher φ_p 's and C_m 's. The increase in the size of the flocculation affects the frictional pressure drop of the biomass-water slurries. Therefore, the effects of φ_p , C_m , and v_m on

the frictional pressure drops of biomass-water slurries are interlinked. The details on the effects of these parameters on the frictional pressure drops of ARB-water slurries in vertical upward flows through pipes are given in our past work and are beyond the scope of the present study (Javed et al., 2022a).

Several other studies on vertical upward flows of aqueous-based suspensions of natural or synthetic fibers also highlight the significance of these variables (i.e., v_m , C_m , and φ_p) on the suspensions frictional pressure drop (Bobkowicz & Gauvin, 1965; Kerekes, 1971; Radin et al., 1975). In the current study, we preferred φ_p over the nominal and mean lengths of the particles because (1) the nominal lengths for the four groups of particles (shown in Table 5.1) were not actual representative measures of the particle length; they were selected based on the classifier sieves' opening sizes and do not represent the PSD of each individual group of particles obtained from the corresponding classifier sieve (Vaezi et al., 2013); and (2) the φ_p contains most of the information about particle shape, including particle length and width, and is commonly used in modelling the behaviour of natural and synthetic fiber suspensions, rather than mean particle length (Cotas et al., 2015; Djalili-Moghaddam & Toll, 2006; Dodson, 1996; Kerekes, 1971; Manhart, 2003).

The complete details of the estimated regression coefficients (a_k , b_k , d_k , e_k , h_k , p_k , q_k , w_k , α_k , β_k , γ) and their corresponding values for the proposed empirical correlation of frictional pressure drop $(\Delta P_f L^{-1})_m$ for vertical upward flows of ARB are given in Table 5.3.

Table 5.3: Estimated regression coefficients for the proposed empirical correlation given in Equation 5.5

	Coefficient symbols	Numerical values of the coefficients of all the independent variables and interaction terms				
		$k = 1$	$k = 2$	$k = 3$	$k = 4$	$k = 5$
Corn stover-water suspension	a_k	5.152857426	-0.610977406	—	—	—
	b_k	4.147552294	-0.701057515	0.05504	-0.00202	2.75E-05
	d_k	3.717609855	-5.886413918	3.837269	-1.02986	0.09864
	e_k	-1.571620908	0.25249123	-0.0173	0.00051	-5.2E-06
	h_k	2.563125834	-0.397898954	0.026406	-0.00076	7.65E-06
	p_k	-1.611295029	0.244678178	-0.01592	0.000449	-4.5E-06
	q_k	0.42768813	-0.063847021	0.004087	-0.00011	1.11E-06
	w_k	-0.040602667	0.005975671	-0.00038	1.03E-05	-1E-07
	α_k	-2.443692217	0.407294429	-0.0317	0.00116	-1.59E-05
	β_k	0.285142165	-0.046851174	0.003587	-0.00013	1.75E-06
	γ	-8.615207045				
	Coefficient symbols	Numerical values of the coefficients of all the independent variables and interaction terms				
		$k = 1$	$k = 2$	$k = 3$	$k = 4$	$k = 5$
Wheat straw-water suspension	a_k	-4.898372442	0.593735586	—	—	—
	b_k	-3.926122381	0.671544489	-0.05327	0.001963	-2.7E-05
	d_k	-4.548943492	6.98814711	-4.35523	1.161894	-0.11104
	e_k	1.973534438	-0.309909274	0.020723	-0.0006	6.04E-06
	h_k	-3.023581893	0.467125299	-0.03081	8.76E-04	-8.8E-06
	p_k	1.871793522	-0.284816585	0.018558	-0.00052	5.2E-06
	q_k	-0.495827536	7.45E-02	-0.0048	0.000134	-1.3E-06
	w_k	4.71E-02	-0.006998131	0.000447	-1.2E-05	1.21E-07
	α_k	2.373647209	-0.397217796	0.031049	-0.00114	1.56E-05
	β_k	-0.280835673	0.046161415	-0.00354	0.000127	-1.72E-06
	γ	-0.763919862				

To develop an optimal predictive model with minimum LOOCV, all the interaction terms for $k = 1$ -5 shown in Table 5.3 were included despite their low impact on the output variable. Figure 5.7 shows the plot of predicted values (obtained using the empirical model in Equation 5.5) versus the entire experimental results (2511 data points) for the frictional pressure drops of ARB-water slurry flows in vertical pipe.

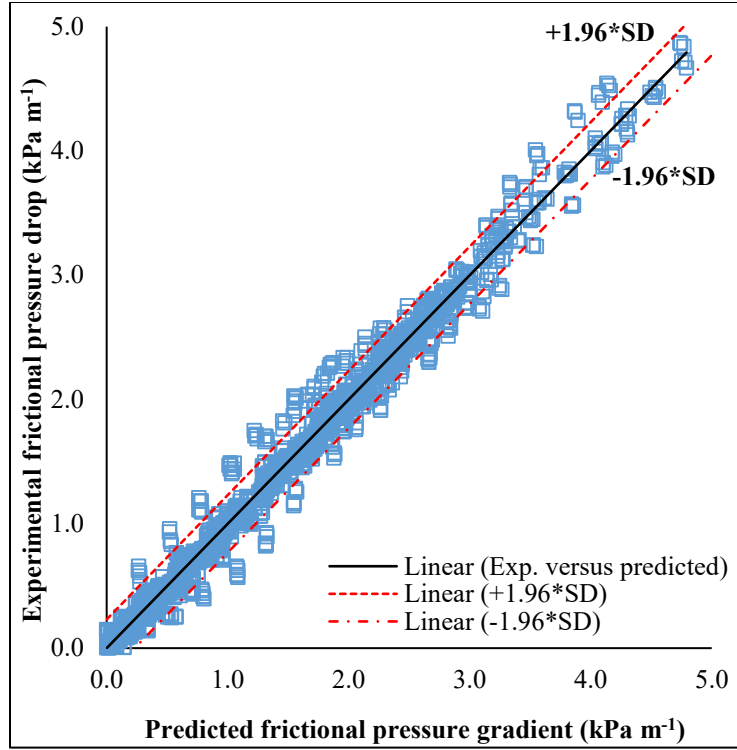


Figure 5.7: Predicted versus experimental results for the entire 2511 data points.

As seen in Figure 5.7, the predicted values of frictional pressure drops seem to be close to the diagonal, and approximately 88% of the data set was found to be within the limits of the 95% confidence interval. To further improve the prediction ability of the empirical model, we used another approach, described in the following section.

5.3.2.2 Modified empirical model

The empirical model (i.e., Equation 5.5) developed in the previous section to predict the frictional pressure drop of both feedstocks (C.S and W.S) of ARB-water slurries in vertical upward flows contained fifth-order terms of C_m and v_m and was limited to the quadratic level of φ_p with all the possible two-way interaction terms of the input variables. However, this model still has a large number of variables (i.e., 96 terms in total for both feedstocks). To investigate the effect of higher order terms of φ_p and their two-way interactions on the dependent/output variable (i.e.,

$[\Delta P_f L^{-1}]_m$) with an intention to further increase the accuracy of the empirical model with the reduced number of terms, we used a different statistical approach to improve the model presented in Equation 5.5.

We randomly split the entire data set (i.e., 2511 experimental measurements) into a 70% training/development set with 1757 data points and a 30% test set containing 754 data points. We considered the minimum threshold for the training set to be 70% to make sure that it contained the entire range of values of the independent variables (i.e., φ_p , C_m , v_m) used in the experiments. This was further validated through visual observations of the entire training set obtained after the random splitting of the experimental data. The model was trained on the training set and its performance was evaluated via residuals on the test set. Figure 5.6 shows that different feedstocks have different effects on the frictional pressure drop of ARB-water slurries in vertical upward flows. Therefore, in the improved form of the numerical model, we considered the feedstock variable as an independent variable in addition to the three input variables, i.e., φ_p , C_m , and v_m . To take the “feedstock” variable into consideration while creating the numerical model in R programming, we first introduced a qualitative variable named wheat straw (W.S) in the model such that if the new variable W.S = 1, the feedstock is wheat straw and otherwise it is corn stover (i.e., when W.S = 0). It is obvious from Figure 5.6 and Equation 5.5 that the association between the input variables and the frictional pressure drop is nonlinear. Therefore, to better describe the curvilinear relationship among the input and output variables, we considered fitting a multiple polynomial regression in the improved numerical model.

When fitting a polynomial regression, the choice of the degree of the polynomial is a tough problem that can be viewed as the trade-off between the bias and variance. To avoid over- or

underfitting issues, we selected the degree of the polynomial for each covariate/independent variable using the hypothesis tests (e.g., the F-test and the t-test). Specifically, we fitted different models in R software ranging from linear to a degree-5 polynomial of each of the independent variables (except the qualitative variable, i.e., W.S) and sought the simplest but sufficient preliminary model via the ANOVA (analysis of variance) test. The detailed statistical analysis of different models is given in Table A3 in Appendix A, which shows the p-values of empirical models containing φ_p with degree-5 polynomials and C_m and v_m both with degree-4 and higher polynomials to be >0.05 (Table 5.4).

Table 5.4: The p-values of the empirical models with higher degrees of independent variables

	φ_p^5	C_m^5	v_m^5	C_m^4	v_m^4
Pr(>F)	0.2631	0.1159	0.07663	0.06147	0.07407

The higher p-values (i.e., >0.05) of the empirical models containing higher degrees of independent variables shown in Table 5.4 indicate that these preliminary models are not statistically significant. It turns out that an empirical model including a φ_p of degree-4, along with the C_m and v_m of degree-3 polynomials and a qualitative factor (W.S), are sufficient to explain the relationship between the covariates and the dependent variable. However, this preliminary model (i.e., model1 in Table A2 in Appendix A) was based on the main effects of the independent variables only with an adjusted R^2 value of the model as 0.866. To further improve this preliminary model and expand our understanding of the relationships among the independent variables, we considered all the two-way interaction terms of the independent variables of the preliminary model. Because not all the terms are statistically significant, we adopted the backward elimination method as used by others (Ahmad & Zhang, 2009; Derksen & Keselman, 1992; Efroymson, 1960) to choose a model. The

backward elimination starts with a complete set of predictors and removes them one by one until the best performing model is found. We then used the Akaike information criterion (AIC) (Aho et al., 2014; Akaike, 1998) to evaluate the quality of the models. The AIC measures the relative information value of the model using the maximum likelihood estimate and the number of predictors in the model. Finally, we obtained a modified empirical model with 1 fourth-order term, 3 third-order terms, 3 second-order terms, 4 first-order terms, and 38 two-way interaction terms to be the best fit for the data, whose AIC reached the lowest number of -6429.33. The values of residual standard error, multiple R^2 , and adjusted R^2 of the modified empirical model were found to be 0.1582, 0.9752, and 0.9745, respectively. Further, the test of significance for the entire regression (considering F statistics) demonstrated that the proposed model was statistically significant because the p-value was $\ll 0.05$ (i.e., $2.2\text{e-}16$ in our case). Equation 5.6 represents the standard form of the modified empirical model:

$$\begin{aligned} \left(\frac{\Delta P_f}{L}\right)_m = \sum_{n=1}^4 \{ & a_n \varphi_p^n + b_n C_m^n + d_n v_m^n \\ & + [e_n \varphi_p + h_n \varphi_p^2 + j_n \varphi_p^3 + k_n \varphi_p^4] C_m^n \\ & + [l_n \varphi_p + p_n \varphi_p^2 + q_n \varphi_p^3 + r_n \varphi_p^4 + t_n C_m + u_n C_m^2 \\ & + w_n C_m^3] v_m^n + [\beta + y_n \varphi_p^n + z_n C_m^n + \alpha_n v_m^n] (W.S) + \delta \} \end{aligned} \quad (5.6)$$

where $a_n, b_n, d_n, e_n, h_n, j_n, k_n, l_n, p_n, q_n, r_n, t_n, u_n, w_n, \beta, y_n, z_n, \alpha_n$, and δ are the regression coefficients of the modified empirical model of the frictional pressure drop $(\Delta P_f L^{-1})_m$ for ARB-water slurries in vertical upward flows. For C.S aqueous slurries, the terms involving the qualitative factor, i.e., $W.S$ in Equation 5.6, will be nullified. For wheat straw-aqueous slurries,

the factor $W.S$ will become unity in Equation 5.6. Table 5.5 shows the values of all the estimated regression coefficients of the modified empirical correlation for $(\Delta P_f L^{-1})_m$.

Table 5.5: Estimated regression coefficients for the modified empirical correlations presented in Equation 5.6

Coefficient symbols	Numerical values of the coefficients of all the independent variables and interaction terms			
	$n = 1$	$n = 2$	$n = 3$	$n = 4$
a_n	4.771525954	-0.224273091	-0.1033297	0.00923145
b_n	-3.124381175	0.279676027	-0.00698905	-
d_n	5.823889009	-3.356237764	0.561358592	-
e_n	3.538293476	-0.303558371	0.007318271	-
h_n	-1.291385827	0.107599634	-0.002520714	-
j_n	0.180510752	-0.014789914	0.000340565	-
k_n	-0.008497715	0.000688881	-1.5687E-05	-
l_n	-6.105833476	3.618567205	-0.564032112	-
p_n	2.107344562	-1.234843044	0.188660957	-
q_n	-0.284847213	0.165559944	-0.024947807	-
r_n	0.013110955	-0.007565649	0.001127809	-
t_n	0.068202911	-0.015076487	0.00055589	-
u_n	-0.005323838	0.0009321	-	-
w_n	0.000132663	-2.45655E-05	-	-
y_n	2.432435641	-0.189657909	-	-
z_n	-0.037552156	0.004889958	-0.000175572	-
α_n	-0.195206654	-	0.012031804	-
β		-7.23296287		
δ		-9.027619948		

In Table 5.5, the coefficients of some of the higher order terms and interactions of independent variables are not given because, as explained earlier, they were eliminated from statistical analysis during preliminary model selection and the backward elimination method; therefore, the corresponding coefficients of these terms will be considered zero after expanding the fourth-order polynomial of the modified empirical correlation given in Equation 5.6. The total number of terms

for the modified empirical model considering both feedstocks was 50 (including variables, interaction terms, and intercepts). Thus, the modified empirical model was less complex, with 50% fewer terms than the previous model (Equation 5.5).

Considering the coefficients of all the independent variables and their mutual interactions for $n = 1$ (Table 5.5), φ_p , v_m , C_m , and the two-way interactions of v_m and C_m with first and second orders of φ_p had a significantly large effect on the output $(\Delta P_f L^{-1})_m$ compared to all the interaction terms for both feedstocks. However, among the coefficients of the independent variables (φ_p , C_m , and v_m) excluding their interaction terms, φ_p had the highest effect on the output $(\Delta P_f L^{-1})_m$ for W.S (because of the larger coefficient of φ_p obtained by adding a_n and y_n compared to C.S), whereas v_m had the largest effect on the output for C.S. More specifically, for W.S-water-based suspensions, variations in φ_p had 2.3 times more impact on the output than C_m and 1.3 times more than v_m . For C.S-aqueous slurries, variations in φ_p had 1.5 times more impact on the output than C_m and v_m had 1.2 times more impact on the output than φ_p ; however, this number was not significant as the impacts of both v_m and φ_p on the output were similar. For both feedstocks, the variations in v_m appeared to be more influential on the output than C_m ; it had 1.8-1.85 times more impact on the output than C_m . In general, the overall impact of φ_p on the output/response of W.S was highest; whereas for C.S, the first-order interaction of v_m and φ_p was highest among all the independent variables and the interaction terms. These results show the different frictional behaviour of both the W.S- and C.S-water slurries in vertical upward flows and reflect the previous experimental findings by the authors on these types of slurries (Javed et al., 2022a, 2022b; Javed et al., 2021). W.S in knife-milled form consists of the rectangular rib-like particles, whereas C.S has different types of particles of non-uniform and complex shapes (Figure

5.1). Further, the φ_p of W.S particles for any nominal size is greater than that of the corresponding nominal sizes of C.S (Table 5.1). This results in the higher contact number (n_c) of all the nominal sizes of W.S particles compared to C.S, which eventually increases the fiber-fiber interaction and hence the flocculation in W.S slurries (Javed et al., 2022a). Therefore, we can see the profound impact of φ_p for W.S on the output compared to C.S in the modified empirical correlation (Equation 5.6). For $n = 2$, v_m and its two-way interactions with first and second orders of φ_p had the largest impact on the output/response compared to all the other independent variables and the interaction terms for both feedstocks, and this impact on the response decreased beyond $n = 2$ (Table 5.5). Since our main objective was to develop the most optimum predictive model, all the interaction terms for $n = 1-4$ shown in Table 5.5 (except those discarded during backward elimination) were included in the modified empirical correlation despite their low impact on the output variable to maintain the model accuracy.

5.3.2.3 Model validation

The proposed modified form of the empirical model (Equation 5.6) was validated in various ways: by investigating statistical graphs (i.e., residuals for the test set), by using the AIC in R programming (4.0.5), and by comparing the experimental and predicted values of the frictional pressure drops. Figure 5.8 shows the plot of residuals for 754 data points of the test set.

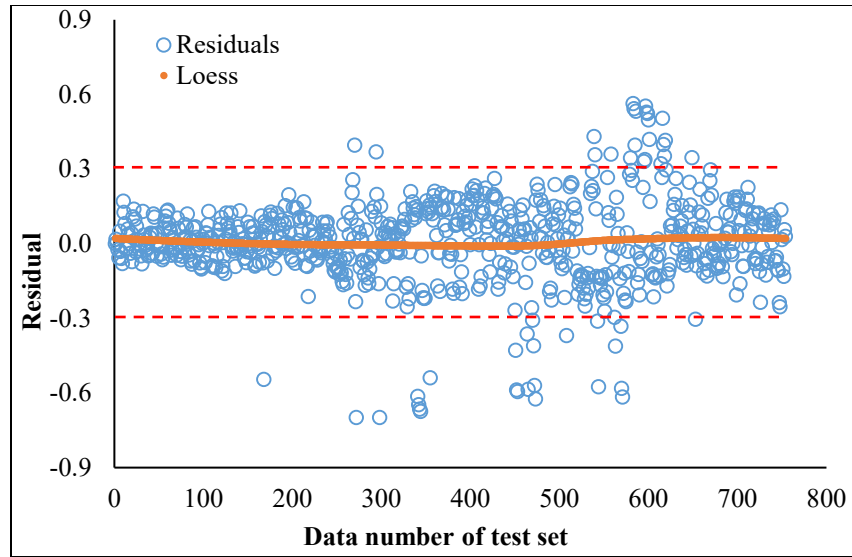


Figure 5.8: Residuals of the modified numerical model for 754 data points.

One assumption of the analysis of variance is to have a constant error term that indicates a constant variance of residuals when scattered randomly around zero. A non-constant error will generate a residual versus fitted plot in a specific pattern that corresponds to an incorrect hypothesis in the prediction (Montgomery et al., 2021). Figure 5.8 shows that most of the residuals are symmetrically distributed, tending to cluster around the LOESS (locally estimated scatter plot smoothing) line within the ± 0.3 bounds of the residual plot. In general, no specific pattern was observed in the plot of the residuals; this validated the adequacy of the proposed model. LOESS regression is used for smoothing a volatile time series. This approach is completely non-parametric, and least squares regression is carried out in localised subsets, which makes it an appropriate method to smoothen any specific numerical vector.

Figure 5.9 (a) shows the complete test data (i.e., 30% of 2511 experimental measurements) and the modeling results for the flow conditions tested for both agricultural residue biomass slurry feedstocks.

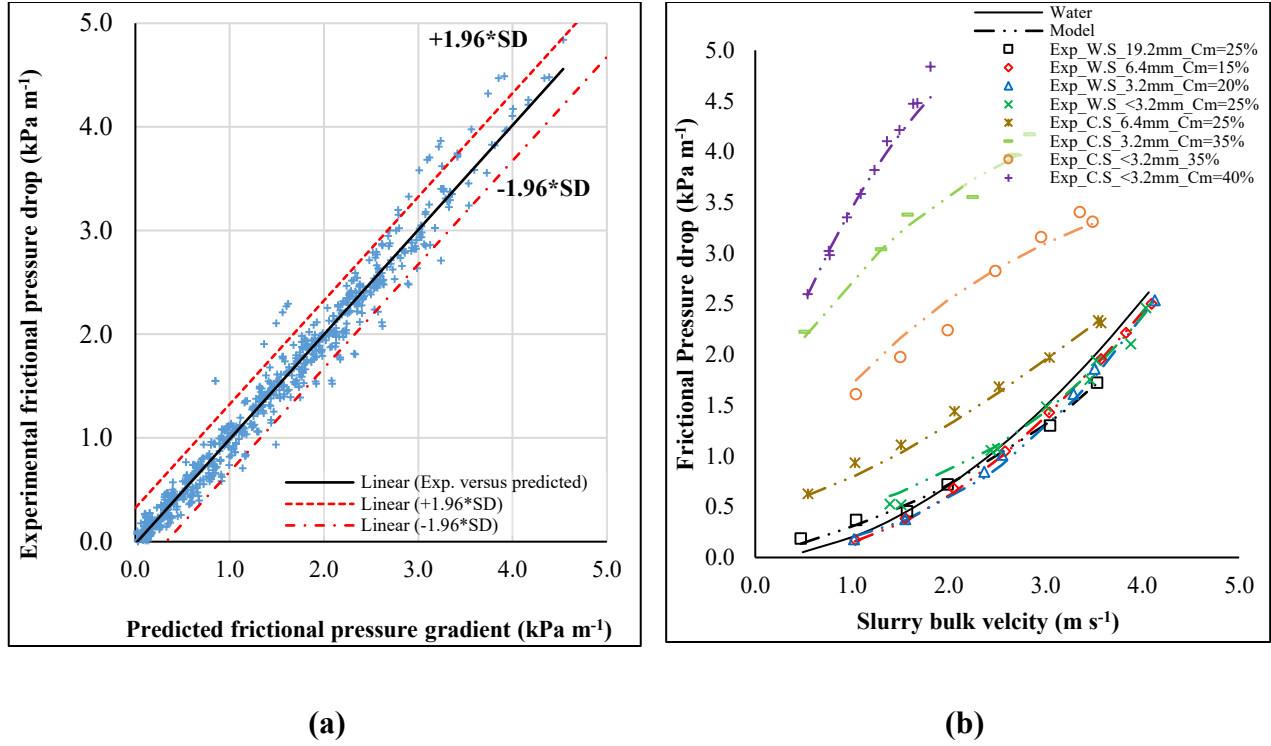


Figure 5.9: (a) Accuracy of the numerical model to predict frictional pressure drops for 754 experimental measurements (i.e., the test set) and (b) A comparison of numerically predicted and experimentally measured frictional pressure drops for different particle sizes and concentrations of agricultural residue biomass-water slurries in vertical upward flows.

As seen in Figure 5.9 (a), all the points are fairly close to the diagonal straight line and there is a linear relationship between the predicted and experimental values. This relationship satisfies one of the assumptions of multiple linear regression (Friedman et al., 2001) and indicates that the functional form of the proposed model is the true relationship between the covariates and the outcome. The predicted values of frictional pressure drops appear very similar to the experimental ones. Most of the data (i.e., $\approx 95\%$) was found to be within the limits of the 95% confidence interval. Another basic assumption of multiple linear regression is to use an additive error. The statistics associated with the additive error between the predicted and experimental values of the frictional

pressure drops for the entire data set were found as mean = -0.00746, SD = ± 0.1662 , IQR = 0.16782, and SEM = 0.0060524. The interquartile range (IQR) expresses the middle (50%) of the values when ordered from lowest to highest. The IQR is obtained by subtracting the median or middle values of the lower and upper half of the data. These values reflect the accuracy of the numerical model.

Figure 5.9 (b) compares the experimentally measured and numerically predicted (using the proposed modified empirical model in Equation 5.6) frictional pressure drops for some specific particle sizes and C_m 's of water-based slurries of both ARB feedstocks flowing through the vertical pipe section at different velocities. As can be seen from the figure, the experimental measurements agree very well with the predicted values $(\Delta P_f L^{-1})_m$ that were obtained by substituting the corresponding values of ϕ_p , C_m (in percentage), and v_m (in m s^{-1}) in the modified empirical model (Equation 5.6). For the results shown in Figure 5.9 (b), the maximum error was observed to be 15.6%. The modified empirical correlation thus obtained by the backward elimination method and AIC was more accurate and contained 50% fewer terms than the previously proposed model given in Equation 5.6. However, this proposed model is limited to the 50 mm diameter vertical pipe section of the closed pipeline loop. Further, a single value of ϕ_p is considered here for each nominal size. Although it represents at least a 50% size range of the cumulative size distribution, further dimensional parameters in the model are worth investigating to represent the PSD of each nominal size used in this study. To develop a universal empirical model for vertical upward flows of the ARB-water slurries, further experiments for larger pipe diameters are needed.

5.3.3 Onset velocity of drag reduction (v_{OD})

In vertical upward flows of water-based slurries of ARB (i.e., C.S and W.S), diverse frictional behaviour depending on the type of feedstock, particle size, and C_m 's for a similar Re_g range was observed. Some slurries exhibited plug flow and transition flow regions together, whereas some slurries seemed to exist completely either in the transition or the plug flow regions (Javed et al., 2022a, 2022b; Javed et al., 2021). For those slurries that demonstrated both the plug flow and transition flow regions together, the onset velocities of drag reduction (v_{OD}) corresponding to their transition points were obtained by developing a code in R programming (4.0.5) to find the coordinates of each transition point. The transition point is shown as the intersection point, D, between the curve of a specific slurry and water in Figure 5.4 (b). This point indicates a shift of flow region of a suspension from plug flow to transition flow at a suspension velocity known as the onset velocity of drag reduction. The entire range of v_{OD} values obtained in vertical upward flows of the aqueous suspensions of both ARB feedstocks is shown in Table A4 and in graphical form in Figure A5 in Appendix A. For most suspensions of every particle size of both feedstocks (except the 19.2 mm and 6.4 mm C.S and W.S, respectively), v_{OD} first decreased with an increase in C_m and then increased after a specific threshold (minimum) concentration (Figure A5 in Appendix A). The reasons for this specific v_{OD} variation trend with respect to C_m and the comparative assessment of frictional behaviour of ARB slurries have been discussed in detail in our earlier study (Javed et al., 2022a).

There is no pre-established correlation for v_{OD} of aqueous-based fiber (natural or synthetic) suspensions in vertical upward flows. However, some correlations have been proposed for the v_{max} (the maximum velocity in the plug flow region) and v_{wt} (the velocity corresponding to the onset of turbulence in the water annulus) for various particle sizes of aqueous-based wood pulp

and fiber suspension flows in horizontal pipes, and these provided the baseline for the present research. Ventura et al., for instance, found that for the v_{max} and v_{wt} for wood pulp fiber suspensions, each correlation depends strongly on pulp consistency (Ventura et al., 2008). Duffy and Lee claimed that v_{OD} depends on pulp consistency in the turbulent flows of several types of mechanical and chemical wood pulp suspensions through horizontal pipes. They found that v_{OD} increased with increasing pulp consistency (Duffy & Lee, 1978). In the current study, based on the v_{OD} values of various C_m 's of ARB slurries, empirical correlations for each particle size of both feedstocks were developed, as shown in Table 5.6.

Table 5.6: Correlations of v_{OD} for vertical upward flows of aqueous suspensions of different agricultural residue biomass feedstocks

Biomass aqueous suspension	Nominal particle length (mm)	Correlations for v_{OD}	R^2
		(m s^{-1})	(-)
Corn stover	19.2	$0.41C_m - 4.853$	1.0
	6.4	$0.0212C_m^2 - 0.5533C_m + 4.9469$	0.99
	3.2	$0.0018C_m^3 - 0.0724C_m^2 + 0.7944C_m - 0.6882$	1.0
	<3.2	$0.0095C_m^2 - 0.3766C_m + 6.2048$	0.98
Wheat straw	19.2	---	---
	6.4	$0.33C_m - 6.71$	1.0
	3.2	---	---
	<3.2	$0.0417C_m^2 - 1.9926C_m + 25.622$	1.0

The unit of C_m used in these correlations is taken in percentages. For W.S slurries of nominal particle sizes of 19.2 mm and 3.2 mm, there was insufficient data to derive a correlation for v_{OD} because most of these suspensions showed a transition flow region for the entire Re_g range, as is explained in our earlier studies (Javed et al., 2022b; Javed et al., 2021). The correlations developed for v_{OD} in Table 5.6 are limited to some specific ranges of C_m 's corresponding to different particle

sizes and feedstocks. However, they can still be helpful in predicting the transition points regarding the onset of drag reduction of the corresponding ARB-water slurries during upward flows in a vertical pipe of a specific diameter.

5.4 Conclusion

The frictional behaviour of aqueous-based ARB slurries in upward flows through a vertical pipe was modeled with experimental measurements and slurry flow conditions. The slurries of corn stover and wheat straw prepared using a wide range of particle sizes and C_m 's were circulated through a 29 m long closed pipeline loop with a 50 mm ID to attain their corresponding frictional pressure drops during counter-gravity flow. An empirical correlation was developed using a multiple linear regression approach with the backward elimination method and Akaike information criterion (AIC) to predict slurry frictional pressure drop as a function of particle type, particle aspect ratio, slurry solid mass concentration, and slurry velocity. There were differences in some of the numerical values of constant terms and the regression coefficients between the feedstocks, highlighting the differences in their frictional behaviour during vertical upward flows. A linear relationship was found between the predicted and the experimental frictional pressure drops with 94.7% of the data within the upper and lower bounds of the 95% confidence interval, which confirmed the accuracy of the model. In addition to the empirical model of slurry frictional pressure drop in vertical upward flows, the correlations for onset velocity of drag reduction (v_{OD}) were presented for each particle size of corn stover in terms of C_m 's, whereas for wheat straw, given the lack of data on frictional behaviour of this type of slurry, correlations for two particle sizes (<3.2 mm and 6.4 mm) were developed. These correlations provide a good understanding to forecast the transition points for the onset of drag reduction developed during vertical upward flows of ARB-water slurries. The proposed empirical model provides a base case for showing the

frictional pressure drops of aqueous-based ARB slurries during upward flows in a vertical pipe with a 50 mm inside diameter. Instead of focusing on modeling the biomass-water slurry behaviour in any typical flow region, we developed a model of frictional pressure gradients covering all the flow regions that appear for the range of flow conditions used during vertical upward flows of ARB slurries in our experimental setup. This correlation can be modified to include the effect of pipe diameter by conducting further experiments on ARB-aqueous slurries for larger diameter pipes that will eventually be useful in designing the large-scale pipeline network and estimating its operational and capital costs for biofuel production on a commercial level.

Chapter 6: Experimental Study on Two-Phase (Solid-Liquid) Flows of Ground Wheat Straw in Inclined Pipes⁵

6.1 Introduction

The substantial rise in the global energy requirement has increased the transportation sector's dependence on fossil fuels. Global energy demand in the transportation sector is met primarily by fossil fuels. Currently, the transportation sector consumes approximately 50% of global fossil fuel energy (Halder et al., 2019). The significant dependence of the transportation and other sectors on fossil fuels results in emission of greenhouse gases (GHGs) which causes global warming (Goldemberg, 2008; Miller et al., 2012) but is also depleting these reserves (Asomaning et al., 2016; Our World in Data, 2022; Vohra et al., 2014). One of the most reliable and sustainable ways to reduce global dependence on fossil fuels is to produce renewable biofuels (i.e., bioethanol, biodiesel, etc.) from biomass (i.e., crops and their residues, wood and its wastes, municipal solid wastes, etc.) (Kim & Dale, 2004; Pootakham & Kumar, 2010; Saleem, 2022; U.S. Energy Information Administration, 2023). In current practice, biomass conversion facilities rely largely on edible food crops to produce bioethanol (Mohanty & Swain, 2019). That said, lignocellulosic biomass (like agricultural and forest residues) seems more promising and has been gaining attention in bioethanol production because of (1) majority of these feedstocks are currently not used around the globe for liquid fuel production (Balat & Balat, 2009; Banerjee et al., 2010), (2) its low initial cost at agricultural farms (Balat & Balat, 2009), (3) its carbon neutrality with high

⁵ A version of this chapter has been accepted for publication as Javed K, Kurian V, Kumar A, “Experimental study on two-phase (solid-liquid) flows of ground wheat straw in inclined pipes”, *Journal of American Society of Agricultural and Biological Engineers* (ASABE), 2023 (in-review).

GHG emission reduction potential when substituting the fossil fuels (Banerjee et al., 2010; Halder et al., 2019; Vohra et al., 2014), and (4) the absence of food security issues with respect to the present and future needs of the world's growing population (Halder et al., 2019).

The high cost of transporting biomass bales from farms to biomass conversion facilities by ground (truck or rail) and the traffic congestion caused by the high frequency of trucks on the road are the main obstacles to commercial bioethanol production from agricultural waste biomass like wheat straw and corn stover (Aden et al., 2002; Kumar et al., 2003, 2005a; Ruth, 1999). A series of studies on the techno-economic and laboratory-scale investigations to address these challenges have been conducted earlier (Kumar et al., 2004, 2005a, 2005b; Luk et al., 2014; Vaezi et al., 2014). The investigations showed that pipeline hydro-transport of chopped agricultural waste biomass from farms to biomass conversion facilities over long distances could be the most cost-effective approach to produce bioethanol commercially on a large-scale. The techno-economic studies, however, were limited to horizontal pipelines (Vaezi et al., 2015). In reality, the long-distance pipeline network would involve horizontal (mostly), inclined (partially), and vertical (mostly in on-site processing) pipe sections. Although the frictional behaviour of agricultural residue biomass (ARB) through vertical pipelines have been explored recently (Javed et al., 2022a, 2022b; Javed et al., 2021), to improve their techno-economic assessments, further experimental studies on the frictional behaviour of these kinds of slurries through inclined pipe sections are needed.

Many studies are available on the hydraulic transport of conventional solids, i.e., sand, glass beads, etc., through inclined pipelines (Al-Mutahar, 2006; De Vreede, 2018; Matousek et al., 2018; Rai, 1972; Shook et al., 1974; Vlasak et al., 2018; Vlasak et al., 2019b). The flow of solids-water mixtures through inclined pipes is more complex than in horizontal and vertical pipes because in

inclined pipes the phases can separate and slip at the same time (Polanský, 2014). Pipe inclination affects the flow characteristics (i.e., pressure drop, concentration distribution across the pipe cross-section, velocity profile, the deposition limit velocity, etc.) of the settling slurries (Kao & JL, 1980; Meng & Lucas, 2017; Vauhkonen et al., 2019; Vlasak et al., 2018; Vlasak et al., 2019a). These characteristics also depend on the mean particle size and density of the solids being conveyed through the pipeline, which may cause the slurries to exhibit different flow regimes, i.e., homogeneous, pseudo-homogeneous, heterogeneous, stratified with a detectable sliding bed, or fully stratified. Each of these regimes has independent empirical correlations for predicting frictional pressure drops (Abulnaga, 2002; Gibert, 1960; Matousek, 2002; Matousek et al., 2018; Miedema et al., 2021; Worster & Denny, 1955). In inclined flows, the frictional pressure drop of the suspension is obtained experimentally by subtracting the hydrostatic head from the measured pressure drop (Doron & Barnea, 1996; Vlasak et al., 2018).

The hydrostatic component is a significant contributor to the pressure drop (both frictional and total) and is determined by the mixture's in situ density, a function of in situ concentration that is typically higher in ascending pipes than in descending ones and is measured using a suitable concentration measuring device (Vlasak et al., 2017; Vlasak et al., 2019a). The in situ concentration gradient across the pipe cross-section is more pronounced in heterogeneous flows of the conventional solids-water slurries through inclined pipes than in pseudo-homogeneous flows. Heterogeneous flows are more difficult to analyze because special techniques are required to measure the in situ concentrations of the suspensions in these regimes. However, under certain flow conditions when the solids are fully suspended, the in situ concentration can be assumed to be equivalent to the delivered concentration for the solids-water suspensions flowing above a specific velocity, known as critical velocity for a pseudo-homogeneous regime (Javed et al.,

2022b; Javed et al., 2021). Fine sand-water suspensions with a mean particle diameter of $d_{50} = 0.04\text{-}0.2$ mm have been found to behave pseudo-homogeneously during flow through horizontal or inclined pipes with slopes $<\pm 25^\circ$, exhibiting a weak concentration gradient across the pipe cross-section for suspension velocities above the critical deposition velocity (Matousek et al., 2022; Vlasak et al., 2019a, 2019b).

Natural or synthetic fiber-water suspension flow over inclined pipe sections is rarely studied. Most studies on hole cleaning in inclined wells use small concentrations of fibers (basal seeds, synthetic fibers, etc.) to improve drilling sweep efficiency by introducing a fiber network that hydrodynamically and mechanically affects the suspended and deposited solids particles (Ahmed & Takach, 2009; Elgaddafi & Ahmed, 2020; Movahedi et al., 2017). It is difficult to analyze the fiber suspensions because they form flocs or intricate networks when flowing through a pipeline (Duffy, 2006). One distinctive feature of these kinds of suspensions is the drag reduction (the percent reduction in suspension friction loss relative to water alone at the same bulk velocity) in certain flow conditions. In most of the work carried out to understand the frictional behaviour of fibrous suspensions, the primary focus has been understanding the flow regions and phenomena behind the particulate-inertial mechanisms (Bobkiewicz & Gauvin, 1965; Kerekes, 1971; Radin et al., 1975; Seely, 1968; Steen, 1989). Agricultural residual biomass (wheat straw, corn stover) suspensions act like wood fiber, chemical wood pulp, and semi-chemical pulp suspensions (Vaezi et al., 2014).

Several laboratory-scale investigations have been conducted earlier to explore the frictional behaviour of wheat straw and corn stover suspension flows in horizontal and vertical pipe sections and found that these suspensions, like other fibrous suspensions, exhibit three flow regions: plug flow, transition flow, and turbulent flow. Four nominal particle sizes were used, 19.2 mm, 6.4 mm,

3.2 mm, and <3.2 mm at saturated mass concentrations ranging from 5-25%, 5-30%, 5-35%, and 5-40%, respectively, for both the wheat straw and corn stover suspensions. It was further discovered through longitudinal frictional pressure drop measurements of the biomass suspensions that for a fixed pipe diameter, the development of these regions depended on multiple factors, including pipe orientation, type of feedstock, the aspect ratio of fibers, suspension velocity, suspension concentration, suspension apparent viscosity, and fiber-carrier fluid density ratio. The suspensions exhibited drag reduction in both horizontal and vertical upward flows after specific slurry velocities, which increased with increases in saturated concentration, slurry velocity, and particle aspect ratio (Javed et al., 2022a, 2022b; Javed et al., 2021; Vaezi et al., 2014). Although water-based slurries of ARB (i.e., wheat straw and corn stover) have been extensively studied by measuring their longitudinal frictional pressure drops flowing through horizontal and vertical pipelines for various mass concentrations, to the best of our knowledge, no work has been done to understand the frictional behaviour of wheat straw-aqueous slurry flows through inclined pipes.

The present study conducts an experimental investigation of the hydro-transport of wheat straw slurries through inclined pipe sections of varying slopes with the aim of understanding the fundamental parameters impacting the slurry's rheological characteristics during the flow. The specific objectives are to:

- Calibrate and commission the inclined pipe section using fine sand-aqueous slurries by comparing experimental frictional pressure drops at various concentrations and flow rates with pre-established empirical correlations.
- Examine the frictional behaviour and flow regions of uphill and downhill flows of wheat straw-aqueous slurries through inclined pipes at different concentrations and flow rates.

- Investigate the conditions of drag reduction for wheat straw-aqueous slurries in both uphill and downhill flows.
- Explore the effect of inclination on the onset velocity of drag reduction of wheat straw-water slurries in both uphill and downhill flows.

6.2 Materials and method

6.2.1 Experimental setup

Figure 6.1 shows the schematic of the experimental setup used in this study which comprises a 29 m long closed pipeline loop with a 50 mm inside diameter and Schedule 40 PVC transparent and carbon steel pipe sections, an open-impeller centrifugal pump (CD80M; Godwin Pumps Ltd., Bridgeport, NJ, USA) with a capacity of $38.52 \text{ m}^3 \text{ h}^{-1}$ for 157 kPa at 1765 rpm and a $\approx 43\%$ efficiency (for water) driven by a 7.45 kW electric motor (CC 068A; Madison Industrial Equipment, Vancouver, BC, Canada) to pump the desired fluid (i.e., water or conventional solids-water or biomass-water slurries), a glycol chiller (KEZA030H8; KeepRite Refrigeration Corp., ON, Canada) to maintain the fluid temperature, a 0.64 m long flow visualisation section, a magnetic flow meter (FMG-424; Omega Eng., Stamford, CT, USA) set at $200D$ (D is the inside diameter of the pipeline) downstream of the slurry pump to measure the bulk velocity of the fluid, a temperature sensor (RTD-E; Omega Eng., Stamford, CT, USA) to monitor the fluid temperature, and a large semi-circular pipe bend (with a curvature radius $[R_c]$ of $14.5D$) upstream of a 7.6 m long inclined pipe section.

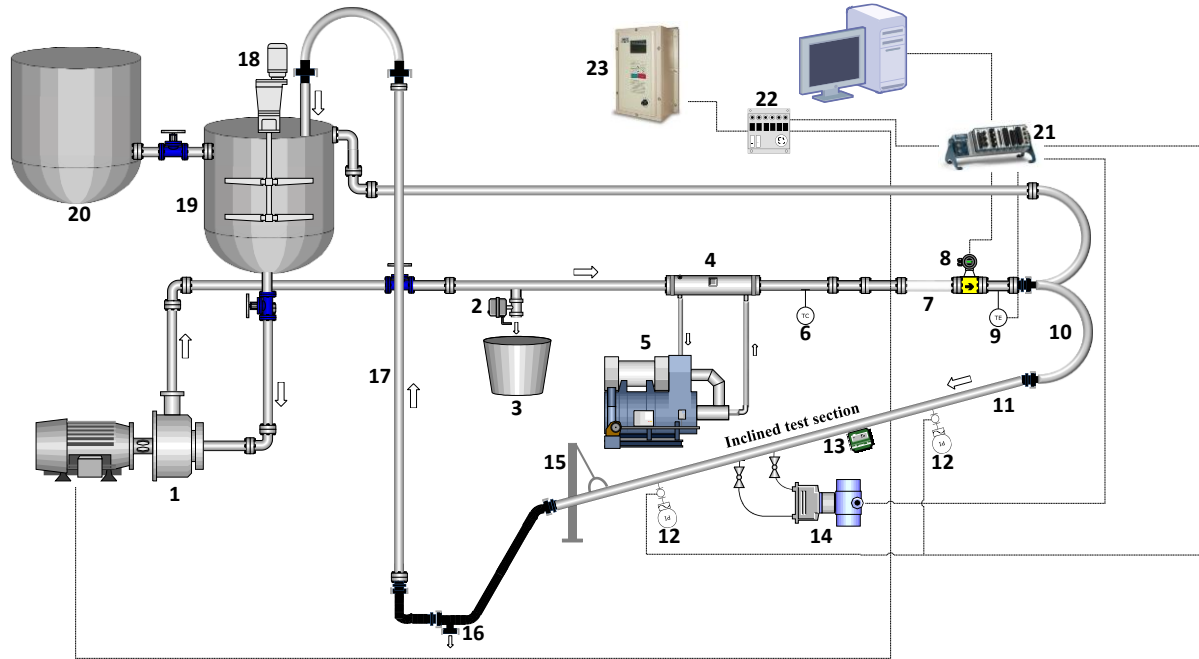


Figure 6.1: Schematic of the experimental setup: (1) centrifugal slurry pump, (2) drain valve-1, (3) drain tub, (4) counter-flow heat exchanger, (5) glycol chiller, (6) thermocouple, (7) flow visualisation section, (8) magnetic flow meter, (9) temperature sensor, (10) semicircular pipe bend, (11) inclined pipe section, (12) pressure transducer, (13) inclinometer, (14) differential pressure transmitter, (15) lifting mechanism for inclined pipe, (16) drain valve-2, (17) return pipe, (18) mixer with double impeller, (19) mixing tank, (20) water supply tank, (21) data logger, (22) watt transducer, (23) variable frequency drive.

It also includes two flush diaphragm pressure transducers (PTs) (PX42G7; Omega Eng., Stamford, CT, USA), each with a range of 0-104 kPa and accuracy of $\pm 0.25\%$ to measure fluid pressures upstream and downstream of the inclined pipe, a digital inclinometer (2170-1; Insize Co. Ltd., Suzhou, Jiangsu, China) with a magnetic base and a range of 0-360° with 0.1° resolution and accuracy of $\pm 0.2^\circ$ to measure the angle of inclination of the inclined pipe section, a differential pressure transmitter (DPT) (FKCT22V55; Fuji Electric Ltd, France) with a range of 0-6 kPa and

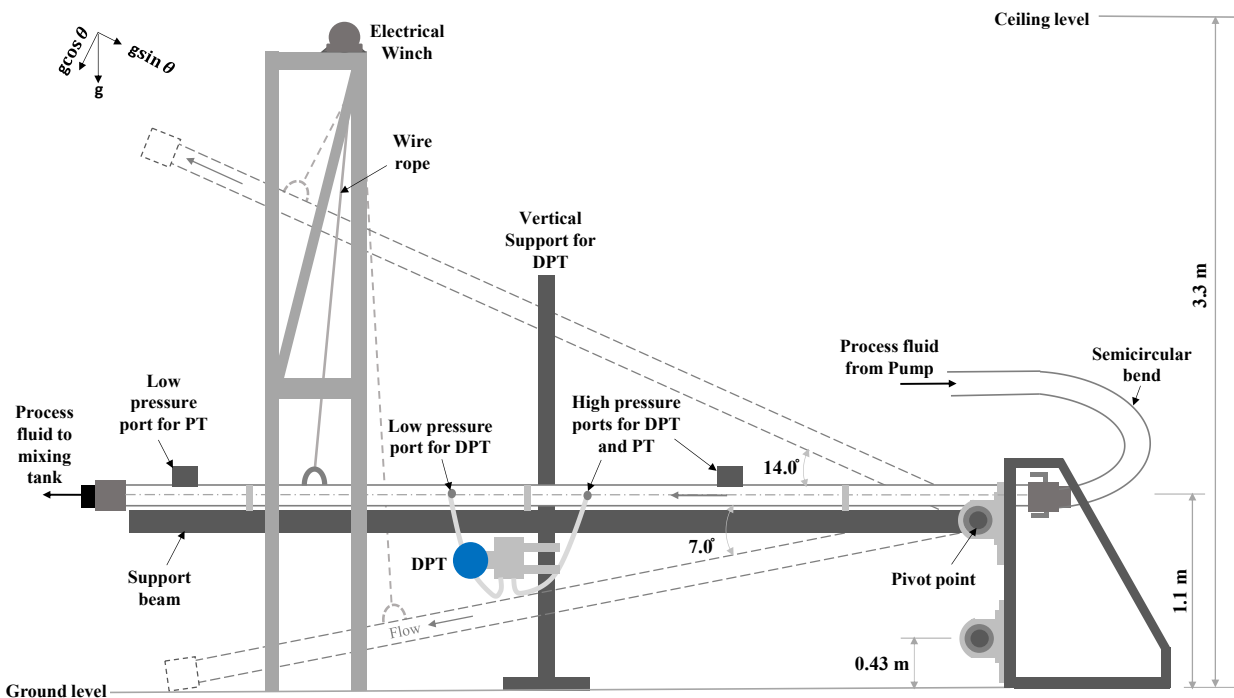
accuracy of $\pm 0.04\%$ (of the adjusted span) to measure the fluid pressure drop across the inclined test section, a conical mixing tank (0.8 m diameter and 455 L capacity) connected to a centrally placed heavy-duty gear-driven vertical mixer (EV6P50M; Lightning Inc., Rochester, NY, USA) with a double impeller powered by a 0.37 kW electric motor (3336P; Baldor reliance, ABB Motors and Mechanical Inc., Fort Smith, AR, USA) to agitate the solids-water slurry in the tank, a watt transducer (PC5; Flex-Core, Columbus, OH, USA) to measure the power consumed by the induction motor of the centrifugal pump for any specific velocity of fluid, and a 14.91 kW variable frequency drive (VFD) controller (MA7200-2020-N1, TECO-Westinghouse Co., Round Rock, TX, US) to change the rotation of the induction motor of the centrifugal pump to obtain the required fluid velocity. Further details on the type of mixer impeller and the heat exchanger used in the experimental setup are given in our earlier studies (Javed et al., 2022b; Vaezi & Kumar, 2014b).

The DPT was connected to the inclined pipe at high- and low-pressure ports with a span (L) of $10D$ through PVC tubes/impulse lines, each with an inner diameter and length of 9.5 mm and 0.89 m, respectively. The specifications of the impulse lines were selected based on best practice (Reader-Harris & McNaught, 2005). The impulse lines contained water that served as a pressure-sensing medium between the fluid flowing inside the inclined pipe and the diaphragm of the DPT. The pressure drop of the fluid flowing inside the inclined pipeline sensed by the DPT was converted to electrical output signals of 4-20 mA. The output signals obtained from all the instruments except the mixer and heat exchanger (i.e., watt transducer, magnetic flow meter, temperature sensor, the DPT, and PTs) connected to the closed pipeline loop were recorded at a frequency of 100 data s^{-1} on a customized data-acquisition system. The data-acquisition system was equipped with a resistance temperature detector (RTD) input module (NI9217; National

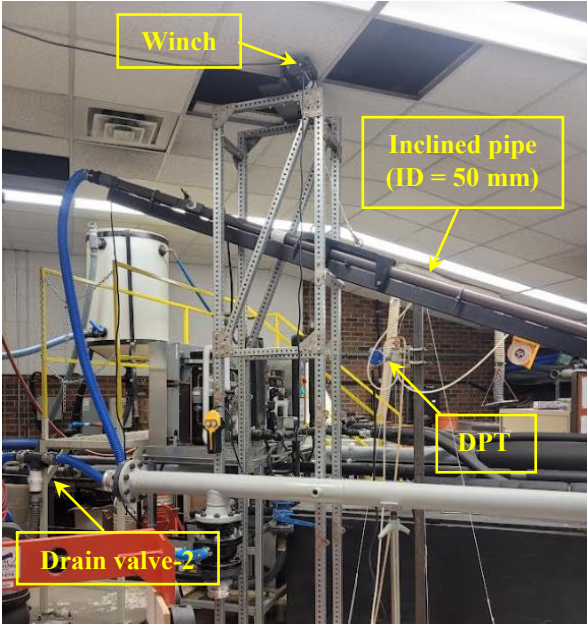
Instrument Corp., Austin, TX, USA), the current excitation module (NI9219; National Instrument Corp., Austin, TX, USA) with four channels each dedicated to different types of measurements, and a data-acquisition program (LabView V.9.0.1f2; National Instrument Corp., Austin, TX, USA).

6.2.2 Physical arrangement for various pipe inclinations

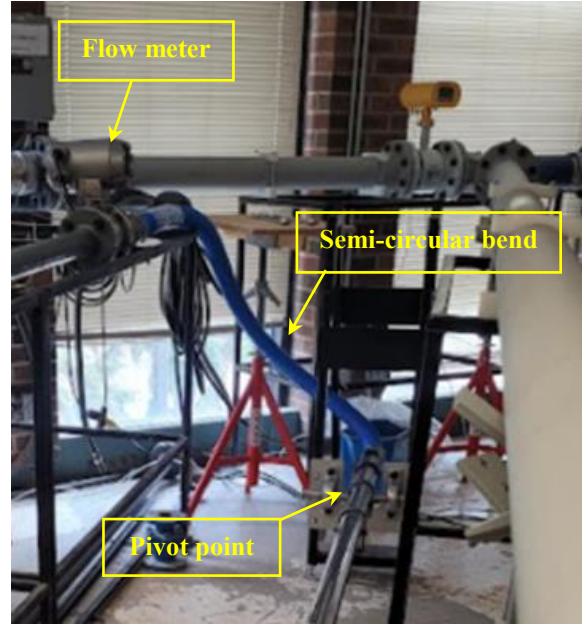
The physical arrangement of the inclined pipe section built in the large-scale fluids lab at several inclination angles is shown in Figure 6.2. The heights of the centerlines of the horizontal pipe sections of the closed pipeline loop and the lab ceiling above the ground were 1.1 m and 3.3 m, respectively. At a height of 1.1 m above ground level, there was a limitation for the inclined pipe section (7.6 m long) to attain an inclination angle (θ) $> 7^\circ$ in the descending position and 14° in the ascending position with respect to the x-axis (Figure 6.2 [a]).



(a)



(b)



(c)

Figure 6.2: (a) Supporting structure and lifting mechanism for the inclined pipe section, (b) The inclined pipe section in ascending position for an inclination angle (θ) = 21°, and (c) The inclined pipe section in horizontal position at a height of 0.43 m above the ground.

To reach the maximum possible angle of inclination for the inclined pipe section in the ascending position, the pivot point of the inclined pipe section was shifted downward from an existing position of 1.1 m to 0.43 m above the ground. With this arrangement, the increase in θ to 21° was possible for the ascending pipe position (Figure 6.2 [b] and [c]). However, this arrangement did not affect the pressure drop measurements of water or slurries in the horizontal position of the inclined pipe with a pivot point placed at any of these heights (Figure A6 in Appendix A). The inclined pipe was attached at its bottom to a support beam made from hollow carbon steel pipe with a rectangular cross-section (76 mm x 38 mm). This support beam was strong enough to minimise the chances of vibrations that could be created during slurry flow through a 7.6 m long

inclined pipe section. The beam was pivoted at one end (i.e., near the large semicircular pipe bend) connected to a wire rope of an electrical winch (SKU-8880429, 1500 lb. 120V AC; Pro. Point Automotive, ON, Canada) at the other end (i.e., near the downstream end of the pipe) for a quick and automatic movement of the inclined pipe section in an upward or downward direction to a desired angle (Figure 6.2 [a]). To avoid the chances of transmitting vibrations from the inclined pipe section to the DPT during pressure measurements, an independent vertical support was used to hold the DPT in the desired position. This vertical support was isolated from the entire support structure of the inclined pipe section (Figure 6.2 [a]). The DPT was provided with a smartly operated moveable base with a locking and unlocking mechanism to move it to a desired position on the vertical support. For any pipe inclination, the position of the DPT was always located at a sufficient distance below the pipe centerline as recommended by the manufacturer (Fuji Electric, 2014). The primary reason for installing the moveable base with the DPT was to keep the lengths of the impulse lines as small as possible while changing the θ for the inclined pipe section; this could help reduce errors in pressure drop measurements (ISO, 2007).

6.2.3 Locations of pressure ports

The downstream and upstream distances of the high- and low-pressure ports of the DPT and PTs with respect to the nearest flow disturbances in the loop were carefully selected to ensure proper flow field recovery and the elimination of the end effect on the pressure measurements. The nearest flow disturbance on the upstream of the high-pressure ports was a semicircular bend and on the downstream of the low-pressure ports was a flexible hose connecting the exit end of the inclined pipe section to drain valve-2 (shown in Figure 6.1 and Figure 6.2 [a]). The maximum permissible distance reported in the literature downstream of the semicircular bend to dissipate the secondary flows is $35D$ (Anwer et al., 1989; Azzola et al., 1986; Rowe, 1970; Vaezi et al., 2014). In our

earlier work, the downstream distances of the low-pressure ports of the DPT and PTs were selected with respect to the corresponding pipe section exits as $5D$ and $12D$, respectively (Javed et al., 2021; Vaezi et al., 2014). Therefore, for the inclined pipe section, the upstream and downstream distances of high- and low-pressure ports for both the DPT and PTs with respect to the corresponding nearest flow disturbance were taken to be equal to or greater than the maximum distance reported in the literature (Javed et al., 2021; Vaezi et al., 2014). These distances are shown in Table 6.1.

Table 6.1: The locations of the high- and low-pressure ports of the DPT and PTs on the inclined pipe section in the closed pipeline loop

Instrument	Span (L)	Distance of high-pressure port from the semicircular bend	Distance of low-pressure port from the inclined pipe's exit
DPT	$10D$	$95D$	$38D$
PT	$91D$	$40D$	$12D$

6.2.4 Feedstock preparation and particle size analysis

The wheat straw bales of dry stalks were obtained with some initial moisture content (MC) directly from farms in Northern Alberta, Canada, and used a commercially available knife mill (SM 100; Retsch Inc., Surrey, BC, Canada) to grind the bales into various particle sizes. The ground straw particles obtained from knife milling were classified by a commercial classifier (BM&M Inc., Surrey, BC, Canada) into four different groups with nominal particle sizes of 19.2 mm, 6.4 mm, 3.2 mm, and <3.2 mm. Further details on the nominal sizes and their significance are given in our earlier work (Vaezi et al., 2013). The nominal sizes were chosen based on the classifier sieve opening sizes. The classifier had seven sieves. The particles obtained in the top three sieves were discarded. The nominal sizes obtained in the bottom four sieves are the four different groups of

particles with specific particle lengths given in Vaezi et al.'s paper (2013). The grinding and classification of wheat straw bales were performed in the laboratory. The current study focuses on the hydro-transport of wheat straw particles of a nominal size of 6.4 mm through an inclined pipe section. Because the duration of the inclined pipe experiments with ARB (see section 6.2.6) was almost twice the duration of the vertical and horizontal pipe experiments, the chance of particle degradation is higher in inclined pipes. Particle degradation occurs due to (1) particle-particle interactions or (2) the multiple passing of slurry through the centrifugal pump in the closed pipeline loop. Based on our previous experience with the degradation of wheat straw particles (Vaezi et al., 2013) and the limitations on achieving higher slurry velocities during the hydro-transport of different nominal particle sizes of wheat straw through vertical pipes (Javed et al., 2022a, 2022b), we selected the nominal size of 6.4 mm for the initial phase of our experiments with the inclined pipe section to get the highest achievable slurry bulk velocity and the lowest effect of particle degradation. We recently performed particle size distribution (PSD) and shape analysis of knife-milled wheat straw particles through dynamic image processing in the Camsizer (Javed et al., 2022a). Table 6.2 shows the particle morphology of wheat straw particles of a nominal size of 6.4 mm obtained from the Camsizer.

Table 6.2: Particle morphology for knife-milled wheat straw particles of the 6.4 mm nominal size using the Camsizer (Javed et al., 2022a)

	D_{90}	D_{50}	D_{10}	$X_{ig}^a \pm \sigma_{ig}^b$	Max.	Min.	Aspect ratio (φ_p)
$d_{FE,max}$ (mm)	6.04	4.85	3.58	4.84±0.93	11.44	3.35	8.70
$d_{c,min}$ (mm)	2.87	1.52	0.59	1.37±0.87	6.14	0.28	

^a $X_{ig} = [(D_{16} + D_{50} + D_{84})/3]$, Graphic mean (Vaezi et al., 2013)

^b $\sigma_{ig} = [\{(D_{84} - D_{16})/4\} + \{(D_{95} - D_5)/6.6\}]$, Graphic standard deviation (Vaezi et al., 2013)

Here, d_{FE_max} is the Feret diameter (the longest distance, at any given angle, between two parallel tangents of a particle projection) or particle length and d_{c_min} is the short chord diameter (the smallest of the longest chords of a particle projection) or particle width. The characteristics' dimensions D_{10} , D_{50} , and D_{90} shown in Table 6.2 for both d_{FE_max} and d_{c_min} are the 10th, 50th, and 90th percentiles derived from the cumulative distributions of the corresponding parameters. X_{ig} and σ_{ig} represent the graphic mean and standard deviations for both d_{FE_max} and d_{c_min} . The complete procedure of the dynamic image processing of ARB using the Camsizer is given in detail in our recent work (Javed et al., 2022a). Figure 6.3 (a) shows the microscopic image of wheat straw particles of a nominal size of 6.4 mm captured by the high-speed Camsizer cameras.

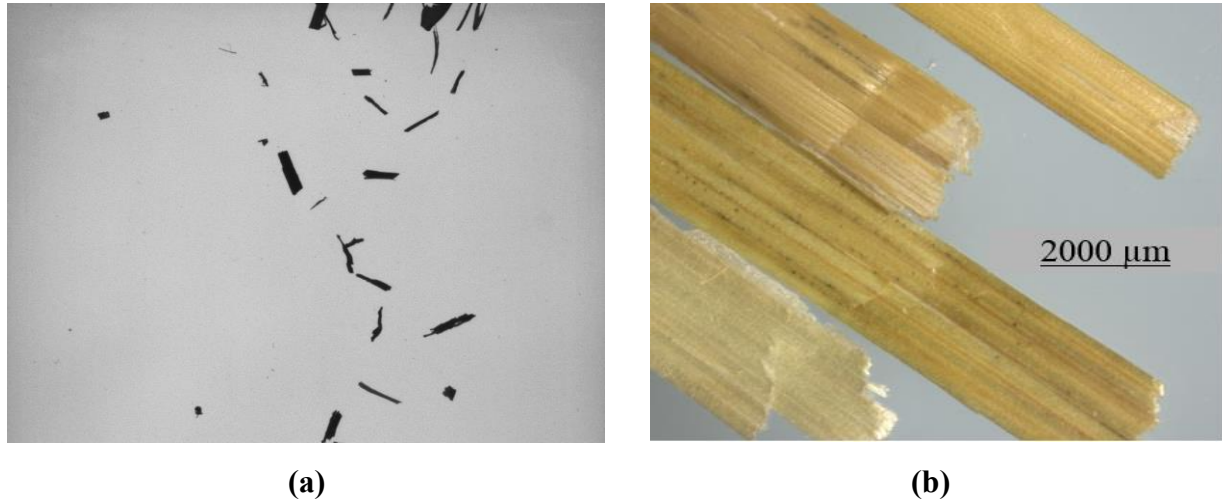


Figure 6.3: Microscopic images for the 6.4 mm nominal size of wheat straw particles taken by (a) high-speed Camsizer digital cameras (not to scale) and (b) light microscope (Zeiss Stemi 508).

Knife-milled wheat straw particles are mostly composed of rectangular rib-like particles and are fibrous (i.e., their aspect ratio is >3.3) in nature with a length range of 3.35-11.44 mm (see Table 6.2) for the 6.4 mm nominal particle size. Further, wheat straw particles have fewer irregularities

and their surfaces are repetitive and less random in nature (Figure 6.3 [b]) than corn stover. More details on the surface features of wheat straw particles can be seen in our previous work (Vaezi et al., 2013).

6.2.5 Slurry preparation

Once the pipeline loop was thoroughly cleaned with water or an occasionally circulating sand-water slurry, clear water was added to the loop to the required level in the mixing tank. The clean water was circulated by the centrifugal pump running at full speed for a few minutes to deaerate the system. To ensure reliable pressure drop measurements, the impulse lines of the DPT were cleaned and filled with clear water while the pipeline loop was running. This removed contaminants (if any) and air bubbles from the impulse lines. Then the pressure drop measurements for clear water were recorded for velocity ranges of 0.5-4.7 m s⁻¹ at a controlled temperature maintained by the chiller. The mixer was then turned on gradually to prevent adding air to the system (resulting from cone formation on the water surface inside the tank). To prepare an aqueous slurry of the nominal 6.4 mm particle size of wheat straw with the desired solid mass concentration of 30%, the pre-measured mass of straw with some initial moisture content was slowly added to the mixing tank. This was the highest mass concentration that could be tested in the slurry loop for this particle size because the inside diameter (ID) of the pipeline was small (i.e., the ID = 50 mm) and for $C_m > 30\%$, the loop clogged at low velocities.

Depending on the initial moisture content of the wheat straw particles and the water temperature inside the loop, the wheat straw-water slurry was continually circulated through the loop for roughly 12 to 14 hours until it became stable (i.e., fully saturated) at the highest attainable C_m . ARB has a propensity to absorb moisture when water is introduced to it; as a result, the slurry's rheology changes throughout pumping until it stabilises at a saturated MC of almost 82% for the

suspended biomass particles (Javed et al., 2022b). After every hour of the slurry's circulation through the pipeline loop, the slurry stability was examined by observing its pressure drop and velocity changes. When these variations in both the pressure drop and velocity fell to about 1.0-2.0% h⁻¹, the wheat straw slurry was deemed stable.

6.2.6 Slurry pressure drop measurements

Once the wheat straw-water slurry was fully saturated or stable at the highest mass concentration, i.e., $C_m = 30\%$, its pressure drop measurements were recorded for the entire range of bulk velocities (0.5-4.7 m s⁻¹) with mutual velocity intervals of 0.5 m s⁻¹ and an angle of inclination (θ) of 0° (i.e., horizontal position) for the inclined pipe section with respect to the x-axis. The θ of the inclined pipe was then changed with the help of an electric winch to the desired angle (i.e., a 7° descending pipe position) and the pressure drop measurements were recorded for the complete range of slurry bulk velocities. A similar procedure was repeated for the ascending position of the inclined pipe section of $\theta = 7^\circ$. All the pressure drop measurements were thus recorded for the wheat straw-water slurry flows at inclined pipe positions of 0°, 7° (ascending), and 7° (descending) and $C_m = 30\%$. For each of the angular positions of the inclined pipe section at $C_m = 30\%$, the pressure drop measurements were recorded after 5 minutes of acquiring the desired pipe angle to avoid any errors in measurements. The slurry was then diluted to $C_m = 25\%$ by adding the required volume of water from the water supply tank to the mixing tank to the desired slurry level as shown in Table A5 in Appendix A.

The slurry was drained using drain valve-1 (shown in Figure 6.1) to a fixed level of 60 gallons (imperial) in the mixing tank after at least 5 minutes of slurry dilution to reach $C_m = 25\%$. The same procedure was then followed for the pressure drop measurements of the wheat straw-water slurry flows at $C_m = 25\%$ and the three positions (0°, 7° ascending, and 7° descending) of the

inclined pipe section as described earlier for a slurry of $C_m = 30\%$. Table A5 in Appendix A shows the levels of wheat straw-water slurry required in the mixing tank to obtain the saturated mass concentrations of 25% to 5% by diluting the slurry from the highest to the lowest concentration at equal intervals of 5%. Every time the wheat straw-water slurry was diluted from a C_m of 25% to 5%, the pressure drops of the corresponding slurry concentrations were recorded at the three angular positions (0° , 7° ascending, and 7° descending) of the inclined pipe section in a similar way as described for $C_m = 30\%$ and 25%. All the pressure drop measurements of the biomass slurry for the range of C_m 's from 30% to 5% were recorded during a single trial of the experimental run. The pressure drop experiments for ARB-water slurries in the inclined pipe were longer in duration (approx. 42-45 h) than those in the vertical and horizontal pipe sections (approx. 22-26 h). Therefore, instead of taking pressure drop measurements at $\theta = 14^\circ$ of the inclined pipe section with the pivot point's position of 1.1 m above ground level, this angle was included for the second trial for the second position of the pivot point at 0.43 m above the ground (Figure 6.2 [a]). To obtain the slurry pressure drops for θ of 0° , 14° , and 21° in the ascending positions of the inclined pipe section, the pivot point of the supporting beam (Figure 6.2 [a] and [c]) was shifted from 1.1 m to 0.43 m before starting the experiment. The procedure for the rest of experiment is the same as described for three angular positions of 0° , 7° ascending, and 7° descending of the inclined pipe section.

6.2.7 Moisture content and density measurements

ASABE S358.3 standards were used to estimate the wet basis or initial MC of the nominal 6.4 mm ground wheat straw particles (ASABE, 2012). To measure the MC, five samples with a net weight of at least 25 g each were collected from the required nominal size of chopped wheat straw particles. They were then oven-dried at 105°C for 24 hours. The saturated density of the particles

was determined by following ASTM C127 standards (ASTM, 2015). The saturated wheat straw particle samples were collected during the dilution phase of the slurry as it ran through the pipeline loop. The samples were spread on a thick paper towel to absorb their surface moisture. A perforated cylinder with a diameter and height of 150 mm was loosely filled with the saturated wheat straw particles and weighed in both air and water. The difference between these weights is the buoyant force acting on the wheat straw particles; from this force, the saturated density of the material was evaluated. On average, the initial MC and the saturated particle density of wheat straw particles were found to be $6.492\% \pm 0.5$ and $1061.03 \text{ kg m}^{-3} \pm 6.62$, respectively. Table 6.3 shows the approximate values of the saturated densities for several volumes and mass percentages of saturated and dry solids of aqueous-based wheat straw slurries considering a density of water to be 1000 kg m^{-3} .

Table 6.3: Volume and mass percentages of saturated and dry solids of wheat straw-water mixtures

Mass percentage of saturated solids	Volume percentage of saturated Solids ^c	Mass percentage of dry solids	Volume percentage of dry solids	Saturated slurry density
(%)	(%)	(%)	(%)	(kg m^{-3})
30	28.76	5.4	5.35	1014.49
25	23.89	4.5	4.45	1012.05
20	19.06	3.6	3.55	1009.62
15	14.25	2.7	2.65	1007.19
10	9.47	1.8	1.76	1004.79
5	4.72	0.9	0.88	1002.39

^cThe volume percentages of dry and saturated solids were evaluated by dividing the volumes of the dry or saturated solids with the total volume of slurry loop.

6.2.8 Calibration of the inclined pipe section

In the current investigation, the inclined test section (the horizontal, ascending, and descending positions) was calibrated by measuring the frictional pressure drops of clear water and aqueous slurries of fine sand ($d_{50} = 0.103$ mm) (at known volumetric concentrations, i.e., $C_V = 1\text{-}5\%$) passing through the pipe section at different velocities and comparing our results to those of corresponding models (Churchill, 1977; Durand, 1953; Durand & Condolios, 1952b; Gibert, 1960; Worster & Denny, 1955). Fine sand ($d_{50} = 0.103$ mm) was selected for the calibration of the experimental setup because (1) the slurries of fine sand with a mean particle diameter (d_{50}) range of 0.04-0.20 mm behave pseudo-homogeneously, that is, the particles remain dispersed because of their interaction with the turbulent eddies of the carrier fluid (Matousek et al., 2022), (2) the limit deposition velocity for the fine sand ($d_{50} = 0.103$ mm) is small (see Table 6.4) and the variation in the deposition velocity for these particles with respect to the pipe inclination is usually not very significant (Spelay et al., 2016), thus providing a wide range of slurry bulk velocities for the pressure drop analysis, (3) the local slip is negligible and the related velocity distribution would be slightly uneven (Matousek, 2002), (4) the delivered and in situ concentrations are almost the same for the fine sand particles because of the very small terminal settling velocity (Javed et al., 2021), thus these particles are suitable given that the experimental setup did not have a concentration measuring device (the reasons for the lack of concentration measuring device in our experimental setup are explained in one of our earlier studies (Javed et al., 2021)), and (5) the concentration gradient across the pipe cross-section would be very small for fine sand particles with no contact bed for velocities higher than the critical deposition velocity (Matousek, 2000, 2002).

The physical properties of the fine sand used in the present study are given in Table 6.4.

Table 6.4: Physical properties of the fine sand solids used in the calibration of the inclined pipe section

Material	Particle density(ρ_s)	Mean particle diameter (d_{50})	Terminal settling velocity(v_t)	Critical deposition velocity	Critical velocity for pseudo-homogenous regime
	(kg m^{-3})	(mm)	(mm s^{-1})	(m s^{-1})	(m s^{-1})
Fine sand ^d	2500	0.103	10.06 (Newitt et al., 1961)	0.52–0.76 (Wasp & Aude, 1970; Wasp et al., 1977)	0.895 (Newitt et al., 1961)

^dTarget Products, AB, Canada; Material grade: LM–125.

The experimental frictional pressure drop of the mixture in the inclined test section (Figure 6.1) was obtained by subtracting the static head caused by the pipe elevation from the pressure drop measured by the DPT connected to the pressure taps of the inclined test section through impulse lines filled with water. Equation 6.1 provides a general expression for the experimental frictional pressure drops of slurry flow through the inclined pipe section.

$$\left(\frac{\Delta P_f}{L}\right)_{m,\theta}^{Exp} = \left(\frac{\Delta P}{L}\right)_{m,\theta}^{Md} - (\rho_m - \rho_w)g \sin \theta \quad (6.1)$$

The indexes m , w , f , and θ represent the slurry (mixture), water (carrier fluid), friction, and pipe inclination with respect to the x-axis, respectively. The terms $\left(\frac{\Delta P_f}{L}\right)_{m,\theta}^{Exp}$ and $\left(\frac{\Delta P}{L}\right)_{m,\theta}^{Md}$ are the experimental frictional pressure and the measured pressure drops of the mixture flowing through an inclined test section of span L ; ρ_m and ρ_w are the mixture and water (carrier fluid) densities, respectively. The mixture density (ρ_m) was calculated using Equation 6.2:

$$\rho_m = \rho_w + C_V(\rho_s - \rho_w) = \rho_w / \{1 - C_m(1 - (\rho_w / \rho_s))\} \quad (6.2)$$

where C_V is the mixture's volumetric concentration for fine sand-water slurries, C_m is the mixture's saturated mass concentration for wheat straw-water slurries, and ρ_s is the density of the fine sand (Table 6.4) or saturated density (i.e., $1061.03 \pm 6.62 \text{ kg m}^{-3}$) of wheat straw particles. The inclination angle (θ) was taken as positive for the ascending position and negative for the descending position of the inclined pipe section, which is common practice for the inclined flows (Kao & JL, 1980; Vlasak et al., 2018). For the horizontal position of the inclined pipe section (i.e., $\theta = 0$), the gravity effect would be zero because the static head term in Equation 6.1 will be diminished, and the pressure drop measured by the DPT will directly give the frictional pressure drop of the slurry. Further, the static component of Equation 6.1 will be eliminated in the situation of water flowing through an inclined pipe section and water present in the impulse lines of the DPT, and we will obtain the frictional pressure drop directly from the DPT.

However, to obtain the total pressure drop of the fluid (mixture or water) in the inclined pipe section, the following expression was used:

$$\left(\frac{\Delta P}{L}\right)_{m,\theta}^{Total} = \left(\frac{\Delta P_f}{L}\right)_{m,\theta}^{Exp} + \rho_m g \sin \theta \quad (6.3)$$

The general relationship to define the theoretical frictional pressure drop $\left(\frac{\Delta P_f}{L}\right)_w$ of water flowing with a bulk velocity (v_w) through a test section of the span (L) with an inner diameter of D is given in Equation 6.4:

$$(\Delta P_f)_w = \rho_w g (h_f)_w = \frac{\rho_w (f_D)_w (L) (v_w)^2}{2D} \quad (6.4)$$

where g , $(f_D)_w$, and $(h_f)_w$ are the acceleration due to gravity, the Darcy-Weisbach friction factor, and the loss of head due to friction for water, respectively. The values of $(f_D)_w$ for the entire range of v_w were evaluated using Churchill's model (Churchill, 1977), which can be applied to all the flow regimes (laminar, transitional, and turbulent) of water through pipes with both smooth and rough surfaces (see Table A6 in Appendix A). Because the inclination of the pipe has no impact on the frictional pressure drop of water (Matousek et al., 2018) for all the inclinations ($-7^\circ \leq \theta \leq +21^\circ$) of the test section in the present work, Churchill's model was used to evaluate the theoretical frictional pressure drops of water. The theoretical frictional pressure drops for fine sand-water slurry flows were evaluated through the inclined pipe section using two semi-empirical models for heterogeneous flows in inclined pipes (Gibert, 1960; Worster & Denny, 1955). For the horizontal pipe section, the famous correlation proposed by Durand and Condolios (Durand, 1953; Durand & Condolios, 1952b) was used to evaluate the theoretical frictional pressure drops for fine sand-aqueous slurries. Table A6 in the appendix shows these semi-empirical models for horizontal and inclined flows.

The plots of the frictional pressure drop and bulk velocity of water at specific volumetric concentrations of aqueous fine sand slurries for inclined pipes at different inclinations with respect to the horizontal pipe position are shown in Figure 6.4. Excellent agreement was found between the experimental values and the corresponding models, validating the reliable design of the experimental setup used in the present work. In the case of water flowing through the inclined test section, the percentage error between the experimental frictional pressure drops and those obtained using Churchill's model was found to be 1.2-5.5% for the entire range of pipe inclinations and water flow rates (Figure 6.4 [a]).

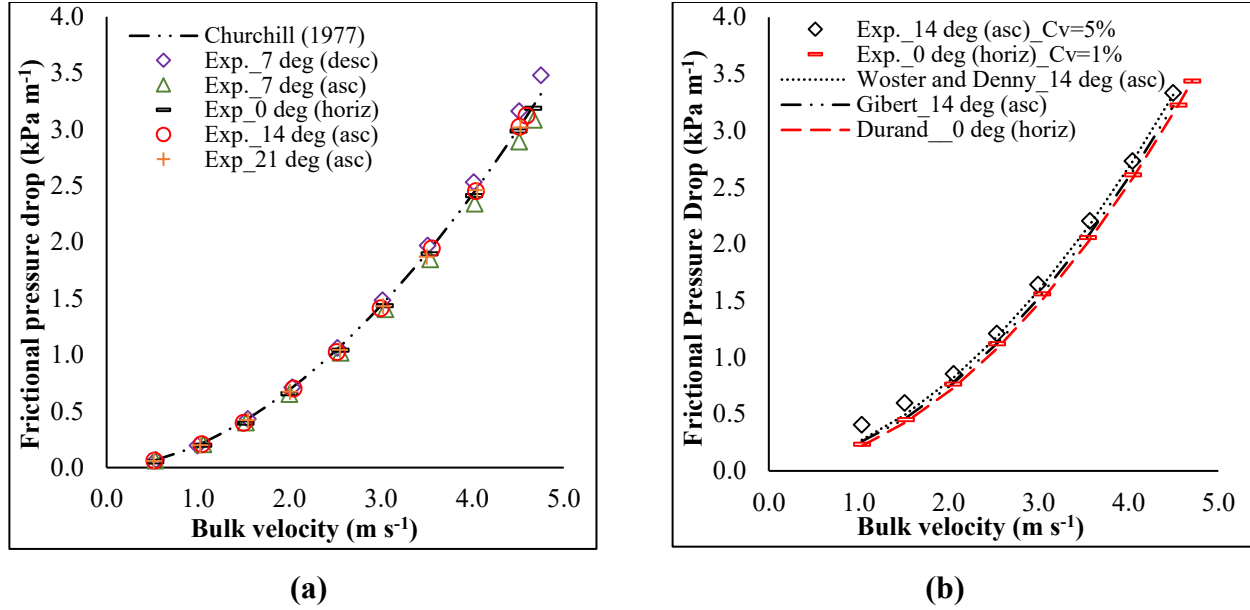


Figure 6.4: Calibration of the inclined pipe section at (a) $\theta = -7^\circ$ to $+21^\circ$ using clear water and (b) $\theta = +14^\circ$ and 0° using fine sand-water slurries of $d_{50} = 0.103$ mm for solid particles at volumetric concentrations of 5% and 1%, respectively

For the fine sand-water slurries (Figure 6.4 [b]; Figure A7 in Appendix A), Worster and Denny's model showed the best fit for all the inclined flows exhibiting the pseudo-homogeneous regime (i.e., for $v_m > 1.0$ m s⁻¹) with a percentage error of 0.16%-8.61%. One reason for good agreement between our experimental results with Worster and Denny's model is that their model was developed considering the negligible effect of the slip velocity. For the largest inclination angle (i.e., $+21^\circ$) and $C_v \geq 3\%$, the experimental results deviated from Worster and Denny's model at low slurry velocities, i.e., $v_m \leq 1.5$ m s⁻¹ (Figure A7 in Appendix A).

The maximum percentage error for the horizontal flows using Durand's model is 7.87% (Figure 6.4 [b]; Figure A7, Appendix A).

6.3 Experimental results and discussion

6.3.1 Frictional behaviour of various solids-water mixtures in inclined flows

6.3.1.1 Classical solids

Figure 6.5 illustrates the frictional pressure drops of fine sand-water slurries flowing at various volumetric concentrations ($C_V = 1-5\%$) and velocities $\geq 1.0 \text{ m s}^{-1}$ through the inclined pipe section at a θ of $+14^\circ$ and $+21^\circ$ relative to the x-axis.

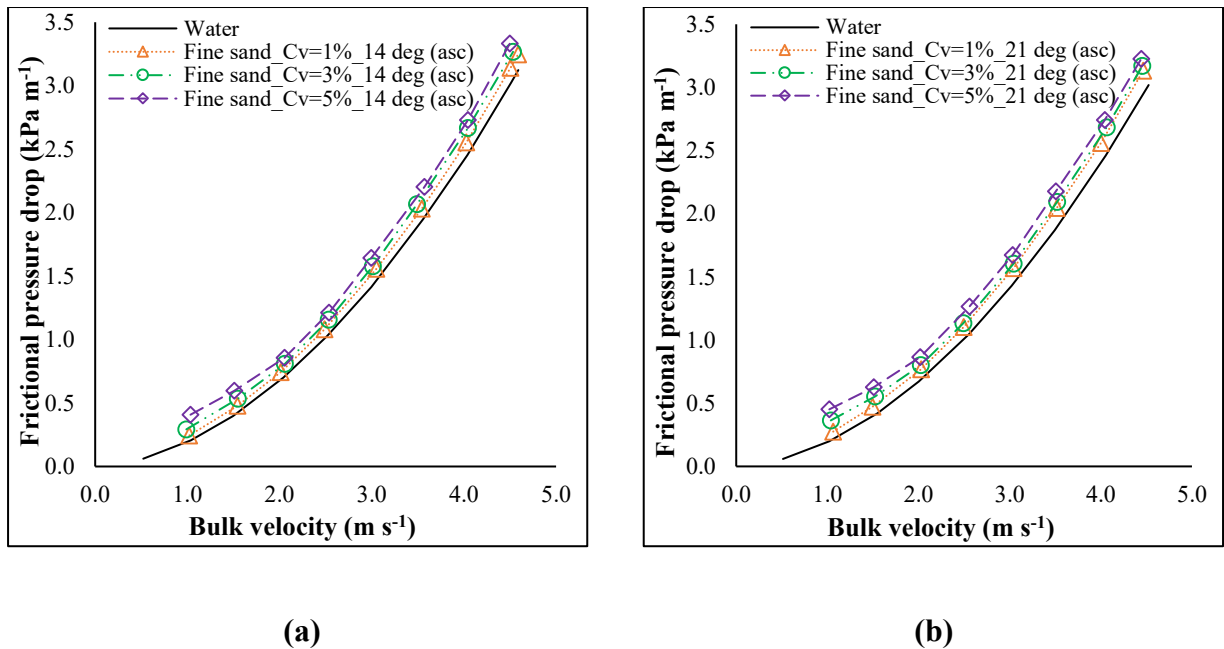


Figure 6.5: Frictional pressure drops for fine sand-water mixtures for velocities $\geq 1.0 \text{ m s}^{-1}$ and volumetric concentrations of $C_V = 1-5\%$ flowing through a 50 mm diameter inclined pipe section of (a) $\theta = +14^\circ$ and (b) $\theta = +21^\circ$.

Figure 6.5 shows that for any pipe inclination, the frictional pressure drop of fine sand-water slurries increases with solid volume concentration and is always greater than that of clear water for similar bulk velocities. The conventional solids-water slurries, which have mean particle diameters of 0.04-0.2 mm, actually show pseudo-homogeneous flow, that is, the solids are evenly

distributed across the pipe's cross-section (Matousek et al., 2022). In pseudo-homogeneous flows of settling slurries, the frictional pressure drop increases with velocity throughout the entire velocity flow range. This increase in frictional pressure drop with respect to slurry velocity follows the shape of a curve similar to that of the carrier fluid alone but at a certain offset from the carrier fluid's curve (Figure 6.5 [a] and [b]), indicating that solid particles contribute to flow friction through their interaction with the carrier fluid instead of through their interaction with each other and the pipe wall.

6.3.1.1.1 Flow visualisation

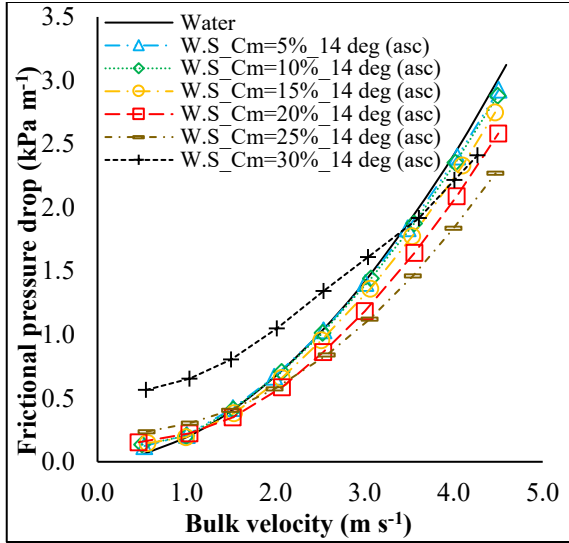
For the fine sand used in our current investigation, the critical deposition velocity and the critical velocity for pseudo-homogeneous flow were evaluated using standard correlations from several sources (Newitt et al., 1961; Wasp & Aude, 1970; Wasp et al., 1977). These values are shown in Table 6.4 and were reconfirmed by capturing the images of the flow patterns of fine sand-water slurries flowing at bulk velocities of 0.5 m s^{-1} and 1.0 m s^{-1} and various mass concentrations ($C_V = 1\text{-}5\%$) through inclined and horizontal pipe positions (shown in Table A7 in Appendix A). It was found through visual observations that for all the slurry concentrations of fine sand at slurry bulk velocities of 0.5 m s^{-1} , stationary bed or dunes formed at the pipe invert at all the slopes. However, as the slurry velocities increased to 1.0 m s^{-1} for any of the pipe inclinations ($-7^\circ \leq \theta \leq +21^\circ$), no bed formation was observed; instead, for most of the pipe slopes, the fine sand particles seemed to be fully dispersed across the pipe cross-section with a minimal concentration gradient at higher angles in the uphill flows. Vlasak et al. (2018) made a similar observation and determined that the influence of pipe inclination on local concentration distribution was insignificant for aqueous slurries of fine sand ($d_{50} = 0.18 \text{ mm}$) running at $C_V = 11\text{-}36\%$ through an inclined pipe section at

low inclination angles ($<\pm 25^\circ$) (Vlasak et al., 2018). Although Vlasak et al. used fine sand, the d_{50} was almost double the size of the particles we used in our present work.

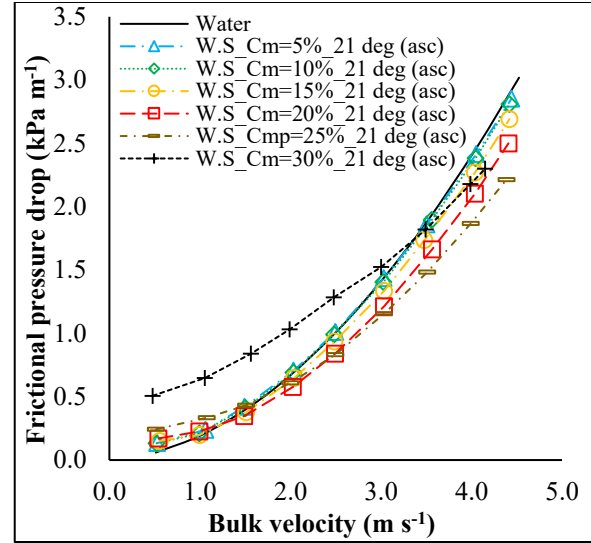
Based on visual observations, findings from the literature, and calculations of specific parameters for the fine sand from pre-established correlations (shown in Table 6.4), it can be deduced that fine sand-water slurries in inclined flows exhibited a pseudo-homogeneous flow for $v_m \geq 1.0 \text{ m s}^{-1}$ and, at lower velocities, i.e., $\leq 1.0 \text{ m s}^{-1}$, these slurries either showed heterogeneous flow with a weak concentration gradient across the pipe cross-section or exhibited a stationary bed for $v_m = 0.5 \text{ m s}^{-1}$. For the fine sand-water suspensions flowing through inclined pipe sections for all the inclinations at $v_m \geq 1.0 \text{ m s}^{-1}$, we evaluated the corresponding frictional pressure drops using the prepared volumetric concentrations (i.e., $C_V = 1\text{-}5\%$) because of the absence of slip.

6.3.1.2 Wheat straw particles

Figure 6.6 shows the frictional pressure drops of 6.4 mm particle size wheat straw-water suspensions flowing at different saturated mass concentrations ($C_m = 5\text{-}30\%$) and velocities of 0.5 m s^{-1} through the pipe section with inclinations of $+14^\circ$ and $+21^\circ$ relative to the x-axis. In inclined flows of wheat straw-water slurries (Figure 6.6; Figure A8, Appendix A), the frictional pressure drops increased in proportion to the increase in the slurry's velocity for any concentration. This is the behaviour of any solids-water suspensions in pipe flows regardless of the type of solids (i.e., classical solids or fibers) and pipe inclination (Javed et al., 2021; Matousek, 2009; Rai, 1972; Steen, 1989). Because the frictional pressure drop has a quadratic relationship with the suspension velocity (Equation 6.4), it increases with an increase in velocity. Equation 6.4 is a general equation for evaluating the frictional pressure drop of water or any suspension. In the case of a suspension, the subscript w (water) is replaced by m (mixture).



(a)



(b)

Figure 6.6: Frictional pressure drops for aqueous slurries of a 6.4 mm particle size of wheat straw for velocities $\geq 0.5 \text{ m s}^{-1}$ and $C_m = 5\text{-}30\%$ flowing through a 50 mm diameter inclined pipe section at (a) $\theta = +14^\circ$ and (b) $\theta = +21^\circ$.

Further, it was observed that for low velocities and all the concentrations of wheat straw-aqueous slurries (Figure 6.6; Figure A8, Appendix A), except for the suspensions of low concentrations, i.e., $C_m = 5\text{-}10\%$ flowing through the ascending pipe position with an inclination angle of -7° , the pressure drops were always above the water curve; however, after specific slurry velocities, they were consistently below the corresponding pressure drops of clear water. This unique characteristic differentiates the wheat straw-water suspensions from the conventional solids-water suspensions in pipe flows where the pressure drop curve is always above the water curve (see Figure 6.5) for the entire range of slurry velocities and mass concentrations. Wheat straw particles are fibrous and behave like other natural or synthetic fiber suspensions (Bobkiewicz & Gauvin, 1965; Javed et al., 2021; Kerekes, 1971; Radin et al., 1975). In the fiber-water suspension flow through pipes, the

fibers interact with each other mechanically, hydro dynamically, or both, forming networks within the carrier fluid and significantly impacting the suspension's rheological characteristics. The presence of fibers in the carrier fluid offers exceptional resistance to the fluid flowing over the fibers. Eventually, it suppresses the fluid's turbulence intensity by damping hydrodynamic instabilities. After a specific suspension velocity, it decreases the frictional pressure drop of fiber-based suspensions with respect to the carrier fluid (Steen, 1989; Vaseleski & Metzner, 1974).

One distinctive feature of knife-milled wheat straw particles over natural or synthetic fibers is the wide range of particle lengths with a low aspect ratio, which increases the probability of the hydrodynamic interaction of these particles with the surrounding fluid (because to prepare a specific solid mass concentration with a required amount of dry mass, the number of particles with a wide range of sizes would be higher than the number with a narrow size distribution, which is typical of synthetic fibers) as well as the interactions among the particles themselves at even low suspension concentrations. For instance, in the present study, a 6.4 mm nominal particle size of wheat straw was used with an aspect ratio of 8.7 (Table 6.2). In contrast, the aspect ratios of nylon fibers used by Kerekes and Douglas were 12-74 (1972). Wheat straw particles tend to reduce turbulence intensity at even low suspension concentrations, reducing the frictional pressure drops of the suspensions relative to the water (or carrier fluid) beyond specific suspension velocities. This behaviour can be observed in Figure 6.6 for wheat straw-water suspensions at $C_m = 5-10\%$.

Further, it is evident from Figure 6.6 that with increases in the slurry concentration, the pressure drops of wheat straw-water suspensions decreased after certain velocities for each concentration of the suspension. This is attributed to the increase in the particle-particle and particle-fluid (hydrodynamic) interactions, which increases the apparent suspension viscosity (Djalili-Moghaddam & Toll, 2006), the strength of the fiber network, and, ultimately, the ability of large

flocs to grow at higher fiber concentrations and low suspension velocities (Duffy, 2006; Javed et al., 2022a). Hence a further increase in the concentration of wheat straw suspension beyond $C_m = 10\%$ flowing through any of the pipe inclinations (-7° to $+21^\circ$) causes more significant suppression of the longitudinal turbulence intensities and, consequently, a further decrease in the frictional pressure drop compared to the water curve. At higher concentrations (i.e., $C_m = 25\text{-}30\%$) of wheat straw-water suspensions for all pipe inclinations, because of extensive increases in the mutual interactions of the wheat straw particles and the strength of their networks, larger flocs will be developed, particularly at low flow rates. Therefore a decrease in the frictional pressure drops of highly concentrated wheat straw suspensions (i.e., $C_m = 25\text{-}30\%$) was observed relative to water at higher velocities. The reasons for this behaviour have been elaborated in section 6.3.2.2. Visual observations (despite the dark brown background, which made the analysis challenging) showed no bed formation for the 6.4 mm particle size wheat straw-water slurries across the whole range of mass concentrations ($C_m = 5\text{-}30\%$) running down the inclined pipe section of any of the slopes (-7° to $+21^\circ$) used in the current investigation, even at the minimal slurry velocity of 0.5 m s^{-1} .

This outcome was on par with an earlier study on the deposition velocity of biomass particles, in which it was discovered that this velocity was $0.21\text{-}0.28 \text{ m s}^{-1}$ for slurries of wheat straw particles with $d_{50} = 4.81 \text{ mm}$ for $C_m = 5\text{-}20\%$ in horizontal flows (Vaezi et al., 2018). Further, in the earlier work, the terminal settling velocity (v_t) of several particle lengths (5-30 mm) of wheat straw was evaluated as $13\text{-}17 \text{ mm s}^{-1}$ in a quiescent medium and it was found that these particles were buoyant (i.e., $[v_m/v_t] \leq 0.021$) specifically for $v_m \geq 0.5 \text{ m s}^{-1}$ and particle sizes of 5-10 mm (Javed et al., 2022a). This means that for $v_m = 0.5 \text{ m s}^{-1}$, it was reasonable to assume that there was no slip between the liquid and solid phases of the 6.4 mm nominal size of wheat straw particles with $d_{50} = 4.85 \text{ mm}$ and that the in situ concentration of the suspension was almost equal to the delivered

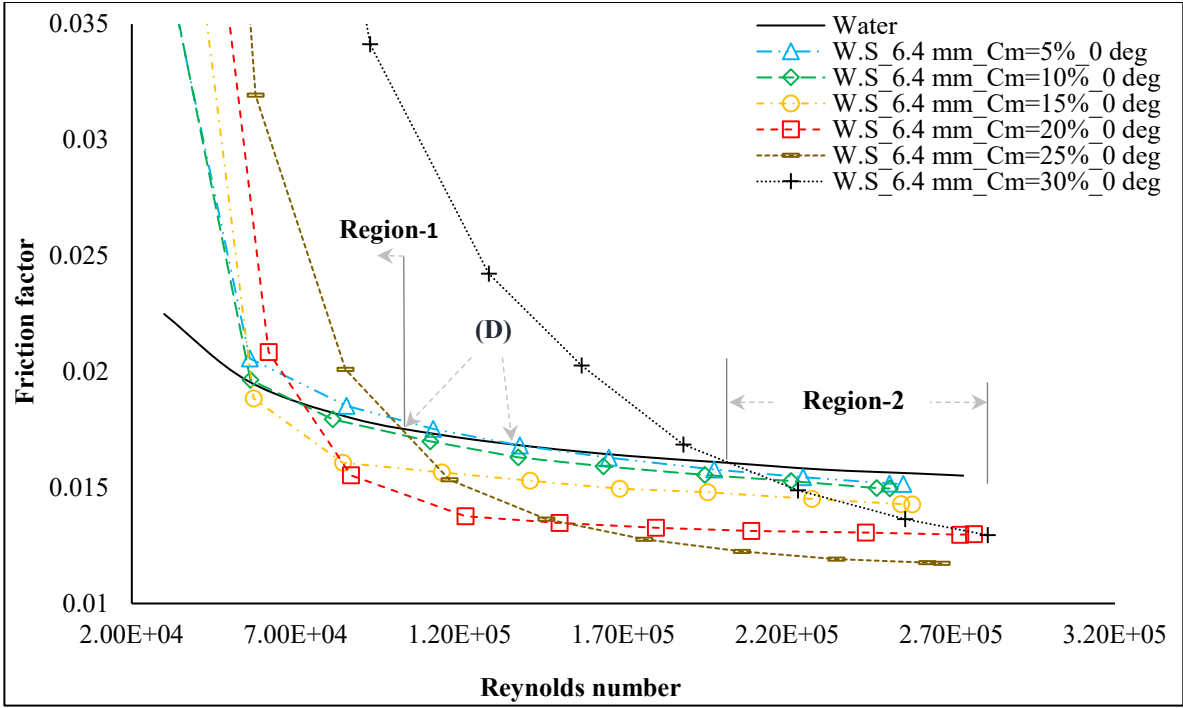
concentration for the minimum slurry velocity used in the current study. Therefore, it was concluded that the biomass-water suspensions were flowing as a heterogeneous mixture with some concentration gradient across the pipe cross-section for all the pipe inclinations at the minimum slurry velocity (i.e., 0.5 m s^{-1}).

Since the delivered concentration of the 6.4 mm nominal particle size of wheat straw suspension was found to be almost equal to the prepared concentration with a maximum difference of 7% (Javed et al., 2022b), the prepared mass concentrations were used (i.e., $C_m = 5\text{-}30\%$) and the saturated slurry densities shown in Table 6.3 to evaluate the frictional pressure drops of these suspensions in a similar fashion as we did for the fine sand-water slurries.

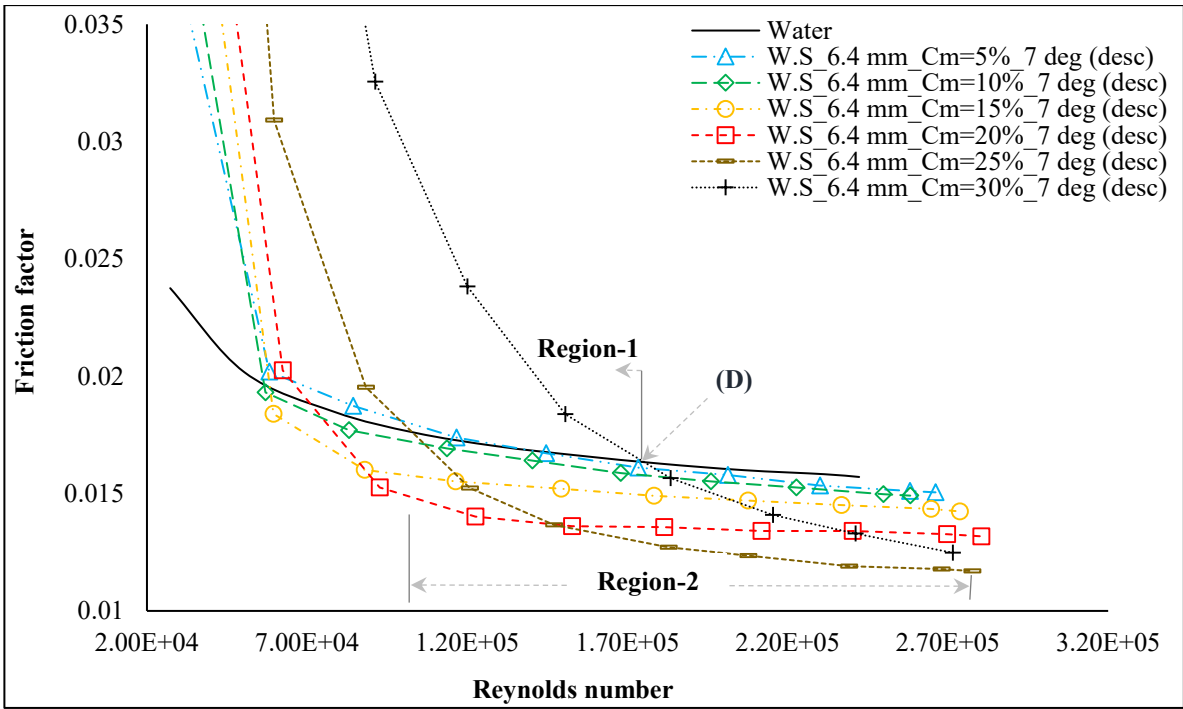
6.3.2 Effect of inclination on frictional behaviour of wheat straw-water slurries

6.3.2.1 Flow regions

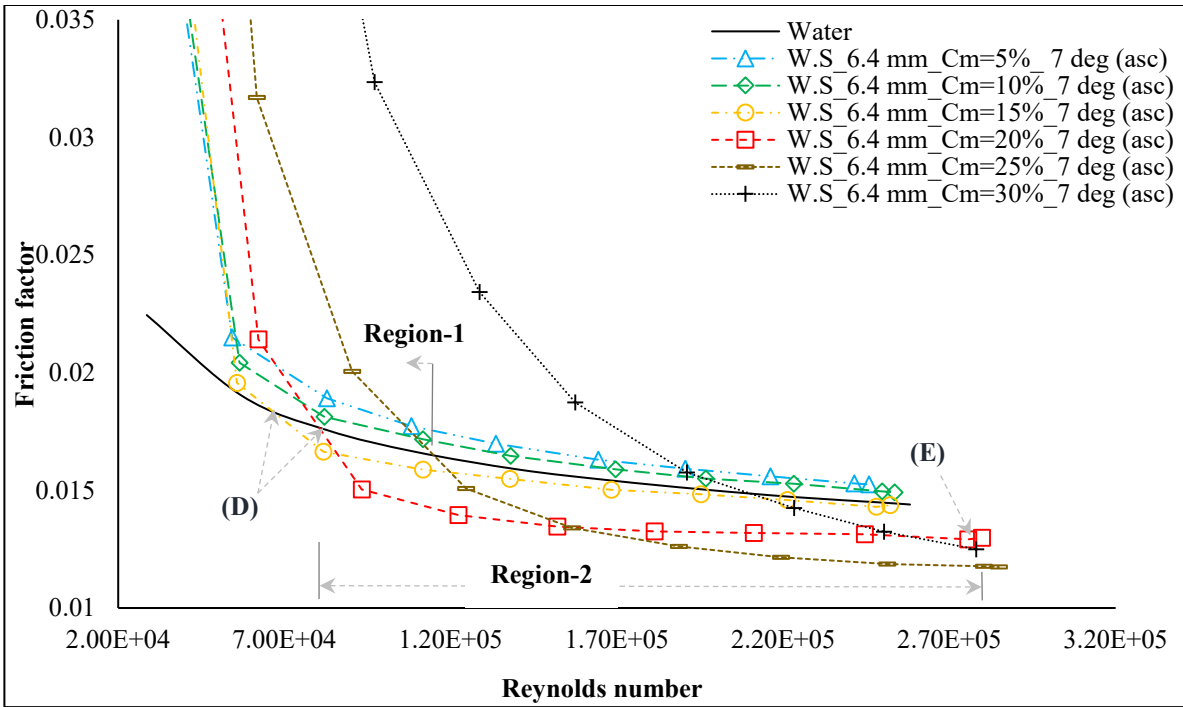
Figure 6.7 shows the friction factor measurements for the 6.4 mm particle size of wheat straw-water slurry flow through a 50 mm diameter inclined pipe section at various slopes (-7° to $+21^\circ$) for slurry bulk velocities $\geq 0.5 \text{ m s}^{-1}$ and a mass concentration range of 5-30%.



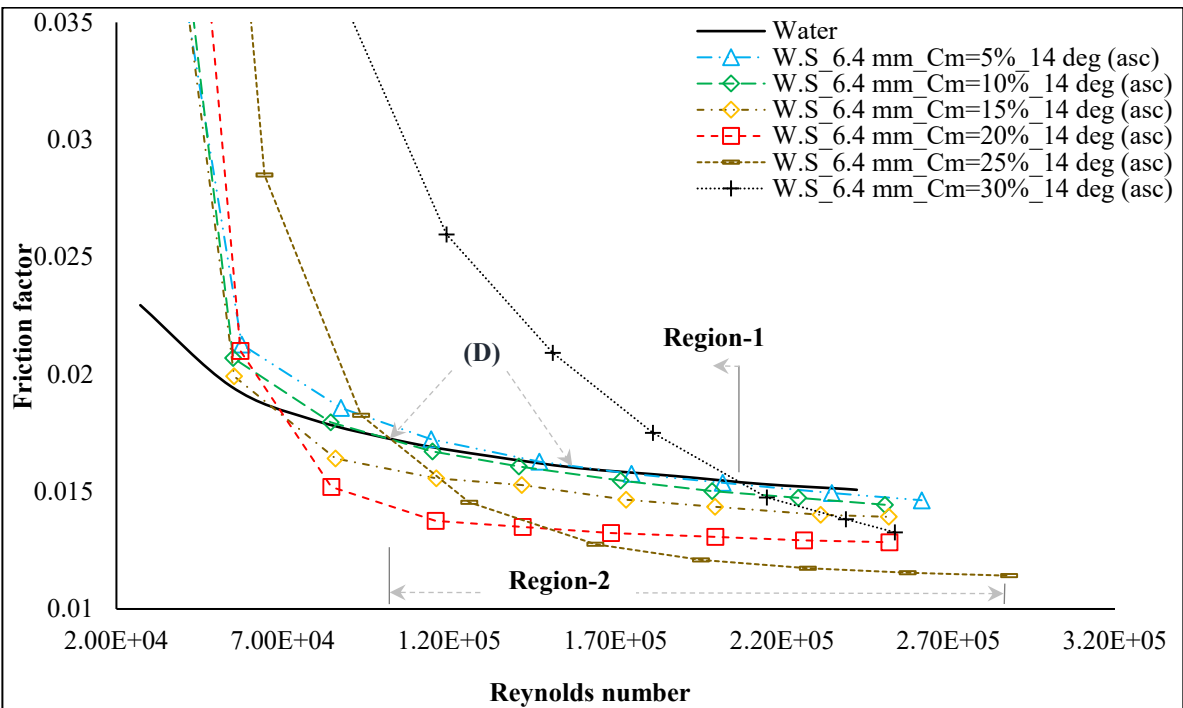
(a)



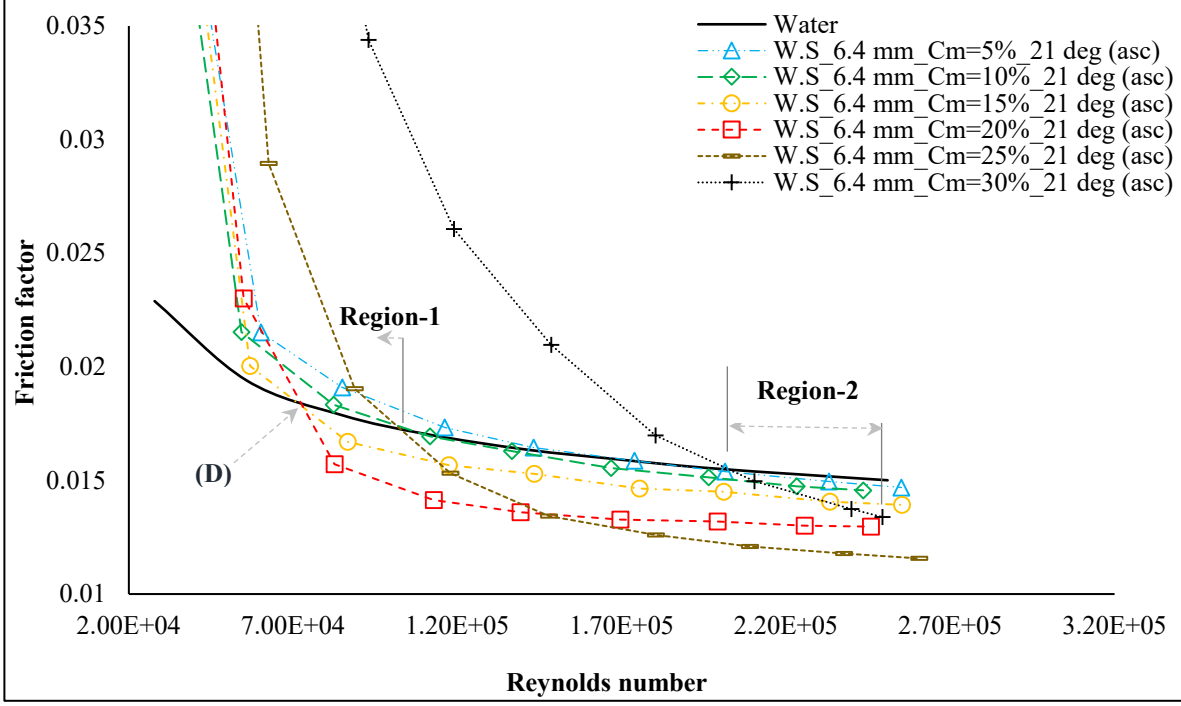
(b)



(c)



(d)



(e)

Figure 6.7: Friction factor versus generalised Reynolds number for velocities $\geq 0.5 \text{ m s}^{-1}$ of the 6.4 mm particle size of wheat straw-water slurry flows through a 50 mm inside diameter pipe section with inclination angles of (a) $\theta = 0^\circ$, (b) $\theta = -7^\circ$, (c) $\theta = +7^\circ$, (d) $\theta = +14^\circ$, (e) $\theta = +21^\circ$ relative to the x-axis

The experimental values of friction factors (f_D) for the wheat straw slurries (Figure 6.7) were determined by substituting index m for w in Equation 6.4 for wheat straw-water mixtures. The corresponding values of slurry frictional pressure drops in Equation 6.4 were calculated using Equation 6.1, and the slurry densities (ρ_m) were determined using Equation 6.2. The generalised Reynolds number (Re_g), obtained using the relation $Re_g = \frac{\rho_m v_m D}{\mu_f}$ (where μ_f is the carrier fluid viscosity in Pascal-sec), was used to express the suspension velocities (Figure 6.7). The ARB-water slurries, during their flow through a horizontal pipe, behave somewhat similarly to wood fiber slurries (Mih, 1967; Robertson, 1957; Sumida & Fujimoto, 2015), chemical wood pulp

suspensions (Duffy & Lee, 1978), and semi-chemical pulp suspensions (Duffy et al., 1976). In earlier studies, three fairly distinct zones – plug flow, transition flow, and turbulent flow – were observed that characterise the flow behaviour of ARB-water suspensions in horizontal pipelines (Javed et al., 2021; Vaezi et al., 2014).

In the first zone, the plug flow region, which appears at a low Reynolds number, a plug of flocculated fibers moves along the central core of the pipe. In this region, the flow appears without any plug-wall interaction, with a progressive increase in annulus size and a rapid fall in the friction factor. The plug is always encompassed by a carrier fluid annulus free of fibers in this region (Mih, 1967; Wiklund et al., 2008; Wiklund et al., 2006), and the suspension's friction factor is always greater than water's at the same flow rate because a flatter velocity profile develops in the core (because of the fiber's plug), which causes a steeper profile near the boundary. This results in an increase in wall shear stress and hence the friction factor (Vaseleski & Metzner, 1974). The size of the annulus is influenced mainly by the Reynolds number of the fiber suspension; it grows larger as the flow rate of the suspension rises, leading to an abrupt decrease in the friction factor of the suspension and, finally, to a transition point (D in Figure 6.7, identified in our earlier study (Vaezi et al., 2014)), where the friction factors of the fiber suspensions and the water are equal (Duffy et al., 1976).

The transition or mixed flow region shows up after the transition point, where an increase in slurry velocity decreases the friction factor at a comparatively lower rate than in the plug flow region. The compressed fibers in the plug prevent the water annulus around it from growing with the suspension velocity. This phenomenon causes the start of the high shear zone in the annulus, where a further increase in the suspension velocity causes the fiber plug to disintegrate at the junction of the annulus and the plug's periphery, and the velocity profile in the core starts changing its shape

to be less blunt than what appeared in the plug flow region (Cotas, 2016; Mih, 1967; Vaseleski & Metzner, 1974). The fiber plug's disintegration continues with an increase in the suspension velocity, and the fragmented fibers continue to mingle with the surrounding annulus until a maximum drop (E in Figure 6.7 [c], from an earlier study (Vaezi et al., 2014)) in the slurry friction factor is achieved with respect to that of the clear water curve. The fiber plug diameter is reduced in the transition flow region until a turbulent flow region appears and the fiber plug completely disappears. The individual fibers in the suspension are fully dispersed in the turbulent flow region across the pipe's cross-section; however, the friction factor curve remains below and parallel to the water curve with an almost constant friction factor at all the subsequent flow rates (Cotas, 2016; Duffy, 1989).

In the present study, the effort was to understand these regions (or zones) based on the friction factor measurements for the range of mass concentrations and bulk velocities of 6.4 mm particle size wheat straw-water suspensions flowing through an inclined pipe section with different slopes (Figure 6.7). In general, all the wheat straw-aqueous suspensions in an inclined pipe of any degree (-7° to $+21^\circ$) demonstrated the characteristics of the plug flow (Region 1) and the transition flow (Region 2) regions together for $C_m = 5\text{-}30\%$ in the entire flow range ($0.5\text{-}4.7 \text{ m s}^{-1}$). No suspension for any pipe inclination exhibited the turbulent flow region under the flow conditions; however, this region is expected to appear at higher flow rates than the maximum suspension velocities achieved in this study.

For any specific mass concentration of wheat straw-water slurry and slope of the inclined pipe section, the friction factor decreased with increasing the Reynolds number. This decrement in the friction factor was more pronounced in higher concentrations of the Reynolds number beyond the transition point (D) because of the increase in the particle-particle interaction at higher

concentrations that suppresses the turbulence intensities more than the suspensions at low concentration, as discussed in earlier studies on other fiber suspensions (Steen, 1989; Vaseleski & Metzner, 1974). For the flow conditions investigated here, the minimal friction factor was obtained at the maximum feasible slurry Reynolds number for $C_m = 25\%$ and any given pipe inclination (Figure 6.7). For the highest mass concentration (i.e., $C_m = 30\%$) of wheat straw suspensions and every pipe inclination, it was possible to decrease the friction factor further, but at high turbulent flows of the suspensions with velocities beyond a specific range of $4.15\text{--}4.7\text{ m s}^{-1}$ depending on the range of pipe inclinations (-7° to $+21^\circ$) used in the present study.

From the friction factor curves of wheat straw-water slurries shown in Figure 6.7, a monotonic change in the transition point (D) was found with respect to certain saturated mass concentrations and pipe inclinations. The axial component of gravity influences the location of the transition point (D) for suspensions with equal mass concentrations in relation to the pipe's angle, as stated in section 6.3.2.2. It was also observed that point E, associated with the minimum friction factor (Figure 6.7 [c]) (or the point of maximum drop in the slurry's friction factor relative to the water curve), was almost recognisable on the friction factor curves for most pipe inclinations and wheat straw-water slurry concentrations until $C_m = 25\%$, after which a further increase in suspension velocity will increase the friction factor instead of decreasing it, as stated in other studies (Duffy, 1989; Vaezi et al., 2014). For $C_m = 30\%$ and any of the pipe inclinations (-7° to $+21^\circ$), it was still possible to achieve a further drop in the friction factor at higher flow rates until point E (not depicted on the graphs); however, all of these possibilities were typically associated with the pump characteristics (section 6.2.4 highlights the pump limitations) used in the current investigation. Further, the wheat straw-water suspensions at $C_m = 5\text{--}10\%$ flowing through an inclined pipe of $\theta = +7^\circ$ were found to exhibit plug flow region (i.e., Region 1) only for the entire range of the

suspension velocity. More research on the frictional behaviour of different particle sizes of wheat straw-aqueous slurries through inclined pipes at $\theta = \pm 7^\circ$ and higher inclination angles (θ) for uphill and downhill flows (e.g., $\pm 14^\circ$ and $\pm 21^\circ$) is required to determine the root cause of this anomaly.

6.3.2.2 Onset velocity of drag reduction (v_{OD})

The onset velocity of drag reduction (v_{OD}) is the velocity at which a suspension's flow zone changes from plug flow to transition flow. This velocity corresponds to the transition point (D) (shown in Figure 6.7) of any suspension. By creating a code in R programming (4.0.5) to get the coordinates of each transition point, the values of v_{OD} (shown in Table A8 and Figure A9 in Appendix A) were determined.

Figure 6.8 depicts the onset velocity of drag reduction in inclined (both uphill and downhill) flows of wheat straw-aqueous suspensions with a 6.4 mm particle size at $C_m \geq 10\%$. In general, the onset velocity of drag reduction for wheat straw-water suspension flowing through any of the slopes of the inclined pipe section (except 7° ascending) reduced with increasing slurry mass concentration up to a particular threshold, as depicted by each curve's lowest value in Figure 6.8.

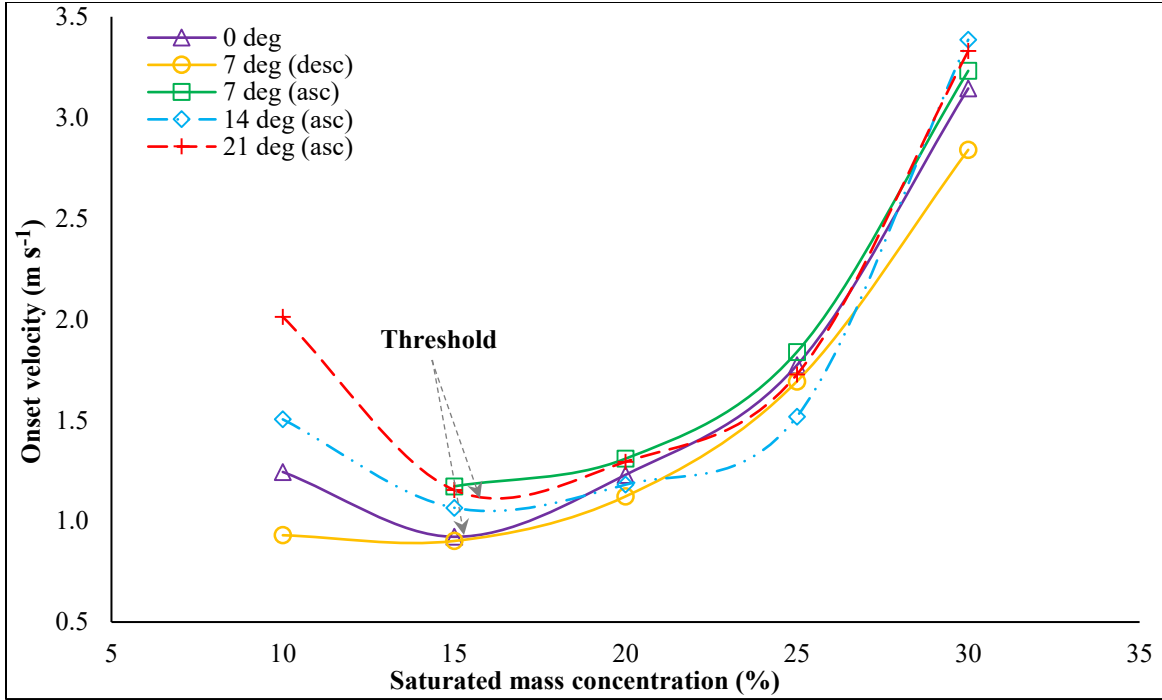


Figure 6.8: Onset velocity of drag reduction (v_{OD}) for the 6.4 mm particle size wheat straw-water slurries of several mass concentrations flowing through an inclined pipe section of varying inclinations (i.e., $\theta = -7^\circ$ to $+21^\circ$) relative to the x-axis.

Similar behaviour for different particle sizes of corn stover-water slurries in upward flows through a vertical pipe section was observed in a recent study (Javed et al., 2022a). The average inter-fiber distance (h_{av}) (Doi & Edwards, 1978a, 1978b) in the wheat straw suspension is greater at lower fiber concentrations (i.e., $C_m = 10\%$) than at higher concentrations of a similar-sized particles (see Table 6.5). The h_{av} was evaluated using the relation $h_{av} = (nX_{ig})^{-1/2}$ (where n ($n = \left[\frac{4}{\pi} C_V \frac{1}{X_{ig}X_{ig,w}^2} \right]$), X_{ig} , and $X_{ig,w}$ are the fiber number fraction, graphic mean length, and the graphic mean width of the wheat straw particles, respectively; see Table 6.2 for the values of X_{ig} and $X_{ig,w}$) originally proposed by Doi and Edwards (1978).

Table 6.5: Mechanistic properties to comprehend the flow behaviour of the 6.4 mm nominal particle size wheat straw-water suspension

Parameters	Saturated mass concentration (C_m) (%)					
	5	10	15	20	25	30
Average inter-fiber distance (h_{av})	5.59	3.93	3.20	2.77	2.47	2.25
Fiber number fraction (n)	0.0067	0.0134	0.0202	0.0269	0.0338	0.0406
Contact number (n_c)	0.83	1.66	2.50	3.34	4.19	5.04
Crowding number (N)	2.40	4.82	7.25	9.69	12.15	14.61
Suspension behaviour regime	dilute	Semi-conc.	Semi-conc.	Conc.	Conc.	Conc.

The lower the value of h_{av} , the more the adhesive forces and hence flocculation. Further, in an earlier study, a hypothesis was proposed that at low fiber concentrations, when there are more void spaces among the fibers, h_{av} decreases with an increase in the suspension velocity (Javed et al., 2022a). Therefore, for the suspension at $C_m = 10\%$, the h_{av} decreases as the flow rate increases, bringing the fibers closer together. On the other hand, the fiber-free annulus grows until the suspension, which is still in the plug flow region, reaches a high flow rate where the fibers are so close together that there are very few empty spaces between them and strong connections form between the fibers. This is where the fiber-fiber interactions are most noticeable. A further increase in suspension velocity at this stage at a high flow rate will cause the plug to disrupt from its outer periphery (which is intact with the annulus) and result in the onset of drag reduction at a high value of v_{OD} for a low concentration ($C_m = 10\%$) of the suspension (Figure 6.8). The fiber number fraction (n) increases and the h_{av} decreases as the slurry concentration is increased further beyond $C_m = 10\%$ (Table 6.5) until the suspension reaches the threshold point, so relatively low flow rates of the suspensions are required to form a plug with a minimum amount of void spaces and a strong inter-fiber connection. As a result, compared to the suspension at a $C_m = 10\%$, the commencement

of drag reduction occurs at somewhat lower slurry velocities at the concentration related to the threshold. An earlier study on vertical upward flows showed a similar trend for corn stover-water suspensions (Javed et al., 2022a).

After the threshold, for every pipe inclination, the onset velocity increased with increasing saturated mass concentrations of the wheat straw-water suspension (Figure 6.8). Kazi et al. (1999) and Duffy and Lee (1978) linked this increase in onset velocity to fiber network strength. The strength of the fiber network in a suspension depends on the number of contacts (n_c) of each fiber with the adjacent ones, which is defined as $n_c = 2C_V(\varphi_p)^2$ (where C_V and φ_p are the saturated solid volumetric concentration and the particle aspect ratio, respectively). The fiber suspension is categorised as being in the concentrated regime when $n_c \geq 3.0$, whereas it is in the dilute regime for $n_c < 1.0$ (Dodson, 1996; Kerekes, 2006). Another way to distinguish between a fiber suspension's dilute and concentrated regimes is the crowding number (N), defined as $N = \frac{2}{3}C_V(\varphi_p)^2$. The suspension is in the concentrated regime if $N > \varphi_p$. The fiber network strength significantly increases in the concentrated regime where the fibers develop coherent networks (Dodson, 1996).

In the present study, the wheat straw-water suspension was close to the concentrated regime (i.e., $n_c \approx 3.0$ and $N > \varphi_p$) at the threshold limit; hence, because of increased adhesion forces and flocculation, the suspension had sufficiently high inter-fiber connections at its threshold limit to strengthen the fiber network, which progressively increased in strength for the subsequent increase in concentration above the threshold limit. Consequently, this suspension needs larger flow rates for concentrations beyond the threshold point (see Figure 6.8) to disrupt the fiber plug boundaries, which increases the onset velocity with concentration. Wheat straw suspensions at 5-10% mass concentration were observed to be in the plug flow region for upflow at a 7° inclination of the pipe

(Figure 6.7 [c]), so their drag reduction onset points are not shown in Figure 6.8. Also, the onset velocities of the suspensions flowing through all the pipe angles at $C_m = 5\%$ mass concentrations were not linear compared to the onset velocities at $C_m = 10\%$. Because of this, the results at $C_m = 5\%$ are not shown in Figure 6.8.

The change in the inclination angle of the pipe typically results in a change in the deposition velocity of the conventional solids-water slurries that is highly dependent on the mean particle size, particle density, and the particle size distribution keeping the pipe diameter constant (Al-Mutahar, 2006; Durand, 1953; Kesely et al., 2019; Wasp & Aude, 1970; Wasp et al., 1977). In the present study, no bed formation was observed for the wheat straw-water slurries of the 6.4 mm particle size at any of the pipe inclinations even at the minimum velocity of 0.5 m s^{-1} (section 6.3.1.2). However, the effect of inclination on the onset velocity of drag reduction for the wheat straw-aqueous suspension can be observed in Figure 6.8; where it was found that at any given concentration, the onset velocity increased with an increase in the inclination of the inclined pipe for $\theta = -7^\circ$, 0° , and $+7^\circ$ and $C_m \geq 10\%$ (except for $C_m = 10\%$, where there was plug flow at $\theta = +7^\circ$). For this range of angles and concentrations, at any specific value of C_m of the suspension, v_{OD} was lowest for $\theta = -7^\circ$ and highest for $\theta = +7^\circ$. For the uphill flows, the axial component of the gravity (i.e., $g \sin \theta$) being opposite to the flow direction of the suspension (Figure 6.2 [a]) decelerates the flow, and hence the suspension moves with low velocity compared to the downhill flows, where the axial component of the gravity is in the suspension's flow direction, which in turn accelerates the flow, causing the suspension to move faster (De Vreede, 2018; Vlasak et al., 2017).

In the present work, the ranges of the highest achievable velocities of wheat straw-water suspension flows for $C_m = 5\text{-}10\%$ as $4.53\text{-}4.69 \text{ m s}^{-1}$ and $4.43\text{-}4.61 \text{ m s}^{-1}$ were obtained at

inclinations of -7° (downhill) and $+7^\circ$ (uphill), respectively. A similar decrease in the suspension velocity for other inclinations (i.e., $+14^\circ$ and $+21^\circ$) was observed, which are not reported here. As the inter-fiber distance, h_{av} , also depends upon slurry velocity and decreases with an increase in slurry velocity, especially when the suspension is in the plug flow region (Javed et al., 2022a), in the downhill flow of a wheat straw-aqueous suspension at $\theta = -7^\circ$, the axial component of the gravity facilitated the flow more than similar conditions for horizontal or uphill flow at $\theta = +7^\circ$, causing the h_{av} to decrease faster for any specific concentration. Ultimately, the fiber plug starts to disintegrate at the plug-annulus interface at a comparatively lower magnitude of v_{OD} than the corresponding v_{OD} for horizontal or uphill flows of similar suspensions. For conventional solids-water slurries flowing in inclined pipes, the in situ concentration is lower in the downflow direction, and the likelihood of particle slip is lower in the upflow direction, resulting in a higher frictional pressure drop for the upward flows. However, the wheat straw-water suspensions behave entirely differently than the conventional solids-water slurries, as discussed in section 6.3.1. As these suspensions have low density, are fibrous, and form networks and flocs, the axial component of gravity has a different effect on these suspensions flowing in inclined pipes.

While comparing the onset velocities of drag reduction for higher slopes of the inclined pipe, i.e., $+14^\circ$ and $+21^\circ$, a similar pattern (i.e., v_{OD} increased when the pipe inclination was increased) was found across the entire range of C_m 's, as observed for lower inclination angles. However, these results were inconsistent with respect to the lower inclination angles (i.e., 0° and $+7^\circ$). Nonmonotonic onset velocity variation at ascending angles of 14° and 21° compared to lower inclination angles (i.e., $+7^\circ$ uphill or horizontal pipe position) needs further investigation. It is challenging to interpret the results at this stage because of the need for more information for fiber suspension flows in inclined pipes. Therefore, more data needs to be collected for the present

research for different particle sizes and pipe inclination angles (i.e., 7° - 21° , both uphill and downhill).

6.3.2.3 Drag reduction (%DR)

Figure 6.9 shows the percentage drag reduction (%DR) by the 6.4 mm particle size of wheat straw-water suspensions flowing at various mass concentrations ($C_m = 5$ -30%) and different bulk velocities through an inclined pipe section of various slopes (i.e., -7° to $+21^\circ$).

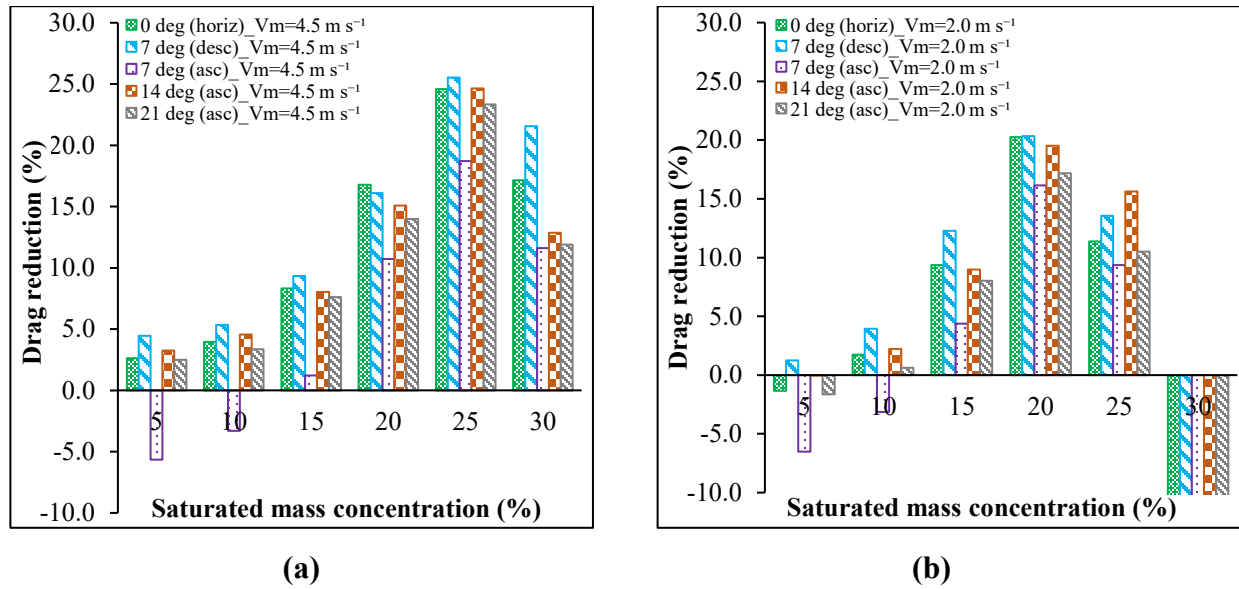


Figure 6.9: Drag reduction of the 6.4 mm particle size of wheat straw-water slurries for $C_m = 5$ -30% flowing through an inclined pipe section of various inclinations (i.e., -7° to $+21^\circ$) and slurry bulk velocities of (a) 4.5 m s^{-1} and (b) 2.0 m s^{-1}

Here the %DR for slurry bulk velocities of 4.5 and 2.0 m s^{-1} is presented. The complete results are given in Figure A10 of Appendix A. For all the pipe inclinations and specific ranges of slurry bulk velocities $\geq v_{OD}$, %DR increased with an increase in the saturated mass concentration of wheat straw-water suspensions until a specific concentration at which the %DR for each suspension was highest. This concentration is known as a critical concentration of maximum drag reduction

$(C_m)_{cr}$. With an increase in C_m , the particle-particle interaction, hence the fiber contact number (n_c), increases, which increases the fiber network strength and the tendency of the suspension to reduce the turbulence intensity and the turbulent momentum transfer, giving rise to an increase in the drag reduction (Javed et al., 2021; Vaezi et al., 2014). The increase in the fiber network with C_m also causes the fiber flocs to grow, hence increases the apparent suspension viscosity, which has a linear relationship with lower values of C_m and a cubic relationship with higher C_m (Djalili-Moghaddam & Toll, 2006). This increase in the viscous nature of the suspension and floc size with C_m affects the drag reduction capabilities of the suspension beyond $(C_m)_{cr}$ because of an increase in the viscous momentum transfer (Xu & Aidun, 2005). Therefore, a maximum %DR at $(C_m)_{cr}$ is observed in this study for wheat straw-water suspensions flowing through inclined pipe section. After the critical concentration $(C_m)_{cr}$, a decrease in %DR occurred instead of an increase (shown in Figure 6.9). A similar phenomenon in vertical upward flows of various particle sizes of wheat straw- and corn stover-water suspensions was observed in the recent work (Javed et al., 2022a).

For suspensions flowing at $v_m \geq 2.5 \text{ m s}^{-1}$ through an inclined pipe section, the $(C_m)_{cr}$ was 25% for all the slopes, whereas for suspensions flowing at comparatively lower velocities (i.e., $< 2.5 \text{ m s}^{-1}$), the $(C_m)_{cr}$ was 20% for all the pipe inclinations (Figure 6.9). The flow characteristics of the fiber suspensions greatly depend on the regimes of the fiber suspension (i.e., dilute, semi-dilute, or concentrated) and the suspension velocity (Bobkiewicz & Gauvin, 1965; Javed et al., 2022a; Kerekes, 2006; Kerekes, 1971; Li et al., 1994; Xu & Aidun, 2005). Kerekes found that the $(C_m)_{cr}$ for inelastic fiber suspensions increased with suspension velocity (for any fiber length) and fiber aspect ratio (1971). In an earlier study, the $(C_m)_{cr}$ for any specific particle size was found to be a strong function of feedstock and suspension velocity, which increased with an increase in v_m (Javed et al., 2022a). At $C_m = 25\%$, the wheat straw-water suspension was in the concentrated

regime (see Table 6.5), so the viscous nature of the fiber suspension (due to high apparent viscosity) dominated the drag reduction characteristics for $v_m < 2.5 \text{ m s}^{-1}$, and we observed the maximum %DR at $C_m = 20\%$ instead of 25% regardless of pipe inclination (Figure 6.9 [b]). In general, it was determined that for most of the suspensions, the $(C_m)_{cr}$ appeared to be a strong function of suspension velocity and was independent of the pipe inclination.

Over the entire range of slopes (-7° to $+21^\circ$) of the inclined pipe section and any of the saturated mass concentrations ($C_m = 5\text{-}30\%$), the %DR was highest for downflows of the suspension at a -7° inclination and lowest for upflows at a $+7^\circ$ inclination. A maximum %DR of 25.53% was achieved with a suspension of $C_m = 25\%$ running at the highest attainable bulk velocity of $v_m = 4.5 \text{ m s}^{-1}$ through an inclined pipe of -7° (i.e., downflow). In downhill flows, the axial component of gravity facilitates the flow, giving the suspension the lowest value of v_{OD} for any specific C_m (Figure 6.8), resulting in a higher %DR compared to the uphill flows of similar flow conditions. The upward inclined flows of the wheat straw suspension at all mass concentrations ($C_m = 5\text{-}30\%$) and slurry velocities ($1.5\text{-}4.5 \text{ m s}^{-1}$) through the inclined pipe section at slopes of $+7^\circ$ to $+21^\circ$ showed an intriguing characteristic. For this range of conditions in uphill flows and any specific mass concentration and velocity, it was found that the %DR first increased when the pipe inclination increased from $+7^\circ$ to $+14^\circ$ and then decreased when the pipe inclination further increased to $+21^\circ$.

A specific trend of variation in the %DR was not observed with a slope for specific mass concentrations in uphill flows. The reason for this anomaly is still an open issue in the research. Extensive experimental data is needed for us to come to a concrete conclusion, as explained in section 6.3.2.2. The highest %DR at any concentration and velocity in uphill flows of the wheat

straw-water slurry was found at the pipe inclination of $+14^\circ$. With a suspension of $C_m = 25\%$ running at the highest attainable bulk velocity of $v_m = 4.5 \text{ m s}^{-1}$ in uphill flows of wheat straw-water slurry through an inclined pipe of $+14^\circ$ inclination, the maximum %DR of 24.64% was achieved. We further observed that suspensions with low onset velocities (see Figure 6.8) in uphill flows (i.e., $+7^\circ$ to $+21^\circ$) exhibited more drag reduction than suspensions with high onset velocities for similar mass concentrations. This was obvious because the sooner the onset of drag reduction, the sooner the suspensions can attain high velocities for similar flow conditions to reach a higher %DR.

6.3.3 Uncertainty analysis

To evaluate the level of uncertainty and repeatability in the pressure drop measurements of the 6.4 mm nominal particle size of wheat straw-aqueous slurries for each pipe inclination, at least two sets of tests (i.e., independent trials) were run for the same range of C_m 's (i.e., 5-30%) and bulk velocities ($0.5\text{-}4.7 \text{ m s}^{-1}$). A typical uncertainty analysis was used to determine the precision uncertainty (P_x) of differential pressure drop measurements and the biased uncertainty (B_x) of the DPT to estimate the overall uncertainty (U_x) using the relation $U_x = (P_x^2 + B_x^2)^{1/2}$ (Javed et al., 2022b; MECE 301, 2018; Moffat, 1988). Broadly speaking, an overall uncertainty of $\pm 0.00497 \text{ kPa m}^{-1}$ to $\pm 0.1793 \text{ kPa m}^{-1}$ was found in the entire pressure drop measurements of wheat straw-aqueous slurries.

Figure 6.10 demonstrates the repeatability of the experimental measurements of the 6.4 mm particle size of wheat straw-aqueous slurries for various C_m 's and angles of inclination of the pipe.

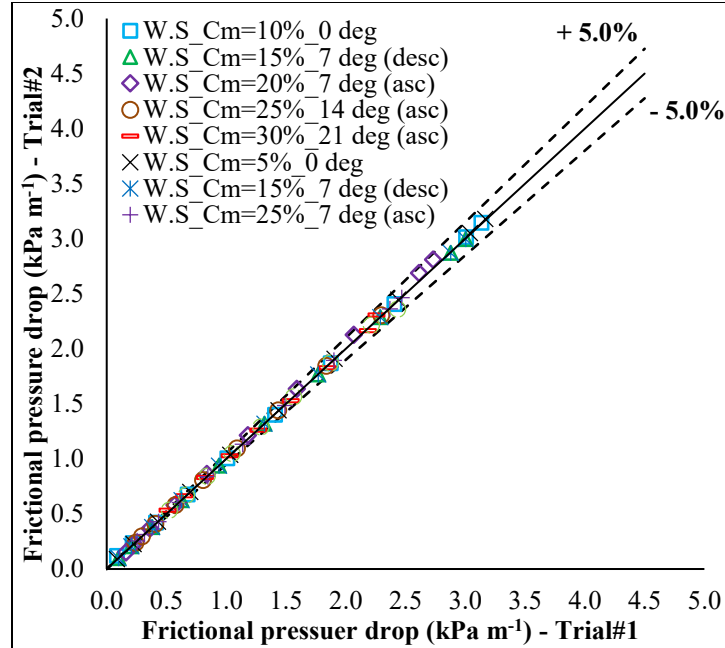


Figure 6.10: The repeatability of the experimental measurements for various mass concentrations of the 6.4 mm nominal particle size of wheat straw-water slurry flow through a 50 mm inside diameter pipe section at different angles of inclination.

The range in the repeated measurements for the complete series of experiments on wheat straw-aqueous slurries was observed to be $\pm 5.0\%$.

6.4 Conclusion

The frictional behaviour of aqueous-based wheat straw suspensions of the 6.4 mm particle sizes through pipe section (ID = 50.8 mm) of different inclinations was experimentally studied. While commissioning the pipeline loop, we found that Worster and Denny's model exhibited the best fit to all the experimental pressure drops of aqueous slurries of fine sand ($d_{50} = 0.103$ mm) in the pseudo-homogeneous regime (i.e., for $v_m > 1.0$ m s⁻¹) for all the inclined flows (uphill or downhill) with an error range of 0.16-8.61%. Wheat straw-aqueous suspensions of the 6.4 mm particle size exhibited the plug flow and transition flow regions together for $C_m = 5$ -30% and the entire flow rate range (0.5-4.7 m s⁻¹) in an inclined pipe with different slopes (-7° to $+21^\circ$), except for

suspensions at low mass concentrations ($C_m = 5\text{-}10\%$) for the lowest slope (i.e., $+7^\circ$) in uphill flows, where only plug flow region existed. For the particle size of wheat straw used in this investigation, both the onset velocity of drag reduction (v_{OD}) and percentage drag reduction (%DR) seem to be a function of concentration (C_m) and pipe inclination (θ). The onset velocity (v_{OD}) achieves its lowest value (threshold) for any pipe inclination at a C_m close to the condition, i.e., $n_c = 3.0$ and $N > \varphi_p$ (where the suspension just enters the concentrated regime), beyond which the slurry behaviour reverses (i.e., v_{OD} rises with C_m) because of a progressive increase in the strength of the fiber network. Drag reduction, on the other hand, increases with C_m for all the inclinations (θ) at $v_m > v_{OD}$ up to a specific mass concentration $(C_m)_{cr}$, where the %DR reaches a plateau and then starts to decline again because of the increase in apparent suspension viscosity. The $(C_m)_{cr}$ depends solely on a certain range of v_m (i.e., it was 25% for $v_m > 2.5 \text{ m s}^{-1}$ and 20% for $v_m < 2.5 \text{ m s}^{-1}$) and is unaffected by the pipe inclination.

In certain aspects, wheat straw-water slurries behave differently in downhill flows than in uphill flows. The downhill flows of slurries showed a minimum v_{OD} and maximum %DR compared to uphill flows at all C_m 's because of the accelerating effect of gravity. For uphill flows with larger angles, i.e., $\theta > +7^\circ$, and the entire range of C_m 's, the v_{OD} increased and the %DR decreased with pipe inclination. In contrast, for uphill flows at $\theta = +7^\circ$, the v_{OD} was the highest and the %DR the lowest of all the inclinations. In general, given similar flow conditions, wheat straw-aqueous suspensions proved to be more effective in lowering drag in downhill flows than in uphill flows. The nonmonotonic variations in v_{OD} and %DR, specifically in uphill flows, suggest it is worth looking at the corresponding results for different types and sizes of ARB-water slurry flows through inclined pipes (both uphill and downhill) at different inclinations. This research can assist in designing and operating a long-distance integrated pipeline network for a commercial

biorefinery by determining the optimum flow conditions for hydro-transporting ARB through inclined pipes.

Chapter 7: Conclusions and Recommendations for Future Work

7.1 Conclusions

This study contributes to understanding the frictional behaviour of pipeline hydro-transport of the agricultural residue biomass (ARB) through vertical and inclined pipes being essential components of long-distance pipeline setup other than horizontal lines for large-scale biofuel production to reduce dependence on fossil fuels and mitigate GHG emissions. The study involved experimental work on a laboratory scale for vertical upward flows of two ARB feedstocks, wheat straw and corn stover, with four different groups of particle sizes through a vertical test section, a part of a 50 mm diameter and 29 m long closed pipeline loop. In contrast, the experimental work on inclined flows was restricted to one particle size group of a single feedstock type, i.e., wheat straw, at various ascending but limited descending pipe inclinations due to confined lab space. Different parameters governing the mechanisms of the suspension's frictional behaviour during its flow through vertical and inclined pipes were examined. Then, an empirical correlation on ARB slurry pressure drops modeled their frictional behaviour over vertical lines that could help in future studies to estimate the exact pumping requirements in long-distance pipeline networks for large-scale biofuel production.

7.1.1 Estimation of ARB suspension's in situ concentration

Because of process limitations and equipment shortages, the current research setup lacked an in situ concentration measuring device. A hypothesis proposed to predict slurry's in situ concentrations from its delivered concentrations in a pseudo-homogeneous regime was validated using different conventional solids with nearly similar particle densities but different terminal settling velocities due to different mean particle diameters up to 500 microns. The delivered

concentrations for fine sand ($d_{50} = 0.103$ mm) with the lowest terminal settling velocities were almost similar to the prepared concentrations, indicating homogeneous suspension because the particles were buoyant. The conventional solids-water slurries of larger mean particle diameters with higher terminal settling velocities than fine sand showed stratified concentration near the bottom of the mixing tank, resulting in delivered concentrations up to 2.5 times higher than the prepared concentrations. These findings, restricted to the current research's experimental setup, show that particle size greatly affected the delivered concentrations of conventional solids with nearly similar particle densities. The hypothesis proposed for conventional solids-water slurries was applied to four nominal particle sizes (i.e., 19.2 mm, 6.4 mm, 3.2 mm, and <3.2 mm) of wheat straw-water suspensions in saturated state, where delivered concentrations of all the suspensions were found to be equal to their corresponding prepared concentrations within 10% variation, indicating the homogeneity of the biomass suspensions in the pipeline for most of the slurry's velocity range with negligible stratified concentration near the mixing tank's bottom, like fine sand. Therefore, the delivered concentration of wheat straw suspensions was not affected by particle size, as with conventional solids, because of the buoyant nature of particles, and was later used as an in situ concentration to evaluate biomass slurry's frictional pressure drops.

7.1.2 Effect of particle size and flow conditions on frictional behaviour of wheat straw-water suspension in vertical upward flows

In the subsequent stage, the effect of particle size and slurry flow conditions on frictional pressure drops of aqueous wheat straw slurries in upward flows through a vertical pipe section was experimentally studied, which led to the identification of different flow regions to understand the slurry's frictional behaviour as a function of velocity and mass concentration. Over the entire velocity range and C_m up to 20%, most wheat straw suspensions exhibited drag-reducing

capabilities in line with mixed (transition) and turbulent flow regions together or mixed flow regions alone, except fine particles (i.e., <3.2 mm), which showed both plug and transition regions. The highly concentrated suspensions with $C_m \geq 25\%$ showed either the plug and transition flow regions in tandem or the plug flow regions alone due to high apparent suspension viscosity.

Generally, the drag reduction increased with particle size and concentration for the suspension velocities beyond 1.5 m s^{-1} due to an increase in the particle-particle interaction and the hydrodynamic interaction with the surrounding fluid, reached a plateau at a specific concentration limit, and then started to decline. This limiting concentration of maximum drag reduction ($(C_m)_{cr}$) was exclusively dependent upon the particle size and flow rate ranges. Because of the longer mean fiber length and wide size range, the largest particle size exhibited a maximum drag reduction of 33.5% at $C_m = 20\%$ for the lowest slurry velocity and 19% at $C_m = 25\%$ for the maximum achievable slurry bulk velocity compared to the other particle sizes. The onset velocities of drag reduction (v_{OD}) differed in different flow conditions and increased with particle size and concentration. Wheat straw-aqueous slurries in vertical upward flows behaved quite differently than those in the horizontal flows at similar flow conditions, particularly at low velocities, thus opening a new gateway in extending this research for larger diameter pipes used in the practical situation.

7.1.3 Effect of particle size and flow conditions on frictional behaviour of corn stover-water suspension in vertical upward flows

The frictional behaviour of a new feedstock (i.e., corn stover) of ARB-water slurry flows in a vertical pipe section was experimentally evaluated as a function of particle size and various flow conditions. Different regimes and rheological characteristics of the fiber suspensions were identified using various dimensionless parameters derived from the particle's morphological

studies. Corn stover-aqueous slurries with the largest particles (19.2 mm) exhibited the transition flow region at low mass concentrations of 5-10% over the entire velocity range, while the other suspensions of all particle sizes (except 19.2 mm at $C_m = 15\%$) showed either the plug and transition flow regions together or the plug flow region alone because of high biomass loadings (i.e., $C_m = 25\text{-}40\%$). The drag reduction increased with particle size and concentration and was highest (32%) for the largest particle size at comparatively lower concentration (i.e., $C_m = 10\%$) and slurry velocity (i.e., $v_m = 1.0 \text{ m s}^{-1}$) than wheat straw. The onset velocity of drag reduction of corn stover suspensions appeared as a function of concentration and particle size. It reached its lowest value (threshold) with increased concentration and particle size. This threshold concentration was found to be close to the condition of development of coherent networks (i.e., $N > \phi_p$). Beyond this threshold concentration for a specific particle size, the onset velocity increased with the concentration because of the strong fiber networks in the large fiber contact numbers.

7.1.4 Comparison of frictional behaviour of ARB feedstock in vertical upward flows

The comparison of frictional behaviour of similar groups of particle sizes of both the feedstock of ARB-water suspension flows through vertical test pipe section at the same flow conditions revealed that corn stover behaves differently than wheat straw for a specific range of concentrations and velocities. At velocities $\geq 2.5 \text{ m s}^{-1}$, corn stover suspensions showed better drag reduction than wheat straw slurries for specific C_m 's, with the most significant difference in drag reduction for longer particles (19.2 mm) at a $C_m = 15\%$ due to the complex nature of the ground material of corn stover with different particle types and shapes. Wheat straw suspensions reduced drag better than maize stover at velocities $\leq 2.0 \text{ m s}^{-1}$, except for the largest particle size. Except for fine particles, corn stover suspensions had lower $(C_m)_{cr}$ than wheat straw suspensions. Beyond

the $(C_m)_{cr}$, some suspensions in both feedstocks displayed an abrupt drag increase at certain flow conditions, with more significant variability in the corn stover.

7.1.5 Modeling the frictional behaviour of ARB slurries in vertical upward flows

A framework was developed in R (4.0.5) using multiple linear regression, backward elimination method, and Akaike information criterion to analyze significant experimental data on pressure drops of both ARB-water slurries in vertical upward flows, and an empirical correlation was proposed to predict the slurry's frictional pressure drops as a function of particle type, particle aspect ratio, slurry solid mass concentration, and slurry velocity. The model's constant factors and regression coefficients differed among feedstock, indicating their different frictional behaviour during vertical upward flows. The proposed empirical model provided a base case for the frictional pressure drops of ARB-water slurries during vertical upward flows in a pipe of 50 mm inside diameter and seemed like a promising way to cover all the flow regions that appeared for the range of flow conditions used for the experimental setup in the current study rather than modeling the behaviour of the biomass-water slurry in any specific flow region independently. Further, the correlations for the onset velocity of drag reduction (v_{OD}) were also developed for different particle sizes of ARB suspensions as a function of their mass concentrations (C_m), which helped interpret the corresponding slurries' transition points for the onset of drag reduction in vertical upward flows through pipes.

7.1.6 Effect of pipe inclination on frictional behaviour of wheat straw suspensions

Finally, a laboratory-scale study examined the frictional behaviour of the 6.4 mm nominal particle length ($d_{50} = 4.85$ mm) wheat straw-water suspensions' uphill and downhill flows for pipe inclinations (θ) and saturated mass concentrations (C_m) of -7° to $+21^\circ$ and 5-30%, respectively, through an inclined test section of the closed pipeline loop. In general, wheat straw aqueous

suspensions exhibited the plug flow and transition flow regions together for the entire range of flow rates, mass concentrations, and pipe slopes except for suspensions at low concentrations ($C_m = 5\text{-}10\%$) for the lowest slope ($+7^\circ$) in uphill flows, where only the plug flow region existed. Further, the v_{OD} and %DR seemed to be a function of C_m and pipe inclination (θ); however, the $(C_m)_{cr}$ depended solely on a certain range of v_m (i.e, it was 25% for $v_m > 2.5 \text{ m s}^{-1}$ and 20% for $v_m < 2.5 \text{ m s}^{-1}$) and was unaffected by the pipe inclination. In certain aspects, wheat straw-water slurries behaved differently in downhill flows than in uphill flows. The downhill flows of slurries showed a minimum v_{OD} and maximum %DR (i.e., 25.53%) compared to uphill flows at all C_m because of the accelerating impact of gravity. For uphill flows with larger angles, i.e., $\theta > +7^\circ$ and the entire range of C_m , the v_{OD} increased and the %DR decreased with pipe inclination. In contrast, for uphill flows at $\theta = +7^\circ$, the v_{OD} was the highest and the %DR was the lowest of all the inclinations. In general, given similar flow conditions, wheat straw-aqueous suspensions proved to be more effective in lowering drag in downhill flows than in uphill flows. The effect of inclination on v_{OD} , %DR, and $(C_m)_{cr}$ brought new perspectives on biomass slurries' pipeline frictional behaviour.

Analyzing ARB-water suspension flow regions in vertical and inclined pipes under different flow conditions; calculating drag reduction onset, maximum drag reduction, and minimum v_{OD} 's threshold concentration; understanding the suspension's rheology by identifying the regimes of fiber suspension behaviour, examining the effects of different particle types, and floc formation conditions; and quantifying the fiber network's strength by evaluating some dimensionless parameters helped understand these suspensions' frictional behaviour in pipeline transport. The developed empirical correlation of frictional pressure drops of agricultural residue biomass-water suspensions in vertical upward flows was a novel contribution to this research. The observed

variations in the flow characteristics of ARB slurries in vertical, horizontal, and inclined flows under similar conditions suggested further exploring these findings for more significant slopes and larger pipeline diameters. These findings could help build a typical long-distance integrated pipeline network for commercial biofuel production by evaluating booster station slurry pump operating conditions, pumping power, and pipe dimensions.

7.2 Recommendations for Future Work

The current study investigated the impact of different flow conditions, such as particle size, a suspension's solid mass concentration, a suspension's bulk velocity, type of biomass particle (i.e., other feedstock), and the slope of the inclined pipe section on a suspension's frictional pressure drop to understand the different mechanisms governing the frictional behaviour of agricultural residue biomass-water suspensions while flowing through vertical and inclined pipe sections. The experimental measurements were performed on vertical and inclined test sections with a 50 mm inside diameter (D), part of a 29 m long closed pipeline loop, each with a span of $10D$. Efforts were made to develop a basic understanding of the slurry's rheology in vertical and inclined pipes, and an empirical correlation on frictional pressure drops of these kinds of slurries through a vertical pipe section was developed. However, these findings were limited to a pipeline diameter of 50 mm and the limited inclination angles imposed by the space restrictions in the lab. In a practical situation, a long-distance integrated pipeline network should have larger pipe diameters and greater degrees of slopes in the inclined pipe sections (especially the downhill slopes). It is necessary to do further research along the lines outlined below to understand how changes in the pipe's diameter and slope will affect the slurry's frictional behaviour.

7.2.1 Investigate the effect of large slopes in inclined pipes on the frictional behaviour of agricultural residue biomass-water suspensions

As reported in section 6.3.2, the frictional behaviour of the 6.4 mm nominal-sized wheat straw-water suspensions in uphill flows was inconsistent at higher inclination angles and consistent at lower ones; this needs further investigation because of the limited experimental data and research in this field. Additionally, the downhill flows were restricted by a maximum inclination of 7°. However, in practical situations, the topography of long-distance pipeline networks and on-site processing typically involves larger pipe slopes. Therefore, it is suggested to explore the frictional behaviour of different particle sizes and feedstocks of agricultural residue biomass-water suspension flows through inclined pipes in a greater range of angles (uphill and downhill) than used in the current investigation.

7.2.2 Develop empirical correlation to model aqueous-based agricultural residue biomass slurry flow behaviour in inclined pipe sections

As stated in section 1.1, Vaezi et al.'s techno-economic analysis of the pipeline hydro-transport of agricultural residue biomass used empirical correlations developed for horizontal pipe flows (2015). However, an integrated pipeline network from bio farms to biorefineries may include horizontal, vertical, and inclined pipe sections. The overall objective of the proposed research is to use the experimentally obtained frictional pressure drop data of agricultural residue biomass (wheat straw and corn stover) slurries flowing in an inclined pipe section to develop an empirical correlation as a function of material type, particle size, slurry density, slurry solid mass concentration, slurry bulk velocity, and angle of inclination. The selection of proper particle size is crucial, especially when dealing with a feedstock that exhibits varying particle size ranges. The proposed study also recommends the inclusion of relevant size parameters and (or) particle size

distribution parameters of ground agricultural residue biomass, as outlined in the recently published standard ANSI/ASABE S631 (ANSI/ASABE, 2023), into the empirical model for calculating the frictional pressure drops of ARB-water slurry flows through inclined pipes. The research can be extended further for the previously developed pressure drop correlations of ARB slurry flows through horizontal and vertical pipe sections.

7.2.3 Examine the impact of pipe diameter on the frictional behaviour of agricultural residue biomass-water slurry

The experimental study of agricultural residue biomass-water slurries through horizontal, inclined, and vertical test sections of a 50 mm diameter closed pipeline loop revealed different technical aspects to explore further. The variations in the onset velocity of drag reduction, $(C_m)_{cr}$, %DR, and threshold concentration for a minimum onset velocity with respect to particle type, size, pipe orientation, and slurry concentrations suggest it is worth investigating the corresponding results for larger diameter pipelines with higher D/D_{50} of 10-20 with respect to the largest nominal particle size (i.e., 19.2 mm) of agricultural residue biomass (where D is the pipe's inner diameter and D_{50} is the mean length of the biomass particles) used in the current investigation. The proposed research could not only explore the frictional behaviour of the agricultural residue biomass slurries for larger-diameter pipelines but also assist in modifying the empirical correlations of frictional pressure drops through horizontal, vertical, and inclined pipe sections using the real-time data of these kinds of slurries.

7.2.4 Techno-economic analysis of pipeline hydro-transport of agricultural residue biomass slurries for an integrated long-distance pipeline network

Vaezi et al.'s techno-economic analysis (2015) did not include a topography based on the GIS mapping of an existing or possible future scenario of a typical biorefinery and farms, which could

consist of vertical and inclined pipes in addition to horizontal lines. Their techno-economic model used the frictional pressure drop correlations of agricultural residue biomass-water suspension flows through horizontal pipes only. The primary reason Vaezi and colleagues did not develop a GIS-based techno-economic model was the need for more knowledge on the empirical correlations of frictional pressure drops of agricultural residue biomass-water slurries through vertical and inclined pipe sections at that time. The proposed study will use relevant empirical correlations of the frictional pressure drops of these slurries through horizontal, vertical, and inclined pipes to conduct a comprehensive techno-economic assessment of aqueous-based agricultural residue biomass slurry flows through a long-distance integrated pipeline network connecting farms to a typical biorefinery.

7.2.5 Investigate the effect of wide particle size range and slurry temperature on the frictional behavior of agricultural residue biomass-water slurry flows through pipes.

The proposed research entails the combination of different nominal particle sizes (specifically, 19.2 mm, 6.4 mm, 3.2 mm, and particles smaller than 3.2 mm) of wheat straw or corn stover. These combinations will be made independently, with a fixed, known mass percentage assigned to each particle size (e.g., 70% mass percentage of 19.2 mm + 30% mass percentage of 3.2 mm, etc.). The first objective is to determine an appropriate method for representing these mixed feedstock's particle size and distribution parameters using the ANSI/ASABE S631 standard. The second objective is to investigate the frictional behavior of the resulting slurries at different mass concentrations and flow conditions, specifically when flowing through pipe sections with varying inclinations. Moreover, the temperature affects the slurry rheology. It is essential to investigate the impact of temperature, particularly over 16°C (maintained in most lab-scale experiments in this study).

7.2.6 Investigate local velocity and concentration profiles of agricultural residue biomass-water slurry flows through horizontal, vertical and inclined pipes

This proposed research suggests investigating the assumed turbulence damping during slurry flow through a pipeline due to the presence of agricultural residue biomass particles by measuring possible variations of local velocity fluctuations and developing velocity profiles across the pipe's cross-section using, e.g., ultrasonic or MRI (magnetic resonance imaging) techniques. Further, the current research found the delivered concentrations of the agricultural residue biomass particles to be almost equivalent to their prepared concentrations and that they can be used as in situ concentrations while measuring the gravity component of the slurry during vertical or inclined flows to obtain the frictional pressure drop. However, at higher concentrations, when the flocs grow because of the coherent networks, it is essential to develop the concentration profiles across the pipe's cross-section (at different pipe orientations i.e., horizontal, vertical, or inclined) using ultrasonic, ERT (electric resistance tomography), or MRI techniques. Because there are no commercially available devices for highly concentrated (i.e., 40% saturated mass concentration) agricultural residue biomass-water slurries, the previously mentioned techniques for the current study must be customized to develop concentration profiles.

Bibliography

- Abas, N., Kalair, A., & Khan, N. (2015). Review of fossil fuels and future energy technologies. *Futures*, 69, 31-49. doi:<https://doi.org/10.1016/j.futures.2015.03.003>
- Abulnaga, B. E. (2002). *Slurry systems handbook* (1st ed.). New York: McGraw-Hill.
- Addie, G. R., Sellgren, A., & Wilson, K. C. (2005). Centrifugal slurry pump concentration limit testing and evaluation phase 1. Retrieved from https://openlibrary.org/works/OL18608717W/Centrifugal_slurry_pump_concentration_limit_testing_and_evaluation--phase_1?edition=key%3A/books/OL16327914M [Accessed: September 04, 2023].
- Aden, A., Ruth, M., Ibsen, K., Jechura, J., Neeves, K., Sheehan, J., . . . Lukas, J. (2002). Lignocellulosic biomass to ethanol process design and economics utilizing co-current dilute acid prehydrolysis and enzymatic hydrolysis for corn stover (NREL/TP-510-32438). Retrieved from the U.S. Department of Energy: <https://doi.org/10.2172/15001119> [Accessed: January 22, 2019].
- Agrawal, Y. K. (2016). Towards turbulence modulation in concentrated solid-liquid flows. (M.Sc. thesis), University of Alberta, Edmonton, AB, Canada.
- Ahmad, Z., & Zhang, J. (2009). Selective combination of multiple neural networks for improving model prediction in nonlinear systems modelling through forward selection and backward elimination. *Neurocomputing*, 72(4-6), 1198-1204. doi:<https://doi.org/10.1016/j.neucom.2008.02.005>
- Ahmed, R. M., & Takach, N. E. (2009). Fiber sweeps for hole cleaning. *SPE Drilling and Completion*, 24(04), 564-573. doi:<https://doi.org/10.2118/113746-PA>
- Aho, K., Derryberry, D., & Peterson, T. (2014). Model selection for ecologists: the worldviews of AIC and BIC. *Ecology*, 95(3), 631-636. doi:<https://www.jstor.org/stable/43495189>
- Akaike, H. (1998). Information theory and an extension of the maximum likelihood principle *In Selected papers of hirotugu akaike* (pp. 199-213): Springer.

- Al-Mutahar, F. (2006). Modeling of critical deposition velocity of sand in horizontal and inclined pipes. (M.Sc. thesis), The University of Tulsa, Tulsa, Oklahoma.
- ANSI/ASABE. (2023). Machine vision method of forage or biomass particle size and size distribution. Retrieved from <https://elibrary.asabe.org/abstract.asp?aid=54331&t=2> [Accessed: August 26, 2023].
- Anwer, M., So, R., & Lai, Y. (1989). Perturbation by and recovery from bend curvature of a fully developed turbulent pipe flow. *Physics of Fluids A: Fluid Dynamics*, 1(8), 1387-1397. doi:<https://doi.org/10.1063/1.857315>
- ASABE. (2012). Moisture measurement for forages. Standard S358. 3. Retrieved from <https://elibrary.asabe.org/standards.asp> [Accessed: June 15, 2018].
- Asomaning, J., Omidghane, M., Chae, M., & Bressler, D. C. (2016). Thermal processing of algal biomass for biofuel production. *Current Opinion in Green and Sustainable Chemistry*, 2, 1-5. doi:<https://doi.org/10.1016/j.cogsc.2016.08.005>
- ASTM. (2015). Standard test method for relative density (specific gravity) and absorption of coarse aggregate - ASTM C127-12. Retrieved from <https://standards.globalspec.com/std/9903948/astm-c127> [Accessed: January 10, 2022].
- Azzola, J., Humphrey, J., Iacovides, H., & Launder, B. (1986). Developing turbulent flow in a U-bend of circular cross-section: measurement and computation. *Journal of Fluid Engineering*, 108(2), 214-221. doi:<https://doi.org/10.1115/1.3242565>
- Balat, M., & Balat, H. (2009). Recent trends in global production and utilization of bio-ethanol fuel. *Journal of Applied Energy*, 86(11), 2273-2282. doi:<https://doi.org/10.1016/j.apenergy.2009.03.015>
- Banerjee, S., Mudliar, S., Sen, R., Giri, B., Satpute, D., Chakrabarti, T., & Pandey, R. (2010). Commercializing lignocellulosic bioethanol: technology bottlenecks and possible remedies. *Journal of Biofuels, Bioproducts and Biorefining: Innovation for a sustainable economy*, 4(1), 77-93. doi:<https://doi.org/10.1002/bbb.188>
- Barnes, H. A., Hutton, J. F., & Walters, K. (1989). *An introduction to rheology* (Vol. 3): Elsevier.

- Bartosik, A. (1996). Modelling the Bagnold stress effects in vertical slurry flow. *Journal of Hydrology and Hydromechanics*, 44(1), 49-58.
- Bartosik, A. (2010). Influence of coarse-dispersive solid phase on the particles-wall shear stress in turbulent slurry flow with high solid concentration. *Archive of Mechanical Engineering*, 57(1), 45-68. doi:<https://doi.org/10.2478/v10180-010-0003-1>
- Belyachits, A. C., Titovitsky, J. A., & Serdyuk, V. M. (2014). Measuring of solid phase concentration in aqueous-cellulose pulp using microwave sensors. *International Journal of Innovative Research in Science, Engineering and Technology*, 3(11), 17101-17106. doi:<https://doi.org/10.15680/IJRSET.2014.0311001>
- Bobkowicz, A. J., & Gauvin, W. (1965). The turbulent flow characteristics of model fibre suspensions. *The Canadian Journal of Chemical Engineering*, 43(2), 87-91. doi:<https://doi.org/10.1002/cjce.5450430210>
- Bragg-Sitton, S. M., Boardman, R., Rabiti, C., & O'Brien, J. (2020). Reimagining future energy systems: Overview of the US program to maximize energy utilization via integrated nuclear-renewable energy systems. *International Journal of Energy Research*, 44(10), 8156-8169. doi:<https://doi.org/10.1002/er.5207>
- Brebner, A. (1964). On the pumping of wood chips through a four-inch aluminum pipe-line. *The Canadian Journal of Chemical Engineering*, 42(3), 139-142.
- BTG. (2023). Products, Consistency measurements of paper and pulp. Retrieved from <https://www.btg.com/consistency-measurement/> [Accessed: August 18, 2023].
- Bunte, K., & Abt, S. R. (2001). *Sampling surface and subsurface particle-size distributions in wadable gravel- and cobble-bed streams for analyses in sediment transport, hydraulics, and streambed monitoring*: United States Department of Agriculture.
- Canada's Net Zero Future. (2021). Retrieved from https://climatechoices.ca/wp-content/uploads/2021/02/Canadas-Net-Zero-Future_FINAL-2.pdf [Accessed: February 16, 2021].
- Center for Climate and Energy Solutions. (2023). Global Emissions. Retrieved from <https://www.c2es.org/content/international->

- [emissions/#:~:text=by%20Sector%2C%202013-.Notes,72%20percent%20of%20all%20emissions](#) [Accessed: August 26, 2023].
- Chapman, A. J., McLellan, B. C., & Tezuka, T. (2018). Prioritizing mitigation efforts considering co-benefits, equity and energy justice: Fossil fuel to renewable energy transition pathways. *Applied Energy*, 219, 187-198. doi:<https://doi.org/10.1016/j.apenergy.2018.03.054>
- Chaurette, J. (2003). Pipe roughness values. Retrieved from https://www.pumpfundamentals.com/download-free/pipe_rough_values.pdf [Accessed: January 05, 2017].
- Chowdhury, R. R., Biswas, S., Alam, M. M., & Islam, A. S. (2016). Turbulent flow analysis on bend and downstream of the bend for different curvature ratio. Paper presented at the 11th American Institute of Physics Conference BUET, Dhaka, Bangladesh. <https://doi.org/10.1063/1.4958380> [Accessed: February 28, 2017].
- Chung, J., Yarim, G., & Savasci, H. (1998). Shape effect of solids on pressure drop in a 2-phase vertically upward transport: silica sands and spherical beads. Paper presented at the 8th International Offshore and Polar Engineering Conference, Montreal, Canada. <https://www.onepetro.org/conference-paper/ISOPE-I-98-011> [Accessed: September 09, 2016].
- Churchill, S. W. (1977). Friction-factor equation spans all fluid-flow regimes. *Journal of Chemical Engineering*, 84(24), 91-92.
- CIMCO Industries limited. (2021). Industrial refrigeration. Retrieved from <https://www.cimcorefrigeration.com/industries/industrial-refrigeration-systems> [Accessed: August 29, 2023].
- Cotas, C., Asendrych, D., Garcia, F., Faia, P., & Rasteiro, M. G. (2015). Turbulent flow of concentrated pulp suspensions in a pipe—numerical study based on a pseudohomogeneous approach. Paper presented at the Proc. COST Action FP1005 Final Conference. Trondheim, Norway. [Accessed: January 09, 2022].
- Cotas, C. I. P. (2016). Modelling of fiber suspensions flow in pipes. (Ph.D. thesis), University of Coimbra, Coimbra, Portugal.

- Cui, H., & Grace, J. R. (2007). Flow of pulp fibre suspension and slurries: A review. *International Journal of Multiphase Flow*, 33(9), 921-934.
- Daily, J., Bugliarello, G., & Troutman, W. (1961). Basic data for dilute fiber suspensions in uniform flow with shear. *Journal of Technical Association of Pulp and Paper Industry*, 44(7), 497.
- De Vreede, M. (2018). Hydraulic transport in inclined large diameter pipelines. (M.Sc. thesis), University of Tu Delft, Delft, Netherlands.
- Derakhshandeh, B., Kerekes, R., Hatzikiriakos, S., & Bennington, C. (2011). Rheology of pulp fibre suspensions: A critical review. *Chemical Engineering Science*, 66(15), 3460-3470.
- Derksen, S., & Keselman, H. J. (1992). Backward, forward and stepwise automated subset selection algorithms: Frequency of obtaining authentic and noise variables. *British Journal of Mathematical and Statistical Psychology*, 45(2), 265-282. doi:<https://doi.org/10.1111/j.2044-8317.1992.tb00992.x>
- Djalili-Moghaddam, M., & Toll, S. (2006). Fibre suspension rheology: effect of concentration, aspect ratio and fibre size. *Journal of Rheologica Acta*, 45(3), 315-320. doi:<https://doi.org/10.1007/s00397-005-0021-y>
- Dodson, C. (1996). Fiber crowding, Fiber contacts and Fiber flocculation. *Journal of Technical Association of Pulp and Paper Industry*, 79(9), 211-216.
- Doi, M., & Edwards, S. (1978a). Dynamics of rod-like macromolecules in concentrated solution. Part 1. *Journal of the Chemical Society, Faraday Transactions 2: Molecular and Chemical Physics*, 74, 560-570. doi:<https://doi.org/10.1039/F29787400560>
- Doi, M., & Edwards, S. (1978b). Dynamics of rod-like macromolecules in concentrated solution. Part 2. *Journal of the Chemical Society, Faraday Transactions 2: Molecular and Chemical Physics*, 74, 918-932. doi:<https://doi.org/10.1039/F29787400918>
- Doron, P., & Barnea, D. (1996). Flow pattern maps for solid-liquid flow in pipes. *International journal of multiphase flow*, 22(2), 273-283.
- Duffy, D., & Lee, P. (1978). Drag reduction in the turbulent flow of wood pulp suspensions. *Appita Journal*, 31, 280-286.

- Duffy, G., Moller, K., Lee, P., & Milne, S. (1974). Design correlations for groundwood pulps and effects of minor variables on pulp suspension flow. *Appita Journal*, 27(5), 327-333.
- Duffy, G. G. (1989). The optimum design of pipelines for transporting wood pulp fibre suspensions. *Appita Journal*, 42(5), 358-361.
- Duffy, G. G. (2006). Measurements, mechanisms and models: Some important insights into the mechanisms of flow of fibre suspensions. *Annual Transactions-Nordic Rheology Society*, 14, 19-31.
- Duffy, G. G., Titchener, A. L., Lee, P. F. W., & Moller, K. (1976). The mechanisms of flow of pulp suspensions in pipes. *Appita Journal*, 29(5), 363-370.
- Durand, R. (1953). Basic relationships of the transportation of solids in pipes-experimental research. *International Association for Hydro-Environment Engineering and Research*, 5th Congr. Minneapolis, 1953.
- Durand, R., & Condolios, E. (1952a). Hydraulic transport of coal and solid materials in pipes (Colloquium on Hydraulic Transport of Coal). Paper presented at the National Coal Board, London, England. <https://trove.nla.gov.au/version/12738715> [Accessed: July 02, 2016].
- Durand, R., & Condolios, E. (1952b). Transport hydraulique et décantation des matériaux solides. *Deuxieme Journée de l'Hydraulique*, 27-55.
- Efroymson, M. A. (1960). Multiple regression analysis. *Mathematical methods for digital computers*, 1, 191-203.
- Elgaddafi, R., & Ahmed, R. (2020). Fibrous Cleanout Fluids in Horizontal and Inclined Wells. Paper presented at the SPE/International & Coiled Tubing Association Well Intervention Conference and Exhibition, The Woodlands, Texas, USA. <https://doi.org/10.2118/199868-MS> [Accessed: June 24, 2022].
- Eliason, J. (2002). Sand media specifications Washington, USA. Retrieved from <https://www.doh.wa.gov/Portals/1/Documents/Pubs/337-104.pdf> [Accessed: February 20, 2019].
- Elliott, D. (1960). The transportation of pulpwood chips in pipelines. *Pulp and Paper in Canada*, 61(5), 170-175.

- Ellis, H. (1970). Effects of shear treatment on drag-reducing polymer solutions and fibre suspensions. *Nature*, 226(5243), 352-353.
- Enayet, M., Gibson, M., Taylor, A., & Yianneskis, M. (1982). Laser-Doppler measurements of laminar and turbulent flow in a pipe bend. *International Journal of Heat and Fluid Flow*, 3(4), 213-219. doi:[https://doi.org/10.1016/0142-727X\(82\)90024-8](https://doi.org/10.1016/0142-727X(82)90024-8)
- Faddick, R. (1963). The aqueous transport of pulpwood chips in a four inch aluminum pipe. (Ph.D. thesis), Queen's University, Kingston, Ontario.
- Faddick, R. R. (1970). The hydraulic transportation of solids in pipelines. (Ph.D thesis), Montana State University-Bozeman, College of Engineering.
- Faia, P., Silva, R., Rasteiro, M. G., & Garcia, F. (2020). Electrical tomography: a review of configurations, and application to fibre flow suspensions characterisation. *Applied Sciences Journal*, 10(7), 2355. doi:<https://doi.org/10.3390/app10072355>
- Faraj, Y. (2013). Measurement and visualisation of slurry flow using electrical resistance tomography. (PhD thesis), University of Leeds, Leeds, UK.
- Faraj, Y., & Wang, M. (2012). ERT investigation on horizontal and vertical counter-gravity slurry flow in pipelines. *Procedia Engineering Journal*, 42, 588-606. doi:<https://doi.org/10.1016/j.proeng.2012.07.452>
- Ferre, A. L., & Shook, C. A. (1998). Coarse particle wall friction in vertical slurry flows. *Particulate Science and Technology Journal*, 16(2), 125-133. doi:<https://doi.org/10.1080/02726359808906790>
- Fetyan, N. A., El-Sayed, A. E.-K. B., Ibrahim, F. M., Attia, Y. A., & Sadik, M. W. (2022). Bioethanol production from defatted biomass of *Nannochloropsis oculata* microalgae grown under mixotrophic conditions. *Environmental Science and Pollution Research Journal*, 29(2), 2588-2597. doi:<https://doi.org/10.1007/s11356-021-15758-6>
- Fock, H., Claesson, J., Rasmuson, A., & Wikström, T. (2011). Near wall effects in the plug flow of pulp suspensions. *The Canadian Journal of Chemical Engineering*, 89(5), 1207-1216.
- Folk, R. L., & Ward, W. C. (1957). Brazos River bar [Texas]; a study in the significance of grain size parameters. *Journal of sedimentary research*, 27(1), 3-26.

- Forrest, F., & Grierson, G. (1931). Friction losses in cast iron pipe carrying paper stock. *Paper Trade Journal*, 92(22), 39-41.
- Friedman, J., Hastie, T., & Tibshirani, R. (2001). *The elements of statistical learning* (Vol. 1): Springer series in statistics New York.
- Frizzel, K. W. (1985). Laboratory Investigations of slurry pipeline for the Yuma Desalting plant (GR-85-4). Retrieved from <https://www.usbr.gov/tsc/techreferences/research/GR-85-04.pdf> [Accessed: April 14, 2017].
- Fuji Electric. (2010). Fuji Electric France, differential pressure (flow) transmitter (FKC-5). Retrieved from http://www.coulton.com/res/fkc_dp_transmitter_edsf6_134b.pdf [Accessed: August 20, 2023].
- Fuji Electric. (2014). Instructions manual and service instructions, FCX-AII-V5 series transmitters. Retrieved from <https://www.instrumart.com/assets/Fuji-FCX-manual.pdf> [Accessed: August 29, 2023].
- Ghatora, S., Kumar, M., Vaezi, M., Kumar, A., & Bressler, D. (2016). Monitoring sugar release during pipeline hydro-transport of wheat straw. *Biomass and Bioenergy*, 93, 144-149. doi:<https://doi.org/10.1016/j.biombioe.2016.07.007>
- Gibert, R. (1960). Transport hydraulique et refoulement des mixtures en conduites. Paper presented at the Annales des Ponts et Chausees. [Accessed: April 16, 2022].
- Gil, M., Schott, D., Arauzo, I., & Teruel, E. (2013). Handling behavior of two milled biomass: SRF poplar and corn stover. *Fuel Processing Technology*, 112, 76-85. doi:<https://doi.org/10.1016/j.fuproc.2013.02.024>
- Gil, M., Teruel, E., & Arauzo, I. (2014). Analysis of standard sieving method for milled biomass through image processing. Effects of particle shape and size for poplar and corn stover. *Fuel*, 116, 328-340. doi:<https://doi.org/10.1016/j.fuel.2013.08.011>
- Goldemberg, J. (2008). Environmental and ecological dimensions of biofuels. Paper presented at the Proceedings of the Conference on the Ecological Dimensions of Biofuels, Washington, DC. https://www.esa.org/biofuels/presentations/Goldemberg_BiofuelsPresentation.pdf [Accessed: November 04, 2021].

- Gow, J. L. (1971). The hydraulic transport of wood chips. (Ph.D thesis), Montana State University-Bozeman, College of Engineering, Bozeman, Montana.
- Halder, P., Azad, K., Shah, S., & Sarker, E. (2019). Prospects and technological advancement of cellulosic bioethanol ecofuel production. *Advances in Eco-fuels for a Sustainable Environment*, 211-236. doi:<https://doi.org/10.1016/B978-0-08-102728-8.00008-5>
- Hellström, L. H., Zlatinov, M. B., Cao, G., & Smits, A. J. (2013). Turbulent pipe flow downstream of a 90 degree bend. *Journal of Fluid Mechanics*, 735, 1-12. doi:<https://doi.org/10.1017/jfm.2013.534>
- Horiba. Camsizer. Retrieved from <https://www.horiba.com/en/en/> [Accessed: Aug 25, 2023].
- Hosseini, S. (2008). Solid–liquid mixing in agitated tanks: experimental and CFD analysis. (M.Sc. thesis), Ryerson University, Toronto, ON, Canada.
- Hoyt, J. (1972). Turbulent flow of drag-reducing suspensions. Retrieved from <https://apps.dtic.mil/sti/citations/tr/AD0746485> [Accessed: March 22, 2020].
- Huber, P., Roux, J., Mauret, E., Belgacem, N., & Pierre, C. (2003). Suspension crowding for a general fibre-length distribution: Application to flocculation of mixtures of short and long papermaking fibres. *Journal of pulp and paper science*, 29(3), 77-85.
- Hunt, W. (1976). Friction factors for mixtures of wood chips and water flowing in pipelines. Retrieved from Banff Springs, Alberta, Canada: [Accessed: April 09, 2018].
- International Energy Agency. (2021). Net Zero by 2050, A roadmap for the global energy sector. Retrieved from https://iea.blob.core.windows.net/assets/deebef5d-0c34-4539-9d0c-10b13d840027/NetZeroBy2050-ARoadmapfortheGlobalEnergySector_CORR.pdf [Accessed: February 12, 2022].
- ISO. (2007). Fluid flow in closed conduits-connections for pressure signal transmissions between primary and secondary elements. Retrieved from <https://www.iso.org/standard/38091.html> [Accessed: February 20, 2016].
- Ito, H. (1960). Pressure losses in smooth pipe bends. *Journal of Basic Engineering*, 82(1), 131-140. doi:<https://doi.org/10.1115/1.3662501>

- Javed, K., Kurian, V., & Kumar, A. (2022a). Comparison of maize stover and wheat straw slurries flow in vertical pipes. *Biosystems Engineering*, 224, 259-282. doi:<https://doi.org/10.1016/j.biosystemseng.2022.10.013>
- Javed, K., Kurian, V., & Kumar, A. (2022b). Effect of particle size and concentration on the frictional behavior of vertical upward flows of wheat straw aqueous slurries. *Chemical Engineering Research and Design Journal*, 186, 614-627. doi:<https://doi.org/10.1016/j.cherd.2022.08.024>
- Javed, K., Vaezi, M., Kurian, V., & Kumar, A. (2021). Frictional behavior of wheat straw-water suspensions in vertical upward flows. *Biosystems Engineering*, 212, 30-45. doi:<https://doi.org/10.1016/j.biosystemseng.2021.09.016>
- Jing, Y. (2009). The influence of chemical and mechanical flocculation on paper formation as assessed by the grammage probability distribution. (M.Sc. thesis), Miami University, Oxford, Ohio.
- Kada, H., & Hanratty, T. J. (1960). Effects of Solids on Turbulence in a Fluid. *American Institute of Chemical Engineers Journal*, 6(4), 624-630. doi:<https://doi.org/10.1002/aic.690060424>
- Kalyanraman, K., Ghosh, D., & Rao, A. (1973). Characteristics of sand water slurry in 90 horizontal pipe bend. *Journal of the Institute of Engineers (India): Mechanical Engineering Division*, 54, 73-79.
- Kao, D., & JL, S. (1980). Flow behaviour of solid-liquid mixtures in pipes on positive and negative grades. Paper presented at the Proceedings, Hydrotransport 7, Cranfield, UK. [Accessed: April 18, 2019].
- Kaushal, D., Kumar, A., Tomita, Y., Kuchii, S., & Tsukamoto, H. (2013). Flow of mono-dispersed particles through horizontal bend. *International Journal of Multiphase Flow*, 52, 71-91. doi:<https://doi.org/10.1016/j.ijmultiphaseflow.2012.12.009>
- Kaushal, D. R., Kumar, A., Tomita, Y., Kuchii, S., & Tsukamoto, H. (2017). Flow of bi-modal slurry through horizontal bend. *KONA Powder and Particle Journal*, 34, 258-274. doi:<https://doi.org/10.14356/kona.2017016>

- Kazi, M. S. N., Duffy, G. G., & Chen, X. D. (1999). Heat transfer in the drag reducing regime of wood pulp fibre suspensions. *Chemical Engineering Journal*, 73(3), 247-253. doi:[https://doi.org/10.1016/S1385-8947\(99\)00047-9](https://doi.org/10.1016/S1385-8947(99)00047-9)
- Kelly, S. E. (2013). Demonstrating reliable high level waste slurry sampling techniques to support hanford waste processing. Paper presented at the Waste Management Symposia, Phoenix, Arizona.
https://inis.iaea.org/collection/NCLCollectionStore/_Public/45/112/45112143.pdf
[Accessed: March 26, 2017].
- Kerekes, R., & Douglas, W. (1972). Viscosity properties of suspensions at the limiting conditions for turbulent drag reduction. *The Canadian Journal of Chemical Engineering*, 50(2), 228-231. doi:<https://doi.org/10.1002/cjce.5450500215>
- Kerekes, R., & Schell, C. (1992). Regimes by a crowding factor. *Journal of Pulp and Paper Science*, 18(1), J32-J38.
- Kerekes, R., Soszynski, R., & Doo, T. (1985). The flocculation of pulp fibres. Paper presented at the Papermaking Raw Materials: Their Interaction with the Production Process and Their Effect on Paper Properties-Transactions of the 8th Fundamental Research Symposium held at Oxford: September 1985. [Accessed: June 02, 2018].
- Kerekes, R. J. (2006). Rheology of suspensions-Rheology of fibre suspensions in papermaking: An overview of recent research. *Nordic Pulp & Paper Research Journal*, 21(5), 598-612. doi:<https://doi.org/10.3183/npprj-2006-21-05-p598-612>
- Kerekes, R. J., & Schell, C. J. (1995). Effects of fiber length and coarseness on pulp flocculation. *Journal of Technical Association of Pulp and Paper Industry*, 78(2), 133-139. doi:<https://api.semanticscholar.org/CorpusID:139663380>
- Kerekes, R. J. E. (1971). Turbulent drag reduction in pipe flow of ideal fibre suspensions (Ph.D. thesis), McGill University, Montreal, QC, Canada.
- Kesely, M., Matousek, V., & Vlasak, P. (2019). Settling slurry flow near deposition velocity in inclined pipe of negative slope. Paper presented at the EPJ Web of Conferences. <https://doi.org/10.1051/epjconf/201921302040> [Accessed: February 12, 2021].

- Kim, J., Yadav, M., & Kim, S. (2014). Characteristics of secondary flow induced by 90-degree elbow in turbulent pipe flow. *Engineering Applications of Computational Fluid Mechanics*, 8(2), 229-239. doi:<https://doi.org/10.1080/19942060.2014.11015509>
- Kim, S., & Dale, B. E. (2004). Global potential bioethanol production from wasted crops and crop residues. *Biomass and bioenergy*, 26(4), 361-375. doi:<https://doi.org/10.1016/j.biombioe.2003.08.002>
- Knutsen, J. S., & Liberatore, M. W. (2009). Rheology of high-solids biomass slurries for biorefinery applications. *Journal of Rheology*, 53(4), 877-892. doi:<https://doi.org/10.1122/1.3143878>
- Krampa, F. N. (2009). Two-fluid modelling of heterogeneous coarse particle slurry flows. (Ph.D. thesis), University of Saskatchewan, Saskatoon, SK, Canada.
- Kropholler, H., & Sampson, W. (2001). The effect of fibre length distribution on suspension crowding. *Journal of Pulp and Paper Science*, 27(9), 301-305.
- Kumar, A., Cameron, J. B., & Flynn, P. C. (2003). Biomass power cost and optimum plant size in western Canada. *Biomass and Bioenergy*, 24(6), 445-464. doi:[https://doi.org/10.1016/S0961-9534\(02\)00149-6](https://doi.org/10.1016/S0961-9534(02)00149-6)
- Kumar, A., Cameron, J. B., & Flynn, P. C. (2004). Pipeline transport of biomass. *Applied Biochemistry and Biotechnology*, 113 (1-3)(1), 27-39. doi:https://doi.org/10.1007/978-1-59259-837-3_4
- Kumar, A., Cameron, J. B., & Flynn, P. C. (2005a). Large-scale ethanol fermentation through pipeline delivery of biomass. Paper presented at the Twenty-Sixth Symposium on Biotechnology for Fuels and Chemicals. https://doi.org/10.1007/978-1-59259-991-2_4 [Accessed: May 07, 2019].
- Kumar, A., Cameron, J. B., & Flynn, P. C. (2005b). Pipeline transport and simultaneous saccharification of corn stover. *Bioresource Technology*, 96(7), 819-829. doi:<https://doi.org/10.1016/j.biortech.2004.07.007>
- Kumar, N., Gopaliya, M. K., & Kaushal, D. (2019). Experimental investigations and CFD modeling for flow of highly concentrated iron ore slurry through horizontal pipeline.

- Particulate Science and Technology*, 37(2), 232-250.
doi:<https://doi.org/10.1080/02726351.2017.1364313>
- Lam, P. S., Sokhansanj, S., Bi, X., & Lim, C. J. (2008). Effect of particle size and shape on physical properties of biomass grinds. Paper presented at the 2008 Providence, Rhode Island, June 29-July 2, 2008. <https://doi.org/10.13031/2013.24879> [Accessed: August 21, 2017].
- Lamb, W. F., Wiedmann, T., Pongratz, J., Andrew, R., Crippa, M., Olivier, J. G., . . . House, J. (2021). A review of trends and drivers of greenhouse gas emissions by sector from 1990 to 2018. *Environmental research letters*, 16(7), 1-31. doi:<https://doi.org/10.1088/1748-9326/abee4e>
- Larson, R. G. (1999). *The structure and rheology of complex fluids* (Vol. 150): Oxford university press New York.
- Lee, R. A., & Lavoie, J.-M. (2013). From first-to third-generation biofuels: Challenges of producing a commodity from a biomass of increasing complexity. *Animal Frontiers*, 3(2), 6-11. doi:<https://doi.org/10.2527/af.2013-0010>
- Li, T. Q., Seymour, J. D., Powell, R. L., McCarthy, M. J., McCarthy, K. L., & Ödberg, L. (1994). Visualization of flow patterns of cellulose fiber suspensions by NMR imaging. *AIChE journal*, 40(8), 1408-1411. doi:<https://doi.org/10.1002/aic.690400812>
- Link, J. M., Faddick, R. R., Pouska, G. A., & Gusek, J. J. (1977). The hydraulic transportation of oil shale. Research report (OSTI ID: 6281926). Retrieved from <https://www.osti.gov/biblio/6281926> [Accessed February 04, 2017].
- Luetgten, C. O., Lindsay, J. D., & Stratton, R. A. (1991). Turbulent dispersion in pulp flow: preliminary results and implications for the mechanisms of fiber-turbulence interactions.
- Luk, J. (2010). Pipeline transport of wheat straw biomass. (M.Sc. thesis), University of Alberta, Edmonton, AB.
- Luk, J., Mohamadabadi, H. S., & Kumar, A. (2014). Pipeline transport of biomass: Experimental development of wheat straw slurry pressure loss gradients. *Biomass and Bioenergy*, 64, 329-336. doi:<https://doi.org/10.1016/j.biombioe.2014.03.046>

- Mahdavi, M., Karimi, S., Shirazi, S. A., & McLaury, B. S. (2016). Parametric study of erosion under high concentrated slurry: experimental and numerical analyses. Paper presented at the ASME 2016 Fluids Engineering Division Summer Meeting collocated with the ASME 2016 Heat Transfer Summer Conference and the ASME 2016 14th International Conference on Nanochannels, Microchannels, and Minichannels. <https://doi.org/10.1115/FEDSM2016-7718> [Accessed: May 09, 2017].
- Maity, S., & Mallick, N. (2022). Trends and advances in sustainable bioethanol production by marine microalgae: A critical review. *Journal of Cleaner Production*, 345(131153), 1-19. doi:<https://doi.org/10.1016/j.jclepro.2022.131153>
- Manhart, M. (2003). Rheology of suspensions of rigid-rod like particles in turbulent channel flow. *Journal of Non-Newtonian Fluid Mechanics*, 112(2-3), 269-293. doi:[https://doi.org/10.1016/S0377-0257\(03\)00105-8](https://doi.org/10.1016/S0377-0257(03)00105-8)
- Masch, F. D., & Denny, K. J. (1966). Grain size distribution and its effect on the permeability of unconsolidated sands. *Water Resources Research*, 2(4), 665-677. doi:<https://doi.org/10.1029/WR002i004p00665>
- Matousek, V. (1997). Flow mechanism of sand-water mixtures in pipelines. (Ph.D. thesis), Technical University Delft, Delft, Netherlands.
- Matousek, V. (2000). Concentration distribution in pipeline flow of sand-water mixtures. *Vodohospodarsky Casopis*, 48(3), 180-196.
- Matousek, V. (2002). Pressure drops and flow patterns in sand-mixture pipes. *Experimental thermal and fluid science*, 26(6), 693-702. doi:[https://doi.org/10.1016/S0894-1777\(02\)00176-0](https://doi.org/10.1016/S0894-1777(02)00176-0)
- Matousek, V. (2005). Pipe-wall friction in vertical sand-slurry flows. Paper presented at the ASME 2005 Fluids Engineering Division Summer Meeting, Houston, Texas, USA. <https://doi.org/10.1115/FEDSM2005-77278>
- Matousek, V. (2009). Pipe-wall friction in vertical sand-slurry flows. *Particulate Science and Technology*, 27(5), 456-468. doi:<https://doi.org/10.1080/02726350903133179>
- Matousek, V., Chara, Z., Konfrst, J., & Novotny, J. (2022). Experimental investigation on effect of stratification of bimodal settling slurry on slurry flow friction in pipe. *Experimental*

- Thermal and Fluid Science*, 132, 110561.
doi:<https://doi.org/10.1016/j.expthermflusci.2021.110561>
- Matousek, V., Kesely, M., & Chara, Z. (2019). Effect of pipe inclination on internal structure of settling slurry flow at and close to deposition limit. *Powder Technology*, 343, 533-541.
doi:<https://doi.org/10.1016/j.powtec.2018.11.035>
- Matousek, V., Krupicka, J., & Kesely, M. (2018). A layered model for inclined pipe flow of settling slurry. *Powder Technology*, 333, 317-326.
doi:<https://doi.org/10.1016/j.powtec.2018.04.021>
- McKibben, M. J. (1993). Wall erosion in slurry pipelines. (Ph.D. thesis), University of Saskatchewan, Saskatoon, SK, Canada.
- MECE 301. (2018). Calibration and uncertainty Analysis. Retrieved from <https://www.coursehero.com/file/25469870/MecE-301-01-Calibration-and-Uncertainty-Analysispdf/> [Accessed: September 02, 2023].
- Meng, Y., & Lucas, G. P. (2017). Imaging water velocity and volume fraction distributions in water continuous multiphase flows using inductive flow tomography and electrical resistance tomography. *Measurement Science and Technology*, 28(5), 055401.
doi:<https://doi.org/10.1088/1361-6501/aa5e83>
- Meyer, H. (1964). An analytical treatment of the laminar flow of annulus forming fibrous suspensions in vertical pipes. *Technical Association of Pulp and Paper Industry*, 47, 78.
- Miedema, S. A. (2015). A head loss model for homogeneous slurry transport for medium sized particles. *Journal of Hydrology and Hydromechanics*, 63(1), 1-12.
doi:<https://doi.org/10.1515/johh-2015-0005>
- Miedema, S. A., Wang, F., Hong, G., & Chen, X. (2021). Dominating factors in slurry transport in inclined pipes. *WEDA Journal of Dredging*, 19(2), 1-19.
- Mih, W. (1967). Velocity profile measurements and a phenomenological description of turbulent fiber suspension pipe flow. *Journal of Technical Association of Pulp and Paper Industry*, 50(5), 237-246.

- Miller, P., Olateju, B., & Kumar, A. (2012). A techno-economic analysis of cost savings for retrofitting industrial aerial coolers with variable frequency drives. *Energy Conversion and Management*, 54(1), 81-89. doi:<https://doi.org/10.1016/j.enconman.2011.09.018>
- Moffat, R. J. (1988). Describing the uncertainties in experimental results. *Experimental Thermal and Fluid Science*, 1(1), 3-17. doi:[https://doi.org/10.1016/0894-1777\(88\)90043-X](https://doi.org/10.1016/0894-1777(88)90043-X)
- Mohamadabadi, H. S. (2009). Characterization and pipelining of biomass slurries. (M.Sc. thesis), University of Alberta, Edmonton, AB.
- Mohanty, S. K., & Swain, M. R. (2019). Bioethanol production from corn and wheat: food, fuel, and future. *Bioethanol Production from Food Crops*, 45-59. doi:<https://doi.org/10.1016/B978-0-12-813766-6.00003-5>
- Moller, K. (1976). A correlation of pipe friction data for paper pulp suspensions. *Industrial & Engineering Chemistry Process Design and Development*, 15(1), 16-19. doi:<https://doi.org/10.1021/i260057a004>
- Moller, K., & O'Sullivan, M. (1974). Annulus formation in plug flow of pulp suspensions. *Technical Association of Pulp and Paper Industry*, 57(3), 165-165.
- Montgomery, D. C., Peck, E. A., & Vining, G. G. (2021). *Introduction to linear regression analysis* (6th ed.): John Wiley & Sons.
- Mordant, N., & Pinton, J.-F. (2000). Velocity measurement of a settling sphere. *The European Physical Journal B-Condensed Matter and Complex Systems*, 18(2), 343-352. doi:<https://doi.org/10.1007/PL00011074>
- Moujaes, S. F. (1984). Measurement of slurry concentration and flow rates in shell and tube slurry heat exchangers. *The Canadian Journal of Chemical Engineering*, 62(1), 62-67. doi:<https://doi.org/10.1002/cjce.5450620109>
- Movahedi, H., Farahani, M. V., & Jamshidi, S. (2017). Application of hydrated basil seeds (HBS) as the herbal fiber on hole cleaning and filtration control. *Journal of Petroleum Science and Engineering*, 152, 212-228. doi:<https://doi.org/10.1016/j.petrol.2017.02.014>

- Nakayama, S. (1994). Microwave measurements of low pulp concentration in papermaking process. *Japanese Journal of Applied Physics.*, 33(6A), 3614-3616. doi:<https://doi.org/10.1143/jjap.33.3614>
- Nasa. (2021). Global climate change. Retrieved from <https://climate.nasa.gov/vital-signs/carbon-dioxide/> [Accessed: August 28, 2023].
- Natural Resources Canada. (2022). Energy reports and publications. Retrieved from <https://natural-resources.canada.ca/maps-tools-and-publications/publications/energy-publications/energy-reports-and-publications/6539> [Accessed: August 25, 2023].
- Newitt, D. M., Richardson, J. F., Abbott, M., & Turtle, R. B. (1955). Hydraulic conveying of solids in horizontal pipes. *Transactions of the institution of Chemical Engineers*, 33, 93-110.
- Newitt, D. M., Richardson, J. F., & Gliddon, B. J. (1961). Hydraulic conveying of solids in vertical pipes. *Transactions of the Institution of Chemical Engineers*, 39(1961), 93-100.
- Ogawa, K., Yoshikawa, S., Suguro, A., Ikeda, J., & Ogawa, H. (1990). Flow characteristics and circular pipe flow of pulp-suspension. *Journal of Chemical Engineering of Japan*, 23(1), 1-6. doi:<https://doi.org/10.1252/jcej.23.1>
- Our World in Data. (2022). Fossil fuels. Retrieved from <https://ourworldindata.org/fossil-fuels> [Accessed: August 26, 2023].
- Pan, N. (1993). A modified analysis of the microstructural characteristics of general fiber assemblies. *Textile Research Journal*, 63(6), 336-345. doi:<https://doi.org/10.1177/004051759306300605>
- Patel, M., Oyedun, A. O., Kumar, A., & Gupta, R. (2019). Predicting the biomass conversion performance in a fluidized bed reactor using isoconversional model-free method. *The Canadian Journal of Chemical Engineering*, 97, 1263-1273. doi:<https://doi.org/10.1002/cjce.23397>
- Philipse, A. P. (1996). The random contact equation and its implications for (colloidal) rods in packings, suspensions, and anisotropic powders. *Langmuir*, 12(5), 1127-1133. doi:<https://doi.org/10.1021/la950671o>

- Pimenova, N. V., & Hanley, T. R. (2003). Measurement of rheological properties of corn stover suspensions. *Applied Biochemistry and Biotechnology*, 106(1), 383-392. doi:<https://doi.org/10.1385/ABAB:106:1-3:383>
- Pipeflow. (2023). Pipe roughness. Retrieved from <http://www.pipeflow.com/sitemap/pipe-roughness> [Accessed: August 31, 2023].
- Polanský, J. (2014). Experimental investigation of slurry flow. Retrieved from University of Leeds, U.K.: https://home.zcu.cz/~rcermak/opvk_htt/VY_02_05.pdf [Accessed: September 20, 2016].
- Pootakham, T., & Kumar, A. (2010). A comparison of pipeline versus truck transport of bio-oil. *Bioresource Technology*, 101(1), 414-421. doi:<https://doi.org/10.1016/j.biortech.2009.07.077>
- Powell, R. L., Morrison, T. G., & Milliken, W. J. (2001). Apparent viscosity of suspensions of rods using falling ball rheometry. *Physics of Fluids*, 13(3), 588-593.
- R. (2022). The R project for statistical computing. Retrieved from <https://www.r-project.org/> [Accessed: August 18, 2023].
- Radin, I., Zakin, J., & Patterson, G. (1975). Drag reduction in solid-fluid systems. *American Institute of Chemical Engineers Journal*, 21(2), 358-371. doi:<https://doi.org/10.1002/aic.690210218>
- Rai, R. (1972). Pressure loss in hydraulic transport of solids in inclined pipes. Paper presented at the Hydrotransport 2, Coventry, England.
- Rao, N. (1985). Process piping design for pulp suspensions. *IPPTA*, 22(4), 27-35.
- Reader-Harris, M., & McNaught, J. (2005). Best practice guide-Impulse lines for differential pressure flowmeters. Retrieved from East Kilbride, Glasgow, UK: <http://www.interpower.com.hk/uploadfile/2014/1231/20141231044753764.pdf> [Accessed: August 08, 2023].
- Retsch Technology. (2007). Operating instructions / manual particle size analysis system Camsizer. Retrieved from

https://faculty.washington.edu/kate1/ewExternalFiles/manual_camsizer_led_en.pdf

[Accessed: September 02, 2023].

- Robertson, A. (1957). The flow characteristics of dilute fiber suspensions. *Journal of Technical Association of Pulp and Paper Industry*, 40(5), 326-334.
- Roitto, V. (2014). Slurry flows in metallurgical process engineering–Development of tools and guidelines. (M.Sc. thesis), Aalto University, Espoo, Finland.
- Rowe, M. (1970). Measurements and computations of flow in pipe bends. *Journal of Fluid Mechanics*, 43(4), 771-783. doi:<https://doi.org/10.1017/S0022112070002732>
- RStudio. (2023). RStudio IDE. Retrieved from <https://posit.co/> [Accessed: August 26, 2023].
- Ruth, M. (1999). Large scale ethanol facilities and short cut for changing facility size. Retrieved from Internal Report, National Renewable Energy Laboratory Technical Memo: [Accessed: March 28, 2019].
- Saleem, M. (2022). Possibility of utilizing agriculture biomass as a renewable and sustainable future energy source. *Heliyon*, e08905. doi:<https://doi.org/10.1016/j.heliyon.2022.e08905>
- Samaniuk, J., Wang, J., Root, T., Scott, C., & Klingenberg, D. (2011). Rheology of concentrated biomass. *Korea-Australia rheology journal*, 23(4), 237-245. doi:<https://doi.org/10.1007/s13367-011-0029-z>
- Schaan, J., Sumner, R. J., Gillies, R. G., & Shook, C. A. (2000). The effect of particle shape on pipeline friction for Newtonian slurries of fine particles. *The Canadian Journal of Chemical Engineering*, 78(4), 717-725. doi:<https://doi.org/10.1002/cjce.5450780414>
- Schmid, C. F., Switzer, L. H., & Klingenberg, D. J. (2000). Simulations of fiber flocculation: Effects of fiber properties and interfiber friction. *Journal of Rheology*, 44(4), 781-809. doi:<https://doi.org/10.1122/1.551116>
- Schroeder, S., Braun, S., Mueller, U., Sonntag, R., Jaeger, S., & Kretzer, J. P. (2020). Particle analysis of shape factors according to American Society for Testing and Materials. *Journal of Biomedical Materials Research Part B: Applied Biomaterials*, 108(1), 225-233. doi:<https://doi.org/10.1002/jbm.b.34382>

- Seely, T. L. (1968). Turbulent tube flow of dilute fiber suspensions. (Ph.D. thesis), Lawrence University, Appleton, WI, USA.
- Seitshiro, I. T. (2013). The pipeline design of settling slurry with analytical models. (Ph.D. thesis), Akita University, Akita, Japan.
- Selima, Y., Fangary, Y., & Mahmoud, N. (2008). Determination of minimum speed required for solids suspension in stirred vessels using pressure measurements. *The Canadian Journal of Chemical Engineering*, 86(4), 661-666. doi:<https://doi.org/10.1002/cjce.20037>
- Shook, C., & Bartosik, A. (1991). The pseudohomogeneous flow approximation for dispersed two-phase systems. *Particulate Science and Technology*, 9(3-4), 119-134. doi:<https://doi.org/10.1080/02726359108906585>
- Shook, C., & Bartosik, A. (1994). Particle wall stresses in vertical slurry flows. *Journal of Powder Technology*, 81(2), 117-124. doi:[https://doi.org/10.1016/0032-5910\(94\)02877-X](https://doi.org/10.1016/0032-5910(94)02877-X)
- Shook, C., Rollins, J., & Vassie, G. (1974). Sliding in inclined slurry pipelines at shutdown. *The Canadian Journal of Chemical Engineering*, 52(3), 300-305. doi:<https://doi.org/10.1002/cjce.5450520302>
- Sokhansanj, S., Turhollow, A., Cushman, J., & Cundiff, J. (2002). Engineering aspects of collecting corn stover for bioenergy. *Biomass and Bioenergy*, 23(5), 347-355. doi:[https://doi.org/10.1016/S0961-9534\(02\)00063-6](https://doi.org/10.1016/S0961-9534(02)00063-6)
- Soszyński, R. M. (1987). The formation and properties of coherent flocs in fibre suspensions. (Ph.D. thesis), University of British Columbia, Vancouver, BC, Canada.
- Spelay, R. B. (2007). Solids transport in laminar, open channel flow of non-Newtonian slurries. (Ph.D. thesis), University of Saskatchewan, Saskatoon, SK, Canada.
- Spelay, R. B., Gillies, R. G., Hashemi, S. A., & Sanders, R. S. (2016). Effect of pipe inclination on the deposition velocity of settling slurries. *The Canadian Journal of Chemical Engineering*, 94(6), 1032-1039. doi:<https://doi.org/10.1002/cjce.22493>
- Steen, M. (1989). On turbulence structure in vertical pipe flow of fiber suspensions. *Nordic Pulp and Paper Research Journal*, 4(4), 244-252. doi:<https://doi.org/10.3183/npprj-1989-04-04-p244-252>

- Sumida, M. (2013). Flow properties of wood pulp suspensions in pipes. *International Journal of Mechanical and Mechatronics Engineering*, 7(11), 2202-2206.
doi:<http://doi.org/10.5281/zenodo.1088908>
- Sumida, M., & Fujimoto, T. (2015). Flow properties of wood pulp-fiber suspensions in circular pipes. *Transactions of the Japan Society of Mechanical Engineers*, 81(823), 10-20.
doi:<https://doi.org/10.1299/transjsme.14-00242>
- Sumner, R., McKibben, M., & Shook, C. (1990). Concentration and velocity distribution in turbulent vertical slurry flow. *Journal of Solid Liquid Flow*, 2(2), 33-42.
- Sumner, R. J. (1993). Concentration variations and their effects in flowing slurries and emulsions. (Ph.D. thesis), University of Saskatchewan, Saskatoon, SK, Canada.
- Sunny, T., Pickering, K. L., & McDonald-Wharry, J. (2021). Improving the alignment of dynamic sheet-formed mats by changing nozzle geometry and their reinforcement of polypropylene matrix composites. *Journal of Composites Science*, 5(9), 226.
doi:<https://doi.org/10.3390/jcs5090226>
- Szeto, R., Overton, J. C., Dos Santos, A. C., Eby, C., Mosier, N. S., Ximenes, E., . . . Erk, K. A. (2021). Rheology of enzyme liquefied corn stover slurries: The effect of solids concentration on yielding and flow behavior. *Biotechnology Progress*, 37(6), e3216.
doi:<https://doi.org/10.1002/btpr.3216>
- Tadros, T. F. (2010). *Rheology of Dispersions: principles and applications*. New Jersey, USA: John Wiley & Sons.
- Talmon, A. (2013). Analytical model for pipe wall friction of pseudo-homogenous sand slurries. *Particulate Science and Technology*, 31(3), 264-270.
doi:<https://doi.org/10.1080/02726351.2012.717588>
- The Conference Board of Canada. (2023). Greenhouse Gas Emissions. Retrieved from [https://www.conferenceboard.ca/\(X\(1\)S\(yahkumbbcbbfjl2xwnv20qc\)\)/hcp/Details/Environment/greenhouse-gas-emissions.aspx?AspxAutoDetectCookieSupport=1](https://www.conferenceboard.ca/(X(1)S(yahkumbbcbbfjl2xwnv20qc))/hcp/Details/Environment/greenhouse-gas-emissions.aspx?AspxAutoDetectCookieSupport=1) [Accessed: September 02, 2023].
- Toda, M., Konno, H., Saito, S., & Maeda, S. (1969). Hydraulic conveying of solids through horizontal and vertical pipes. *International Chemical Engineering*, 9(3), 553-560.

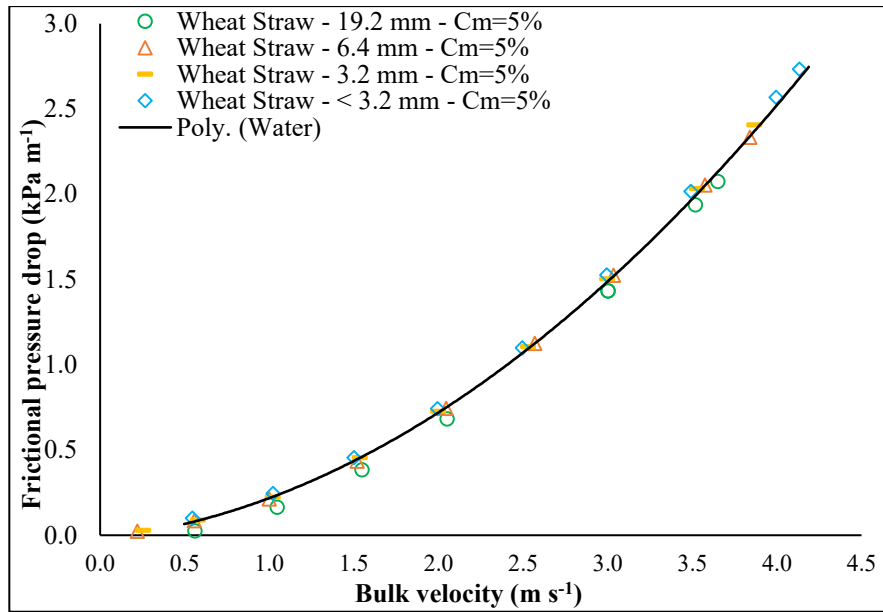
- Törmänen, M., Niemi, J., Löfqvist, T., & Myllylä, R. (2006). Pulp consistency determined by a combination of optical and acoustical measurement techniques. *Measurement Science and Technology*, 17(4), 695-702. doi:<https://doi.org/10.1088/0957-0233/17/4/014>
- U.S. Energy Information Administration. (2023). Biomass explained. Biomass-renewable energy from plants and animals. Retrieved from <https://www.eia.gov/energyexplained/biomass/> [Accessed: August 19, 2023].
- Uesugi, M., & Kishida, H. (1986). Frictional resistance at yield between dry sand and mild steel. *Soils and Foundations*, 26(4), 139-149. doi:https://doi.org/10.3208/sandf1972.26.4_139
- United Nations. (2022). Department of Economic and Social Affairs. Population Division. World Population Prospects 2022. Retrieved from <https://population.un.org/wpp/Graphs/DemographicProfiles/Line/900> [Accessed: September 03, 2023].
- Vaezi, M. (2014). Experimental and techno-economic studies of pipeline hydro-transport of agricultural residue biomass to a biorefinery. (Ph.D. thesis), University of Alberta, Edmonton, AB, Canada.
- Vaezi, M., Katta, A. K., & Kumar, A. (2014). Investigation into the mechanisms of pipeline transport of slurries of wheat straw and corn stover to supply a bio-refinery. *Biosystems Engineering*, 118, 52-67. doi:<https://doi.org/10.1016/j.biosystemseng.2013.11.006>
- Vaezi, M., & Kumar, A. (2014a). Development of correlations for the flow of agricultural residues as slurries in pipes for Bio-refining. *Biosystems Engineering*, 127, 144-158. doi:<https://doi.org/10.1016/j.biosystemseng.2014.08.018>
- Vaezi, M., & Kumar, A. (2014b). The flow of wheat straw suspensions in an open-impeller centrifugal pump. *Biomass and Bioenergy*, 69, 106-123. doi:<https://doi.org/10.1016/j.biombioe.2014.07.009>
- Vaezi, M., Nimana, B., & Kumar, A. (2015). Is the pipeline hydro-transport of wheat straw and corn stover to a biorefinery realistic? *Biofuels, Bioproducts and Biorefining*, 9(5), 501-515. doi:<https://doi.org/10.1002/bbb.1556>
- Vaezi, M., Pandey, V., Kumar, A., & Bhattacharyya, S. (2013). Lignocellulosic biomass particle shape and size distribution analysis using digital image processing for pipeline hydro-

- transportation. *Biosystems Engineering*, 114(2), 97-112.
doi:<https://doi.org/10.1016/j.biosystemseng.2012.11.007>
- Vaezi, M., Verma, S., & Kumar, A. (2018). Application of high-frequency impedancemetry approach in measuring the deposition velocities of biomass and sand slurry flows in pipelines. *Chemical Engineering Research and Design*, 140, 142-154.
doi:<https://doi.org/10.1016/j.cherd.2018.10.013>
- Valone, T. F. (2021). Linear global temperature correlation to carbon dioxide level, sea level, and innovative solutions to a projected 6 C warming by 2100. *Journal of Geoscience and Environment Protection*, 9(03), 84. doi:<https://doi.org/10.4236/gep.2021.93007>
- Van Dijk, M., Morley, T., Rau, M. L., & Saghai, Y. (2021). A meta-analysis of projected global food demand and population at risk of hunger for the period 2010–2050. *Nature Food*, 2(7), 494-501. doi:<https://doi.org/10.1038/s43016-021-00322-9>
- Vaseleski, R. C., & Metzner, A. (1974). Drag reduction in the turbulent flow of fiber suspensions. *AIChE Journal*, 20(2), 301-306. doi:<https://doi.org/10.1002/aic.690200214>
- Vauhkonen, M., Hänninen, A., Jauhiainen, J., & Lehtikangas, O. (2019). Multimodal imaging of multiphase flows with electromagnetic flow tomography and electrical tomography. *Measurement Science and Technology*, 30(9), 094001. doi:<https://doi.org/10.1088/1361-6501/ab1ef7>
- Ventura, C., GarCia, F., Ferreira, P., & Rasteiro, M. (2008). Flow dynamics of pulp fiber suspensions. *Technical Association of Pulp and Paper Industry*, 7(8), 20-26.
doi:<http://hdl.handle.net/10316/13399>
- Verma, A. K., Singh, S., & Seshadri, V. (2006). Pressure drop for the flow of high concentration solid-liquid mixture across 90° horizontal conventional circular pipe bend. *Indian Journal of Engineering & Materials Sciences*, 13, 477-483.
doi:<http://nopr.niscpr.res.in/handle/123456789/7584>
- Viamajala, S., McMillan, J. D., Schell, D. J., & Elander, R. T. (2009). Rheology of corn stover slurries at high solids concentrations—effects of saccharification and particle size. *Bioresource technology*, 100(2), 925-934.
doi:<https://doi.org/10.1016/j.biortech.2008.06.070>

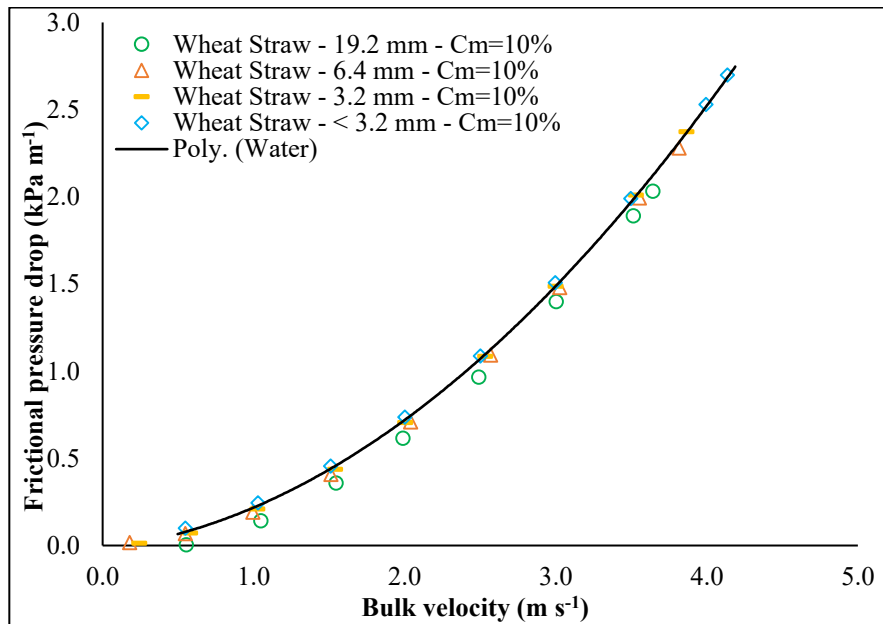
- Viswanadham, B. V. S. (2018). Online lectures on index properties and soil classification systems - II. Retrieved from <https://archive.nptel.ac.in/course.html> [Accessed: August 29, 2023].
- Vlasak, P., Chara, Z., Konfrst, J., & Kysela, B. (2017). Flow of heterogeneous slurry in horizontal and inclined pipes. Paper presented at the Proceedings of the 18th International Conference on Transport & Sedimentation of Solid Particles, Prague (Czech Republic), 369.
- Vlasak, P., Chara, Z., Matousek, V., Kesely, M., & Konfrst, J. (2018). Experimental investigation of settling slurry flow in inclined pipe sections. Paper presented at the Proc. 24th Int. Conf. Eng. Mech., Svratka, Czech Republic, Pap. <https://doi.org/10.21495/91-8-909>
- Vlasak, P., Chara, Z., Matousek, V., Konfrst, J., & Kesely, M. (2019a). Effect of pipe inclination on flow behaviour of fine-grained settling slurry. Paper presented at the EPJ Web of Conferences. <https://doi.org/10.1051/epjconf/201921302094>
- Vlasak, P., Chara, Z., Matousek, V., Konfrst, J., & Kesely, M. (2019b). Experimental investigation of fine-grained settling slurry flow behaviour in inclined pipe sections. *Journal of Hydrology and Hydromechanics*, 67(2), 113-120. doi:<https://doi.org/10.2478/johh-2018-0039>
- Vohra, M., Manwar, J., Manmode, R., Padgilwar, S., & Patil, S. (2014). Bioethanol production: Feedstock and current technologies. *Journal of Environmental Chemical Engineering*, 2(1), 573-584. doi:<https://doi.org/10.1016/j.jece.2013.10.013>
- Walmsley, M., & Berry, C. (2001). The flow behaviour of inorganic-wood fibre slurries in pressurised pipes. Paper presented at the 55th Appita Annual Conference, Hobart, Australia 30 April-2 May 2001.
- Wasp, E., & Aude, T. (1970). Deposition velocities, transition velocities, and spatial distribution of solids in slurry pipelines. Paper presented at the 1st International British Hydromechanics Research Association Hydraulic Transport of Solids in Pipes Conference, War Wickshire University, Coventry, England, Sept. 1-4, 1970. <https://trid.trb.org/view/19585>
- Wasp, E. J., Kenny, J. P., & Gandhi, R. L. (1977). Solid-liquid flow: slurry pipeline transportation.[Pumps, valves, mechanical equipment, economics]. *SER. Bulk Material Handling Journal*, 1(4). doi:<https://www.osti.gov/biblio/6343851>

- White, F. M. (2009). *Fluid Mechanics* (7th ed.). Rhode Island USA: McGraw-Hill.
- Wiklund, J., Fock, H., Rasmuson, A., & Stading, M. (2008). Near wall studies of pulp suspension flow. Paper presented at the 6th International Symposium on Ultrasonic Doppler Methods for Fluid Mechanics and Fluid Engineering.
- Wiklund, J. A., Stading, M., Pettersson, A. J., & Rasmuson, A. (2006). A comparative study of UVP and LDA techniques for pulp suspensions in pipe flow. *AIChE Journal*, 52(2), 484-495. doi:<https://doi.org/10.1002/aic.10653>
- Wilson, K. C., Addie, G. R., Sellgren, A., & Clift, R. (2006). *Slurry transport using centrifugal pumps* (3rd ed.). NY, USA: Springer.
- Worster, R., & Denny, D. (1955). Hydraulic transport of solid material in pipes. *Proceedings of the Institution of Mechanical Engineers*, 169(1), 563-586. doi:https://doi.org/10.1243/PIME_PROC_1955_169_064_02
- Xu, H. J., & Aidun, C. K. (2005). Characteristics of fiber suspension flow in a rectangular channel. *International Journal of Multiphase Flow*, 31(3), 318-336. doi:<https://doi.org/10.1016/j.ijmultiphaseflow.2004.12.003>
- Zidanšek, A., Blinc, R., Jeglič, A., Kabashi, S., Bekteshi, S., & Šlaus, I. (2009). Climate changes, biofuels and the sustainable future. *International Journal of Hydrogen Energy*, 34(16), 6980-6983. doi:<https://doi.org/10.1016/j.ijhydene.2008.11.004>

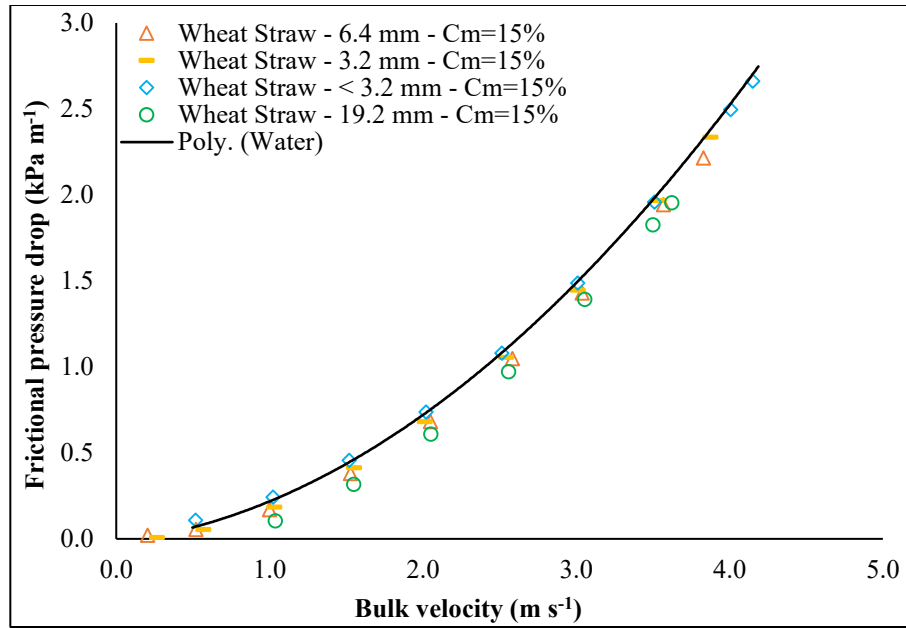
Appendix A



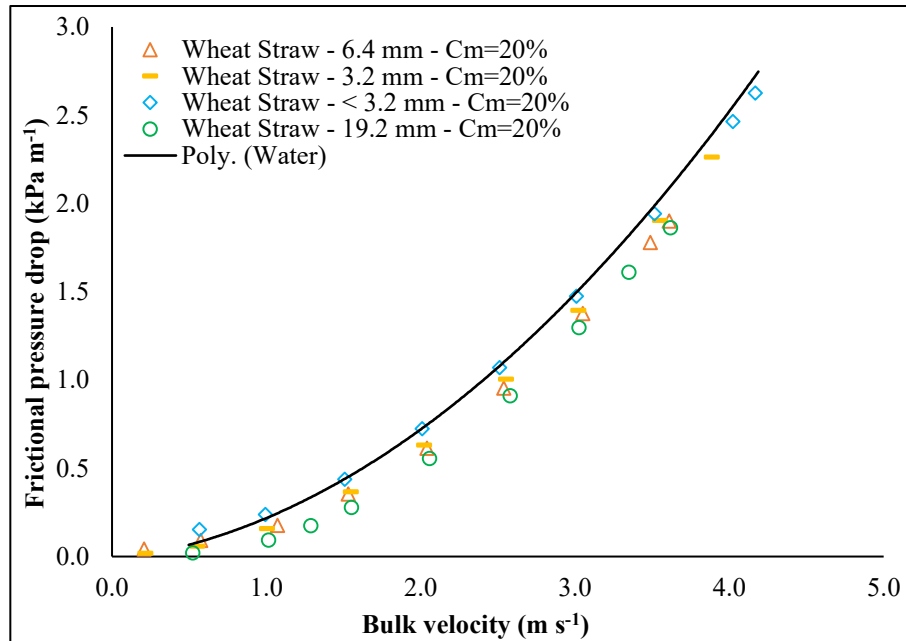
(a)



(b)

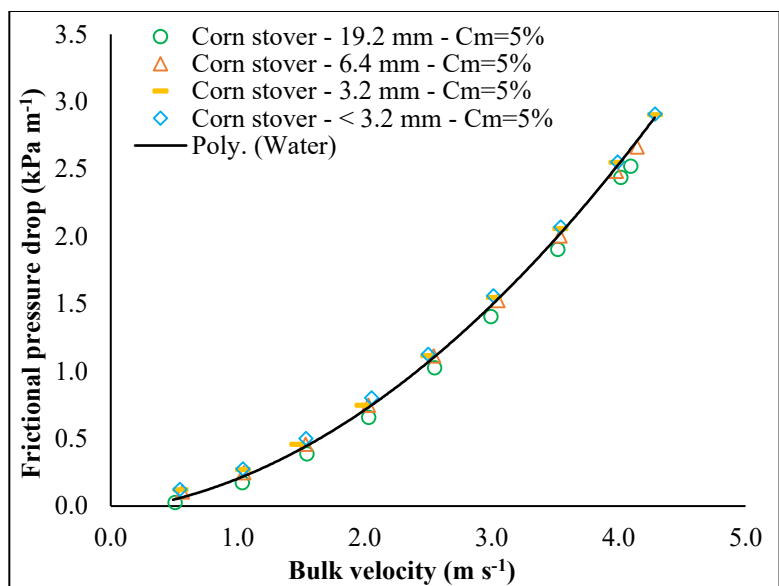


(c)

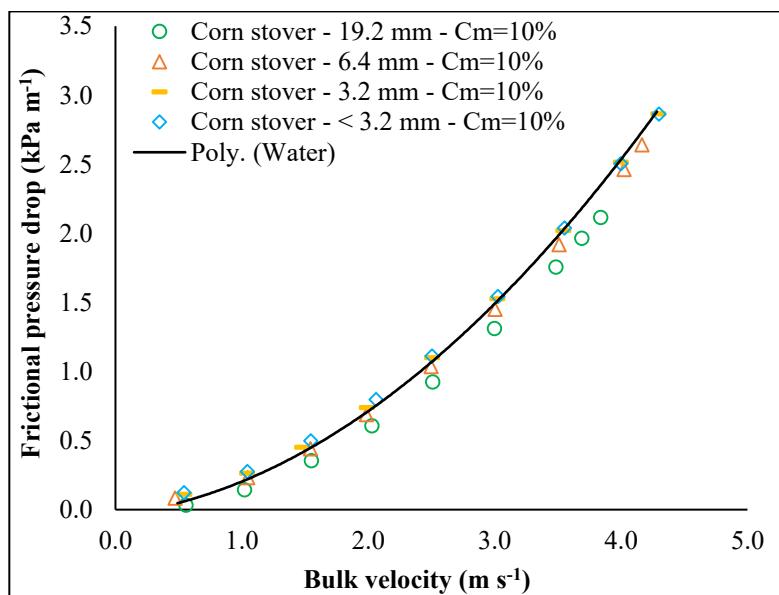


(d)

Figure A1: The effect of particle size in vertical upward flows of wheat straw aqueous slurries on frictional pressure drops for the entire range of bulk velocities at the saturated mass concentrations of (a) 5%, (b) 10%, (c) 15%, and (d) 20%.



(a)



(b)

Figure A2: The effect of particle size in vertical upward flows of corn stover-aqueous slurries on frictional pressure drops for the entire range of bulk velocities at the saturated mass concentrations of (a) 5% and (b) 10%.

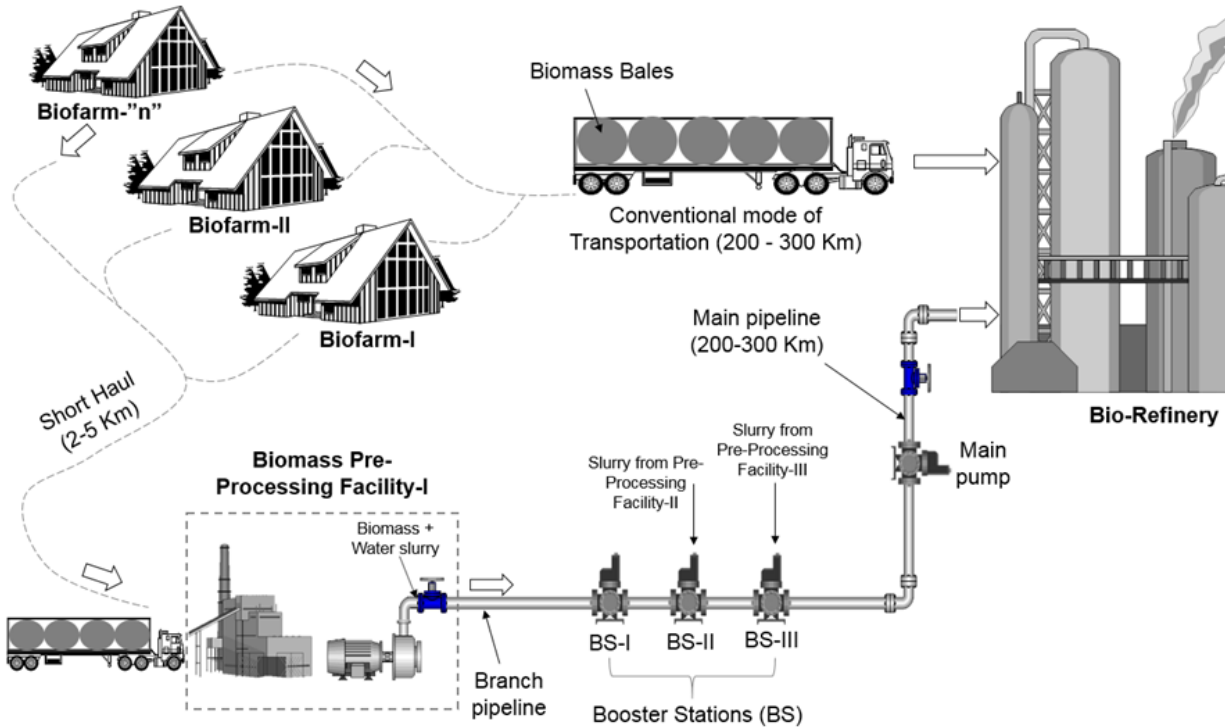


Figure A3: Conceptualization of biomass hydro-transport through a long-distance integrated pipeline setup from bio farms to biorefineries for large-scale biofuel production (not to scale).

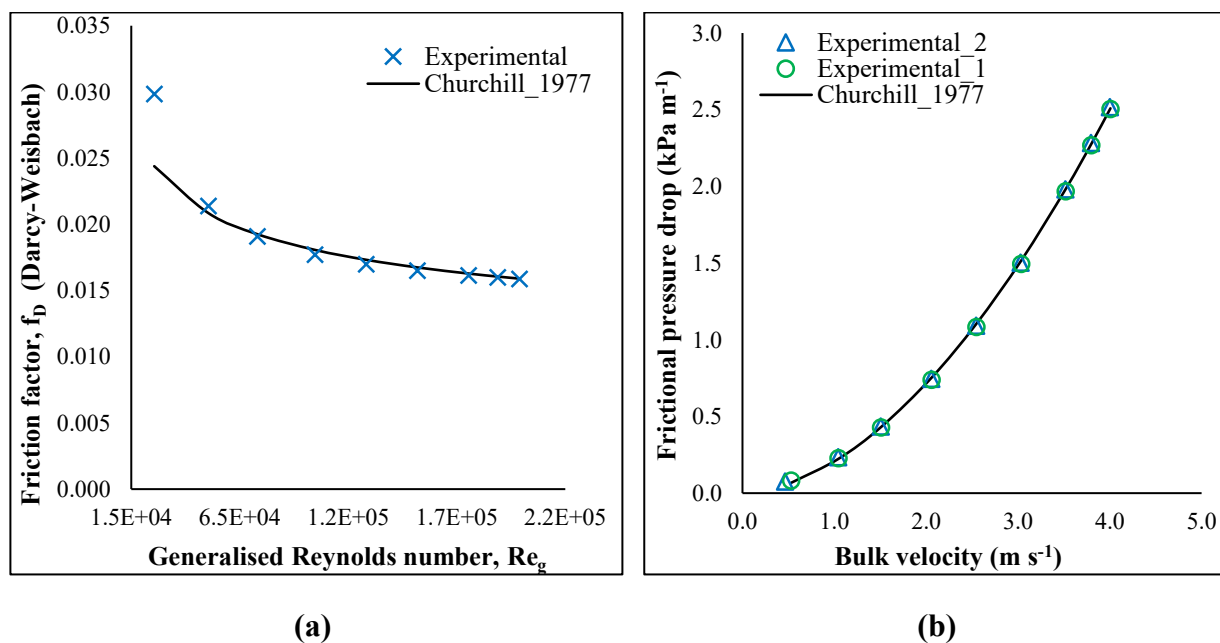


Figure A4: Calibration of vertical test section (ID = 50 mm) of a 29 m long closed pipeline loop using clear water: (a) Friction factor versus generalised Reynolds number and (b) Frictional pressure drop versus bulk velocity.

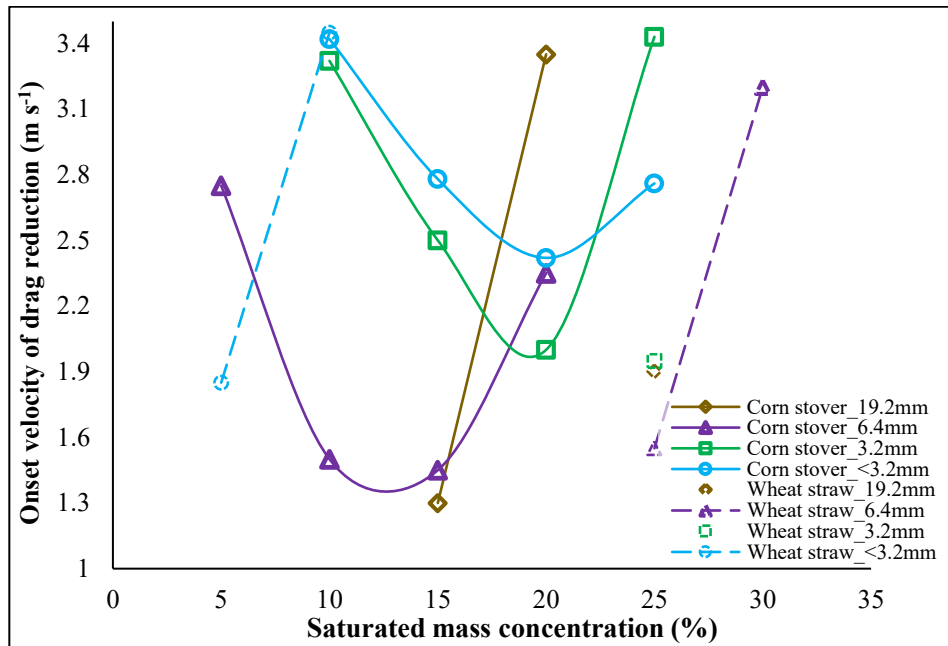
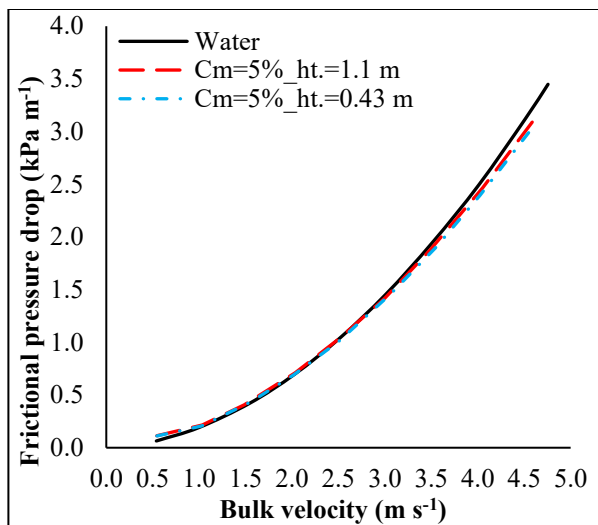
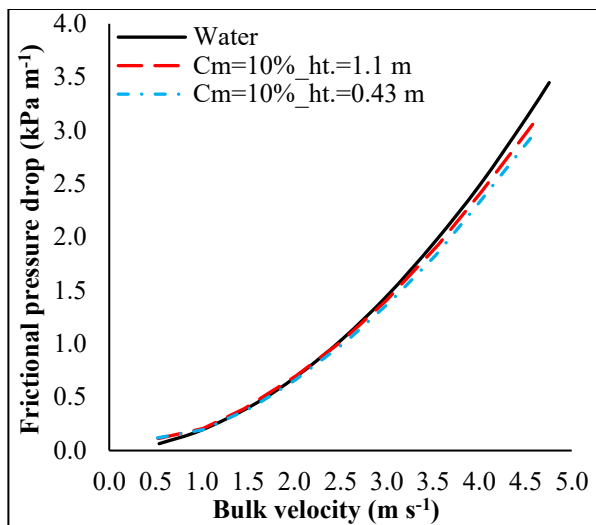


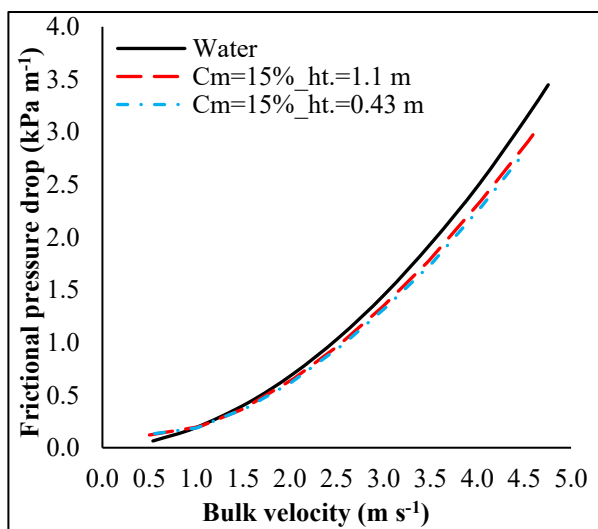
Figure A5: Onset velocity of drag reduction obtained at several mass concentrations of wheat straw- and corn stover-aqueous slurries with nominal particle sizes of 19.2 mm, 6.4 mm, 3.2 mm, and <3.2 mm while flowing upward in a vertical pipe.



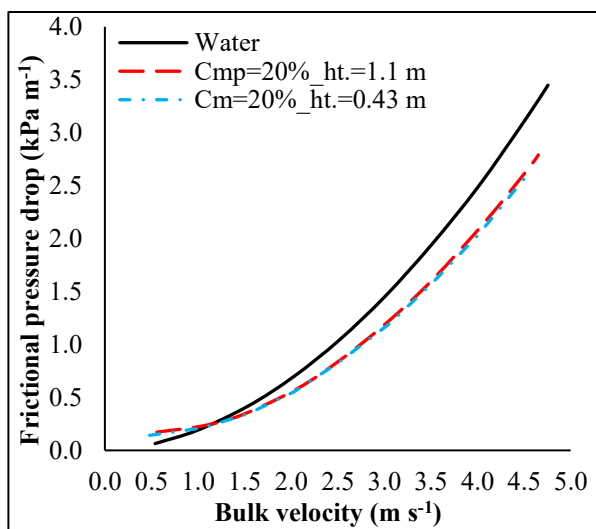
(a)



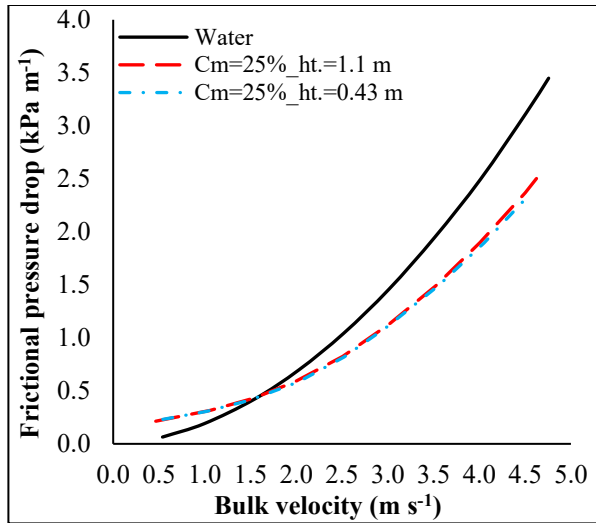
(b)



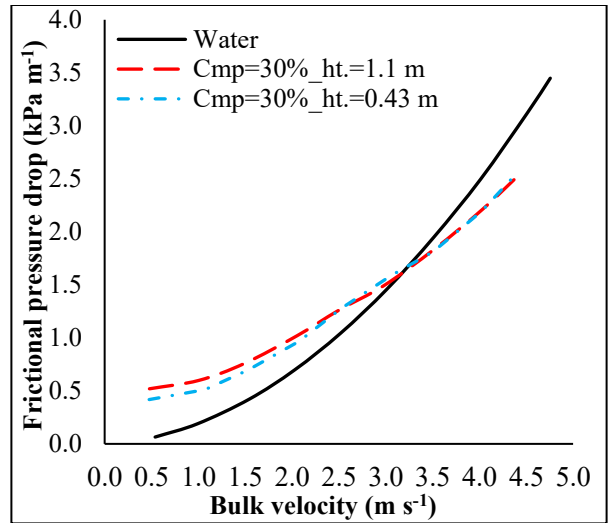
(c)



(d)

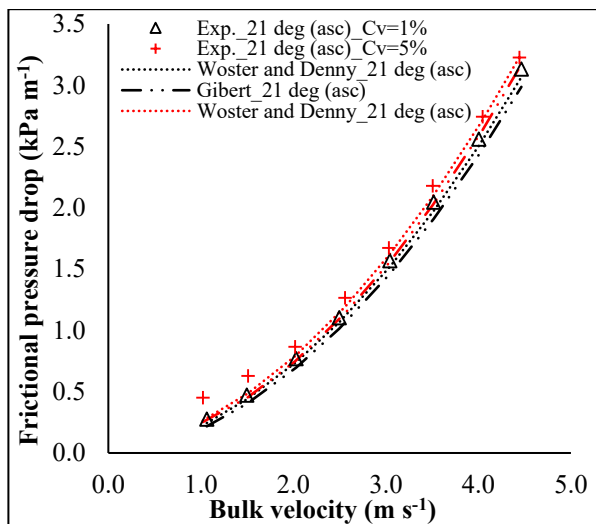


(e)

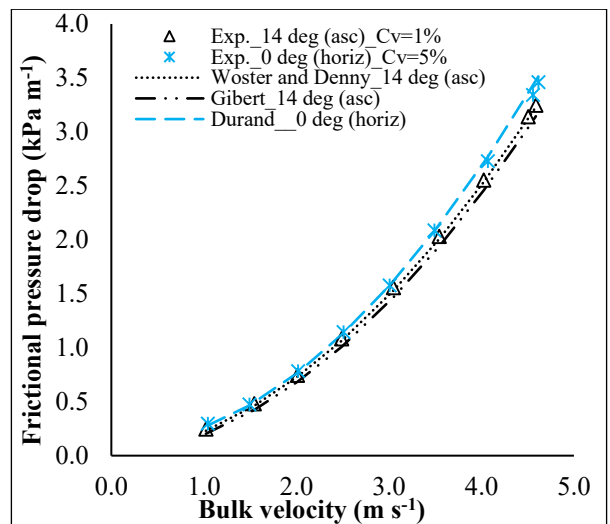


(f)

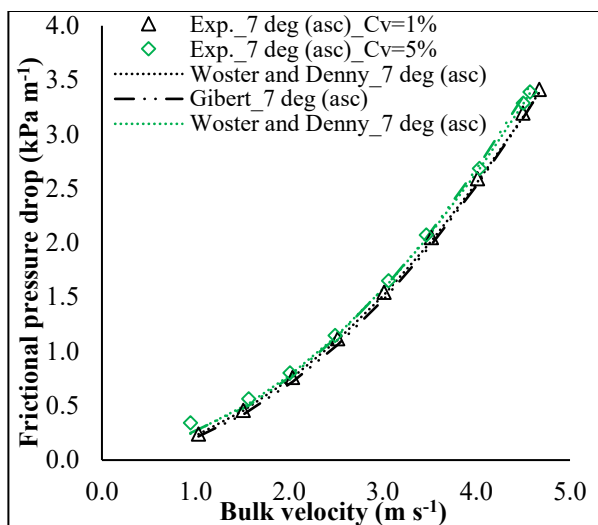
Figure A6: Frictional pressure drop measurements of aqueous slurries of the 6.4 mm nominal particle size of wheat straw for $C_m = 5\text{-}30\%$ flowing through an inclined pipe at $\theta = 0^\circ$ (i.e., horizontal position with respect to the x-axis) at different heights (hts.) above ground level.



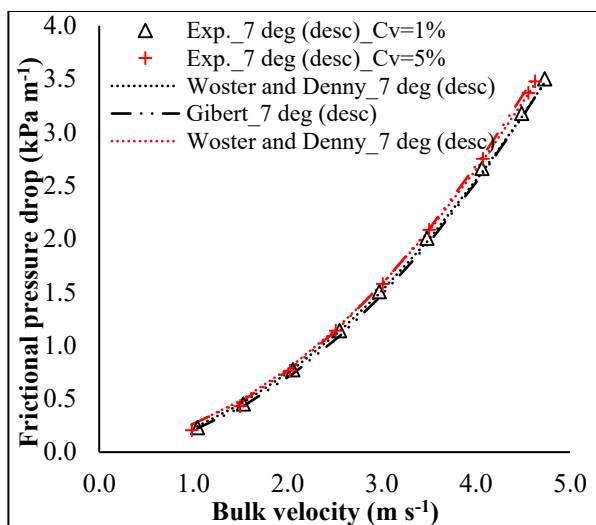
(a)



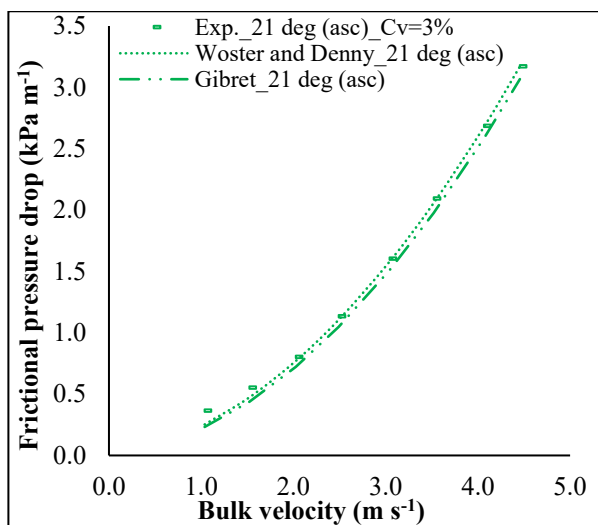
(b)



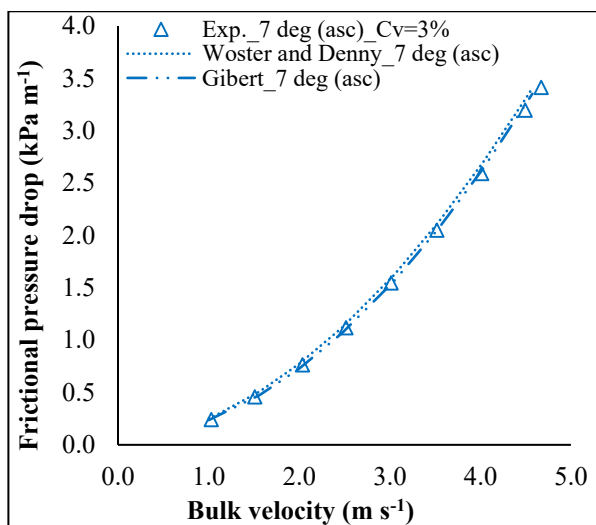
(c)



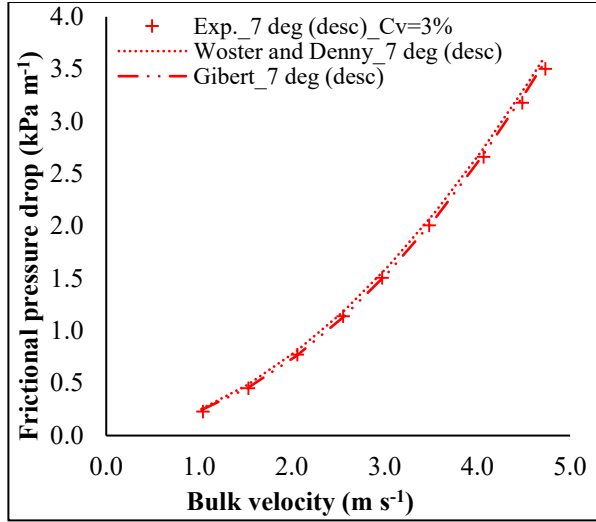
(d)



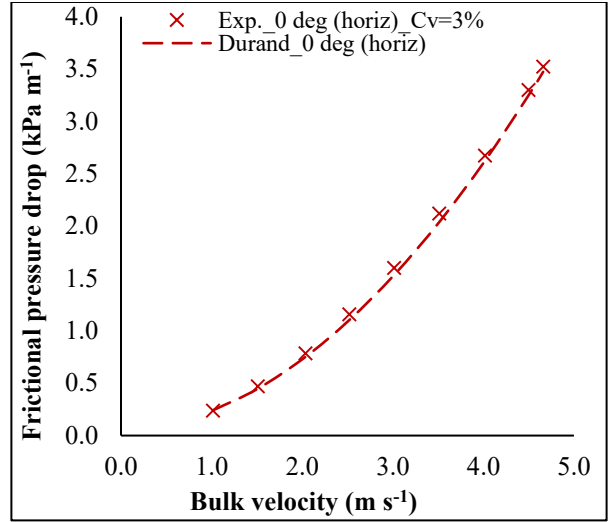
(e)



(f)

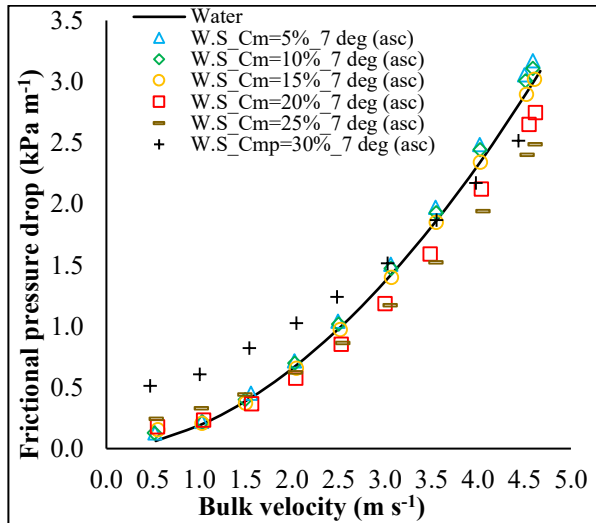


(g)

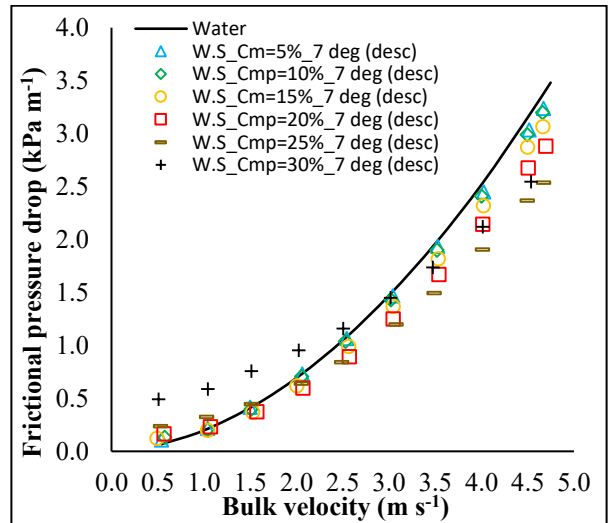


(h)

Figure A7: Calibration of the inclined pipe section at various inclinations (i.e., $\theta = -7^\circ$ to $+21^\circ$) and ranges of volumetric concentrations ($C_v = 1\%$ - 5%) of fine sand-water slurries with a mean diameter of solid particles of $d_{50} = 0.103$ mm.



(a)



(b)

Figure A8: Frictional pressure drops for aqueous slurries of the 6.4 mm particle size of wheat straw for velocities $\geq 0.5 \text{ m s}^{-1}$ and $C_m = 5\text{-}30\%$ flowing through a 50 mm diameter inclined pipe section at (a) $\theta = +7^\circ$ and (b) $\theta = -7^\circ$.

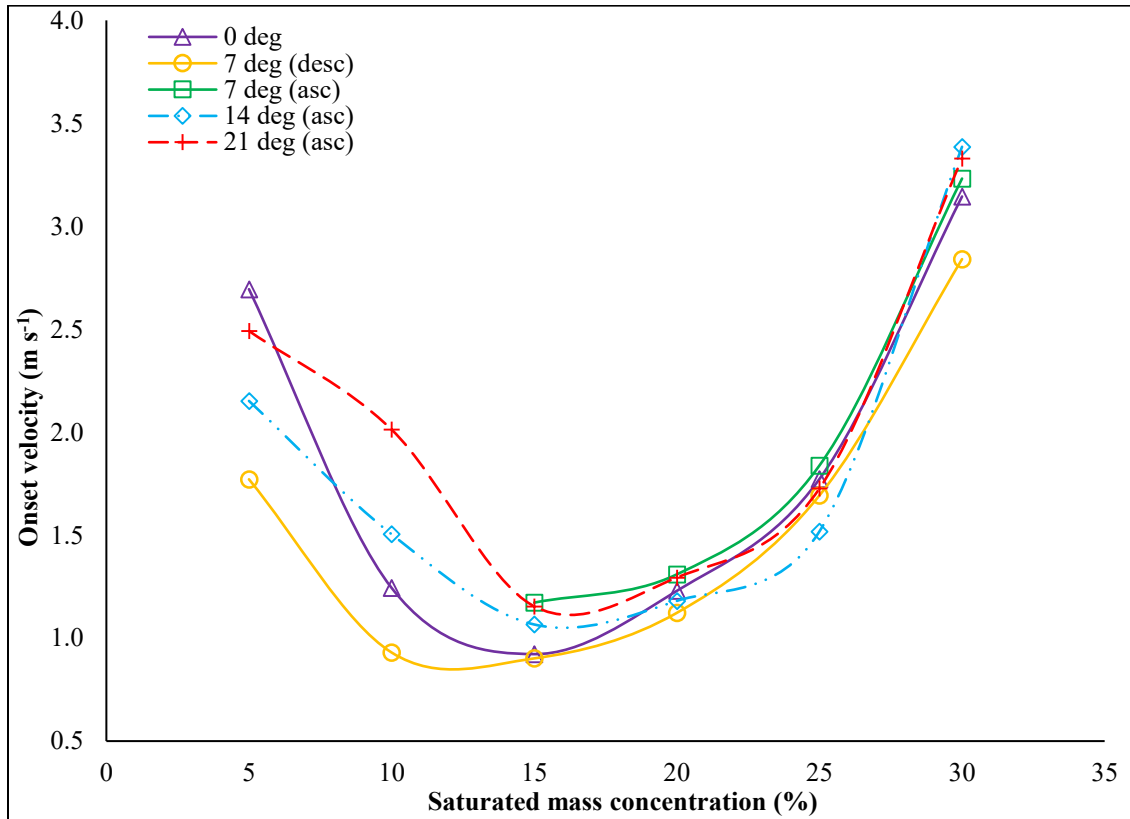
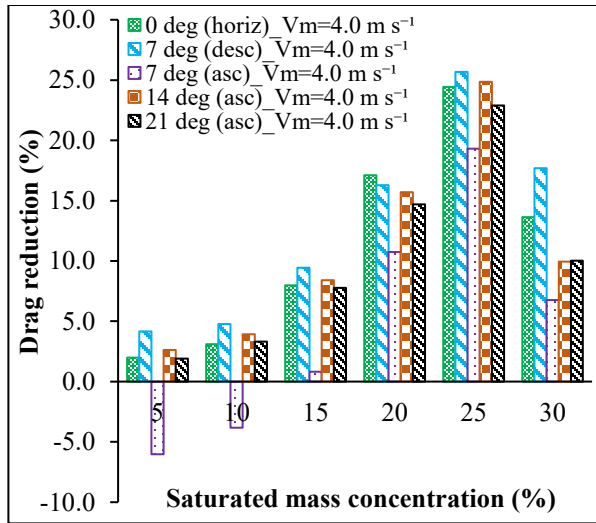
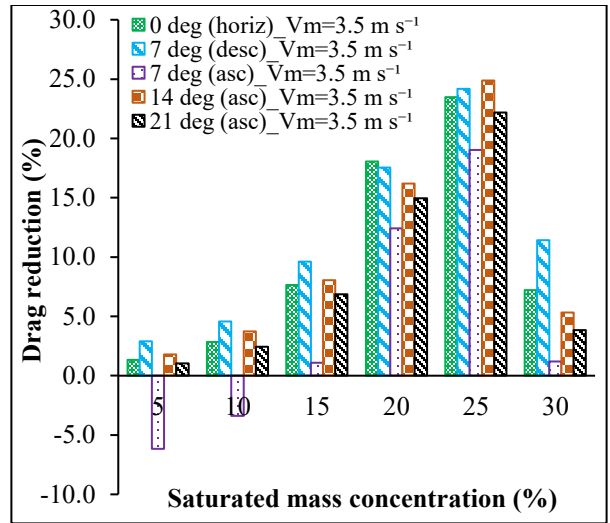


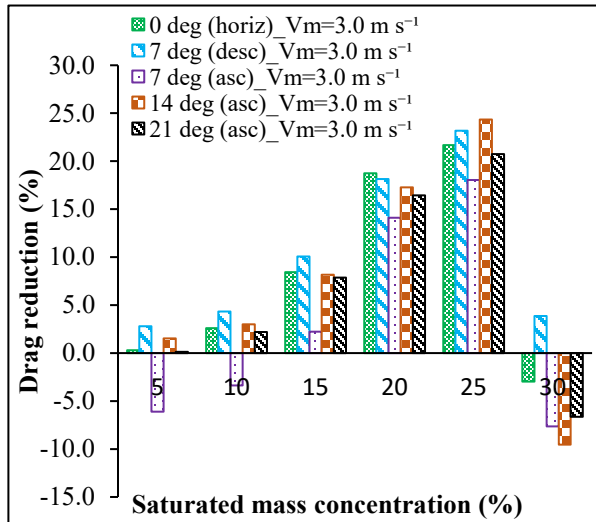
Figure A9: Onset velocity of drag reduction obtained at several mass concentrations of wheat straw-aqueous slurries with nominal particle size of 6.4 mm while flowing through inclined pipe section of various slopes.



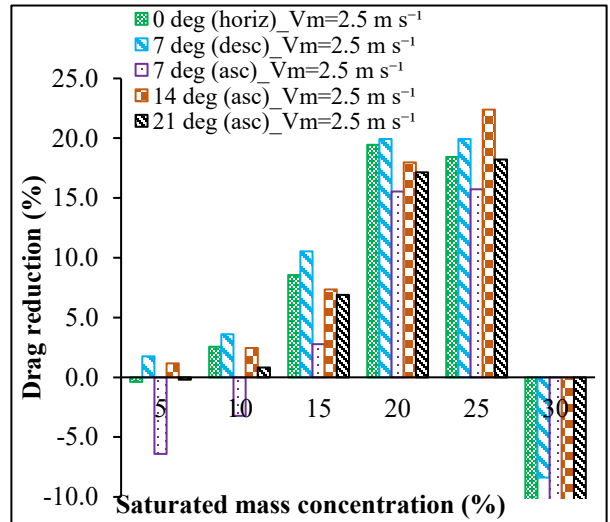
(a)



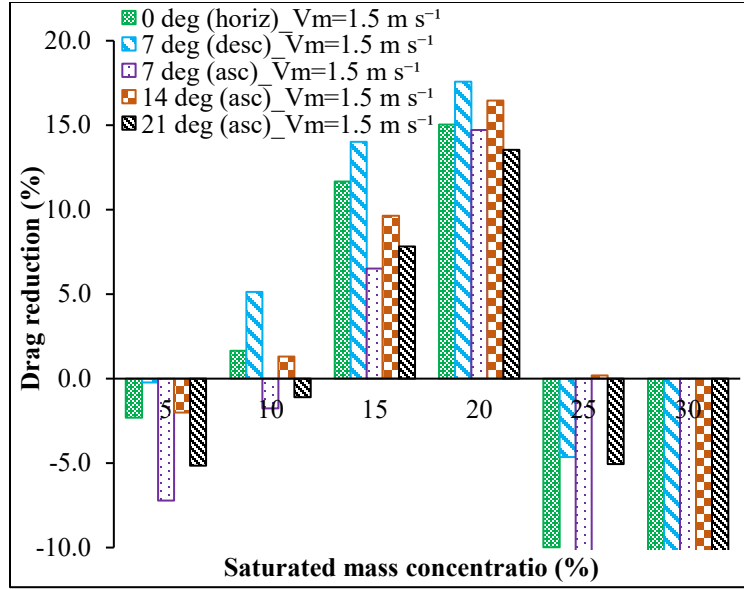
(b)



(c)



(d)



(e)

Figure A10: Drag reduction of the 6.4 mm particle size of wheat straw-water slurries for $C_m = 5\text{-}30\%$ flowing through an inclined pipe section of various inclinations (i.e., -7° to $+21^\circ$) and slurry bulk velocities of (a) 4.0 m s^{-1} , (b) 3.5 m s^{-1} , (c) 3.0 m s^{-1} , (d) 2.5 m s^{-1} , and (e) 1.5 m s^{-1} .

Table A1: Camsizer analysis of one of three subsamples from all four nominal particle sizes of wheat straw and corn stover

Wheat straw _Nominal particle size = <3.2 mm										
Size class (-)	Size class (mm)	Retained q_3 (%)	Passing Q_3 (%)	d_{c_min} (mm)	d_{FE_max} (mm)	SPHT ^a	Symm ^b	b/l_3^c	RDNS ^d	PDN ^e
0	0.2	4	4	0.143	0.65	0.495	0.789	0.35	-1	1064825
0.2	0.4	15.7	19.7	0.299	1.225	0.458	0.786	0.342	0.103	242477
0.4	0.6	16.9	36.6	0.503	1.799	0.434	0.779	0.351	0.098	58556
0.6	0.8	22.8	59.4	0.7	2.25	0.436	0.784	0.371	0.09	33225
0.8	1	15.6	75	0.896	2.365	0.504	0.785	0.44	0.079	11534
1	1.2	10.4	85.4	1.082	2.605	0.496	0.763	0.463	0.085	5029
1.2	1.4	6.9	92.3	1.289	2.791	0.5	0.746	0.511	0.052	2251
1.4	1.6	3.1	95.4	1.489	3.057	0.432	0.697	0.523	-1	761
1.6	1.8	1.5	96.9	1.688	3.674	0.322	0.635	0.49	0.059	260
1.8	2	0.8	97.7	1.904	4.014	0.243	0.543	0.497	0.056	113
2	2.2	0.5	98.2	2.074	4.171	0.273	0.58	0.521	0.015	46
2.2	2.4	0.1	98.3	2.299	4.861	0.202	0.565	0.48	0.028	10
2.4	2.6	0.1	98.4	2.525	5.266	0.184	0.573	0.499	0.027	11
2.6	2.8	0.1	98.5	2.668	4.807	0.108	0.577	0.557	0.021	2
2.8	3	0	98.5	0	0	1	0	0	-1	0
3	3.2	0	98.5	0	0	1	0	0	-1	0
3.2	3.4	0	98.5	0	0	1	0	0	-1	0
3.4	3.6	0	98.5	0	0	1	0	0	-1	0
3.6	3.8	0	98.5	0	0	1	0	0	-1	0
3.8	4	0	98.5	0	0	1	0	0	-1	0
4	4.2	0	98.5	0	0	1	0	0	-1	0
4.2	4.4	0	98.5	0	0	1	0	0	-1	0
4.4	4.6	0	98.5	0	0	1	0	0	-1	0
4.6	4.8	0	98.5	0	0	1	0	0	-1	0
4.8	5	0	98.5	0	0	1	0	0	-1	0
5	5.2	0.1	98.6	0	0	1	0	0	-1	1
5.2	5.4	0.3	98.9	5.259	11.175	0.067	0.578	0.471	0	2
5.4	5.6	0	98.9	0	0	1	0	0	-1	0
5.6	5.8	0	98.9	0	0	1	0	0	-1	0
5.8	6	0	98.9	0	0	1	0	0	-1	0
6	6.2	0	98.9	0	0	1	0	0	-1	0
6.2	6.4	0	98.9	0	0	1	0	0	-1	0
6.4	6.6	0	98.9	0	0	1	0	0	-1	0

6.6	6.8	0	98.9	0	0	1	0	0	-1	0
6.8	7	0	98.9	0	0	1	0	0	-1	0
7	7.2	1.1	100	7.146	15.223	0.044	0.61	0.47	0	2
7.2	7.4	0	100	0	0	1	0	0	0	0
7.4	7.6	0	100	0	0	1	0	0	0	0
7.6	7.8	0	100	0	0	1	0	0	0	0
7.8	8	0	100	0	0	1	0	0	0	0
8	8.2	0	100	0	0	1	0	0	0	0
8.2	8.4	0	100	0	0	1	0	0	0	0
8.4	8.6	0	100	0	0	1	0	0	0	0
8.6	8.8	0	100	0	0	1	0	0	0	0
8.8	9	0	100	0	0	1	0	0	0	0
9	9.2	0	100	0	0	1	0	0	0	0
9.2	9.4	0	100	0	0	1	0	0	0	0
9.4	9.6	0	100	0	0	1	0	0	0	0
9.6	9.8	0	100	0	0	1	0	0	0	0
9.8	10	0	100	0	0	1	0	0	0	0
10	1000	0	100	0	0	1	0	0	0	0
Wheat straw _Nominal particle size = 3.2 mm										
Size class (-)	Size class (mm)	Retained q_3 (%)	Passing Q_3 (%)	d_{c_min} (mm)	d_{FE_max} (mm)	SPHT	Symm	b/l_3	RDNS	PDN
0	0.2	0.7	0.7	0.129	0.525	0.583	0.789	0.457	-1	1311359
0.2	0.4	11.4	12.1	0.292	2.944	0.341	0.605	0.167	0.071	203124
0.4	0.6	8.4	20.5	0.502	3.568	0.278	0.793	0.174	0.054	36792
0.6	0.8	12.4	32.9	0.702	3.59	0.34	0.816	0.223	0.07	28165
0.8	1	7.8	40.7	0.914	3.537	0.455	0.83	0.309	0.089	7770
1	1.2	10.7	51.4	1.102	3.69	0.491	0.846	0.338	0.074	7413
1.2	1.4	11.3	62.7	1.297	3.424	0.565	0.829	0.428	0.062	6042
1.4	1.6	10.1	72.8	1.498	3.495	0.606	0.828	0.476	-1	3789
1.6	1.8	8.6	81.4	1.695	3.593	0.615	0.821	0.516	0.068	2572
1.8	2	6.1	87.5	1.894	3.747	0.604	0.798	0.547	0.057	1431
2	2.2	4.1	91.6	2.091	3.999	0.587	0.783	0.559	0.054	773
2.2	2.4	2.9	94.5	2.293	4.382	0.537	0.75	0.558	0.068	452
2.4	2.6	2	96.5	2.49	4.683	0.515	0.73	0.561	0.069	253
2.6	2.8	1.3	97.8	2.692	4.807	0.503	0.73	0.597	0.05	151
2.8	3	0.9	98.7	2.89	5.309	0.436	0.679	0.569	0.045	74
3	3.2	0.5	99.2	3.087	5.621	0.405	0.683	0.572	0.045	37
3.2	3.4	0.3	99.5	3.304	7.084	0.247	0.541	0.498	0.048	18
3.4	3.6	0.1	99.6	3.526	6.695	0.206	0.428	0.533	0.015	10

3.6	3.8	0.2	99.8	3.716	7.501	0.223	0.543	0.509	0.012	7
3.8	4	0.1	99.9	3.859	7.11	0.185	0.598	0.546	0.018	3
4	4.2	0	99.9	4.066	6.503	0.316	0.707	0.626	0.001	2
4.2	4.4	0	99.9	0	0	1	0	0	-1	0
4.4	4.6	0.1	100	4.494	7.41	0.145	0.583	0.606	0	1
4.6	4.8	0	100	0	0	1	0	0	0	0
4.8	5	0	100	0	0	1	0	0	0	0
5	5.2	0	100	0	0	1	0	0	0	0
5.2	5.4	0	100	0	0	1	0	0	0	0
5.4	5.6	0	100	0	0	1	0	0	0	0
5.6	5.8	0	100	0	0	1	0	0	0	0
5.8	6	0	100	0	0	1	0	0	0	0
6	6.2	0	100	0	0	1	0	0	0	0
6.2	6.4	0	100	0	0	1	0	0	0	0
6.4	6.6	0	100	0	0	1	0	0	0	0
6.6	6.8	0	100	0	0	1	0	0	0	0
6.8	7	0	100	0	0	1	0	0	0	0
7	7.2	0	100	0	0	1	0	0	0	0
7.2	7.4	0	100	0	0	1	0	0	0	0
7.4	7.6	0	100	0	0	1	0	0	0	0
7.6	7.8	0	100	0	0	1	0	0	0	0
7.8	8	0	100	0	0	1	0	0	0	0
8	8.2	0	100	0	0	1	0	0	0	0
8.2	8.4	0	100	0	0	1	0	0	0	0
8.4	8.6	0	100	0	0	1	0	0	0	0
8.6	8.8	0	100	0	0	1	0	0	0	0
8.8	9	0	100	0	0	1	0	0	0	0
9	9.2	0	100	0	0	1	0	0	0	0
9.2	9.4	0	100	0	0	1	0	0	0	0
9.4	9.6	0	100	0	0	1	0	0	0	0
9.6	9.8	0	100	0	0	1	0	0	0	0
9.8	10	0	100	0	0	1	0	0	0	0
10	1000	0	100	0	0	1	0	0	0	0
Wheat straw _Nominal particle size = 6.4 mm										
Size class	Size class	Retained	Passing	d_{c_min}	d_{FE_max}	SPHT	Symm	b/l_3	RDNS	PDN
(-)	(mm)	q_3	Q_3	(mm)	(mm)					
0	0.5	2.4	2.4	0.33	3.531	0.373	0.613	0.158	0.063	209980
0.5	1	15.2	17.6	0.782	4.651	0.314	0.78	0.211	0.049	15063
1	1.5	27.6	45.2	1.252	4.864	0.435	0.811	0.305	0.078	9470
1.5	2	21.3	66.5	1.728	5.01	0.504	0.805	0.39	0.064	3675

2	2.5	14.4	80.9	2.236	5.532	0.493	0.763	0.443	0.064	1497
2.5	3	9.2	90.1	2.728	6.308	0.461	0.733	0.475	0.049	626
3	3.5	4.7	94.8	3.192	6.895	0.377	0.651	0.496	0.081	244
3.5	4	1.9	96.7	3.742	8.02	0.262	0.621	0.488	0.037	65
4	4.5	1	97.7	4.218	9.258	0.169	0.56	0.473	0.039	25
4.5	5	0.8	98.5	4.756	9.457	0.207	0.627	0.531	0.021	14
5	5.5	0.8	99.3	5.214	12.894	0.097	0.493	0.412	0.008	10
5.5	6	0.1	99.4	5.623	10.195	0.127	0.61	0.552	0	1
6	6.5	0.2	99.6	6.111	10.063	0.13	0.681	0.607	0	1
6.5	7	0	99.6	0	0	1	0	0	-1	0
7	7.5	0.4	100	7.14	11.544	0.124	0.675	0.624	0	2
7.5	8	0	100	0	0	1	0	0	0	0
8	8.5	0	100	0	0	1	0	0	0	0
8.5	9	0	100	0	0	1	0	0	0	0
9	9.5	0	100	0	0	1	0	0	0	0
9.5	10	0	100	0	0	1	0	0	0	0
10	10.5	0	100	0	0	1	0	0	0	0
10.5	11	0	100	0	0	1	0	0	0	0
11	11.5	0	100	0	0	1	0	0	0	0
11.5	12	0	100	0	0	1	0	0	0	0
12	12.5	0	100	0	0	1	0	0	0	0
12.5	13	0	100	0	0	1	0	0	0	0
13	13.5	0	100	0	0	1	0	0	0	0
13.5	14	0	100	0	0	1	0	0	0	0
14	14.5	0	100	0	0	1	0	0	0	0
14.5	15	0	100	0	0	1	0	0	0	0
15	15.5	0	100	0	0	1	0	0	0	0
15.5	16	0	100	0	0	1	0	0	0	0
16	16.5	0	100	0	0	1	0	0	0	0
16.5	17	0	100	0	0	1	0	0	0	0
17	17.5	0	100	0	0	1	0	0	0	0
17.5	18	0	100	0	0	1	0	0	0	0
18	18.5	0	100	0	0	1	0	0	0	0
18.5	19	0	100	0	0	1	0	0	0	0
19	19.5	0	100	0	0	1	0	0	0	0
19.5	20	0	100	0	0	1	0	0	0	0
20	1000	0	100	0	0	1	0	0	0	0
Wheat straw _Nominal particle size = 19.2 mm										
Size class	Size class	Retained	Passing	d_{c_min}	d_{FE_max}	SPHT	Symm	b/l_3	RDNS	PDN
(-)	(mm)	q_3 (%)	Q_3 (%)	(mm)	(mm)					

0.5	1	8.2	10	0.745	6.579	0.232	0.745	0.151	0.04	18618
1	1.5	15.9	25.9	1.262	7.25	0.342	0.81	0.215	0.069	8670
1.5	2	18.2	44.1	1.743	7.673	0.407	0.808	0.278	0.068	4807
2	2.5	14.2	58.3	2.227	8.201	0.433	0.792	0.325	0.075	2258
2.5	3	10.6	68.9	2.729	8.905	0.422	0.769	0.356	0.06	1147
3	3.5	6.8	75.7	3.211	10.286	0.376	0.715	0.369	0.082	527
3.5	4	6	81.7	3.744	11.073	0.315	0.653	0.38	0.066	344
4	4.5	3.5	85.2	4.225	11.335	0.273	0.616	0.424	0.064	175
4.5	5	3.4	88.6	4.718	14.128	0.208	0.58	0.371	0.066	118
5	5.5	2.3	90.9	5.221	15.649	0.164	0.551	0.366	0.035	65
5.5	6	1.9	92.8	5.731	14.4	0.178	0.583	0.418	0.037	48
6	6.5	1.8	94.6	6.231	18.885	0.153	0.581	0.338	0.032	30
6.5	7	1.2	95.8	6.699	18.009	0.125	0.551	0.386	0.044	18
7	7.5	0.7	96.5	7.246	24.206	0.112	0.589	0.328	0.045	10
7.5	8	1.2	97.7	7.764	25.541	0.071	0.58	0.312	0.027	7
8	8.5	0.7	98.4	8.18	20.079	0.182	0.54	0.408	0.105	5
8.5	9	0.3	98.7	8.785	16.395	0.102	0.559	0.536	0	2
9	9.5	0.6	99.3	9.214	25.221	0.064	0.516	0.364	0.069	3
9.5	10	0	99.3	0	0	1	0	0	-1	0
10	10.5	0	99.3	0	0	1	0	0	-1	0
10.5	11	0.7	100	10.77 5	23.971	0.056	0.634	0.45	0	3
11	11.5	0	100	0	0	1	0	0	0	0
11.5	12	0	100	0	0	1	0	0	0	0
12	12.5	0	100	0	0	1	0	0	0	0
12.5	13	0	100	0	0	1	0	0	0	0
13	13.5	0	100	0	0	1	0	0	0	0
13.5	14	0	100	0	0	1	0	0	0	0
14	14.5	0	100	0	0	1	0	0	0	0
14.5	15	0	100	0	0	1	0	0	0	0
15	15.5	0	100	0	0	1	0	0	0	0
15.5	16	0	100	0	0	1	0	0	0	0
16	16.5	0	100	0	0	1	0	0	0	0
16.5	17	0	100	0	0	1	0	0	0	0
17	17.5	0	100	0	0	1	0	0	0	0
17.5	18	0	100	0	0	1	0	0	0	0
18	18.5	0	100	0	0	1	0	0	0	0
18.5	19	0	100	0	0	1	0	0	0	0
19	19.5	0	100	0	0	1	0	0	0	0
19.5	20	0	100	0	0	1	0	0	0	0
20	1000	0	100	0	0	1	0	0	0	0

Corn stover _Nominal particle size = <3.2 mm										
Size class (-)	Size class (mm)	Retained q_3 (%)	Passing Q_3 (%)	d_{c_min} (mm)	d_{FE_max} (mm)	SPHT	Symm	b/l_3	RDNS	PDN
0.2	0.4	14.4	17.9	0.3	0.79	0.537	0.776	0.488	0.115	697027
0.4	0.6	17.8	35.7	0.504	1.366	0.458	0.759	0.458	0.119	162599
0.6	0.8	22.2	57.9	0.7	1.848	0.428	0.752	0.454	0.108	75726
0.8	1	17.4	75.3	0.896	2.002	0.5	0.761	0.512	0.101	31250
1	1.2	12.3	87.6	1.096	2.276	0.493	0.755	0.533	0.092	13762
1.2	1.4	6.9	94.5	1.29	2.476	0.517	0.741	0.566	0.065	5101
1.4	1.6	3.4	97.9	1.484	2.828	0.465	0.708	0.568	-1	1729
1.6	1.8	1.3	99.2	1.681	3.242	0.376	0.657	0.555	0.049	507
1.8	2	0.5	99.7	1.885	3.822	0.271	0.606	0.524	0.042	145
2	2.2	0.2	99.9	2.083	4.083	0.254	0.58	0.529	0.028	44
2.2	2.4	0.1	100	2.27	4.121	0.289	0.637	0.571	0.038	17
2.4	2.6	0	100	2.521	5.171	0.199	0.58	0.5	0.027	2
2.6	2.8	0	100	0	0	1	0	0	0	0
2.8	3	0	100	0	0	1	0	0	0	0
3	3.2	0	100	0	0	1	0	0	0	0
3.2	3.4	0	100	0	0	1	0	0	0	0
3.4	3.6	0	100	0	0	1	0	0	0	0
3.6	3.8	0	100	0	0	1	0	0	0	0
3.8	4	0	100	0	0	1	0	0	0	0
4	4.2	0	100	0	0	1	0	0	0	0
4.2	4.4	0	100	0	0	1	0	0	0	0
4.4	4.6	0	100	0	0	1	0	0	0	0
4.6	4.8	0	100	0	0	1	0	0	0	0
4.8	5	0	100	0	0	1	0	0	0	0
5	5.2	0	100	0	0	1	0	0	0	0
5.2	5.4	0	100	0	0	1	0	0	0	0
5.4	5.6	0	100	0	0	1	0	0	0	0
5.6	5.8	0	100	0	0	1	0	0	0	0
5.8	6	0	100	0	0	1	0	0	0	0
6	6.2	0	100	0	0	1	0	0	0	0
6.2	6.4	0	100	0	0	1	0	0	0	0
6.4	6.6	0	100	0	0	1	0	0	0	0
6.6	6.8	0	100	0	0	1	0	0	0	0
6.8	7	0	100	0	0	1	0	0	0	0
7	7.2	0	100	0	0	1	0	0	0	0
7.2	7.4	0	100	0	0	1	0	0	0	0
7.4	7.6	0	100	0	0	1	0	0	0	0

7.6	7.8	0	100	0	0	1	0	0	0	0
7.8	8	0	100	0	0	1	0	0	0	0
8	8.2	0	100	0	0	1	0	0	0	0
8.2	8.4	0	100	0	0	1	0	0	0	0
8.4	8.6	0	100	0	0	1	0	0	0	0
8.6	8.8	0	100	0	0	1	0	0	0	0
8.8	9	0	100	0	0	1	0	0	0	0
9	9.2	0	100	0	0	1	0	0	0	0
9.2	9.4	0	100	0	0	1	0	0	0	0
9.4	9.6	0	100	0	0	1	0	0	0	0
9.6	9.8	0	100	0	0	1	0	0	0	0
9.8	10	0	100	0	0	1	0	0	0	0
10	1000	0	100	0	0	1	0	0	0	0
Corn stover _Nominal particle size = 3.2 mm										
Size class	Size class	Retained	Passing	d_{c_min}	d_{FE_max}	SPHT	Symm	b/l_3	RDNS	PDN
(-)	(mm)	q_3	Q_3	(mm)	(mm)					
0.2	0.4	2.3	4.4	0.343	3.712	0.222	0.699	0.15	0.069	52722
0.4	0.6	9.1	13.5	0.515	3.431	0.442	0.686	0.185	0.063	53700
0.6	0.8	6.8	20.3	0.701	3.444	0.344	0.783	0.242	0.084	40858
0.8	1	12.4	32.7	0.944	4.995	0.356	0.79	0.234	0.086	17912
1	1.2	17.9	50.6	1.082	4.545	0.404	0.815	0.295	0.113	19774
1.2	1.4	8	58.6	1.28	3.274	0.54	0.798	0.441	0.107	7852
1.4	1.6	6.2	64.8	1.502	3.469	0.582	0.793	0.489	-1	4090
1.6	1.8	6.4	71.2	1.7	3.682	0.582	0.789	0.516	0.096	3249
1.8	2	5.9	77.1	1.899	3.87	0.583	0.782	0.54	0.078	2309
2	2.2	5.2	82.3	2.1	4.203	0.552	0.763	0.546	0.066	1580
2.2	2.4	4.5	86.8	2.298	4.41	0.546	0.758	0.561	0.076	1107
2.4	2.6	3.6	90.4	2.497	4.631	0.523	0.743	0.578	0.065	732
2.6	2.8	2.8	93.2	2.694	5.141	0.452	0.714	0.565	0.034	475
2.8	3	2.2	95.4	2.895	5.242	0.466	0.722	0.587	0.046	302
3	3.2	1.5	96.9	3.084	5.48	0.438	0.706	0.593	0.057	179
3.2	3.4	1.1	98	3.301	6.268	0.351	0.651	0.553	0.046	107
3.4	3.6	0.5	98.5	3.488	6.4	0.324	0.632	0.58	0.023	51
3.6	3.8	0.5	99	3.703	6.413	0.354	0.663	0.603	0.02	36
3.8	4	0.3	99.3	3.89	7.462	0.291	0.641	0.535	0.019	19
4	4.2	0.2	99.5	4.089	7.491	0.266	0.61	0.563	0.044	13
4.2	4.4	0.2	99.7	4.29	9.404	0.149	0.37	0.474	0.014	5
4.4	4.6	0	99.7	4.499	7.441	0.301	0.692	0.627	0	3
4.6	4.8	0.2	99.9	4.723	9.334	0.117	0.615	0.511	0	7
4.8	5	0	99.9	4.934	9.574	0.134	0.579	0.516	0	1

5	5.2	0.1	100	5.071	10.425	0.162	0.657	0.488	0	1
5.2	5.4	0	100	0	0	1	0	0	0	0
5.4	5.6	0	100	0	0	1	0	0	0	0
5.6	5.8	0	100	0	0	1	0	0	0	0
5.8	6	0	100	0	0	1	0	0	0	0
6	6.2	0	100	0	0	1	0	0	0	0
6.2	6.4	0	100	0	0	1	0	0	0	0
6.4	6.6	0	100	0	0	1	0	0	0	0
6.6	6.8	0	100	0	0	1	0	0	0	0
6.8	7	0	100	0	0	1	0	0	0	0
7	7.2	0	100	0	0	1	0	0	0	0
7.2	7.4	0	100	0	0	1	0	0	0	0
7.4	7.6	0	100	0	0	1	0	0	0	0
7.6	7.8	0	100	0	0	1	0	0	0	0
7.8	8	0	100	0	0	1	0	0	0	0
8	8.2	0	100	0	0	1	0	0	0	0
8.2	8.4	0	100	0	0	1	0	0	0	0
8.4	8.6	0	100	0	0	1	0	0	0	0
8.6	8.8	0	100	0	0	1	0	0	0	0
8.8	9	0	100	0	0	1	0	0	0	0
9	9.2	0	100	0	0	1	0	0	0	0
9.2	9.4	0	100	0	0	1	0	0	0	0
9.4	9.6	0	100	0	0	1	0	0	0	0
9.6	9.8	0	100	0	0	1	0	0	0	0
9.8	10	0	100	0	0	1	0	0	0	0
10	1000	0	100	0	0	1	0	0	0	0
Corn stover _Nominal particle size = 6.4 mm										
Size class	Size class	Retained	Passing	d_{c_min}	d_{FE_max}	SPHT	Symm	b/l_3	RDNS	PDN
(-)	(mm)	q_3	Q_3	(mm)	(mm)					
0.5	1	5.2	7.7	0.788	4.653	0.371	0.759	0.296	0.05	7869
1	1.5	9.4	17.1	1.262	5.386	0.355	0.749	0.279	0.057	6358
1.5	2	11.6	28.7	1.751	5.624	0.43	0.764	0.358	0.078	4137
2	2.5	12.6	41.3	2.25	6.107	0.446	0.759	0.413	0.066	2697
2.5	3	14.4	55.7	2.751	6.578	0.45	0.751	0.461	0.05	1936
3	3.5	12.7	68.4	3.245	7.356	0.411	0.731	0.485	0.049	1174
3.5	4	8.3	76.7	3.719	8.081	0.367	0.682	0.506	0.043	569
4	4.5	6.7	83.4	4.237	9.317	0.293	0.661	0.48	0.036	333
4.5	5	4.5	87.9	4.73	10.221	0.264	0.652	0.5	0.027	163
5	5.5	4.1	92	5.228	11.692	0.21	0.633	0.478	0.014	110
5.5	6	4.1	96.1	5.752	12.204	0.175	0.628	0.489	0.016	88

6	6.5	2.2	98.3	6.282	13.925	0.136	0.635	0.461	0.037	39
6.5	7	0.9	99.2	6.753	11.403	0.19	0.627	0.595	0.015	13
7	7.5	0.4	99.6	7.273	14.171	0.197	0.538	0.531	0.35	4
7.5	8	0.1	99.7	7.639	14.258	0.144	0.633	0.545	0	1
8	8.5	0.3	100	8.22	16.245	0.108	0.613	0.511	0	2
8.5	9	0	100	0	0	1	0	0	0	0
9	9.5	0	100	0	0	1	0	0	0	0
9.5	10	0	100	0	0	1	0	0	0	0
10	10.5	0	100	0	0	1	0	0	0	0
10.5	11	0	100	0	0	1	0	0	0	0
11	11.5	0	100	0	0	1	0	0	0	0
11.5	12	0	100	0	0	1	0	0	0	0
12	12.5	0	100	0	0	1	0	0	0	0
12.5	13	0	100	0	0	1	0	0	0	0
13	13.5	0	100	0	0	1	0	0	0	0
13.5	14	0	100	0	0	1	0	0	0	0
14	14.5	0	100	0	0	1	0	0	0	0
14.5	15	0	100	0	0	1	0	0	0	0
15	15.5	0	100	0	0	1	0	0	0	0
15.5	16	0	100	0	0	1	0	0	0	0
16	16.5	0	100	0	0	1	0	0	0	0
16.5	17	0	100	0	0	1	0	0	0	0
17	17.5	0	100	0	0	1	0	0	0	0
17.5	18	0	100	0	0	1	0	0	0	0
18	18.5	0	100	0	0	1	0	0	0	0
18.5	19	0	100	0	0	1	0	0	0	0
19	19.5	0	100	0	0	1	0	0	0	0
19.5	20	0	100	0	0	1	0	0	0	0
20	1000	0	100	0	0	1	0	0	0	0
Corn stover _Nominal particle size = 19.2 mm										
Size class	Size class	Retained	Passing	d_{c_min}	d_{FE_max}	SPHT	Symm	b/l_3	RDNS	PDN
(-)	(mm)	q_3	Q_3	(mm)	(mm)					
0.5	1	2.7	4.5	0.731	6.041	0.214	0.579	0.164	0.039	9793
1	1.5	5.9	10.4	1.278	7.268	0.26	0.593	0.224	0.068	4641
1.5	2	8	18.4	1.766	7.624	0.331	0.705	0.287	0.06	3160
2	2.5	10.9	29.3	2.249	8.066	0.363	0.732	0.33	0.062	2500
2.5	3	11.8	41.1	2.764	8.887	0.382	0.743	0.359	0.057	1640
3	3.5	12.1	53.2	3.237	9.104	0.411	0.746	0.405	0.07	1216
3.5	4	10.1	63.3	3.74	10.058	0.385	0.731	0.43	0.057	746
4	4.5	8.6	71.9	4.241	10.509	0.353	0.71	0.454	0.039	497

4.5	5	7.9	79.8	4.743	11.469	0.337	0.689	0.463	0.043	342
5	5.5	5.7	85.5	5.225	11.868	0.317	0.68	0.475	0.039	199
5.5	6	4.2	89.7	5.765	13.346	0.259	0.675	0.466	0.024	108
6	6.5	3.6	93.3	6.224	17.013	0.197	0.6	0.416	0.046	76
6.5	7	3	96.3	6.793	15.383	0.165	0.596	0.468	0.022	55
7	7.5	1.1	97.4	7.195	17.554	0.172	0.508	0.438	0.002	18
7.5	8	1.2	98.6	7.778	16.138	0.102	0.545	0.504	0.007	13
8	8.5	0.6	99.2	8.322	18.046	0.178	0.657	0.483	0.023	6
8.5	9	0.2	99.4	8.653	15.807	0.109	0.214	0.549	0	2
9	9.5	0.1	99.5	9.172	20.295	0.088	0.684	0.451	0	1
9.5	10	0.2	99.7	9.799	22.588	0.057	0.664	0.435	0	1
10	10.5	0.3	100	10.17 4	24.014	0.047	0.623	0.423	0	1
10.5	11	0	100	0	0	1	0	0	0	0
11	11.5	0	100	0	0	1	0	0	0	0
11.5	12	0	100	0	0	1	0	0	0	0
12	12.5	0	100	0	0	1	0	0	0	0
12.5	13	0	100	0	0	1	0	0	0	0
13	13.5	0	100	0	0	1	0	0	0	0
13.5	14	0	100	0	0	1	0	0	0	0
14	14.5	0	100	0	0	1	0	0	0	0
14.5	15	0	100	0	0	1	0	0	0	0
15	15.5	0	100	0	0	1	0	0	0	0
15.5	16	0	100	0	0	1	0	0	0	0
16	16.5	0	100	0	0	1	0	0	0	0
16.5	17	0	100	0	0	1	0	0	0	0
17	17.5	0	100	0	0	1	0	0	0	0
17.5	18	0	100	0	0	1	0	0	0	0
18	18.5	0	100	0	0	1	0	0	0	0
18.5	19	0	100	0	0	1	0	0	0	0
19	19.5	0	100	0	0	1	0	0	0	0
19.5	20	0	100	0	0	1	0	0	0	0
20	1000	0	100	0	0	1	0	0	0	0

^a “SPHT” refers to the sphericity of the particle. For a sphere, the numerical value of SPHT will be 1.

^b “Symm” refers to the lowest of the measured set of symmetry values taken from different directions for a specific particle.

^c “ b/l_3 ” is the ratio of the minimum cord diameter (d_{c_min}) to the maximum Feret diameter (d_{FE_max}). This is a reciprocal of the particle aspect ratio.

^d “RDNS” indicates the roundness of the corners and edges of the particle.

^e “PDN” indicates the number of particle detections. The higher PDN value indicates that the measured values of the particle shape characteristics are more reliable.

Table A2: Preliminary empirical models including the main effects of different degrees of independent variables

Obs. No.	Preliminary regression models
1	model1 <- lm('Frictional pressure drop' ~ poly(AR,4) + poly(Cm,3) + poly(Vm,3) + Wheatstraw, data = data_train)
2	model2 <- lm('Frictional pressure drop' ~ poly(AR,5) + poly(Cm,3) + poly(Vm,3) + Wheatstraw, data = data_train)
3	model3 <- lm('Frictional pressure drop' ~ poly(AR,4) + poly(Cm,4) + poly(Vm,3) + Wheatstraw, data = data_train)
4	model4 <- lm('Frictional pressure drop' ~ poly(AR,4) + poly(Cm,3) + poly(Vm,4) + Wheatstraw, data = data_train)
5	model5 <- lm('Frictional pressure drop' ~ poly(AR,4) + poly(Cm,5) + poly(Vm,3) + Wheatstraw, data = data_train)
6	model6 <- lm('Frictional pressure drop' ~ poly(AR,4) + poly(Cm,3) + poly(Vm,5) + Wheatstraw, data = data_train)
7	Model7 <- lm('Frictional pressure drop' ~ poly(AR,3) + poly(Cm,3) + poly(Vm,3) + Wheatstraw, data = data_train)

Note: The symbol “AR” is the particle aspect ratio. This symbol was used while developing a code in R software.

Table A3: ANOVA test to select the most suitable preliminary empirical model including the highest possible orders of independent variables

ANOVA (model1, model2) – Significance of fifth order of AR						
Model	Res. Df	RSS	Df	Sum of squares	F	Pr(>F)
model1	1745	222.0				
model2	1744	221.84	1	0.15937	1.2529	0.2631
ANOVA (model1, model3) – Significance of fourth order of C_m						
Model	Res. Df	RSS	Df	Sum of squares	F	Pr(>F)
model1	1745	222.0				
model3	1744	221.56	1	0.44486	3.5017	0.06147
ANOVA (model1, model4) – Significance of fourth order of v_m						
Model	Res. Df	RSS	Df	Sum of squares	F	Pr(>F)
model1	1745	222.0				
model4	1744	221.59	1	0.40586	3.1942	0.07407
ANOVA (model1, model5) – Significance of fifth order of C_m						
Model	Res. Df	RSS	Df	Sum of squares	F	Pr(>F)

model1	1745	222.0				
model5	1743	221.45	2	0.5482	2.1574	0.1159
ANOVA (model1, model6) – Significance of fifth order of v_m						
Model	Res. Df	RSS	Df	Sum of squares	F	Pr(>F)
model1	1745	222.0				
model6	1743	221.35	2	0.65339	2.5726	0.07663
ANOVA (model1, model7) – Significance of third order of AR						
Model	Res. Df	RSS	Df	Sum of squares	F	Pr(>F)
model1	1745	222.0				
model7	1746	226.66	-1	-4.6562	36.599	1.771e-09

Table A4: Onset velocities of drag reduction (v_{OD}) obtained using experimental data for agricultural residue biomass slurries in vertical upward flows in R software

Obs. No.	Feedstock	Nominal particle size (mm)	Saturated mass concentration (C_m) (%)	Onset velocity of drag reduction (v_{OD}) (m s⁻¹)
1	Corn stover	19.2	15	1.2988
2	Corn stover	19.2	20	3.3493
3	Corn stover	6.4	5	2.7211
4	Corn stover	6.4	10	1.5014
5	Corn stover	6.4	15	1.4487
6	Corn stover	6.4	20	2.3484
7	Corn stover	3.2	10	3.1872
8	Corn stover	3.2	15	2.3767
9	Corn stover	3.2	20	1.9918
10	Corn stover	3.2	25	3.3817
11	Corn stover	<3.2	10	3.3614
12	Corn stover	<3.2	15	2.7657
13	Corn stover	<3.2	20	2.3889
14	Corn stover	<3.2	25	2.7414
15	Wheat straw	19.2	25	1.8742
16	Wheat straw	6.4	25	1.5379
17	Wheat straw	6.4	30	3.1872
18	Wheat straw	3.2	30	1.9715
19	Wheat straw	<3.2	20	2.4659
20	Wheat straw	<3.2	25	1.8945
21	Wheat straw	<3.2	30	3.4101

Table A5: Preparation of the aqueous-based slurry of the 6.4 mm nominal particle size of wheat straw for the desired saturated solid mass concentration

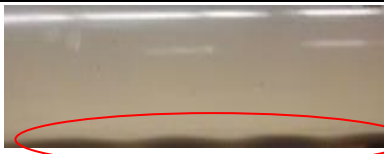



Apparent mass concentration of saturated solid-water slurry (%)	Mass of fresh straw required for the corresponding apparent concentration (Kg)	Initial volume of water required in the mixing tank to prepare a slurry of maximum apparent mass concentration (Imperial gallon)	Volume of saturated slurry in the mixing tank (Imperial gallon)	New volume of slurry in the mixing tank after each dilution step to get the next desired concentration (Imperial gallon)
30	19.905	56.75	60	-
25	16.545	-	60	75.4
20	13.202	-	60	79.16
15	9.876	-	60	85.48
10	6.568	-	60	98.12
5	3.276	-	60	136.75

Table A6: Empirical and semi-empirical models taken from the literature used for the calibration of inclined and horizontal pipe sections in the present study

Authors	Model	Pipe inclination wrt the x-axis
Worster and Denny (1955)	<p><u>Basic model:</u></p> $-\Delta I_{m,\theta} = -(I_{m,\theta} - I_w) = -\Delta I_{m,0} \cos \theta + (\rho_m - \rho_w)g \sin \theta$ $- \left[\left(\frac{dP}{dL} \right)_{m,\theta} - \left(\frac{dP}{dL} \right)_w \right]$ $= - \left[\left(\frac{dP}{dL} \right)_{m,0} - \left(\frac{dP}{dL} \right)_w \right] \cos \theta + (\rho_m - \rho_w)g \sin \theta$ <p><u>Measured pressure drop by DPT:</u></p> $- \left(\frac{dP}{dL} \right)_{m,\theta}^{Md} = - \left(\frac{dP}{dL} \right)_w - \left[\left(\frac{dP}{dL} \right)_{m,0} - \left(\frac{dP}{dL} \right)_w \right] \cos \theta + (\rho_m - \rho_w)g \sin \theta$ <p><u>Total pressure drop:</u></p> $- \left(\frac{dP}{dL} \right)_{m,\theta}^{Total} = - \left(\frac{dP}{dL} \right)_w - \left[\left(\frac{dP}{dL} \right)_{m,0} - \left(\frac{dP}{dL} \right)_w \right] \cos \theta + \rho_m g \sin \theta$	Inclined (ascending or descending)

	<u>Frictional pressure drop component:</u> $-\left(\frac{dP}{dL}\right)_{m,\theta}^f = -\left(\frac{dP}{dL}\right)_w - \left[\left(\frac{dP}{dL}\right)_{m0} - \left(\frac{dP}{dL}\right)_w\right] \cos \theta$	
Durand & Condolios (1953)	$I_m = I_w \left[1 + 81 \left\{ \frac{v^2 \sqrt{C_d}}{gD(S-1)} \right\}^{-\frac{3}{2}} C_V \right]$	Horizontal
Gibert (1960)	$I_{m,\theta} = I_w \left[1 + 81 \left\{ \frac{v^2 \sqrt{C_d}}{gD(S-1)} \right\}^{-\frac{3}{2}} C_V (\cos \theta)^{\frac{3}{2}} \right] + \{1 + C_V(S-1)\} \sin \theta$	Inclined (ascending or descending)
Churchill (1977)	$f_D = \left[\left(\frac{8}{Re} \right)^{12} + \left(\frac{1}{(A+B)^{\frac{3}{2}}} \right)^{\frac{1}{12}} \right]$ $A = \left[2.457 \ln \left(\frac{1}{\left(\frac{7}{Re} \right)^{0.9} + \left(\frac{0.27e}{D} \right)} \right) \right]^{16}$ $B = \left(\frac{37530}{Re_e} \right)^{16}$ $\epsilon = \frac{e}{D}$ <p>ϵ = Relative roughness e = Absolute roughness (mm) $Re = \frac{\rho_w \cdot D \cdot v}{\mu_w}$</p>	Horizontal, vertical, and inclined

Table A7: Flow patterns of fine sand and wheat straw-water slurries in inclined pipe sections

Slurry velocity y ($m\ s^{-1}$)	Fine sand		Flow pattern
	Side view		
0.5			Static dunes
	$C_V=1\%, \theta=0^\circ$	$C_V=3\%, \theta=+14^\circ$	
0.5			Static bed






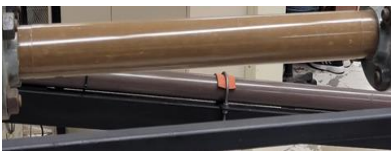



	$C_V=3\%, \theta=+21^\circ$	$C_V=5\%, \theta=-7^\circ$	
0.5			Static dunes
	$C_V=1\%, \theta=+7^\circ$		
1.0			Dispersed
	$C_V=3\%, \theta=0^\circ$	$C_V=5\%, \theta=+21^\circ$	
	Wheat straw		
0.5			Dispersed (No bed formation)
	$C_m=30\%, \theta=0^\circ$	$C_m=30\%, \theta=+7^\circ$	
0.5			Dispersed (No bed formation)
	$C_m=30\%, \theta=-7^\circ$	$C_m=30\%, \theta=+14^\circ$	
0.5			Dispersed (No bed formation)
	$C_m=30\%, \theta=+21^\circ$	$C_m=30\%, \theta=+21^\circ$	

Table A8: Onset velocities of drag reduction (v_{OD}) obtained in R software using experimental data for 6.4 mm particle size of wheat straw-water slurries in inclined flows at various slopes

Obs. No.	Feedstock	Pipe inclination angle (θ) ($^{\circ}$)	Saturated mass concentration (C_m) (%)	Onset velocity of drag reduction (v_{OD}) (m s^{-1})
1	Wheat straw	-7	5	1.7713
2	Wheat straw	-7	10	0.9303
3	Wheat straw	-7	15	0.90178
4	Wheat straw	-7	20	1.1227
5	Wheat straw	-7	25	1.6929
6	Wheat straw	-7	30	2.8404
7	Wheat straw	0	5	2.6944
8	Wheat straw	0	10	1.2439
9	Wheat straw	0	15	0.9225
10	Wheat straw	0	20	1.2297
11	Wheat straw	0	25	1.7727
12	Wheat straw	0	30	3.1446
13	Wheat straw	+7	5	-
14	Wheat straw	+7	10	-
15	Wheat straw	+7	15	1.1725
16	Wheat straw	+7	20	1.3098
17	Wheat straw	+7	25	1.8383
18	Wheat straw	+7	30	3.2318
19	Wheat straw	+14	5	2.1519
20	Wheat straw	+14	10	1.5046
21	Wheat straw	+14	15	1.0662
22	Wheat straw	+14	20	1.1809
23	Wheat straw	+14	25	1.5181
24	Wheat straw	+14	30	3.3861
25	Wheat straw	+21	5	2.4917
26	Wheat straw	+21	10	2.0127
27	Wheat straw	+21	15	1.1546
28	Wheat straw	+21	20	1.2943
29	Wheat straw	+21	25	1.7267
30	Wheat straw	+21	30	3.3299

Appendix B

Experimental determination of terminal settling velocity of ARB

To achieve higher production capacities for biorefineries, Our research group have found that the pipeline hydro-transport of lignocellulosic biomass is techno economically favorable mode of delivery than trucking (Vaezi et al., 2015). However, due to the variations in sizes, shapes, surface features, and coarseness of biomass particles obtained from knife mill operation, there is a need to accurately predict the terminal settling velocity and flow regimes of these particles in still water to understand the rheological behaviour of their slurries. Therefore, we carried out a laboratory-scale investigation with the following main objectives.

- To experimentally investigate the terminal settling velocity of different lengths of the agricultural residue biomass particles in a bounded quiescent medium.
- To find the biomass particles' hydrodynamic behaviour (i.e., flow regimes) in a quiescent medium.
- To explore the buoyant nature of the biomass particles concerning the mixture velocity during pipeline hydro-transport.

Material and Method:

We took two samples of 10 g weight of knife-milled 19.2 mm nominal-sized particles of each feedstock of agricultural residue biomass (i.e., corn stover and wheat straw). We manually separated different types (sub-categories) of particles (Figure B1).

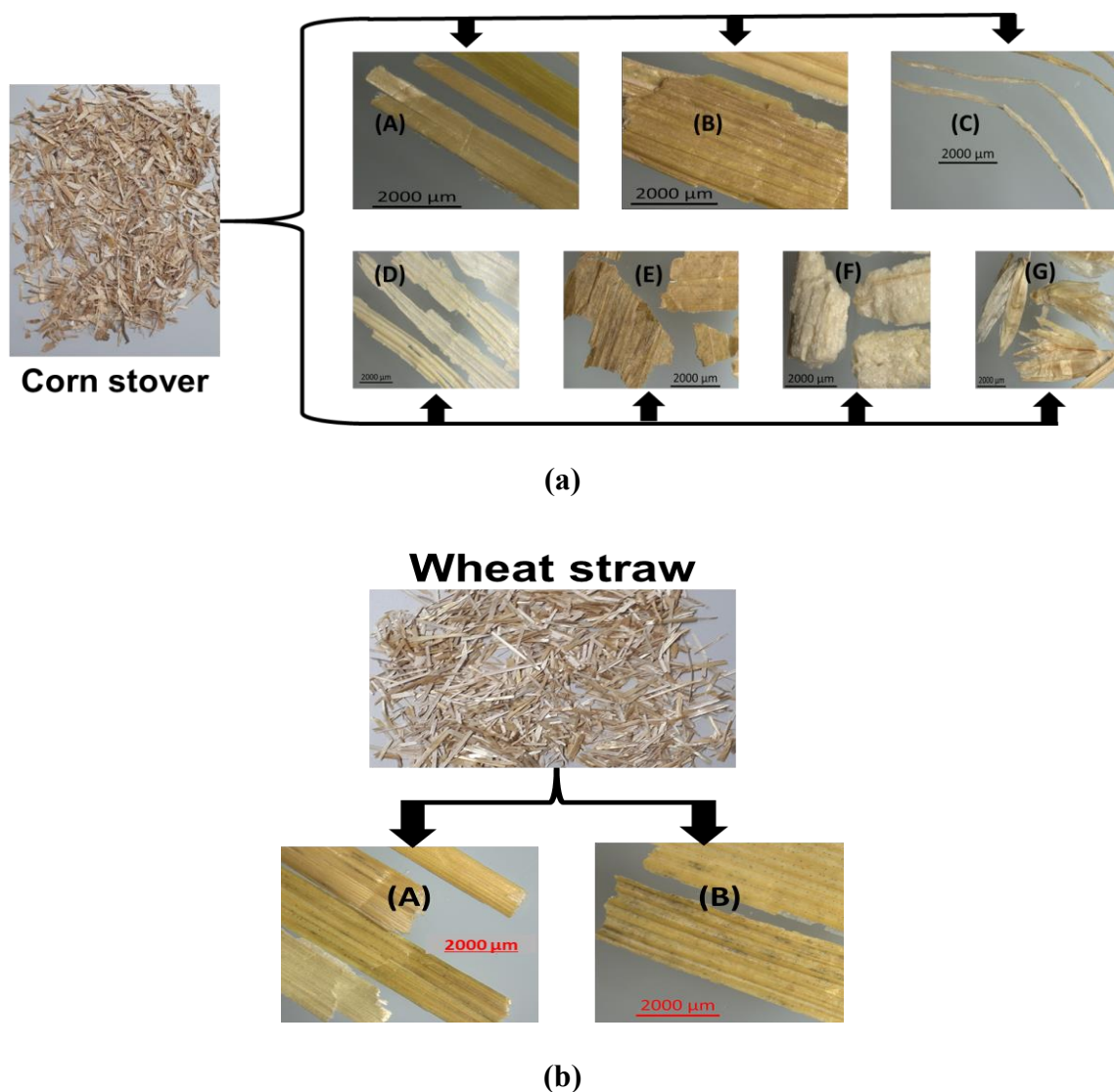


Figure B1: Microscopic images of sub-categories of particles obtained from samples of 19.2 mm nominal size of (a) corn stover, and (b) wheat straw samples. Type A: Rib like particles with plane surfaces, Type B: Rib like particles with rough surfaces, Type C: Hair-like particles, Type D: Flake-like particles, Type E: Wide flake-like particles, Type F: Irregular shaped thick particles, Type G: Mixed form particles.

We found seven different types of particles in corn stover, whereas, in wheat straw, we obtained two different types of particles, as shown in Figure B1. Figure B2 shows the mass percentages of

different types of particles of corn stover. Whereas, for wheat straw, the mass percentages of both the classes (i.e., type A and type B particles) were almost similar (i.e., 50% each).

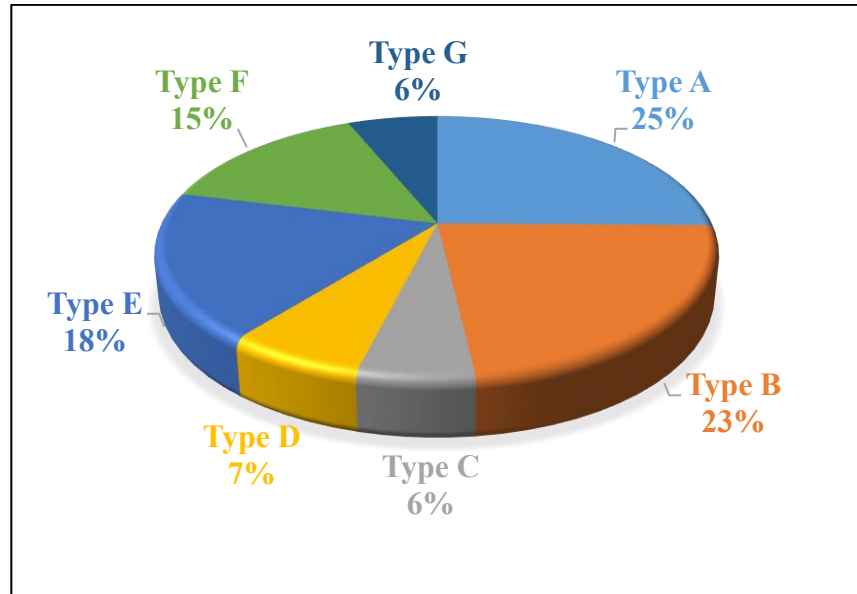


Figure B2: Mass percentage (average) of sub-categories of particles separated from corn stover sample of 19.2 mm nominal length.

As type A and B for corn stover collectively had 50% mass percentage, and for wheat straw, each of these types had a 50% mass percentage. Therefore, in the first phase of our experimentation, we only focused on determining these particle types' terminal settling velocities. We considered only two widths, i.e., 2 mm and 1 mm of the particles for the analysis during this phase. Each of the sub-category of particles of both the feedstocks were cut to the require particle lengths of 5-30 mm. For accuracy, the particle dimensions (i.e., length, width, and thickness) were measured using Zeiss Stemi 508 Microscope. We collected many particles of each length and width of both types A and B of corn stover and wheat straw for experimentation. Table B1 and Table B2 demonstrate the physical properties of the particles of type A and B for both the feedstocks.

Table B1: Physical properties of particles of Type A and B for Wheat straw and Corn stover

Material/ Particle type	Particle length (l_p) (mm)	Particle width (w_p) (mm)	Particle thickness (t_p) (mm)	Particle aspect ratio (-)	Particle volume (mm ³)	Mass of dry particle (mg)	Saturated particle density (Kg m ⁻³)
W.S A152	5.94	2.02	0.5	2.94	5.999	0.783	1050
W.S A1102	10.63	1.74	0.5	6.11	9.253	1.28	1050
W.S A1152	15.34	1.78	0.5	8.62	13.644	2.1	1050
W.S A1202	20.54	1.90	0.5	10.83	19.489	2.633	1050
W.S A1252	25.00	2.36	0.5	10.61	29.444	4.333	1050
W.S A1302	30.00	2.17	0.5	13.80	32.610	4.1	1050
W.S B152	4.70	2.34	0.5	2.00	5.507	0.717	1050
W.S B1102	11.37	2.04	0.5	5.56	11.626	1.833	1050
W.S B1152	15.11	2.09	0.5	7.21	15.820	1.933	1050
W.S B1202	19.74	1.99	0.5	9.92	19.641	3.333	1050
W.S B1252	25.00	2.40	0.5	10.41	30.014	5.133	1050
W.S B1302	30.00	1.90	0.5	15.77	28.527	5.233	1050
C.S A152	5.06	2.08	0.962	2.44	10.114	1.5	1060.838
C.S A1102	10.34	1.82	0.654	5.69	12.273	4.5	1060.838
C.S A1152	15.13	1.89	0.510	8.02	14.568	7.4	1060.838
C.S A1202	20.00	2.65	0.652	7.54	34.611	5.6	1060.838
C.S A1252	25.00	2.40	0.775	10.43	46.437	12.1	1060.838
C.S A1302	30.00	2.11	0.783	14.25	49.454	16.5	1060.838
C.S B152	5.60	1.99	0.554	2.82	6.158	1.3	1060.838
C.S B1102	11.09	2.18	0.712	5.09	17.191	3.1	1060.838
C.S B1152	15.70	2.32	0.433	6.78	15.738	3.8	1060.838
C.S B1202	20.08	2.14	0.458	9.37	19.713	6.6	1060.838
C.S B1252	25.00	2.41	0.423	10.39	25.443	5.2	1060.838
C.S B1302	30.00	2.22	0.404	13.53	26.866	11.2	1060.838
C.S B151	5.55	1.22	0.359	4.54	2.435	1.6	1060.838
C.S B1101	11.05	1.27	0.481	8.70	6.744	2.2	1060.838
C.S B1151	14.98	1.13	0.475	13.24	8.046	2.3	1060.838
C.S B1201	20.37	1.26	0.440	16.14	11.302	2.1	1060.838
C.S B1251	25.00	1.22	0.407	20.43	12.443	2.7	1060.838
C.S B1301	30.00	1.33	0.850	22.60	33.846	11.3	1060.838

Table B2: Derived physical properties of particles of Type A and B for Wheat straw and Corn stover

Material/ Particle type	d_v (mm)	A_p (mm²)	d_p (mm)	Surface Area (mm²)	d_s (mm)	Sphericity (-)	Effective particle density (Kg m⁻³)
W.S A152	2.2544	11.9989	3.9086	31.9590	3.1895	0.4996	130.57
W.S A1102	2.6047	18.5060	4.8541	49.3862	3.9649	0.4316	138.33
W.S A1152	2.9647	27.2883	5.8944	71.6942	4.7771	0.3852	153.91
W.S A1202	3.3388	38.9771	7.0447	100.3934	5.6530	0.3488	135.12
W.S A1252	3.8312	58.8875	8.6590	145.1306	6.7968	0.3177	147.17
W.S A1302	3.9638	65.2193	9.1126	162.6125	7.1945	0.3035	125.73
W.S B152	2.1910	11.0150	3.7450	29.0729	3.0421	0.5188	130.13
W.S B1102	2.8107	23.2518	5.4411	59.9207	4.3673	0.4142	157.69
W.S B1152	3.1146	31.6405	6.3471	80.4829	5.0615	0.3787	122.21
W.S B1202	3.3475	39.2817	7.0721	100.2974	5.6503	0.3510	169.71
W.S B1252	3.8557	60.0279	8.7424	147.4568	6.8510	0.3167	171.03
W.S B1302	3.7910	57.0542	8.5231	146.0103	6.8174	0.3092	183.45
C.S A152	2.6831	10.5185	3.6596	34.7680	3.3267	0.6505	148.31
C.S A1102	2.8619	18.7734	4.8891	53.4351	4.1242	0.4815	366.67
C.S A1152	3.0302	28.5637	6.0306	74.4890	4.8693	0.3873	507.96
C.S A1202	4.0433	53.0786	8.2208	135.7035	6.5723	0.3785	161.80
C.S A1252	4.4595	59.9052	8.7335	162.2843	7.1873	0.3850	260.57
C.S A1302	4.5541	63.1605	8.9676	176.5975	7.4975	0.3690	333.64
C.S B152	2.2741	11.1227	3.7632	30.6467	3.1233	0.5301	211.11
C.S B1102	3.2021	24.1552	5.5458	67.1934	4.6247	0.4794	180.32
C.S B1152	3.1092	36.3706	6.8050	88.3337	5.3026	0.3438	241.45
C.S B1202	3.3516	43.0362	7.4024	106.4277	5.8204	0.3316	334.81
C.S B1252	3.6492	60.1698	8.7527	143.5181	6.7589	0.2915	204.37
C.S B1302	3.7159	66.5151	9.2027	159.0557	7.1154	0.2727	416.89
C.S B151	1.6691	6.7807	2.9383	18.4250	2.4217	0.4750	657.17
C.S B1101	2.3441	14.0295	4.2264	39.9037	3.5639	0.4326	326.20
C.S B1151	2.4861	16.9516	4.6458	49.1991	3.9573	0.3947	285.87
C.S B1201	2.7843	25.7120	5.7217	70.4423	4.7352	0.3457	185.81
C.S B1251	2.8750	30.5891	6.2408	82.5119	5.1249	0.3147	217.00
C.S B1301	4.0133	39.8306	7.1214	132.9020	6.5041	0.3807	333.87

Where d_v , A_p , d_p , and d_s are volume equivalent spherical diameter, projected area, projected diameter, and surface equivalent spherical diameter of the biomass particles, respectively. We evaluated these parameters using the following relations.

$$d_v = \left[\frac{6V}{\pi} \right]^{\frac{1}{3}} \quad (\text{Eq. B1})$$

$$A_p = L_p \cdot W \quad (\text{Eq. B2})$$

$$d_p = \left[\frac{4A_p}{\pi} \right]^{1/2} \quad (\text{Eq. B3})$$

$$d_s = \left[\frac{SA}{\pi} \right]^{1/2} \quad (\text{Eq. B4})$$

$$\text{Surface area} = SA = 2[(l_p \cdot w_p) + (w_p \cdot t_p) + (l_p \cdot t_p)] \quad (\text{Eq. B5})$$

$$\text{Sphericity} = \left[\frac{d_s}{d_v} \right]^{-2} \quad (\text{Eq. B6})$$

We obtained the effective particle density (Table B1) by dividing the particle's mass by volume, including open and closed pores. This density is critical, including flow around the particles like fluidization, sedimentation, flow through packed beds, etc.

Figure B3 shows the experimental setup for determining the terminal settling velocity of biomass particles.

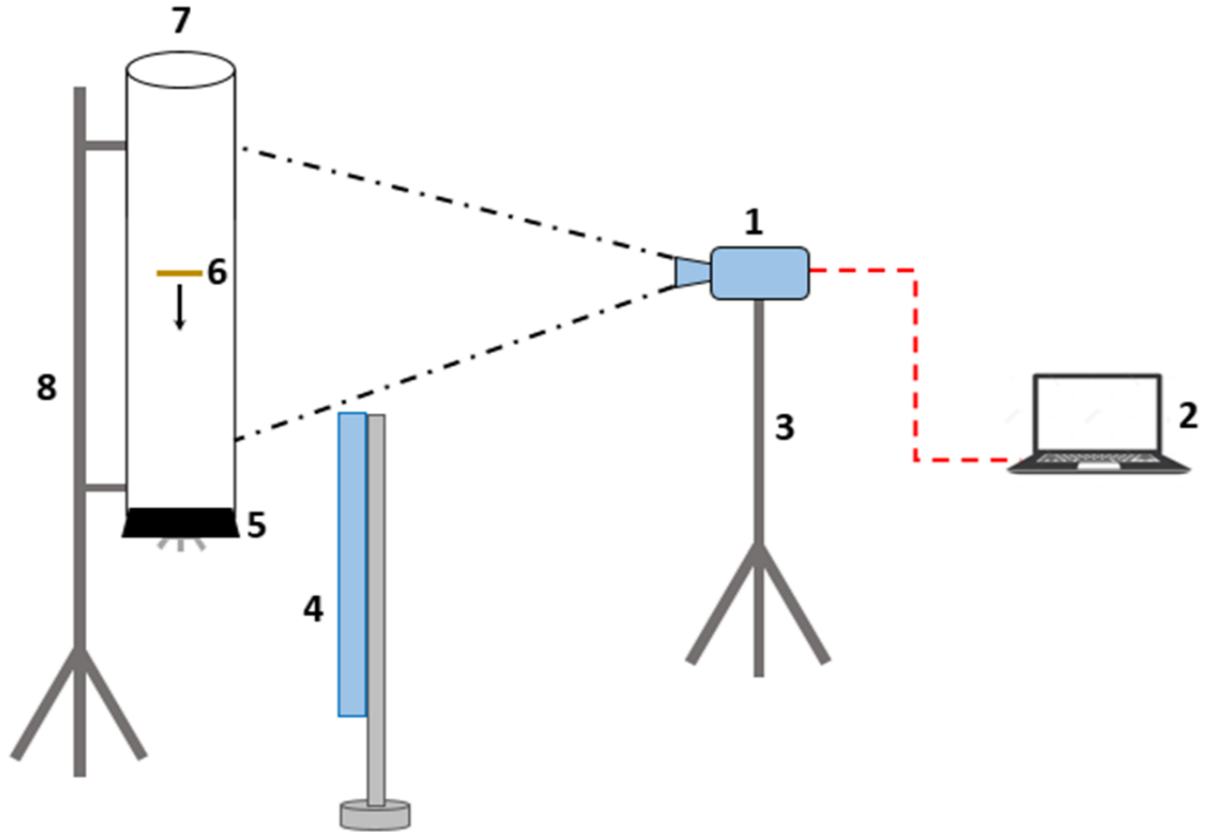


Figure B3: Schematic of the experimental setup - (1) High resolution digital camera, (2) Computer, (3) Tripod stand, (4) Light source, (5) Expandable plug, (6) Settling of biomass particle, (7) Vertical transparent test section, (8) Fixed support for test section.

We filled the vertical transparent test section of 50.8 mm inner diameter and length of 0.305 m with water and left it overnight at room temperature to remove air from the system. The pre-cut biomass particles of known dimensions (Table B1) were soaked in water in a separate container until saturated. We dropped the saturated particle of known dimensions from the top of the pipe (filled with water) with a non-stick tweezer. We recorded the particle movement with a high-resolution camera. We then analysed the recorded video of biomass particles falling in the still water in open-source software (Tracker 5.1.5) for evaluating the terminal settling velocity of the particle. A similar procedure was adopted for a 100 mm inner diameter of the pipe section.

Results and Discussion:

Figure B4 shows the evaluation of the terminal settling velocity of wheat straw particle (type A) of 10 mm length and 2 mm width using Tracker software.

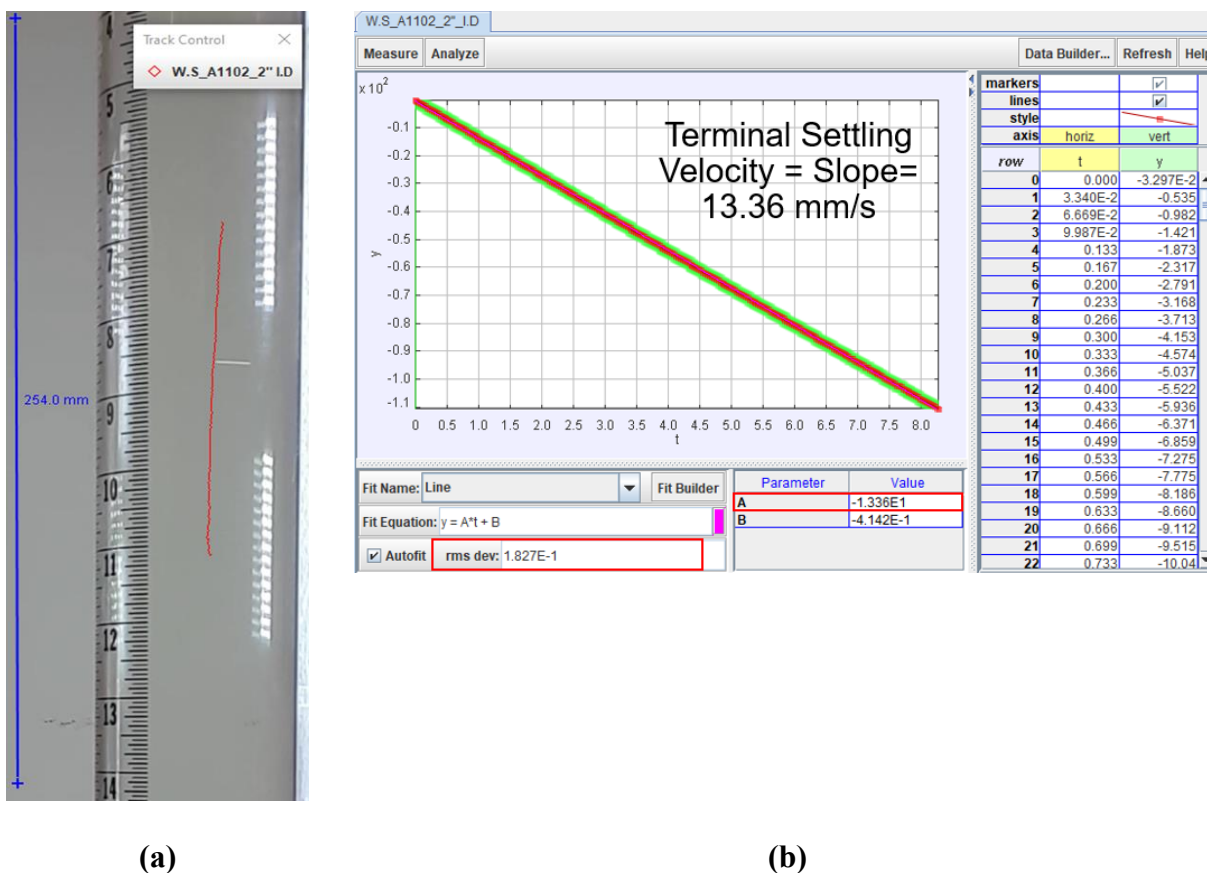


Figure B4: Illustration of a typical experiment showing (a) particle's fall trajectory, and (b) settling velocity evaluated by Tracker software (Version: 5.1.5).

We evaluated the terminal settling velocity of only those particles whose longitudinal axis was perpendicular to the fall direction (i.e., downward) as shown in Figure B4 (a). The standard error in evaluating the terminal settling velocity was found in the range of 0.0012-0.38 mm/s. Further, the experiments for terminal settling velocities of each particle size were repeated three times. Figures B5-B7 show the results of terminal settling velocities of different lengths and widths of

type A and B particles of corn stover and wheat straw in 50.8 mm and 100 mm diameter vertical test sections.

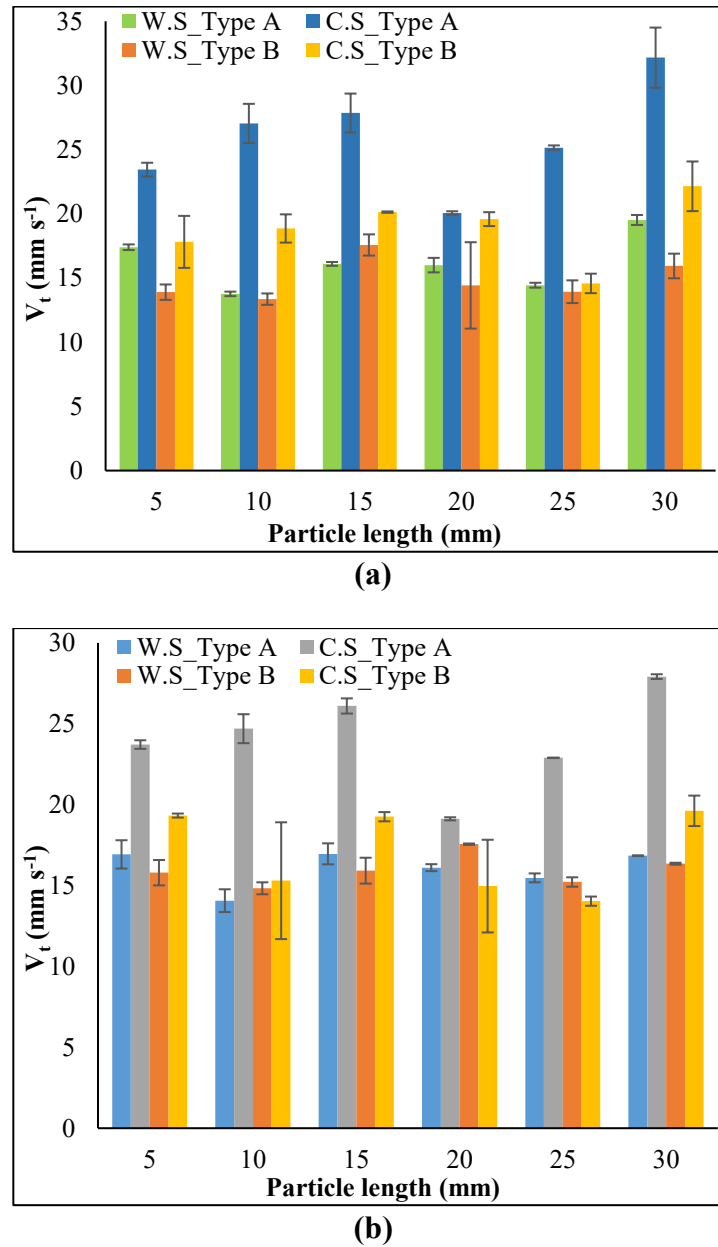
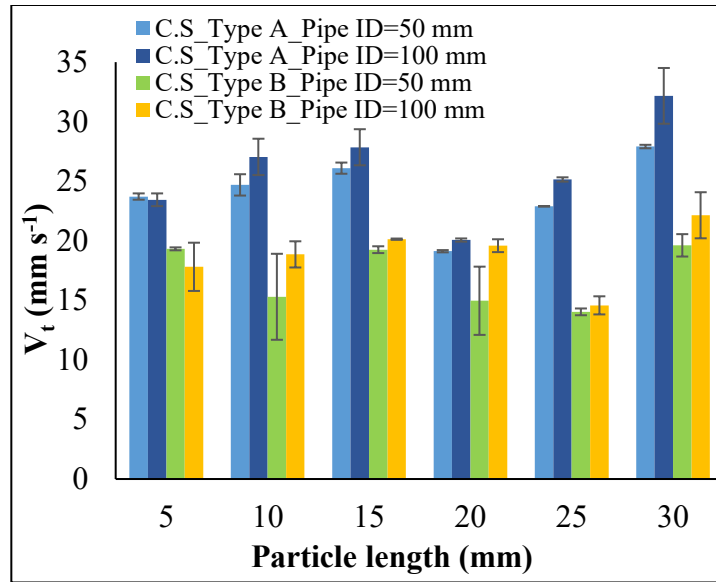
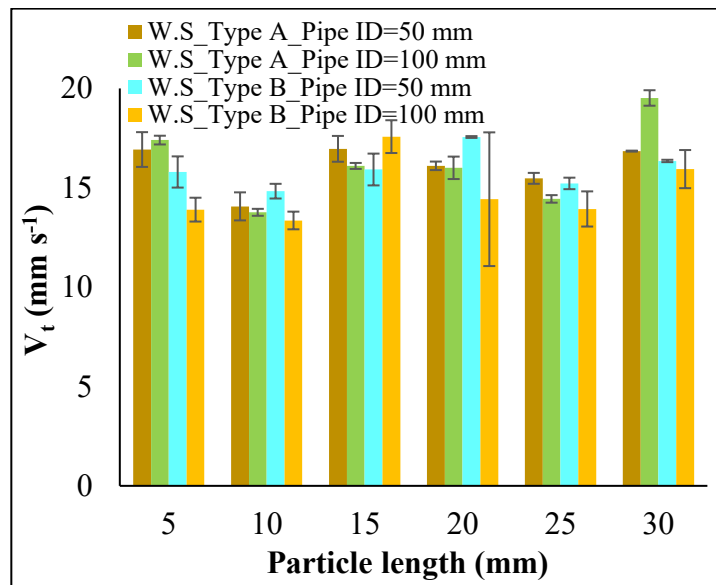


Figure B5: Terminal settling velocity (v_t) versus length of corn stover (C.S) and wheat straw (W.S) particles 2 mm wide obtained experimentally in quiescent water for pipes (a) 100 mm and (b) 50 mm in diameter at room temperature.

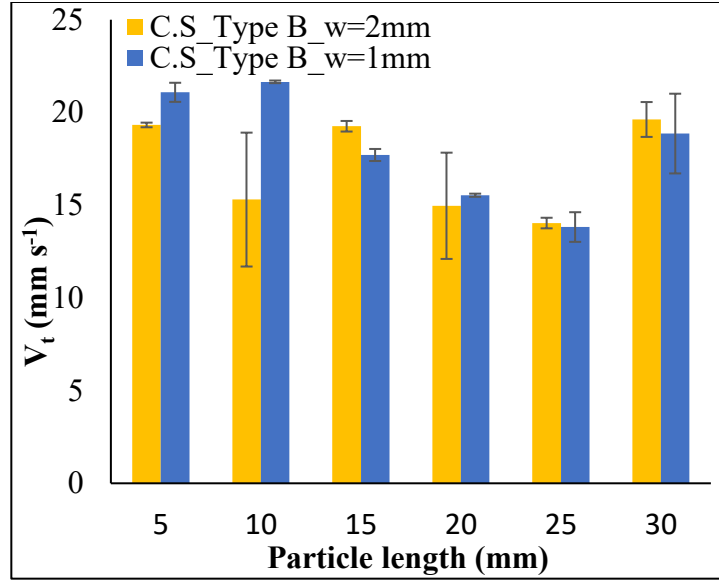


(a)

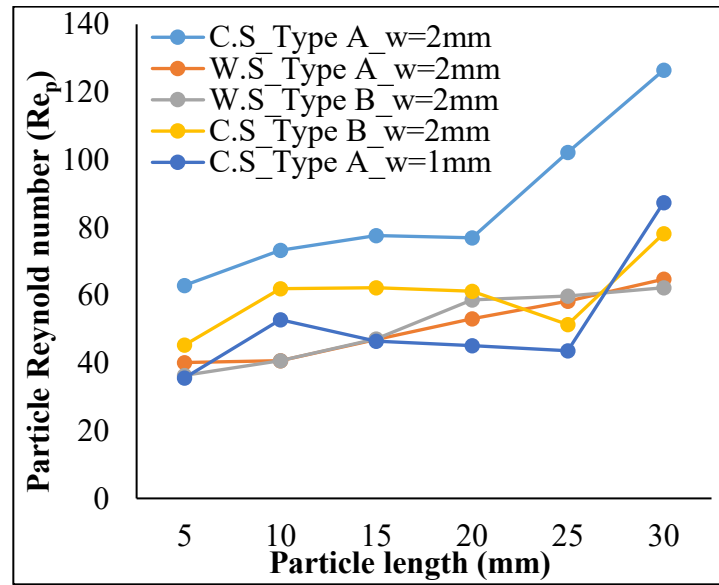


(b)

Figure B6: Effect of pipe diameter on terminal settling velocity of Type A, and B particles of various lengths and 2 mm width of (a) corn stover, (b) wheat straw, in quiescent water at room temperature.



(a)



(b)

Figure B7: (a) Effect of particle width on terminal settling velocity of various lengths of corn stover in quiescent water in a 50 mm dia. Pipe, (b) Particle Reynolds number versus length for various feedstocks, types, and particle widths for 50 mm pipe diameter pipe.

The data in Figures B5–B7 are the mean values of three independent measurements of the associated parameters for each particle size. Particle Reynolds number ($Re_p = \frac{d_p \rho_w v_t}{\mu_w}$) was

evaluated using the water properties (i.e., temperature, density, dynamic viscosity) contained in the vertical test section and the volume equivalent diameter of each biomass particle. Based on the results presented in Figures B5-B7, we concluded that:

- The terminal settling velocity of biomass particles depends upon the type of feedstock, particle type of a specific feedstock, particle length or aspect ratio, and the fall attitude in the vertical column.
- For most corn stover particles (both type A and B), terminal settling velocity increased with increasing the particle length irrespective of the pipe diameter; however, wheat straw particles did not consistently follow the same trend.
- Generally, we found the terminal settling velocities of type A corn stover particles to be 25%-96% greater than those of the wheat straw type A particles. In contrast, type B particles of corn stover showed 3%-41% greater velocities than the corresponding (i.e., type B) wheat straw particles of the same lengths and widths in both vertical columns.
- The terminal settling velocity of type A particles of corn stover was always more significant than its type B particles for both the diameters tested.
- We found no significant effect of particle width on the terminal settling velocity of corn stover for the range of conditions.
- The particle Reynolds numbers for wheat straw and corn stover were found in the ranges of 36-64 and 45-127, respectively.
- The results revealed that all the particles (Type A and B) of both the feedstocks would be neutrally buoyant (i.e., $\frac{v_t}{v_m} \leq 0.021$ for the mixture velocities $v_m \geq 1.0 \text{ m s}^{-1}$ during pipeline hydro-transport. This statement is valid for the feedstocks' largest particle size (i.e., 19.2mm).

Appendix C

Procedure for delivered concentration measurement of conventional solids

The delivered concentration was measured using medium sand, glass beads, and fine sand at a full mixer speed, level of mixing tank as 70 gallons (imperial), and constant slurry bulk velocity of 3.0 m s^{-1} . Full mixer speed and the stated slurry level in the mixing tank were selected to create harmony between the pressure drop tests performed for the conventional slurries and the delivered concentration tests. This selection was based on experimental evidence of getting different values of C_{Vd} at two different mixer speeds for a specific prepared concentration (C_{Vp}) of medium sand. As the critical deposition velocity (v_D) varies due to changes in slurry concentration (Wasp & Aude, 1970; Wasp et al., 1977), therefore, for the entire range of concentrations of all the materials tested in the current investigation, the v_D in the form of the range has been shown in Table 2.1. The slurry bulk velocity of 3.0 m s^{-1} was selected to be more than the minimum deposition velocity (v_D) and the critical velocity (v_4) for pseudo-homogeneous regime (Table 2.1) for all the selected materials to ensure the flow was homogeneous for getting accurate results. Further, visual observations through the flow visualization section (part no: 4 in Figure 2.1) also validated the homogeneity of any particular mixture's flow during samplings for C_{Vd} . The following general method was devised for measuring the C_{Vd} .

- a. Calculation of the required mass of the solids needed to make desired prepared concentrations (C_{Vp}) for a specific volume of the loop at a known water temperature.
- b. Fill the closed vertical loop with water up to the desired level of the mixing tank and let the water run inside the loop for some time to get the desired temperature and remove air.
- c. Turn on the mixer and add solids of known mass into the mixing tank to get desired C_{Vp} .

- d. Let the slurry run for some time to remove air from the system.
- e. Set the bulk velocity of the slurry at 3.0 m s^{-1} after the complete evacuation of air from the system.
- f. Collect the slurry sample in a bucket (25 l) carefully to avoid wastage (due to overflow) by lifting the return pipe hose (Figure 3.1) and recording the collection time.
- g. Measure the total volume of the mixture ($V_{mix.}$) using the calibrated container (Figure C1 [a]).
- h. Remove water completely from the collected mixture with great care after settling down all the particles, and put it back into the mixing tank to avoid a change in C_{vp} due to the sample withdrawal.
- i. Measure the mass of solids after removing water. This mass was termed a wet mass of solids because it still contained some water despite complete extraction in the previous step.
- j. Add a similar amount of wet mass from a separate source (container) into the closed loop to maintain consistency in C_{vp} in the loop. This wet mass was prepared separately as a backup material to compensate for the slurry loop deficiency during sampling.
- k. Scatter the wet mass of solids (obtained in step “i”) on water-absorbent paper and leave for a few days until it completely dries by air.
- l. Measure the mass of the dried mass of solids (m_s).



(a)



(b)

Figure C1: Samples collected for delivered concentration (a) Mixture (b) Dry solids.

- m. Calculate the volume of dried solids (V_s) using Eq. C1

$$V_s = \frac{m_s}{\rho_s} \quad (\text{Eq. C1})$$

- n. Calculate the volumetric delivered concentration (C_{vd}) using Eq. C2

$$C_{vd} = \left[\frac{V_s}{V_{mix.}} \right] \times 100 \quad (\text{Eq. C2})$$

- o. Collect three samples for each C_{vp} to calculate the corresponding values of C_{vd} using the previous steps.

There were two possible sources of errors in the delivered concentration analysis, which could affect the accuracy of the measurements. The first probable source was the surface water left in the bucket while separating water from wet sand, as explained in step-g above. The surface water left in the bucket was collected further despite having a minimal quantity to avoid errors. The second source was the entrapped water within sold particles in a wet sample (obtained in step-i)

and the surface water on individual solid particles. The delivered concentration was evaluated by completely drying the wet mass of sand in the air for several days to reduce measurement errors. The results of C_{vd} obtained for medium sand, glass beads, and fine sand at corresponding values of C_{vp} , keeping the bulk velocity constant at $v = 3.0 \text{ m s}^{-1}$, are shown in Table C1. Every single value of C_{vd} mentioned in Table C1 represents an average of three samples collected for corresponding C_{vp} .

Table C1: Correlations of delivered concentration (C_{vd}) at $v = 3.0 \text{ m s}^{-1}$

Prepared Concentration (C_{vp}) (%)	Delivered Concentration (C_{vd}) (%)	$\left(\frac{C_{vd}}{C_{vp}}\right)$	$\left(\frac{C_{vd}}{C_{vp}}\right)_{Avge}$
Medium Sand ($d_p = 0.447$ mm)			
1.0	2.168856993	2.168856993	2.085
2.5	5.208175179	2.083270072	
3.0	6.547643911	2.18254797	
5.0	9.524170581	1.904834116	
Glass Beads ($d_p = 0.5$ mm)			
1.0	2.31261913	2.31261913	2.5185
2.5	6.728006565	2.691202626	
5.0	12.75827645	2.551655291	
Fine Sand ($d_p = 0.103$ mm)			
1.0	0.97850734	0.97850734	0.9878
3.0	2.891214301	0.9637381	
5.0	5.106018804	1.021203761	

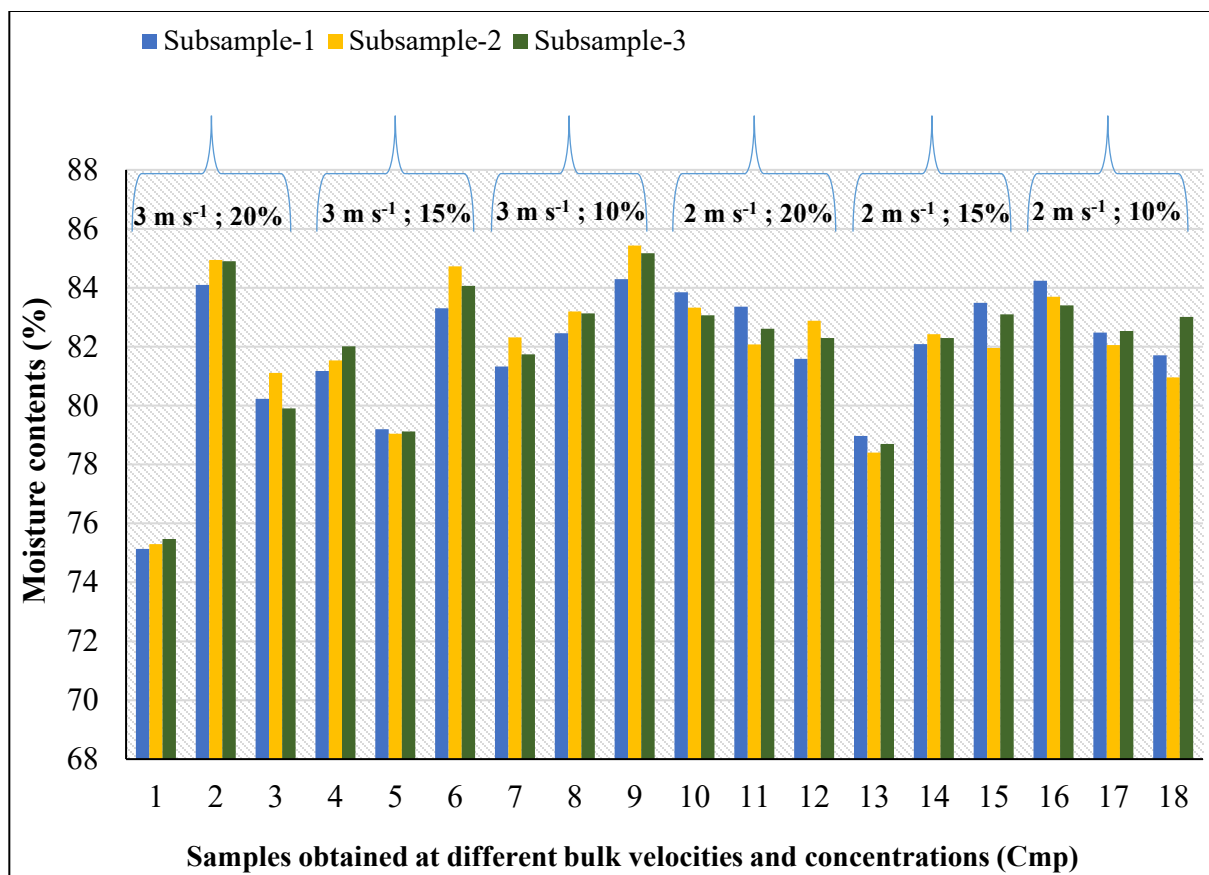


Figure C2: Moisture contents of 19.2 mm nominal size of wheat straw particles obtained from Thermogravimetric analyser (TGA 710).

Appendix D

Proposed design of 100 mm diameter closed pipeline loop

To upscale the pipeline facility in our lab at the University of Alberta, we proposed the complete design and layout of a 100 mm inside diameter, 39 m long closed pipeline loop based on our experience gained during experimentation in a large-scale fluids lab with a 50.8 mm inside diameter closed circuit pipeline facility and the extensive literature review on pipeline design. Figure D1 depicts the entire layout.

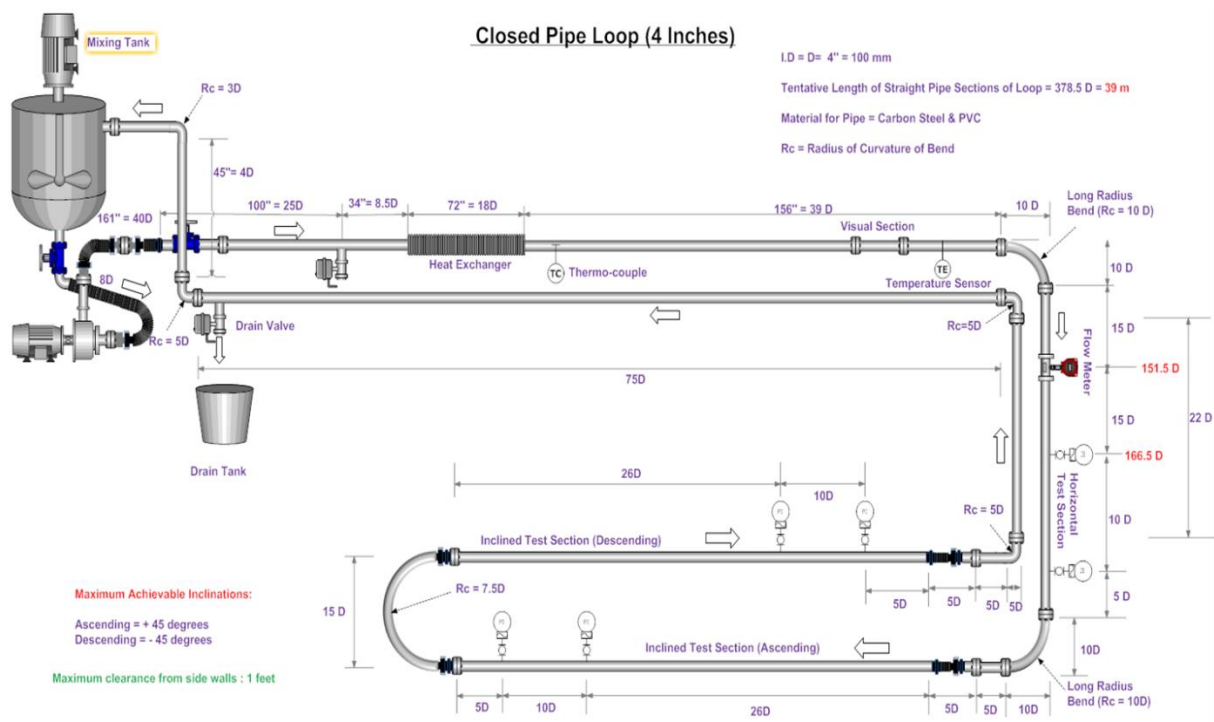


Figure D1: Proposed 100 mm diameter (ID) design and 39 m of closed pipeline loop to upscale the experimental setup for pipeline hydro-transport of biomass at large-scale fluids lab.